Michail Michailov
Editor

SPRINGER SERIES IN SURFACE SCIENCES 47

Nanophenomena at Surfaces

Fundamentals of Exotic Condensed Matter Properties

Springer

SPRINGER SERIES IN SURFACE SCIENCES

Series Editors: G. Ertl, H. Lüth and D.L. Mills

This series covers the whole spectrum of surface sciences, including structure and dynamics of clean and adsorbate-covered surfaces, thin films, basic surface effects, analytical methods and also the physics and chemistry of interfaces. Written by leading researchers in the field, the books are intended primarily for researchers in academia and industry and for graduate students.

Please view available titles in *Springer Series in Surface Sciences*
on series homepage http://www.springer.com/series/409

Michail Michailov
(Editor)

Nanophenomena at Surfaces

Fundamentals of Exotic Condensed Matter Properties

With 145 Figures

Springer

Volume Editor:

Associate Professor Dr. Michail Michailov
Bulgarian Academy of Sciences
Institute of Physical Chemistry
Georgi Bonchev Street, Block 11, 1113 Sofia, Bulgaria
E-mail: mike@ipc.bas.bg

Series Editors:

Professor Dr. Gerhard Ertl
Fritz-Haber-Institute der Max-Planck-Gesellschaft, Faradayweg 4–6,
14195 Berlin, Germany

Professor Dr. Hans Lüth
Institut für Schicht- und Ionentechnik
Forschungszentrum Jülich GmbH,
52425 Jülich, Germany

Professor Douglas L. Mills, Ph.D.
Department of Physics, University of California,
Irvine, CA 92717, USA

Springer Series in Surface Sciences ISSN 0931-5195
ISBN 978-3-642-16509-2 e-ISBN 978-3-642-16510-8
DOI 10.1007/978-3-642-16510-8
Springer Heidelberg Dordrecht London New York

Cover design: Integra Software Services Pvt. Ltd., Pondicherry

Printed on acid-free paper

Springer is part of Springer Science+Business Media (www.springer.com)

This book is dedicated to the memory of

Iwan N. Stranski
(1897–1979)

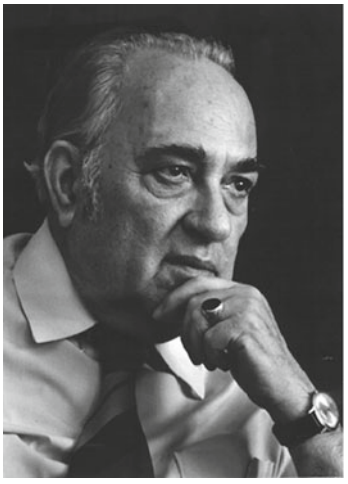

Rostislaw Kaischew
(1908–2002)

distinguished scholars who pioneered important ideas in the classical theory of crystal growth and phase formation

Preface

Being tightly technologically oriented, the contemporary scientific knowledge often suffers from lack of passion. The present book, dedicated to two distinguished scholars, Prof. Iwan N. Stranski and Prof. Rostislaw Kaischew, intends to illuminate this ardor as a state of the human mind moving science forward.

In the 1920s, Iwan N. Stranski along with Walther Kossel, introduced one of the fundamental physical concepts in crystal growth, "the half-crystal position" or kink site, implemented later in the classical Kossel–Stranski model of the crystal structure. In 1938 Stranski and Krastanow discovered the famous Stranski–Krastanow growth mode of epitaxial layers. In 1934 Stranski and Kaischew formulated the theory of mean separation work, revealing thereby the identity of the thermodynamic and kinetic approaches to Gibbs's problem of the equilibrium of small phases. In the same year they published the first kinetic treatment of the nucleation rate of crystals, droplets, and bubbles. On that background, Stranski and Kaischew developed in great detail fundamental aspects of nucleation theory, equilibrium shape of crystals, homo- and heteroepitaxial growth of thin atomic layers, and electrocrystallization. In a series of studies in 1950–1951, Kaischew extended the Gibbs–Curie–Wulff theorem of equilibrium shape of crystals to the case of crystals on foreign substrate. This refinement, known as "generalized Gibbs–Curie–Wulff–Kaischew theorem," and the conditions derived for two- or three-dimensional nucleation on a foreign substrate formed later the theoretical background of thin epitaxial film growth. These highlights of the Sofia school in crystal growth as well as the outstanding scientific life and personality of both Iwan N. Stranski and Rostislaw Kaischew have inspired the present edition.

The influence of Stranski's and Kaischew's scientific style on their coworkers and students has been immense. I had no chance to meet Stranski personally, but I had the privilege of working in Kaischew's Department of Crystal Growth at the Institute of Physical Chemistry in Sofia for more than 25 years and my impressions of his outstanding life stem from that time. Rostislaw Kaischew was a man of vision and strong scientific intuition. Being a fascinating teacher, he possessed the talent of attracting people and involving them in science. Founder of the Institute of Physical Chemistry at the Bulgarian Academy of Sciences, Kaischew was its director for more than 30 years (1958–1989).

The personality of Iwan N. Stranski was strongly respectable. Consecutively, as founder and head of the Department of Physical Chemistry at Sofia University (1925–1944), director of the Institute of Physical Chemistry at the Technical University in Berlin (1944–1949), rector of the Technical University in Berlin (1951–1953), and deputy director of the Fritz Haber Institute of Physical Chemistry at the Max Planck Society (1953–1967), Iwan N. Stranski, known as the father of crystal growth, had a great impact on the international academic and research community.

A distinctive feature of the scientific ideas of Stranski and Kaischew, implemented in the classical theory of phase formation, is their simplicity. The model they have introduced in crystal growth reflects in a nice and proper way Karl Popper's concept of science: "The method of science depends on our attempts to describe the world with simple theories: theories that are complex may become untestable, even if they happen to be true. Science may be described as the art of systematic over-simplification – the art of discerning what we may with advantage omit." The invention of the kink site and the theory of mean separation work are probably one of the best examples of Popper's thought. In 1996 during the second Stranski–Kaischew conference in Pamporovo Ski Center, Bulgaria, the fascinating speaker Joost Frenken demonstrated for the first time a spectacular high-temperature STM movie, revealing real-time attachment and detachment of individual atoms at atomic steps and kinks. Kaischew, 88 years old at that time, attended the lecture. At the end of the talk, deeply moved, he said, "I have never believed that in my life I would be blessed to see direct experimental evidence of our imagination of the mechanisms of crystal growth. Even being so simple, our model suggested in 1934 seems to be true."

Most of the authors contributing to this book are among the founders of the Stranski–Kaischew crystal growth club established in the early 1990s by a series of international meetings in Bulgaria. In 1992–1993, I spent a year as a coworker of Boyan Mutaftschiev in his laboratory in CNRS, Nancy, and that was the place and time where these meetings have been inspired. Being a close friend of Stranski and a favorite student of Kaischew, Boyan was a keen connoisseur of the history of crystal growth. He had the gift to fascinate people by involving them in the values of "the old time of classical science." Actually, our discussions in Nancy incited me to initiate this series of workshops on surface physics in Bulgaria. Kaischew strongly encouraged this idea and the first workshop was held in February 1994. Known at present as "Stranski–Kaischew Workshops in Surface Physics," these regular meetings have kept the spirit of the classical school in crystal growth and have attracted outstanding researchers in surface science. Kurt Binder, Harald Brune, Alex Chernov, Theodore Einstein, Joost Frenken, Doon Gibbs, Martin Henzler, Masakazu Ichikawa, Kenneth Jackson, Dimo Kashchiev, Raymond Kern, David Landau, Alexander Latyshev, Thomas Michely, Andrey Milchev, Chaouqui Misbah, Boyan Mutaftschiev, Anton Naumovets, Hiroo Omi, Herbert Pfnuer, Matthias Scheffler, Robert F. Sekerka, Stoyan Stoyanov, Kunio Takayanagi, Erio Tosatti, Michael Tringides, Peter Varga, Ellen Williams, and Zhenyu Zhang are among the lecturers who built up the reputation of this series of meetings. However, it is my personal privilege to acknowledge in a particular way two of them. David Landau

and Kurt Binder involved themselves in this project with extraordinary enthusiasm and great concern. Their contribution to the lectures, discussions, and scientific programs had been substantial in all past six workshops.

Aiming to find answers closer to the question "why" rather than "how" the things in surface physics happen, this enthusiastic team of scientists outlined the center of attention of Stranski–Kaischew meetings. This center is manifested by the title of the present volume too: "Nanophenomena at Surfaces: Fundamentals of Exotic Condensed Matter Properties." A glance at the chapter titles shows a diversity of topics discoursed in this book. Being focused on the point "Why the matter has exotic behavior when the size of systems and their space dimensions are reduced?" this edition covers *Structure and properties of confined crystals on surfaces* (K. Binder), *Atomic interactions in two-dimensional overlayers* (T. Einstein), *Surface diffusion phenomena and surface pattern formation* (E. Williams and M. Michailov), *Quantum size effects in low-dimensional structures* (M. Tringides and Z. Zhang), *Electronic properties of nanostructures and metallic nano-wires* (M. Ichikawa and H. Pfnuer), *Biologically inspired nanophysics, proteins and polymer chains* (D. Landau and A. Milchev), *Step bunching phenomena* (A. Latyshev and S. Stoyanov). It is my hope that the reader will find here important bridges between classical, quantum, and nano concepts in condensed matter physics. Being dedicated to the memory of Iwan N. Stranski and Rostislaw Kaischew, I believe that the present book will stimulate further advances in nanoscale surface physics and will encourage young people in science.

Finally, I am grateful to my colleagues and friends from the Institute of Physical Chemistry in Sofia, Vessela Tsakova for her sincere support in sharing through hard times our common cause of Stranski–Kaischew meetings, Stoyan Stoyanov and Andrey Milchev for their valuable advices in program preparation, and Dimo Kashchiev for his ceaseless encouragement in the realization of the present book.

Sofia, Bulgaria Michail Michailov
October 2010

Contents

Contributors

M.S. Altman Department of Physics, Hong Kong University of Science and Technology, Hong Kong, China, phaltman@ust.hk

S. Bhattacharya Max Planck Institute for Polymer Research, Mainz, Germany, swaticb@gmail.com

K. Binder Institute of Physics, Johannes Gutenberg-Universität, Mainz, Germany, kurt.binder@uni-mainz.de

Y.H. Chui Institut für Physik, Johannes Gutenberg-Universität, Mainz, Germany

T.L. Einstein Department of Condensed Matter Physics, University of Maryland, College Park, MD, USA, einstein@umd.edu

M. Hupalo Ames Laboratory-USDOE and Department of Physics and Astronomy, Iowa State University, Ames, IA, USA, hupalo@ameslab.gov

M. Ichikawa Department of Applied Physics, Graduate School of Engineering, The University of Tokyo, Bunkyo-ku, Tokyo, Japan, ichikawa@ap.t.u-tokyo.ac.jp

Y. Jia School of Physics and Engineering, Zhengzhou University, Zhengzhou, Henan, China; Materials Science and Technology Division, Oak Ridge National Laboratory, Oak Ridge, TN, USA, jiayu@zzu.edu.cn

S.S. Kosolobov Institute of Semiconductor Physics, Siberian Branch, Russian Academy of Sciences, Novosibirsk, Russia, kosolobov@thermo.isp.nsc.ru

D.P. Landau Center for Simulational Physics, The University of Georgia, Athens, GA, USA, dlandau@hal.physast.uga.edu

A.V. Latyshev Novosibirsk State University, Novosibirsk, Russia, latyshev@thermo.isp.nsc.ru

Y.W. Li Center for Simulational Physics, The University of Georgia, Athens, GA, USA, ywli@hal.physast.uga.edu

M.M.T. Loy Department of Physics, Hong Kong University of Science and Technology, Hong Kong, China, phloy@ust.hk

K.L. Man Department of Physics, Hong Kong University of Science and Technology, Hong Kong, China, mickmkl@ust.hk

M. Michailov "Rostislaw Kaischew" Institute of Physical Chemistry, Bulgarian Academy of Sciences, Sofia, Bulgaria, mike@ipc.bas.bg

A. Milchev Institute of Physical Chemistry, Bulgarian Academy of Sciences, Sofia, Bulgaria; Max Planck Institute for Polymer Research, Mainz, Germany, milchev@ipc.bas.bg

P. Nielaba Physics Department, University of Konstanz, Konstanz, Germany

M.M. Özer Materials Science and Technology Division, Oak Ridge National Laboratory, Oak Ridge, TN, USA; Department of Physics and Astronomy, The University of Tennessee, Knoxville, TN, USA, mozer@utk.edu

H. Pfnür Institut für Festkörperphysik, Abteilung ATMOS, Leibniz Universität Hannover, Hannover, Germany, pfnuer@fkp.uni-hannover.de

A. Ricci Institut für Physik, Johannes Gutenberg-Universität, Mainz, Germany

V. Rostiashvili Max Planck Institute for Polymer Research, Mainz, Germany, rostiash@mpip-maimz.mpg.de

P. Rous Department of Physics, University of Maryland, Baltimore, MD, USA

R. Sathiyanarayanan Department of Condensed Matter Physics, University of Maryland, College Park, MD, USA

S. Sengupta Centre for Advanced Materials, Indian Association for the Cultivation of Science, Jadavpur, Kolkata, India; Department of Chemical, Biological and Macromolecular Sciences, S. N. Bose National Center for Basic Sciences, Salt Lake, Kolkata, India

S. Stoyanov Department of Phase Transitions and Crystal Growth, Institute of Physical Chemistry, Bulgarian Academy of Sciences, Sofia, Bulgaria, stoyanov@ipc.bas.bg

C. Tao Department of Physics, University of California, Berkeley, CA, USA, cgtao@berkeley.edu

M.C. Tringides Ames Laboratory-USDOE and Department of Physics and Astronomy, Iowa State University, Ames, IA, USA, tringides@ameslab.gov

T. Vilgis Max Planck Institute for Polymer Research, Mainz, Germany, vilgis@mpip-maimz.mpg.de

H.H. Weitering Department of Physics and Astronomy, The University of Tennessee, Knoxville, TN, USA; Materials Science and Technology Division, Oak Ridge National Laboratory, Oak Ridge, TN, USA, hanno@utk.edu

E.D. Williams Department of Physics, University of Maryland, College Park MD, USA, edw@umd.edu

T. Wüst Center for Simulational Physics, The University of Georgia, Athens, GA, USA, twuest@hal.physast.uga.edu

R. Yongsunthon Corning Incorporated, Corning, New York, NY, USA, YongsuntR@corning.com

Z. Zhang Materials Science and Technology Division, Oak Ridge National Laboratory, Oak Ridge, TN, USA; Department of Physics and Astronomy, The University of Tennessee, Knoxville, TN, USA; ICQD, University of Science and Technology of China, Hefei, Anhui, China, zhangz@ornl.gov

Chapter 1
Confined Crystals on Substrates: Order and Fluctuations in Between One and Two Dimensions

K. Binder, Y.H. Chui, P. Nielaba, A. Ricci, and S. Sengupta

Abstract The effect of lateral confinement on a crystal of point particles in $d = 2$ dimensions in a strip geometry is studied by Monte Carlo simulations and using phenomenological theoretical concepts. Physically, such systems confined in long strips of width D can be realized via colloidal particles at the air–water interface, or by adsorbed monolayers at suitably nanopatterned substrates, etc. As a generic model, we choose a repulsive interparticle potential decaying with the twelfth inverse power of distance. This system has been well studied in the bulk as a model for two-dimensional melting. The state of the system is found to depend very sensitively on the boundary conditions providing the confinement. For corrugated boundaries commensurate with the order of the bulk (i.e., a triangular crystalline lattice structure), both orientational and positional orders are enhanced, and near the boundaries surface-induced order persists also at temperatures where the system is fluid in the bulk. For incommensurate corrugated boundaries, however, soliton staircases near the boundaries form, causing a pattern of standing strain waves in the strip. However, smooth unstructured repulsive boundaries enhance orientational order only, positional long-range order is destroyed. The strip then exhibits a vanishing shear modulus. A comparison with surface effects on phase transitions in simple Ising and XY-models is also made. Finally, possible applications are discussed.

1.1 Introduction

The research that is briefly reviewed here has three main motivations:

(i) Colloidal systems allow to carry out experiments of unprecedented detail, comparable to computer simulations: by confocal microscopy techniques, one can

K. Binder (✉)
Institute of Physics, Johannes Gutenberg-Universität, Staudinger Weg 7,
D-55099 Mainz, Germany
e-mail: kurt.binder@uni-mainz.de

M. Michailov (ed.), *Nanophenomena at Surfaces,* Springer Series in Surface Sciences 47,
DOI 10.1007/978-3-642-16510-8_1,

provide "snapshot pictures" of all the positions of the colloidal particles; by fluorescent labeling one can track down the motion of arbitrarily selected particles with time; by suitable choice of solvent, and surface treatment of the particles, inter-particle forces are tunable to a large extent: thus, such systems are model systems allowing to study order and disorder in condensed matter in much greater detail than previously possible [1–4].

(ii) Confinement allows to probe order–disorder phenomena via the sensitivity to boundary conditions [5]. This concept is particularly interesting for two-dimensional crystals, which in a sense are "critical systems" [6–10] throughout the parameter range where crystallinity occurs. Confinement then causes an interesting "crossover" between quasi-one-dimensional [11, 12] behavior and two-dimensional behavior (melting of Kosterlitz–Thouless [6–8] type!). Wall effects then naturally lead to introduce the concept of "surface critical exponents" [13, 15] (Fig. 1.1).

(iii) Confinement of a crystal naturally may lead to misfits, and the crystal may release its strain by defect formation: our recent simulations [12] have suggested that, as a consequence, soliton staircases [16] may form, and deformation patterns appear which can be interpreted as standing strain waves [12].

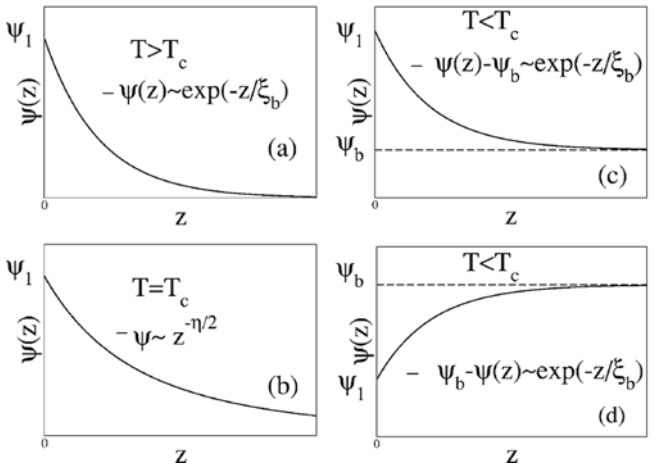

Fig. 1.1 Schematic variation of a local one-component order parameter $\psi(z)$ as a function of the distance z from a wall (or free surface, respectively) that is located at $z = 0$. At temperature $T = T_c$ occurs a second-order phase transition in the bulk (order parameter $\psi_b > 0$ for $T < T_c$). In cases (**a**)–(**c**) it is assumed that at the wall at $z = 0$ a local surface field H_1 conjugate to the order parameter $\psi_1 = \psi(z = 0)$ acts. Surface-induced ordering then occurs in a region of order ξ_b (bulk correlation length) for $T > T_c$, while at $T = T_c$ a power-law decay occurs (**b**), $\psi \propto z^{-\eta/2}$, where η describes the decay of critical correlations in the bulk. Case (**d**) refers to a "neutral surface" ($H_1 = 0$), assuming a reduction of ordering at the surface (e.g., caused by "missing neighbors"). Also for $T < T_c$ the range over which $\psi(z)$ deviates from ψ_b is given by ξ_b

1.2 The Simulated Model

An experimental model system for two-dimensional colloidal crystals and their melting behavior is obtained by bringing spherical colloids (diameter in the micrometer range) that contain a superparamagnetic nanoparticle in their core at the water–air interface, orienting the magnetic field perpendicular to the interface, so that a (uniformly) repulsive interaction decaying with distance r as r^{-3} results [17–19]. Varying the strength of the magnetic field, the strength of this interaction can be tuned. This system has become very popular as an experimental model system for the study of melting in $d = 2$ dimensions [20].

Other related $d = 2$ orderings can be prepared in dusty plasmas [21], lattices of spherical block copolymer micelles in thin films [22], superstructures of small molecules or atoms adsorbed on stepped surfaces [23], etc. For this reason, we shall not address a particular physical system, but rather consider a generic model.

Our model consists of point particles in the two-dimensional xy-plane, interacting with the "soft disk" potential which is just the repulsive term of a Lennard-Jones potential

$$V(r) = \varepsilon(\sigma/r)^{12} \tag{1.1}$$

choosing units such that $\varepsilon = 1$ and $\sigma = 1$. In the Monte Carlo simulations, we use a cutoff $r_c = 5\sigma$, because for $r > r_c$, $V(r)$ is completely negligible. Due to this short range of the potential, it is computationally more convenient than the r^{-3} potential, and moreover in the bulk the properties of the model have already been very thoroughly studied [24]; e.g., choosing a density $\rho = 1.05$ it is known that melting (presumably via a KTHNY [6–8] transition) occurs at $T \approx 1.35$ (note that for (1.1) the equation of state does not depend on ρ and T separately, it is only the combination $\rho(\varepsilon/k_B T)^{1/6}$ that matters [25]). So choosing $T = 1$ ensures to obtain states deep in the solid crystalline phase, where the particles form a defect-free triangular lattice structure.

The emphasis of this chapter is to understand the effect of boundaries. Two types of boundaries are considered (Fig. 1.2): so-called structured walls, consisting of two rows of particles frozen in the perfect crystalline order (appropriate for the chosen density). These walls have the proper corrugation in y-direction commensurate with the bulk lattice structure. We are not aware that this type of boundary condition has already been realized in the laboratory (simulation can go beyond experiment!), but for colloids it is perhaps realizable by suitable interference of laser fields: this remains a challenge for the experimentalists.

The other type of wall is provided by a flat structureless boundary, running along the y-direction, and described by another repulsive power law

$$V_{\text{wall}} = \varepsilon_{\text{wall}}(\sigma/x)^{10} \tag{1.2}$$

As described in [5], $\varepsilon_{\text{wall}}$ can be chosen such (namely $\varepsilon_{\text{wall}} = 0.0005$) that the perfect crystalline order in x-direction also remains undisturbed, if the origin

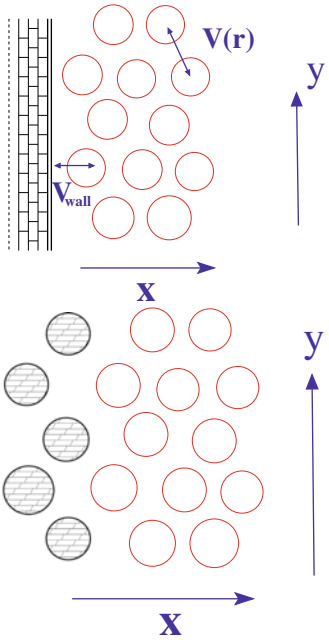

Fig. 1.2 Schematic description of the two types of walls used in this chapter to confine the triangular crystal. Walls are oriented along the y-axis. The *upper part* shows the case of planar walls, the *lower part* shows the case of "structured walls" (cf. text). The frozen particles (*shaded*) interact with the mobile particles (*open circles*) with the same pair potential, (1.1), as acts in the bulk

($x = 0$) would coincide with the position of a row of particles in the lattice. We call this type of wall "planar wall." In both cases, we choose two parallel and identical walls a distance D apart and consider first the case that this distance D is commensurate with the triangular lattice structure, i.e., an integer number n_x of parallel rows of particles fits in between the two walls, with the undisturbed lattice spacing. In the y-direction parallel to the walls, we choose a periodic boundary condition at a distance $L_y = n_y a$, a being the lattice spacing of the triangular lattice.

1.3 Results for Crystals with Commensurate Confinement

Now crystals show two types of long-range order, positional long-range order and orientational long-range order, and the question that we ask is, how are these orderings affected by the presence of walls?

It is easy to see that the positional order in the direction perpendicular to the walls is enhanced, in comparison with the bulk; see the density distributions $\rho(x)$ in the x-direction (Fig. 1.3). This enhancement relative to the bulk occurs for both planar and structured wall boundary conditions, in the solid phase (Fig. 1.3, top). Even in the liquid phase (Fig. 1.3, bottom) there occurs a pronounced layering effect. While the amplitude of this layering near the walls does depend somewhat on the type of boundary condition, the range over which it extends into the bulk is the same for both boundary conditions, as expected (Fig. 1.1) since this range just is a type of bulk correlation length. When one studies the temperature dependence of

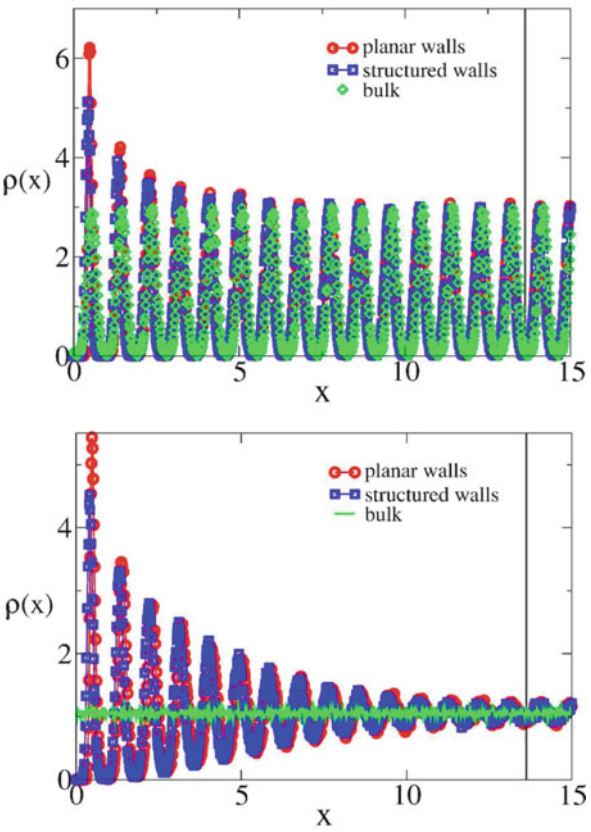

Fig. 1.3 Density distribution $\rho(x)$ plotted vs. x for a system of 900 particles in a $D \times L$ geometry, with periodic boundary conditions in the y-direction, $L = n_y a_0$, $D = n_x a_0 \sqrt{3}/2$, with lattice spacing $a_0 = (2/\sqrt{3}\rho)^{1/2} = 1.049$. *Top part* refers to $T = 1.2$ and *bottom part* refers to $T = 1.6$. Only the *left part* of the strip is shown in each case (the center of the strip, $x = D/2$, is marked by a *vertical line*). A strip with "planar wall" and with "structured wall" boundary condition is included, cf. text, as well as the density distribution of a corresponding bulk system

this correlation length in the liquid phase, one finds a pronounced increase as the temperature is lowered toward the melting transition temperature [5], as expected due to the KTHNY [6–8] character of the transition.

Orientational order, appropriate for a triangular lattice, is characterized by local order parameter $\psi_6(\vec{r}_k)$ and associated correlation function $g_6(y)$

$$\psi_6(\vec{r}_k) = (1/6) \sum_{j\,(\text{n.n. of } k)} \exp(6\mathrm{i}\phi_{jk}),\ g_6(y) = |\langle \psi_6(\vec{r}_k)\psi_6(\vec{r}_\ell)\rangle| \qquad (1.3)$$

where $\vec{r}_k = (x_k, y_k)$ is the position of the xth particle and $y = |y_k - y_\ell|$. The angle between a bond connecting particles k and j and a reference direction (e.g., the y-direction) is denoted as ϕ_{jk}. One sums $\exp(6\mathrm{i}\phi_{jk})$ over all six nearest neighbors of k, so $\psi_6(\vec{r}_k) = 1$ for a perfect triangular lattice. Also this orientational order is strongly enhanced by the walls (Fig. 1.4), and the orientational correlation length that one can extract from this decay also increases as one approaches melting [5] (the correlation length for orientational order is found to be somewhat larger than its counterpart for positional order (as expected, since it is only the former length

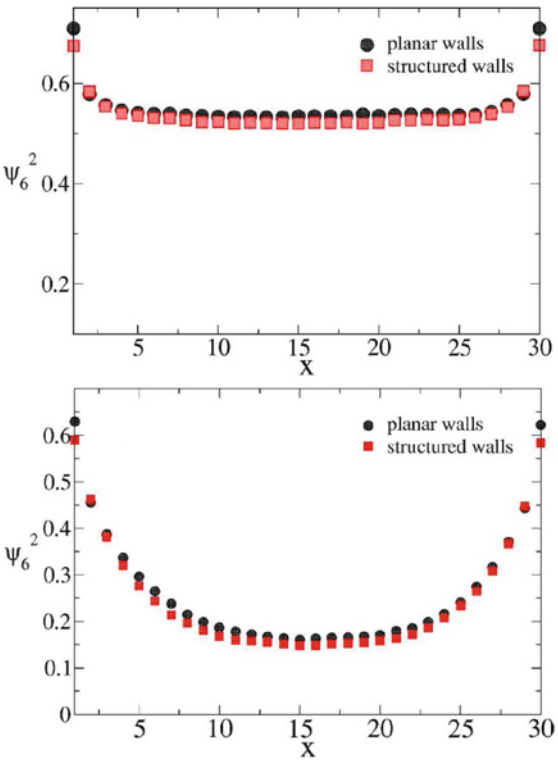

Fig. 1.4 Plot of the local orientational order parameter square $\langle|\psi_6(x)|^2\rangle$ vs. x for the same system as in Fig. 1.3, for $T = 1.2$ (*top part*) and $T = 1.6$ (*bottom part*). *Circles* refer to the planar wall and *square* to the structured wall boundary condition

that diverges at the fluid–hexatic transition [7]). From Fig. 1.4 it is clear that for strips of any finite width D the melting transition is strongly affected by finite size rounding: the walls induce a significant orientational order also in the fluid phase, and so the average mean square order parameter $\langle\bar{\psi}_6^2\rangle = \int \mathrm{d}x\langle|\psi_6(x)|^2\rangle/D$ decays gradually with increasing temperature and stays nonzero also in the fluid phase for any value $D < \infty$.

In contrast to this enhancement of order due to the walls, seen in Figs. 1.3 and 1.4, a different behavior results when we study the positional order in the y-direction parallel to the walls. Defining for a crystal row in the y-direction the static structure factor $S(q)$, assuming also an orientation of the wavevector $\vec{q}$ along the y-direction, as

$$S(q) = (1/n_y)\sum_{\ell,\ell'}\langle\exp[\mathrm{i}q(y_\ell - y'_{\ell'})]\rangle \tag{1.4}$$

one obtains at $T = 1$ (i.e., far below the melting temperature) the behavior shown in Fig. 1.5: for structured walls, the expected picture for a crystal indeed results: There are sharp Bragg peaks at the positions $qd/2\pi = 1, 2, 3, \ldots$, with $d = a_0$ now, distinct from the background ("thermal diffusive scattering"). As expected, the height of these peaks decreases with increasing q, due to the effect of the Debye–Waller

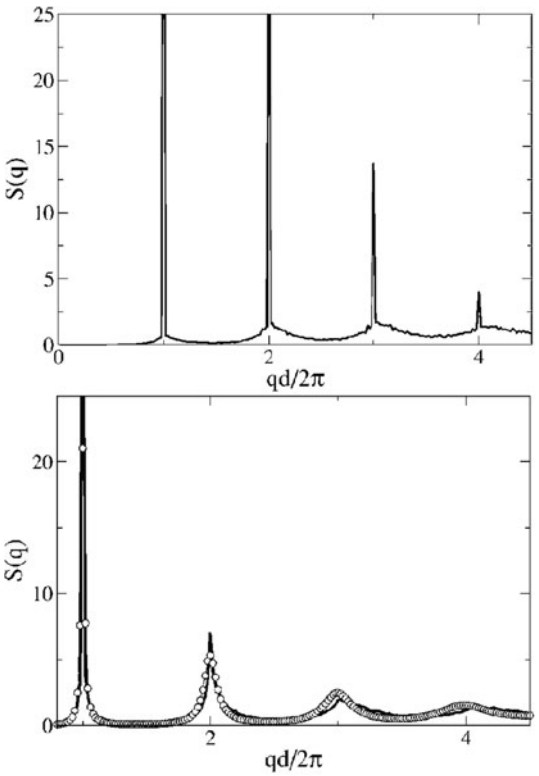

Fig. 1.5 Static structure factor $S(q)$ at $T = 1$ plotted vs. $qd/2\pi$ for structured walls (*top part*) and for planar walls (*bottom part*). All data are for systems with $n_x = 30$ rows and $n_y = 100$ particles per row along the y-direction, and the data were averaged over all rows. For the planar walls the full curve is a fit to (1.5)

factor [16]. The width of these Bragg peaks does not increase with increasing q, as it should be.

In contrast, for planar walls the structure factor behaves qualitatively different; it looks similar like a fluid structure factor: only the first peak is very high and rather sharp, but the higher order peaks (at $qd/2\pi = 2, 3, \ldots$) are systematically broadened. In this case $S(q)$ is in almost quantitative agreement with the theoretical result for a one-dimensional harmonic chain [11]

$$S(q) = \sinh(q^2\delta^2/2)[\cosh(q^2\delta^2/2) - \cos(qd)] \tag{1.5}$$

with Hamiltonian

$$\mathcal{H} = \frac{1}{2}\sum_{\ell}\left[\pi_\ell^2/m + mc^2(y_{\ell+1} - y_\ell - d)^2/d^2\right] \tag{1.6}$$

where point particles of mass m have positions y_ℓ and conjugate momenta π_ℓ. In the classical ground state one has a one-dimensional crystal, particles residing at positions $y_n = y_0 + nd$, $n = 1, 2, \ldots,$ d, being the lattice spacing. The parameter c plays the role of a sound velocity. From (1.6) it is straightforward to compute the

displacement correlation function

$$\langle (u_n - u_0)^2 \rangle = n\delta^2, \quad \delta = a\sqrt{k_B T/(mc^2)} \tag{1.7}$$

Equations (1.5) and (1.7) imply that a one-dimensional crystal melts continuously at $T = 0$, and as $T \to 0$ the correlation length $\xi = a^3/(2\pi\delta^2) \propto 1/T \to \infty$ as $T \to 0$ [5, 11].

The different character of the lateral order (in the y-direction) for systems with planar walls is evident when one compares snapshot pictures of superimposed configurations (Fig. 1.6). For the structured wall case, the triangular lattice structure is nicely recognized. The size of the irregular dots measures the mean square displacement of the particles around the lattice sites. Clearly these displacements are smaller near the structured wall – the effective periodic potential created by such a wall enhances order.

The situation is very different for the planar wall case, however: the displacement distributions of the particles around the lattice positions now are very anisotropic, indicating a pronounced softness of the system along the y-direction. This behavior is reminiscent of a two-dimensional smectic phase, and it shows up also in the behavior of the elastic constants (Fig. 1.7). For a perfect triangular crystal structure, in the bulk, the symmetry relations $C_{11} = C_{22}$ and $C_{12} = C_{33}$ hold (we use here the Voigt notation for the elastic constants). This symmetry is broken in a strip of finite width due to the walls, but increasing the width $D = na_0\sqrt{3}/2$ one finds a rapid convergence toward bulk for planar walls: while C_{11}, C_{22}, C_{12} converge to bulk behavior, C_{33} does not, and rather $C_{33}(n) = C_{33}^{\text{bulk}}/2$, apparently independent of the number n of rows in the strip! Since the elastic moduli in the bulk are $C_{22} \approx 127$, $C_{33} \approx 41$ (in units of $k_B T/\sigma^2$), and the pressure is $p = 17.5$, the shear modulus $\mu = C_{33} - p$ in the strip vanishes (at least approximately). The planar boundaries provide an elastic distortion of long range to the crystal and hence modify the crystalline behavior significantly.

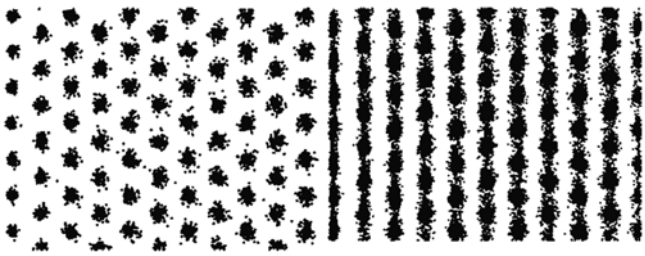

Fig. 1.6 Configuration of the particles in the first nine rows adjacent to the left wall at $T = 1.0$, for the structured wall (*left*) and the planar wall (*right*). One thousand configurations of a run lasting 10^6 Monte Carlo steps per particle are superimposed, fixing the center of mass of the total system of mobile particles in each configuration in the same position. A system with $n_x = 30$ rows and $n_y = 30$ particles per row was used, with periodic boundary conditions in the y-direction

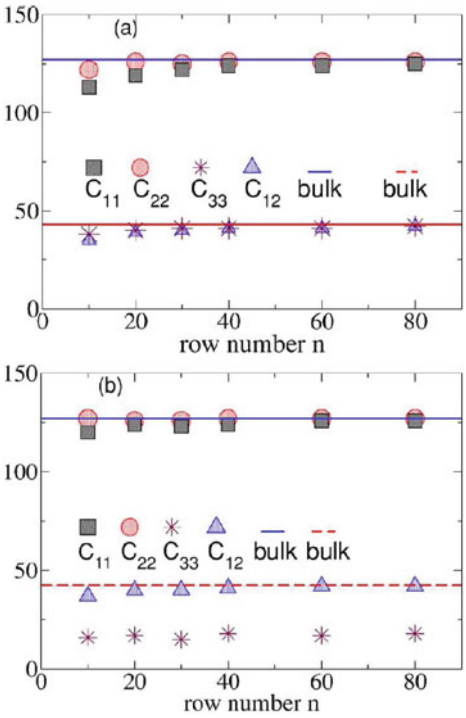

Fig. 1.7 Elastic constants (in units of $k_B T/\sigma^2$) for systems at $k_B T/\varepsilon = 1.0$ for structured walls (*top part*) and planar walls (*bottom part*). *Horizontal straight lines* show the bulk values, obtained for a system with periodic boundary conditions in both x- and y-directions

1.4 Insight Gained from the Harmonic Theory of Two-Dimensional Crystals

In order to better understand the anomalous behavior of crystalline strips with planar walls, it is useful to examine the mean square displacement correlation function in the y-direction, $G(y) = \langle |u_y(y) - u_y(0)|^2 \rangle$, where $\vec{u} = (u_x, u_y)$ is the displacement vector of a particle relative to its position in the perfect triangular lattice. Choosing for simplicity a $D \times L$ geometry with periodic boundary conditions also in the x-direction, one finds $\{\vec{Q} = (Q_x, Q_y)\}$

$$\langle [u_y(y) - u_y(0)]^2 \rangle = (2/N) \sum_{Q_x} \sum_{Q_y} \langle u_y(\vec{Q}) u_y(-\vec{Q}) \rangle [1 - \cos(y Q_y)] \tag{1.8}$$

where Q_x, Q_y are "quantized" as follows:

$$Q_x/\pi = -1, -1 + \frac{2}{D}, -1 + \frac{4}{D}, \ldots, +1 - \frac{2}{D} \tag{1.9}$$

$$Q_y/\pi = -1, -1 + \frac{2}{L}, -1 + \frac{4}{L}, \ldots, +1 - \frac{2}{L} \tag{1.10}$$

Using the continuum approximation for a two-dimensional harmonic solid [16], the correlator in (1.8) becomes [16]

$$\langle u_\alpha(\vec{Q})u_\beta(-\vec{Q})\rangle = \frac{k_B T/Q^2}{(\lambda+2\mu-p)}\hat{Q}_\alpha\hat{Q}_\beta + \frac{k_B T/Q^2}{\mu-p}(\delta_{\alpha\beta}-\hat{Q}_\alpha\hat{Q}_\beta) \qquad (1.11)$$

where $\hat{Q}_\alpha = Q_\alpha/|\vec{Q}|$ is the Cartesian component ($\alpha = x, y$) of a unit vector in the direction of $\vec{Q}$, and the Lamé coefficient $\lambda = (C_{11} - C_{33})/2$ (=42, for $k_B T/\varepsilon = 1$ in our model).

Since all parameters in (1.8), (1.9), (1.10), and (1.11) are hence explicitly known for the present model, (1.8) can straightforwardly be evaluated numerically (Fig. 1.8). On the other hand, in the limit $a_0 \ll D \ll L$ one can convert the sum over Q_y into an integral and thus obtain analytical results approximately, to show that then a crossover from a two-dimensional behavior to the one-dimensional behavior (1.7) occurs,

$$G(y) \propto \ln y\ ,\ \ a_0 \ll y \ll D\ln D \qquad \text{(two dimensions)} \qquad (1.12)$$

$$G(y) \propto y,\ \ D\ln D \ll y \ll L \qquad \text{(one dimension)} \qquad (1.13)$$

Using the results obtained for μ, λ, and p from the simulation, we have worked out (1.8) for $D = 20a_0\sqrt{3}/2$, $L = 500a_0$, i.e., the largest system for which we have also carried out a Monte Carlo simulation (Fig. 1.8). The results show that for $y \le 40$ indeed a logarithmic increase of $G(y)$ is compatible with the data, as expected from (1.12). For $y > 40$, a faster increase sets in (but it is difficult to numerically verify (1.13), since the periodic boundary condition, $G(y) = G(L-y)$,

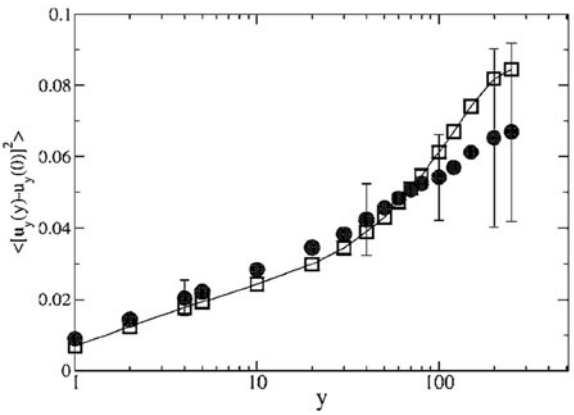

Fig. 1.8 Comparison of $G(y)$ according to the harmonic theory ((1.8), (1.9), (1.10), and (1.11), *squares*) and corresponding Monte Carlo data (*full dots* with error bars), for a system with $n_x = 20$ rows containing $n_y = 500$ particles each. $G(y)$ is given in units of $\sigma^2(\sigma = 1)$. Periodic boundary conditions are used in both the x- and y-directions. Note the logarithmic scale of the abscissa, while the ordinate has a linear scale

reduces the increase of $G(y)$ already for $y \approx L/4$ [5]). Moreover, the results from the numerical implementation of the harmonic theory are in almost perfect quantitative agreement with the Monte Carlo data, implying that at the chosen temperature (far below melting) anharmonic effects still are insignificant.

This quasi-one-dimensional behavior of elongated two-dimensional strips is only one ingredient to understand the anomalous behavior of crystalline strips confined by planar walls: the other ingredients are critical surface effects. One finds that in the region where the logarithmic increase $G(y)$ with y occurs, the prefactor of this increase is about a factor of 2 larger for rows adjacent to a wall than for rows in the bulk (Fig. 1.9). Actually this behavior is expected by analogy with the two-dimensional XY-model [6, 15, 26]. Remember that a two-dimensional crystal is a critical system, where there is no true positional long-range order [7–10], but rather a power-law decay of a suitably defined correlation function. To remind the reader of this analogy and clarify what it implies for correlations near free surfaces [15, 26], we approximate the XY-model as

$$\mathcal{H}_{xy} = -J \sum_{\ell,j} \cos(\phi_\ell - \phi_j) \approx \frac{1}{2} J \sum_{\langle \ell,j \rangle} (\phi_\ell - \phi_j)^2 \tag{1.14}$$

Here J is the exchange constant, and we have a lattice (site j) where unit vectors occur, characterized by their orientation angle ϕ_j relative to the y-axis in the xy-plane. The quantity of interest is the spin correlation function

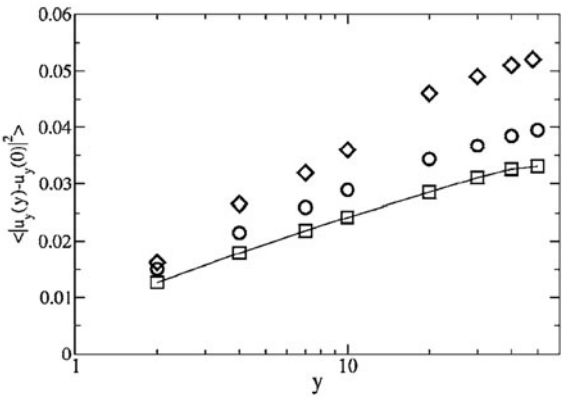

Fig. 1.9 Plot of $G(y)$ vs. y (logarithmic scale!) for two-dimensional crystalline strips at $k_B T/\varepsilon = 1.0$ and $n_x = 20$ rows containing $n_y = 100$ particles each. *Squares* show the prediction of the corresponding harmonic theory of a bulk system, while *circles* and *diamonds* are Monte Carlo data. *Circles* show data for a system with periodic boundary conditions, while *diamonds* show data for a system with planar walls, using only the displacement of particles adjacent to the walls. $G(y)$ is given in units of $\sigma^2 (\sigma = 1)$

$$g(\vec{r}) = \langle \vec{S}(\vec{r}_0) \cdot \vec{S}(\vec{r}_0 + \vec{r}) \rangle = \langle \cos[\phi(\vec{r} + \vec{r}_0) - \phi(\vec{r}_0)] \rangle$$
$$\approx \exp\left\{ -\frac{1}{2} \langle [\phi(\vec{r} + \vec{r}_0) - \phi(\vec{r}_0)]^2 \rangle \right\} \tag{1.15}$$

Equations (1.14) and (1.15) make the analogy to harmonic solids transparent – the angles $\{\phi_j\}$ correspond to the displacement vectors $\vec{u}_j$ and $\langle [\phi(\vec{r}+\vec{r}_0) - \phi(\vec{r}_0)]^2 \rangle$ corresponds to the displacement correlation $G(y)$. Now the well-known power-law decay of $g(\vec{r})$, $g(r) \propto r^{-\eta_b}$, immediately follows from a logarithmic variation of the angular displacement correlation

$$\langle [\phi(\vec{r} + \vec{r}_0) - \phi(\vec{r}_0)]^2 \rangle = (k_B T / 2\pi J) \ln(\pi r / a_0), \quad r \gg a_0 \tag{1.16}$$

which yields $\eta_b = k_B T/(2\pi J)$. Equation (1.16) is the analog of (1.12).

When one introduces the continuum approximation that corresponds to (1.14) namely

$$\mathcal{H} = \frac{J}{2} \int [\nabla \phi]^2 \mathrm{d}x \mathrm{d}y \tag{1.17}$$

one can treat the problem of a semiinfinite half-space (with a free boundary at $x = 0$) by postulating a von Neumann boundary condition

$$\partial G(\vec{r}_1, \vec{r}_2)/\partial x_1 \mid_{x_1 = 0} = 0 \tag{1.18}$$

for the correlation function $G(\vec{r}_1, \vec{r}_2) = \langle \phi(\vec{r}_1) \phi(\vec{r}_2) \rangle$. Using (1.17) and (1.18) one can show [26] that

$$\langle \exp[\mathrm{i}\phi(\vec{r}_1)] \exp[\mathrm{i}\phi(\vec{r}_2)] \rangle \propto (y_2 - y_1)^{-\eta_{||}}, \quad \eta_{||} = 2\eta_b \tag{1.19}$$

when both sites $\vec{r}_1$, $\vec{r}_2$ lie at the surface ($x_1 = x_2 = 0$), η_b being the exponent quoted in (1.16). When only one site is in the surface, while the other site is deep in the bulk, one rather predicts a power law $g(x) \propto x^{-\eta_\perp}$, where scaling [27] yields $\eta_\perp = 3\eta_b/2$. While there are no data available to test the latter relation, Fig. 1.9 provides a test for the analog of the relation $n_{||} = 2\eta_b$ for the surface behavior of the displacement correlation of a solid.

1.5 Effects due to Incommensurate Confinement: Soliton Staircases and Strain Density Waves

We now focus on the case where the confinement creates a misfit in the system [12], such that we still have a total number of $N = n_x n_y$ particles, with a linear dimension $L_y = n_y a$ where a is the lattice spacing appropriate for an ideal, undistorted triangular lattice, with periodic boundary conditions in the y-direction, but the thickness D of the strip no longer has the commensurate value $D = n_x(a\sqrt{3}/2)$ but rather

$D = (n_x - \Delta)a\sqrt{3}/2$. Note that in the case of structured walls, the commensurate confinement is achieved by putting the two rows of fixed particles that are just adjacent to the rows of mobile particles at a distance $D' = (n_x + 1)(a\sqrt{3}/2)$, of course; now this distance rather is $D' = (n_x + 1 - \Delta)(a\sqrt{3}/2)$.

When we start the system at $\Delta = 0$ and increase Δ in small steps ($\Delta = 0.25$), equilibrating at each value of Δ the system carefully before increasing Δ further, we can monitor the stress–strain characteristics of the system (Fig. 1.10). As expected, for $\Delta = 0$ the crystal is stress free, and for $\Delta > 0$ the stress increases linearly with Δ. At $\Delta = 2.0$ we observe a jump in the stress–strain curve, where the stress suddenly decreases strongly: inspection of the system configuration reveals that a transition $n_x \to n_x - 1$ in the number of rows parallel to the confining boundaries

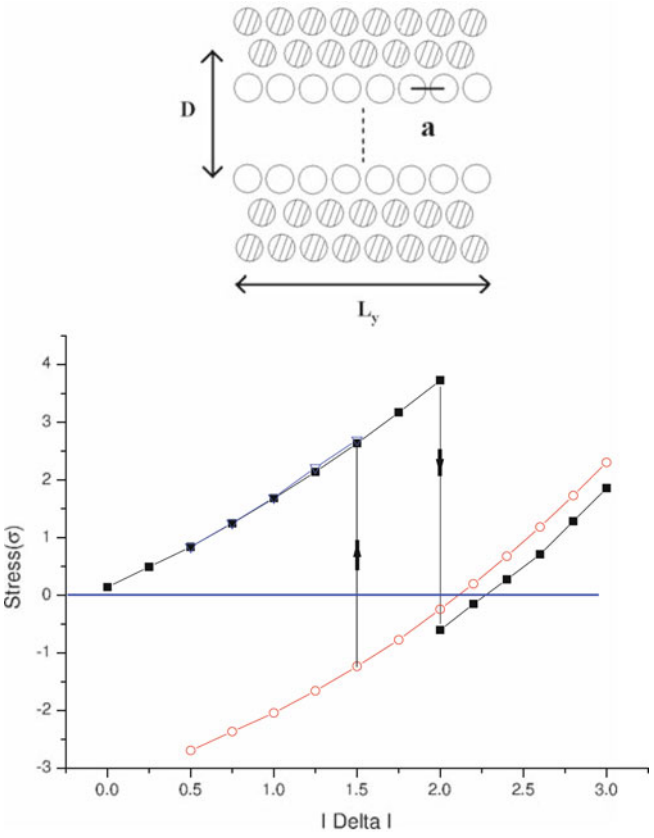

Fig. 1.10 Internal stress $\sigma = \sigma_{yy} - \sigma_{xx}$ (in Lennard-Jones units) at $k_B T/\varepsilon = 1.0$ in the confined crystalline strip plotted vs. Δ, for the case of a system started with $n_x = 30$, $n_y = 108$ (*full symbols*) and a system started with $n_x = 29$, $n_y = 108$ (plus the 108 extra particles appropriately distributed in the 29 rows, as described in the text (*open symbols*)). *Curves* are guides to the eye only. The *upper insert* shows a schematic sketch of the geometry, the frozen particles being shown as *shaded circles*, mobile particles are *not shaded*

has occurred. The n_y particles contained in the row that has disappeared have to be redistributed over the remaining $n_x - 1$ rows, and thus these rows now contain over the distance L_y more than n_y particles (on average). However, the structured wall boundary condition still provides a corrugation potential with a periodicity of the lattice spacing a (corresponding to n_y particles over a distance L_y). As a result, the lattice of the crystal with $n_x - 1$ rows no longer is commensurate with the corrugated boundary potential provided by the "structured walls" [12].

It turns out that (for $k_B T/\varepsilon \leq 1.0$) it is too energetically unfavorable to put any of the n_y extra particles into the two rows immediately adjacent to the frozen particles, while extra particles can occur in all the $(n_x - 3)$ inner rows of the strip. If we assume that the same number of extra particles should occur in any of these rows, we conclude that on average every inner row has $n_d = n_y/(n_x - 3)$ extra particles, and hence the average lattice spacing in the y-direction now is $a' = an_y/(n_y + n_d) = a(n_x - 3)/(n_x - 2)$.

However, due to the corrugation potentials at the confining walls, the strip does not simply adapt the structure of a (distorted) triangular lattice with uniform lattice spacing a' in y-direction: while such a uniform periodicity with lattice spacing a' is indeed found in the center of the strip, near the confining boundaries a more complicated pattern emerges (Fig. 1.11), namely a "soliton staircase" containing n_d steps. This pattern is evident both from superimposed configuration snapshots (Fig. 1.11) and from strain patterns (Fig. 1.12). The strain $u_{ij} = \partial u_i/\partial x_j + \partial u_j/\partial x_i$ is calculated from the particle configurations, where $u_i(\vec{R}_n)$ is the i-component of the displacement vector of the particle labeled by n relative to the site $\vec{R}_n$ of the reference lattice and x_i stand for the (two-dimensional) Cartesian coordinates x, y [12].

Note that the pattern of the soliton adjacent to the boundaries resulting from the transition typically exhibits some irregularity. Studying the kinetics of this transition

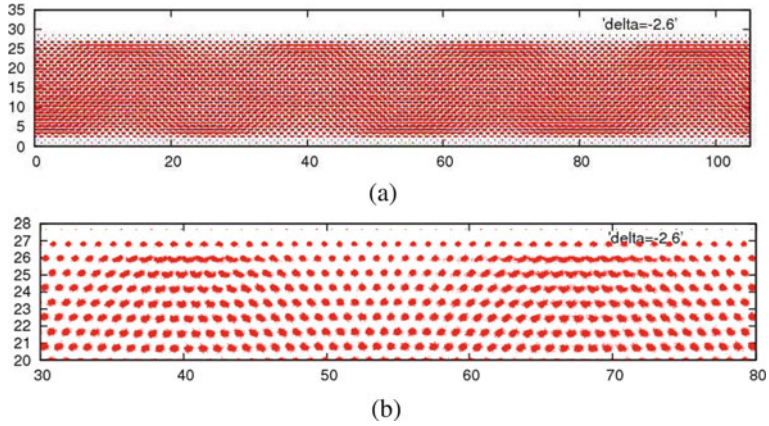

Fig. 1.11 Particle configuration in a system with $n_x = 30$, $n_y = 108$, $\Delta = 2.6$, where a transition $n_x \to n_x - 1$ has occurred, at a temperature $k_B T/\varepsilon = 1.0$. (**a**) 750 superimposed positions of the particles and (**b**) close-up of the structure near the upper wall. Numbers shown along the axes indicate the Cartesian coordinates of the particles

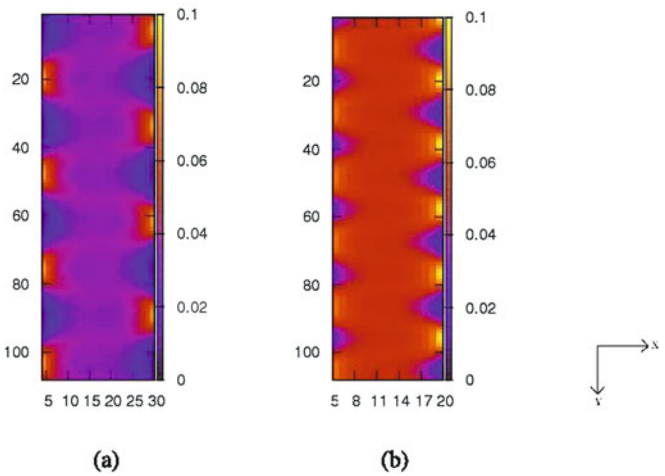

Fig. 1.12 Strain patterns of a system at $k_B T/\varepsilon = 0.1$ for (**a**) $n_y = 108$, $n_x = 30$ and (**b**) $n_y = 108$, $n_x = 20$. The calibration bars are shown on the right-hand side of the graphs, and the orientation of the coordinate axes is indicated at the right side

[28] $n_x \to n_x - 1$ one finds that defects need to be nucleated one by one, and hence a time-consuming equilibration process is needed to generate an (approximately) periodic arrangement of the defects (solitons) along the y-direction (note that at nonzero temperature anyway we must expect large thermal fluctuations of these defects around their average positions). In fact, sometimes states are formed where the number of defects n_d deviates from the theoretical value as estimated above. Presumably these are metastable configurations, separated by (large) barriers from the equilibrium behavior.

Therefore, we have artificially prepared [12] other initial states, where for a given misfit Δ we put $n_y + n_d$ particles in the $n_x - 3$ inner rows, with the n_d excess particles in each of these rows initially at random positions. Indeed we find that this way of preparation of the system leads to a much more regular pattern of the resulting strain density waves (Fig. 1.12).

The periodicity of the soliton staircase shows up very nicely when one studies the Lindemann parameter $\ell(n)$ defined as $\langle u_x^2(\vec{R}_n)\rangle - \langle u_x(\vec{R}_n)\rangle^2$ [12] but this shall not be further elaborated here. However, we emphasize that by such confinement of crystals with boundaries that create misfit we can create a superstructure (via the wavelength of the strain density wave pattern) which is of the same order as the thickness of the strip.

1.6 Conclusions

In this brief review, confinement of two-dimensional crystals in strip geometry was considered, based on Monte Carlo simulations of a generic model and pertinent theoretical considerations. It was argued that the confinement has particularly dramatic

effects on the ordering, given the fact that a two-dimensional crystal is a "critical system" (lack of positional long-range order, possibility that melting happens according to the KTHNY scenario).

Assuming a confinement that is commensurate with the crystal structure, it was shown that confinement enhances the positional order in the direction perpendicular to the boundary ("layering") and that orientational order parallel to the boundary always gets enhanced. However, positional order parallel to the flat boundary ("planar wall") gets weakened or even destroyed. Both the crossover to quasi-one-dimensional behavior of strips of finite width and surface critical behavior contribute to these effects, and the shear elastic constant of the strip was found to be (almost) zero.

Particularly interesting are compressed strips, where transitions occur from n to $n - 1$ rows parallel to the walls. The "structured wall" boundary condition then implies incommensurability with the periodicity of the film, leading to the formation of "soliton staircases" along the boundaries, and the solitons act as cores of standing strain waves in the system.

While the original motivation of this research stems from colloidal crystals [17–20], we emphasize that related phenomena could occur in very different systems, e.g., various semiconductor devices such as quantum dot superlattices [29], lattice-mismatched fused GaAs/In P wafers [30], $Ge_x\ S_{i_{1-x}}$/Si heterostructures [31], and rotationally misaligned Si wafers covalently bonded together [32]. In all such systems boundary-induced strain fields can occur. A particularly nice example where the misfit between a crystal and a frozen boundary can be controlled by external magnetic field is superconducting vortex lattices [33]. A very interesting aspect, closely related to the work reviewed here but out of scope of this chapter, is unconventional nonlinear mechanical response properties of confined solids [34, 35]. Thus, we feel that the phenomena described in the present brief review should have widespread applications in the physics of condensed matter.

Acknowledgments This research was partially supported by the Deutsche Forschungsgemeinschaft (DFG), Project TR 6/C4.

References

1. W.C. Poon, P.N. Pusey, in: *Observation, Prediction and Simulation of Phase Transitions in Complex Fluids*, ed. by M. Baus, F. Rull, J.P. Ryckaert (Kluwer, Dordrecht, 1995) p. 3
2. T. Palberg, Colloidal crystallisation dynamics. Curr. Opin. Colloid Interface Sci **2**, 607 (1997)
3. H. Löwen, Colloidal soft matter under external control. J. Phys.: Condens. Matter. **13**, R415 (2001)
4. W.C. Poon, Colloids as big atoms. Science **304**, 830 (2004)
5. A. Ricci, P. Nielaba, S. Sengupta, K. Binder, Ordering of two-dimensional crystals confined in strips of finite width. Phys. Rev. E **75**, 011405 (2007)
6. J.M. Kosterlitz, D.J. Thouless, Ordering, metastability and phase transitions in two-dimensional systems. J. Phys. C**6**, 1181 (1973)

7. B.I. Halperin, D.R. Nelson, Dislocation-mediated melting in two dimensions. Phys. Rev. B**19**, 2457 (1979)
8. A.P. Young, Melting and the vector Coulomb gas in two dimensions. Phys. Rev. B**19**, 1855 (1979)
9. B. Jancovici, Infinite susceptibility without long-range order: the two-dimensional harmonic "solid". Phys. Lett. **19**, 20 (1967)
10. N.D. Mermin, Crystalline order in two dimensions. Phys. Rev. **176**, 250 (1968)
11. V.J. Emery, J.D. Axe, One-dimensional fluctuations and the chain-ordering transformation in Hg_3AsF_6. Phys. Rev. Lett. **40**, 1507 (1978)
12. Y.-H. Chui, S. Sengupta, K. Binder, Soliton staircases and standing strain waves in confined colloidal crystals. EPL **83**, 58004 (2008)
13. K. Binder, P.C. Hohenberg, Phase transitions and static spin correlations in ising models with free surfaces. Phys. Rev. B**6**, 3461 (1972)
14. K. Binder, P.C. Hohenberg, Surface effects on magnetic phase transitions. Phys. Rev. B**9**, 2194 (1974)
15. B. Berche, Bulk and surface properties in the critical phase of the two-dimensional XY model. J. Phys. A**36**, 585 (2003)
16. P.M. Chaikin, T. C. Lubensky, *Principles of Condensed Matter Physics* (Cambridge University Press, Cambridge, MA, 1995)
17. K. Zahn, R. Lenke, G. Maret, Two-stage melting of paramagnetic colloidal crystals in two dimensions. Phys. Rev. Lett. **82**, 2721 (1999)
18. K. Zahn, G. Maret, Dynamic criteria of melting in two dimensions. Phys. Rev. Lett. **85**, 3656 (2000)
19. M. Köppl, P. Henseler, A. Erbe, P. Nielaba, P. Leiderer, Layer reduction in driven 2D-colloidal systems through microchannels. Phys. Rev. Lett. **97**, 208302 (2006)
20. C. Eisenmann, P. Keim, U. Gasser, G. Maret, Melting of anisotropic colloidal crystals in two dimensions. J. Phys., Condens. Matter, **16**, S4095 (2004)
21. L.-W. Teng, P.-S. Lu, I. Lin, Microscopic observation of confinement-induced layering and slow dynamics of dusty-plasma liquids in narrow channels. Phys. Rev. Lett. **90**, 245004 (2003)
22. R.A. Segalman, A. Hexemer, E.J. Kramer, Edge effects on the order and freezing of a 2D array of block copolymer spheres. Phys. Rev. Lett. **91**, 196101 (2003)
23. K. Binder, in *Cohesion and Structure of Surfaces, Ch. III*, ed. by D.G. Pettifor (Elsevier, Amsterdam, 1995), p. 121
24. K. Bagchi, H.C. Andersen, W. Swope, Observation of a two-stage melting transition in two dimensions. Phys. Rev. E **53**, 3794 (1996)
25. J.P. Hansen, I.R. Mc Donald, *Theory of Simple Liquids* (Academic, London, 1986)
26. J.L. Cardy, Conformal invariance and surface critical behavior. Nucl. Phys. B**240**, 514 (1984)
27. K. Binder, in *Phase Transitions and Critical Phenomena, Vol 8*, ed. by. C. Domb and J.L. Lebowitz (Academic, New York, NY, 1983) p.1
28. Y.-H. Chui, S. Sengupta, I.M. Snook, K. Binder, The observation of formation and annihilation of solitons and standing strain wave superstructures in a two-dimensional colloidal crystal. J. Chem. Phys. **132**, 074701 (2010)
29. E. Sarigiannidou, E. Monroy, B. Daudin, J.L. Rouvière, A.D. Andreev, Strain distribution in GaN/AlN quantum-dot superlattices. Appl. Phys. Lett. **87**, 203112 (2005)
30. Z.L. Liau, Strained interface of lattice-mismatched wafer fusion. Phys. Rev. B**55**, 12899 (1997)
31. D.D. Prević, B. Bahierathan, H. Lafontaine, D.C. Houghton, D.W. Mc Comb, Kinetic critical thickness for surface wave instability vs. misfit dislocation formation in Ge_xSi_{1-x}/Si (100) heterostructures. Physica A **239**, 11(1997)
32. M. Nielsen, B.O. Poulson, C. Kumpf, F. Feidenhans, R.L. Johnson, F. Jensen, F. Grey, Mapping strain fields in ultrathin bonded Si wafers by x-ray scattering. Appl. Phys. Lett. **80**, 3412 (2002)

33. R. Bessling, R. Niggebrugge, P.H. Kes, Transport properties of vortices in easy flow channels: a Frenkel-Kontorova study, Phys. Rev. Lett. **82**, 3144 (1999); N. Kokubo, R. Besseling, V.M. Vinokur, P.H. Kes, Model locking of vortex matter driven through mesoscopic channels. Phys. Rev. Lett. **88**, 247004 (2002)
34. D. Chaudhuri, S. Sengupta, Anomalous structural and mechanical properties of solids confined in quasi-one-dimensional strips. J. Chem. Phys. **128**, 194702 (2008)
35. D. Chaudhuri, S. Sengupta, Constrained deformation of a confined solid: anomalous failure by nucleation of smectic bands. Phys. Rev. Lett. **93**, 115702 (2004)

Chapter 2
Multisite Interactions in Lattice-Gas Models

T.L. Einstein and R. Sathiyanarayanan

Abstract For detailed applications of lattice-gas models to surface systems, multisite interactions often play at least as significant a role as interactions between pairs of adatoms that are separated by a few lattice spacings. We recall that trio (3-adatom, non-pairwise) interactions do not inevitably create phase boundary asymmetries about half coverage. We discuss a sophisticated application to an experimental system and describe refinements in extracting lattice-gas energies from calculations of total energies of several different ordered overlayers. We describe how lateral relaxations complicate matters when there is direct interaction between the adatoms, an issue that is important when examining the angular dependence of step line tensions. We discuss the connector model as an alternative viewpoint and close with a brief account of recent work on organic molecule overlayers.

2.1 Introduction

A thorough understanding and characterization of surface energetics is important for fabricating nanostructures with desired morphological features. To this end, lattice-gas models have been very successful in categorizing structural properties, energetics, and evolution of adatoms and steps on surfaces, as discussed in a variety of reviews [1–4]. They have also been applied to analogous but more complicated systems [5], such as electrochemistry [6]. The underlying viewpoint is that a set of interactions is sufficient to understand both equilibrium and dynamic surface processes. Lattice-gas models provide a powerful and convenient route to explore how microscopic energies influence the statistical mechanics of nanoscale to submonolayer structures on crystalline surfaces. Such models underlie most Monte Carlo (and transfer matrix) simulations. They assume that overlayer atoms (or other adsorbed units) sit at particular high-symmetry sites of the substrate. The parameters

T.L. Einstein (✉)
Department of Condensed Matter Physics, University of Maryland, College Park, MD 20742-4111, USA
e-mail: einstein@umd.edu

M. Michailov (ed.), *Nanophenomena at Surfaces,* Springer Series in Surface Sciences 47,
DOI 10.1007/978-3-642-16510-8_2,

of the model are then the interaction energies between such atoms and/or the barriers associated with hops between the high-symmetry positions.

The use of lattice-gas models proceeds in two generic ways. In the first, one posits a few energies that are likely to dominate the physics of interest and then computes with Monte Carlo simulations the desired equilibrium or dynamic properties, deriving thereby the values of these energies from fits [1, 7, 8]. The dangers of this approach are (1) the properties of interest may be relatively insensitive to the specific interactions and (2) there may be other interactions that are non-negligible, so that the deduced energies are effective rather than actual.

The second approach [9–12] begins by actually computing the (many) energies of importance, a task that is now possible with efficient density functional theory packages such as VASP (the Vienna ab initio simulation package) [13, 14]. This process can be used to compute interaction energies between relatively distant neighbors. One should also compute multi-atom interactions, which can also be significant [3, 15]. As above, these interactions are then used in Monte Carlo simulations to test whether they account adequately for experimentally observed properties such as phase diagrams, equilibrium island shapes, or step fluctuations. This approach is appealing because the calculated interaction energies can be self-consistently checked for completeness, thereby mitigating the second danger mentioned above. Assuming that one has sufficient computational power to compute all the interactions that contribute at the level of the desired precision, there is still the danger that the interactions depend sensitively on the local environment, making a simple lattice-gas description inadequate. These caveats notwithstanding, lattice-gas models have been extensively used in the realm of surface physics to describe such diverse phenomena as phase transitions, phase diagrams, equilibrium island shapes, concentration-dependent diffusion, step fluctuations, and growth.

The basic assumptions that underlie lattice-gas models are as follows: (i) all atoms sit at high-symmetry positions and local relaxations produce the final structure; (ii) a finite set of effective interactions is sufficient to understand all the surface processes; and (iii) interactions are not sensitive to local positions of the adatoms. In the simplest scenario, only pair interactions between nearest neighbors are considered. However, in certain cases, like the orientation dependence of step stiffness and the equilibrium shape of islands, long-range pair interactions and multisite interactions are required for a complete description [8, 12, 16–20]. The substrates in these studies are typically mid- or late transition or noble metals, where the electronic indirect interaction leads to rich behavior [3].

Explicitly, the lattice-gas Hamiltonian of adatoms on a surface is written as

$$\mathcal{H} = \sum_{m=1}^{M} E_m \sum_{\langle ij\rangle_m} n_i n_j + \sum_{T} E_{\mathrm{T}} \sum_{\langle ijk\rangle_T} n_i n_j n_k + \sum_{Q} E_{\mathrm{Q}} \sum_{\langle ijk\ell\rangle_Q} n_i n_j n_k n_\ell + \cdots \quad (2.1)$$

where n_i is the occupancy of the high-symmetry lattice site indexed i; $n_i = 1$ denotes an occupied site; and $n_i = 0$ denotes an empty site. Interactions between adatom pairs up to the mth-neighbor pair E_m are included in the model (Fig. 2.1);

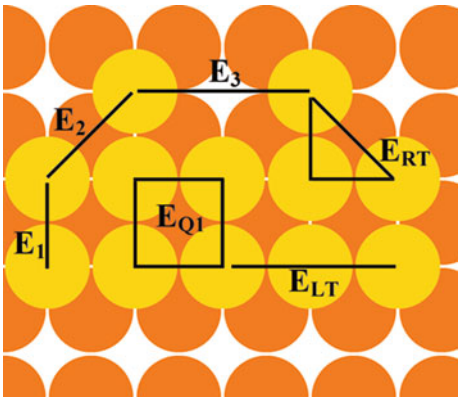

Fig. 2.1 Illustration of NN (nearest neighbor), NNN (next NN), and three NN (third NN) pairs with interaction energies E_1, E_2, and E_3, respectively. Also shown are the isosceles right triangle (RT) with energy E_{RT} or, more formally, E_{112} (denoting a pair of NN legs and one NNN leg), and an isosceles linear triangle (LT) with energy E_{LT} or, more formally, E_{113}. Lastly, the most compact quarto interaction has interaction energy E_{Q1} or, more formally, E_{1111}. For clarity [and physical relevance], here and in Fig. 2.5, the adatoms are placed in center sites, as for homoepitaxy on the (100) face of an fcc crystal like Cu, rather than atop sites as for homoepitaxy on a simple cubic crystal

accordingly, interactions between adatom pairs that are separated by distances greater than the mth neighbor distance are expected to be insignificant. E_{T} stands for three-adatom non-pairwise "trio" interactions, with the index running over all trimer configurations of significant strength. Similarly, E_{Q} stands for four-adatom non-pairwise (and with trios also subtracted) "quarto" interaction. (The possibility of quarto interactions has been known for over three decades [3, 21], but, to the best of our knowledge, it has been invoked only once in an actual calculation of adsorbate energetics [22]) until very recently [23, 24]. If necessary, pair interactions with a longer range and/or higher order multi-site interactions (possibly, five-adatom quintos) are included in the model till adequate convergence between theoretical predictions and experimental observations is obtained. However, the inclusion of a large number of interaction parameters makes the lattice-gas model intractable, thereby severely undermining the efficacy of lattice-gas models in characterizing overlayer systems.

The nature of the interactions leading to the lattice-gas pair energies has been reviewed extensively [3, 25–27] so we will present just a quick summary. If there is charge transfer (workfunction change) during the adsorption process, the adsorbates can interact electrostatically. Other "direct" interactions between the adatoms themselves can occur when the adatoms are at NN (nearest-neighbor) or perhaps NNN (next NN) sites. These are strong interactions, comparable to the binding energy, with the substrate playing a minor, sometimes negligible role; they are liable to produce relaxations that thwart straightforward application of lattice-gas models (cf. Sect. 2.5.2). When adatoms are sufficiently separated that there is insignificant overlap of the electron orbitals, there can still be an "indirect" interaction – weaker but

of longer range – mediated by substrate electrons or the elastic field. Elastic interactions tend to be of one sign and decay monotonically with adsorbate separation distance d, like d^{-3} asymptotically. They are generally taken to be isotropic, even when unjustified by the elastic tensor, since computing elastic Green's functions in the anisotropic case is notoriously difficult [28]. The electronic indirect interaction has richer behavior, oscillating in sign and reflecting the isotropy or anisotropy of the substrate wavefunctions in the surface plane [29]. Asymptotically it is dominated by the Fermi wavevector and has the Friedel behavior

$$d^{-n} \sin(2k_F d + \Phi) \tag{2.2}$$

where d is the [lateral] distance between the adsorbates; this result is non-perturbational, the phase factor Φ distinguishing it from the well-known perturbational RKKY expression [30]. (For a non-isotropic Fermi surface, the appropriate wavevector has *velocity* parallel to $\mathbf{d}$; see [3] for details.) In the bulk, $n = 3$, but at a metal surface the leading term is canceled by that from its image charge, yielding $n = 5$. For trio interactions an expression similar to (2.2) holds to lowest order, with d replaced by the perimeter of the triangle formed by the adatoms. Here the decay is even faster, with $n = 7$. In short, interactions mediated by bulk states have negligible strength for values of d for which the asymptotic expression is valid.

The situation is strikingly different when there is a metallic surface state (i.e., a surface band that crosses the Fermi energy), such as found near the $\bar{\Gamma}$ point on the (111) faces of noble metals (associated with the (111) necks of the Fermi surface). For this case n is 2 and 5/2 for pair and trio interactions, respectively, so that the asymptotic regime is physically important [31]. Indeed, trio interactions may play a role in the formation of 2D clusters of Cu/Cu(110) [32]. Furthermore, the Fermi "surface" is circular, and k_F is much smaller than its bulk counterpart, leading to the dramatic oscillations (with wavelength $\pi/k_F \approx 15$ Å) seen in STM experiments [33].

Most of the content of this and the second, third, and fifth sections of this chapter were included in the first author's presentation at the Vth Stranski-Kaischew Surface Science Workshop (SK-SSW'2005): "Nanophenomena at Surfaces – Fundamentals of Exotic Condensed Matter Properties" in Pamporovo, but have been updated. Each section provides references from which the content was adapted and from which more information can be obtained.

2.2 Recollection of Two Effects on Statistical Mechanics

In this section we recall two remarkable implications of trio interactions for phase diagrams [15]. While these ideas are not new, they have been largely ignored by the community and so bear repeating.

2.2.1 Pitfall in Transforming Trio Strength Between Lattice-Gas and Ising Models

Many researchers recast the lattice-gas model into an Ising model before doing computations. This seemingly innocent procedure invites pitfalls when multisite interactions are involved. Here we offer a particular example: what seems like a relatively modest three-spin interaction can correspond to an unphysically large trio interaction in the lattice-gas Hamiltonian. Our example involves a square lattice with $M = 2$ (first and second neighbor pair interactions) and the right-triangle trio E_{RT} corresponding to two E_1 legs at right angles and an E_2 hypotenuse (or E_{112} for short, in a general formal notation [3]).

The mapping to spin language, with $s_i = \pm 1$, is $n_i = (1 + s_i)/2$. We see

$$\mathcal{H} = \left(\frac{E_1}{4} + \frac{E_{\mathrm{RT}}}{2}\right) \sum_{\langle ij \rangle_1} s_i s_j + \left(\frac{E_2}{4} + \frac{E_{\mathrm{RT}}}{4}\right) \sum_{\langle ij \rangle_2} s_i s_j + \frac{E_{\mathrm{RT}}}{8} \sum_{\langle ijk \rangle_{\mathrm{RT}}} s_i s_j s_k \quad (2.3)$$

In Ising or spin language, the three coefficients are called $-J_1$, $-J_2$, and $-J_{\mathrm{RT}}$, respectively. For the pair interactions, we easily see that

$$\frac{J_2}{J_1} = \frac{E_2/E_1 + E_{\mathrm{RT}}/E_1}{1 + 2E_{\mathrm{RT}}/E_1} \approx \frac{E_2}{E_1} \text{ for } |E_{\mathrm{RT}}| \lesssim 4|E_1| \quad (2.4)$$

One might then naively – but incorrectly – expect that $J_{\mathrm{RT}}/J_1 \approx E_{\mathrm{RT}}/E_1$. Instead

$$\frac{J_{\mathrm{RT}}}{J_1} = \frac{E_{\mathrm{RT}}/E_1}{2 + 4E_{\mathrm{RT}}/E_1} \quad \Leftrightarrow \quad \frac{E_{\mathrm{RT}}}{E_1} = \frac{2J_{\mathrm{RT}}/J_1}{1 - 4J_{\mathrm{RT}}/J_1} \quad (2.5)$$

This highly non-linear relation leads to a surprising result: For $J_{\mathrm{RT}}/J_1 \lesssim 1/4$, $E_{\mathrm{RT}}/E_1 \gg J_{\mathrm{RT}}/J_1$. Furthermore, if J_{RT}/J_1 increases to slightly above 1/4, E_{RT}/E_1 becomes large and negative. A similar effect would occur in the opposite direction for $E_{\mathrm{RT}}/E_1 \approx -1/2$, a larger magnitude than one is likely to encounter.

Finally, it is unfortunate (to say the least) that some researchers (including prominent ones) denote the lattice-gas energy parameters as J. Even in the simplest case of just a nearest-neighbor interaction, the lattice-gas energy differs from the Ising energy by a factor of 4; thus, misinterpretation and numerical inaccuracies are very likely.

2.2.2 Effect on Phase Boundaries: Asymmetries Not Inevitable

A trio interaction, which breaks particle–hole symmetry (or up-down symmetry in the Ising viewpoint), is generally expected to lead inevitably to substantial asymmetries in phase diagrams about half-monolayer coverage. A rather surprising finding of numerical [Monte Carlo] calculations is that a single type of trio interaction need

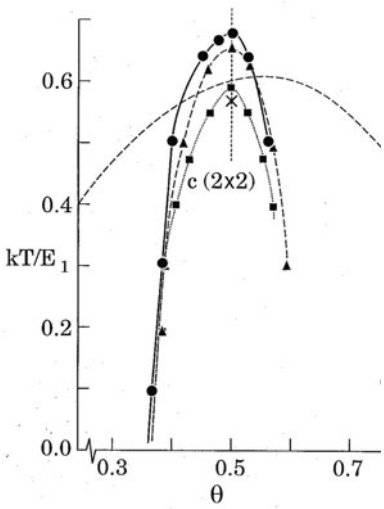

Fig. 2.2 Illustration, for a $c(2 \times 2)$ overlayer on a square lattice, of the heuristic guideline, based on scaling the elementary excitation, used to predict which trios produce observable asymmetries in phase boundaries. For the simplest case of an NN repulsion, E_1, the disordering temperature is known exactly from the Onsager solution to the Ising model; it is indicated by the $\times$ on the temperature-coverage phase diagram. The effect of adding a right-triangle trio repulsion E_{RT}, a linear trio repulsion E_{LT}, or both was studied using Monte Carlo for the case $E_{\mathrm{RT}} = E_{\mathrm{LT}} = E_1/4$; the results for the three cases are plotted with *filled triangles*, *squares*, and *circles*, with *dashed, dotted*, and *solid curves*, respectively, added to guide the eye. The behavior at $\theta = 0.5$ is anticipated by (2.7) and (2.8). The *dashed* and *dotted curves* appear symmetric about $\theta = 0.5$ (*short-dotted line*); only with both trios present does the [*solid*] phase boundary become noticeably asymmetric. In the plots at the right, the $\times$'s and dots indicate occupied and vacant sites, respectively, in a perfectly ordered configuration, with the large symbols denoting a vacancy ($\theta < 1/2$) or extra adatom ($\theta > 1/2$), respectively. The *arrows* on the plots depict the lowest energy excitations, with the linetype of the shaft corresponding to the linetype of the phase boundary on the phase diagram; for each linetype, this excitation energy is the same for $\theta < 1/2$ and $\theta > 1/2$. According to the heuristic prescription, these energies scale the disordering temperature. When both trios are present, there is "frustration" over which excitation to use, the prescription fails, and asymmetries occur. In the phase diagram, the *broad dashed curve* is the result of a mean-field calculation, plotted at half its magnitude (i.e., $T_{\mathrm{c}}(\theta = 0.5) \approx 1.2E_1$); not only is this prediction of T_{c} far too high and too broad, it also erroneously predicts substantial asymmetry. From [15]

not necessarily do so. (See also the discussion by Persson of the role of adsorption in sites not of high symmetry, the equivalence to trio interactions, and the rich effects on temperature-coverage phase diagrams [2, 34].) This result, illustrated in Fig. 2.2 for the case of a $c(2 \times 2)$ overlayer with $E_1 > 0$ and E_{RT}, is in sharp contrast to the observation in 2D calculations which treat fluctuations approximately – mean-field and quasi-chemical approximations – that trios must produce such asymmetries [35]. Likewise we see that a linear trio E_{LT} alone does not produce an asymmetry. However, when both E_{RT} and E_{LT} are present, the expected notable asymmetry does appear. To comprehend this effect of trios on the phase boundary, we need some way to assess the difference in the way the trio interactions affect the lower temperature

ordered phase compared to the higher temperature disordered phase. Evidently the breaking by trios of the particle–hole symmetry of the pair interaction lattice-gas hamiltonian, and the resulting asymmetry in the ground state energy, is not the crux.

We describe a crude approximation scheme for assessing the change in the disordering temperature T_c of an ordered phase from a known value $T_c(0)$ for some Hamiltonian to $T_c(E_{new})$ for a more complicated Hamiltonian with a new interaction energy E_{new}. While we have applied our procedure [36] to a wide range of problems, we still have no formal derivation. In essence, the idea is that T_c scales with the lowest energy excitation from the ground state. In [36] we show, e.g., that for a $c(2 \times 2)$ overlayer with half-monolayer coverage, characterized by a nearest-neighbor repulsion E_1 and a smaller second-neighbor interaction E_2,

$$T_c(E_2) = T_c(E_2 = 0)\left(1 - \frac{4E_2}{3E_1}\right) \tag{2.6}$$

For this simple problem, Barber [37] showed that the exact coefficient is $\sqrt{2} \approx 1.41$ rather than $4/3 \approx 1.33$; on the other hand, our value is much better than the mean-field prediction of 1. For this same problem, the effect of a right-triangle trio interaction E_{RT} (with $E_2 = 0$) is given by

$$\frac{3E_1 + 2E_{RT}}{T_c(E_{RT})} = \frac{3E_1}{T_c(0)} \quad \Rightarrow \quad T_c(E_{RT}) = T_c(E_{RT} = 0)\left(1 + \frac{2E_{RT}}{3E_1}\right) \tag{2.7}$$

Similarly, for a linear trio E_{LT}

$$\frac{3E_1 + E_{LT}}{T_c(E_{LT})} = \frac{3E_1}{T_c(0)} \quad \Rightarrow \quad T_c(E_{LT}) = T_c(E_{LT} = 0)\left(1 + \frac{E_{LT}}{3E_1}\right) \tag{2.8}$$

We caution that this procedure is applicable only if the new interaction does not alter the symmetry of the ordered state and works well only if the nearby elementary excitation from the fully ordered state is uniquely defined. Thus, it works well for a $(\sqrt{3} \times \sqrt{3})$ overlayer on a hexagonal net but not for a $p(2 \times 2)$. It is also curious that this procedure requires a lattice-gas picture in which the number of atoms is conserved (i.e., a canonical ensemble or Kawasaki dynamics); if the atom instead hopped to a "bath" (i.e., a grand canonical ensemble, or fixed chemical potential, or a single spin flip in a spin analogue (Glauber dynamics)), the predictions are quite poor.

To assess the effect of trios on the symmetry of the temperature-coverage phase boundary of a $c(2 \times 2)$ overlayer, we look at the elementary excitation near a defect, either an extra adatom or a missing one (see Fig. 2.2). For just a right-triangle trio, there are no such trios (no $2E_{RT}$) in the excited state when there is a vacancy; when there is an extra adatom, there are two RT trios in the ordered state which are lost in hopping to the nearest neighbor (where another two RT trios occur). So in both cases, there is no change in the number of RT trios, i.e., no change proportional to E_{RT} is involved. A similar effect occurs with a linear trio, but with a different

elementary excitation (see Fig. 2.2). In either case, we saw that the phase boundary computed using Monte Carlo appears symmetric. Only when both trios are present does a marked asymmetry occur. However, a noteworthy inadequacy of this simple picture is its inability to give any idea of the coverage dependence of T_c (M.E. Fisher, private communication).

2.3 Applications to Gases on Metals

As an example of the state of the art in quantitatively determining adsorbate–adsorbate interactions from combined theory and experiment, we discuss the study of $c(2 \times 2)$ N on Fe(001) by Österlund et al. [8]. Since there is just one ordered phase, one might expect to be able to extract information about only a handful of interactions, say $E_1 > 0$, E_2, and a trio, from STM observations. The authors use a new concept called configuration distribution analysis (CDA) to extract much more information from high-resolution images. Around each nitrogen adatom they obtain a site map of possible adsorption sites. By comparing the resulting experimental conditional probabilities with those obtained from Monte Carlo simulations with a lattice-gas model, they can refine estimates of the various interactions.

The authors first consider a long-established analysis [38, 39] of the pair correlation function $g(j)$, from which they deduce $E_j = -k_B T \ln g(j)$, for jth neighbors, between fractional coverages $\Theta = 0.037$ and 0.15. They find very little NN site occupation and enhanced NNN occupation. For $j > 4$ there is no significant deviation from a random distribution ($g = 1$). From the data they find $E_1 = 0.13\,\text{eV}$ and $E_2 = -0.013\,\text{eV}$. Concerned about poor statistics at $\Theta = 0.037$, the authors also carried out Monte Carlo simulations and used a least-squares fit of data at all the coverages, finding similar energies: $E_1 = 0.14\,\text{eV}$, $E_2 = -0.023\,\text{eV}$, and $E_3 = 0.003\,\text{eV}$. They then did a CDA analysis in conjunction with Monte Carlo simulations (seemingly at $\Theta = 0.108$), supplemented by a comparison of measured and simulated island-size distributions. They thus determined $E_1 = 0.13\,\text{eV}$, $E_2 = -0.018\,\text{eV}$, $E_3 = 0.019\,\text{eV}$, and trio interaction energies $E_{223} = -0.012\,\text{eV}$, and $E_{225} = 0.006\,\text{eV}$. (These trios correspond to RT and LT triangles on a larger scale, with insignificant direct interactions.) If 3NN (third NN) sites are considered in the CDA, then E_3 decreases to $0.015\,\text{eV}$. If trios are omitted from the CDA analysis, E_1 is unchanged but E_2 increases in magnitude to $-0.038\,\text{eV}$, while E_3 diminishes to $0.003\,\text{eV}$. In other words, fitted pair interactions are actually effective interactions that include omitted interactions in some average, unspecified way. The effect seems to be largest for the most prominent legs of the omitted interactions, in this case NNN.

The authors also include an elastic repulsion, taken to have the asymptotic isotropic form C/R^3 with strength $C/a^3 = 0.15\,\text{eV}$, where a is the Fe lattice constant (2.87 Å). Hence, the *electronic* components of the three pair interactions (for the CDA analysis including trios and configurations to $j = 3$) are -0.2, -0.71, and $-0.04\,\text{eV}$, respectively. (There is no comment about adjusting the trios.) Note, remarkably, that $|E_1^{\text{el}}| < |E_2^{\text{el}}|$. The authors conclude that the electronic interaction

is short range. The embedded atom method (EAM), for metals on metals, predicts that the indirect interaction is repulsive and proportional to the number of shared substrate atoms [3]. On very general grounds one expects R^{-5} decay of the envelope in (2.2). We caution that the distinction between electronic and elastic has long been recognized as subtle [40] and that the asymptotic limit of the elastic interaction is likely to be significantly modified at separations $\mathcal{O}(a)$ by more rapidly decaying terms in the multipole series [41].

2.4 Refined Schemes for Extracting Interaction Energies

To extract estimates of interaction energies when there are many such parameters are a delicate task typically one obtains a large number of simultaneous equations by computing the total interaction of a large variety of different overlayer structures. One should have more overlayer structures than interactions so as to be able to check for robustness of the deduced values. While informal schemes had formerly seemed sufficient [42], it is safer and sounder to use formal cross-validation schemes used by several groups [12, 43] to study overlayer systems.

In recent work [44] we used the leave-n_v-out cross-validation method [45] to fit the computed energies for Cu(110) to the interaction parameters (cf. Sect. 2.6). This method is expected to perform better than the more commonly used leave-one-out cross-validation scheme [45]. We calculated the interaction strengths in the following way: for a particular supercell, we computed total energies for, say, n different configurations of adatoms. In addition, we posit the number of significant interactions n_i. We then use n_i (out of n) equations to solve for the interaction energies. These interactions are then used to predict the energies of the remaining $n_v = n - n_i$ equations. We then compute the root mean squared (rms) of the prediction error per adatom for all configurations j ($1 \le j \le n_v$), each with a_j adatoms in it:

$$\Delta E_{\mathrm{rms}} = \sqrt{\frac{1}{n_v}\sum_{j=1}^{n_v}(\Delta E_j)^2} \quad \Delta E_j = \frac{E^{\mathrm{pred}} - E^{\mathrm{VASP}}}{a_j} \tag{2.9}$$

We repeat this procedure for different partitions of (n,n_i), and sets of interactions from only those partitions whose ΔE_{rms} values are lower than a specified threshold value (10 meV/adatom in Ref. [44]) are considered for the final averaging of interaction values. Finally, we find the value of n_i that leads to the best convergence. As a check, we perform this procedure on two different computational supercells.

2.5 Effect of Relaxations in Homoepitaxy with Direct Lateral Interactions

When direct interactions play a significant role, such as for (1×1) homoepitaxial partial monolayers, one must be wary of relaxation-induced modification of

energies near steps or island edges. From bond energy, bond order, bond length reasoning [46], one can expect such atoms – which lack their full complement of near-neighbor bonds, to move closer to the remaining neighbors to partially compensate for the loss. Persson showed that relaxation in the form of adsorption away from high-symmetry sites can lead to effective trio interactions, and attendant effects, in systems with ostensibly only pair interactions [2, 34]. Our goal here is to show that these relaxation effects are especially significant for multisite interactions, where the relaxations are not along the bond directions. Furthermore, multisite interactions, in general, have a large elastic component; hence, a careful consideration of relaxation effects is needed while computing them. We discuss in particular how strain-related effects are important when calculating the step stiffness on Cu(100). Because of adatom relaxation near steps, the inclusion of non-pairwise, quarto interaction between four adatoms is required on this square-lattice surface in order to preserve a lattice-gas description.

2.5.1 Multisite Interactions in Step-Stiffness Asymmetry

Step stiffness (which earlier served as the mass in the 1D fermion model of steps) underlies how steps respond. It is one of the three parameters of the step-continuum model [47], which has proved a powerful way to describe step behavior on a coarse-grained level, without recourse to a myriad of microscopic energies and rates. In the analogy between 2D configurations of steps and worldlines of spinless fermions in $(1 + 1)$D, step stiffness $\tilde{\beta}$ plays the role of the mass of the fermion. As the inertial term, stiffness determines how a step responds to fluctuations, to driving forces, and to interactions with other steps.

We summarize our lattice-gas-based computations of the orientation dependence of step stiffness for the (001) and (111) faces of Cu [48, 49]. This work illustrates both successes and some shortcomings of using a lattice-gas model with just NN interactions: whereas the step stiffness on Cu(111) is well described by NN interactions alone, the step stiffness on Cu(001) requires the inclusion of NNN and perhaps even trio interactions. We discuss only the latter.

The step stiffness $\tilde{\beta}(\theta) \equiv \beta(\theta) + \beta''(\theta)$ weights deviations from straightness in the step Hamiltonian, where θ is conventional designation of the azimuthal misorientation angle; it measured from the close-packed direction. Here β is the step-free energy per length (or, equivalently, the line tension, since the surface is maintained at constant [zero] charge [50]). The stiffness is inversely proportional to the step diffusivity, which measures the degree of wandering of a step perpendicular to its mean direction. This diffusivity can be readily written down in terms of the energies ε_k of kinks along steps with a mean orientation $\theta = 0$: in this case, all kinks are thermally excited. Conversely, experimental measurements of the low-temperature diffusivity (via the scale factor of the spatial correlation function) can be used to deduce the kink energy. A more subtle question is how this stiffness depends on θ. Even for temperatures much below ε_k, there are always a non-vanishing number

of kinks when $\theta \neq 0$, the density of which is fixed by geometry (and so are proportional to $\tan\theta$). In a bond-counting model, the energetic portion of the $\beta(\theta)$ is canceled by its second derivative with respect to θ, so that the stiffness is due to the entropy contribution alone. Away from close-packed directions, this entropy can be determined by simple combinatoric factors at low temperature T [51–53].

Interest in this whole issue has been piqued by Dieluweit et al.'s finding [54] that the stiffness as predicted in the above fashion, assuming that only NN interactions E_1 are important, underestimates the values for Cu(001) derived from two independent types of experiments: direct measurement of the diffusivity on vicinal Cu surfaces with various tilts and examination of the shape of (single-layer) islands. The agreement of the two types of measurements assures that the underestimate is not an anomaly due to step–step interactions. In that work, the effect of NNN interactions E_2 was crudely estimated by examining a general formula obtained by Akutsu and Akutsu [55], showing a correction of order $\exp(-E_2/k_BT)$, which was glibly deemed to be insignificant. In subsequent work the Twente group [56] considered steps in just the two principal directions and showed that by including an attractive NNN interaction, one could evaluate the step-free energies and obtain a ratio consistent with the experimental results in [54]. They later extended their calculations [57] to examine the stiffness.

To make contact with experiment, one typically first gauges the diffusivity along a close-packed direction and from it extracts the ratio of the elementary kink energy ε_k to T. Arguably the least ambiguous way to relate ε_k to bonds in a lattice-gas model is to extract an atom from the edge and place it alongside the step well away from the new unit indentation, thereby creating four kinks [58]. Removing the step atom costs energy $3E_1 + 2E_2$ while its replacement next to the step recovers $E_1 + 2E_2$. Thus, whether or not there are NNN interactions, we identify $\varepsilon_k = -\frac{1}{2}E_1 = \frac{1}{2}|E_1|$ (since the formation of Cu islands implies $E_1 < 0$); thus, as necessary, $\varepsilon_k > 0$.

In the low-temperature limit, appropriate to the experiments [54], we have shown that

$$\frac{k_BT}{\tilde{\beta}a} = \frac{m\sqrt{(1-m)^2 + 4me^{E_2/k_BT}}}{(1+m^2)^{3/2}} \underset{m\to 0^+}{\longrightarrow} \frac{m+m^2}{\left(1+m^2\right)^{3/2}} \tag{2.10}$$

where m is the step-edge in-plane slope.

Figure 2.3 compares (2.10) to corresponding exact solutions at several temperatures when $E_2 = E_1/10$. We see that (2.10) overlaps the exact solution at temperatures as high as $T_c/6$. As the temperature increases, the stiffness becomes more isotropic, and (2.10) begins to overestimate the stiffness near $\theta = 0°$. In Fig. 2.4 (using the experimental value [59] $\varepsilon_k = 128\,\text{meV} \Rightarrow E_1 = -256\,\text{meV}$), we compare (2.10) to the NN Ising model at $T = 320\,\text{K}$, as well as to the experimental results of [54]. For strongly attractive (negative) E_2, $k_BT/\tilde{\beta}a$ decreases significantly. In fact, when E_2/E_1 is 1/6, so that $-E_2/2k_BT = (E_2/E_1)(\varepsilon_k/k_BT) \approx (1/6)4.64$, the model-predicted value of $k_BT/\tilde{\beta}a$ has decreased to less than half its $E_2 = 0$ value, so about 3/2 the experimental ratio. For the NNN interaction alone to

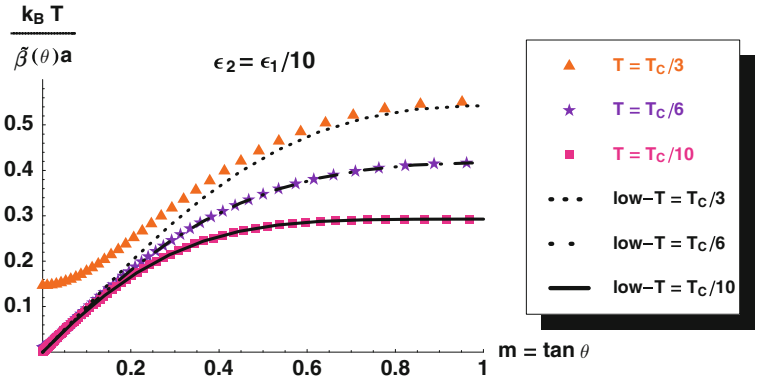

Fig. 2.3 The range of validity of (2.10) is examined by comparing it to exact numerical solutions of the SOS model at several temperatures. In the legend T_c refers to the NN lattice-gas (Ising) model; for $|E_1| = 256\,\text{meV}$, $T_c = 1685\,\text{K}$. From [48]

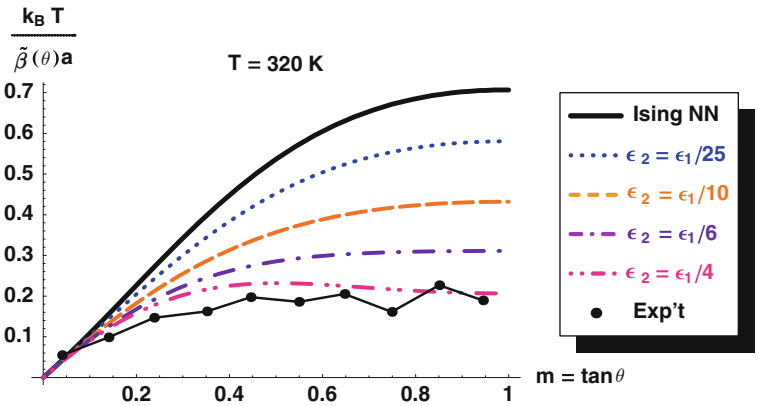

Fig. 2.4 Equation (2.10) is plotted for a range of values of E_2 (*epsilon* on the plot, where E_1 and E_2 are NN and NNN interaction energies, respectively, in a lattice-gas picture. The *solid curve* denoted "Ising NN" corresponds to $E_2 = 0$. The *dots* labeled "Exp't" are taken from figure 2 of [54] and were derived from the equilibrium shape of islands on Cu(001) at 302 K, with line segments to guide the eye. To clarity, we omit similar data derived from correlation functions of vicinal surfaces at various temperatures. Note that for $E_2 = E_1/4$ there is a maximum near $\tan\theta = 1/2$ that is not observed in experimental data. From [48]

account for the factor-of-4 discrepancy between model/theory and experiment [54], Fig. 2.4 shows that $E_2/E_1 \approx 0.3$ would be required.

2.5.2 *Effect of Trio Interactions*

If we include an RT trio (E_{112}) the effective NN lattice-gas energy E_1^{eff} is $E_1 + 2E_{\text{RT}}$ and more significantly the effective NNN interaction energy is $E_2 + E_{\text{RT}}$. Thus, E_{RT} must be attractive (negative) if it is to help account for the discrepancy in

figure 2 of [54] between the model and experiment. Furthermore, by revisiting the configurations discussed in the penultimate paragraph of the Introduction, we find that the kink energy ε_k becomes $-\frac{1}{2}E_1 - E_{RT}$. Thus, for a repulsive E_{RT}, $|E_1|$ will be larger than predicted by an analysis of, e.g., step-edge diffusivity that neglects E_{RT}. Lastly, the close-packed edge energy, i.e., the $T = 0$ line tension $\beta(0) = -\frac{1}{2}E_1 - E_2$, becomes $-\frac{1}{2}E_1 - E_2 - 2E_{RT}$.

We also investigated the strain-related effects on calculated trio interaction energies on Cu(100), where Dieluweit et al. [54] showed that the NN Ising model cannot explain the experimentally observed step-stiffness anisotropy. In a response, we showed that the addition of an effective NNN attractive interaction could resolve the discrepancy. The effective NNN interaction (E_2) can be written as the sum of two components as illustrated in Fig. 2.5a:

- a pairwise second neighbor interaction energy (E_2)
- an orientation-dependent right-isosceles trio interaction energy (E_{RT})

However, when we used VASP to calculate these interactions, we found a large repulsive value of around 50 meV for the right-isosceles trio interaction energy (E_{RT}). Such a value cancels the calculated attractive second-neighbor interactions (E_2) thereby reducing the model to an NN Ising model. Thus, in the end the discrepancy between theory and experiment could not be resolved.

To see the effect of relaxation, we repeated the calculations with a bigger supercell ($4 \times 4 \times 14$). If an adatom stripe has kinks, there can be two types of right-isosceles trios, ones with one/two adatoms on the step-edge and ones with no adatoms on the step edge (Fig. 2.5b). Since the local geometry of these two adatoms is different, we could expect the trio interaction energies to be different because the RT trio adatoms (E'_{RT}) inside a stripe cannot relax as much laterally as the trios with its vertices on the step (E_{RT}). The trio energy that we calculated earlier corresponds to a linear combination of E_{RT} and E'_{RT}, weighted more dominantly by E'_{RT}. However, the calculation of the step stiffness depends on broken step-edge trios, which necessarily correspond to E_{RT}. To distinguish these two trios here, we calculated the

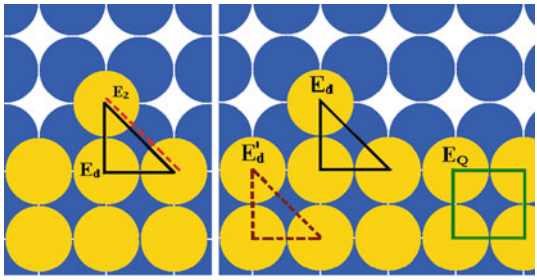

Fig. 2.5 (**a**) Effective NNN interactions on a (100) surface [of an fcc crystal], (**b**) multisite interactions E_d (*solid triangle*),E'_d (*broken triangle*), and E_Q (*square*), where the subscript d is RT in our notation. The trio E_d has adatoms on the step edge whereas E'_d has no adatoms on the step edge. From [23]

energies of four different adatom configurations and we solved the resultant linear system of equations. With this correction, at the step-edge $E_{\mathrm{RT}} \approx 12.5$ meV/atom, and the effective NNN interaction is thus $E_2^{\mathrm{eff}} = E_2 + E_{\mathrm{RT}} \approx -35$ meV/atom.

Though E_{RT} is still repulsive, its magnitude is lower than that of the attractive E_2. The ratio of the effective NN interaction to the effective NNN interaction is

$$E_2^{\mathrm{eff}}/E_1^{\mathrm{eff}} \sim 1/9 \quad \text{while} \quad E_2/E_1 \sim 1/7 \tag{2.11}$$

which is much closer to experimental expectations.

Distinguishing between the step-edge trios E_{RT} and the bulk trios E'_{RT} is not compatible with a proper lattice-gas picture, where interactions should not depend on local position and geometry. We can remedy this problem by introducing a quarto interaction. This quarto interaction distinguishes between the two trios because it is present only in bulk trios E'_{RT}:

$$E'_{\mathrm{RT}} = (3/4)E_{\mathrm{Q}} + E_{\mathrm{RT}} \tag{2.12}$$

This yields the value of the quarto interaction to be $E_{\mathrm{Q}} = 53$ meV. This is a significant amount of energy (compared with collinear trio $E_{\mathrm{LT}} = -15$ meV/atom and third-nearest-neighbor interaction $E_3 = -8$ meV/atom [60]) and hence is likely to have consequences in calculations of other properties.

In summary, when calculating trio interactions from first principles, however, care must be taken; they can be exquisitely sensitive to the geometry and structure of the supercell used to calculate them. Such sensitivity to local relaxation can complicate a simple lattice-gas description. To account for the relaxation of trios near step edges, for example, we introduce a non-pairwise quarto interaction E_{Q} among four neighboring adatoms. We find that such an interaction is necessary to bridge the theoretical step stiffness with experimental measurements on Cu(100). In that case, we find what amounts to a relatively large, repulsive quarto interaction $E_{\mathrm{Q}} = 53$ meV that has significant physical consequences in our problem and presumably more generally. (In the same paper [23] we find that the inclusion of trio interactions can account for the difference in A- and B-step formation energies on Pt(111).)

2.6 Connector Models

The expansion in m-adatom interactions can become cumbersome and unwieldy if the multiparticle energies do not become smaller after, say, quarto interactions. Seeking an alternative approach to circumvent this issue, Tiwary and Fichthorn (TF) [24] proposed the connector model (named after the construction-kit toy [61]), which focuses on the vertices rather than the links of a cluster of adatoms. For example, consider four adatoms forming an NN square. In the lattice-gas model, the total energy would be $4E_1 + 2E_2 + 4E_{\mathrm{RT}} + E_{\mathrm{Q}}$. In the connector model with just NN spokes (spokes of half the NN bond length and oriented in the appropriate

directions), this total energy is just four times the energy of a connector hub with two perpendicular spokes. For this lattice, there are just five types of connectors, having one, two, three, or four spokes, the two-spoke case having a straight and a right-angle conformation. More often, one must use connectors with NN and NNN spokes. For the square of four adatoms, there would still be just one connector, with an NNN spoke between the two perpendicular NN spokes (called D6 in [24]). For the straight-conformation two NN spoke case, one can add one NNN spoke in one distinct conformation, two NNN spokes in three conformations, three or four (or 0) each in one distinct conformation, summing to seven possibilities. In other cases there will be even more. With three NN spokes, the number of possibilities is even larger. One of the main features of this model is that the type of connector contains information about the local geometry of the adatom; hence relaxation effects are expected to be built into the model. However, to keep the number of fitted energies reasonable, TF use just eight connectors: D1 for an isolated atom; D2 and D3 for just one NN or NNN spoke, respectively; D4 and D5 for two NN or NNN spokes in the same direction (linear), respectively; D7 with three NN spokes and two NNN spokes between them; and D8 for all eight spokes. Thus, as for lattice-gas interactions, success requires that the investigator have enough insight into the system to select the connectors that capture the essence of the problem.

Other applications to date have been to (110) fcc surfaces, where the rectangular symmetry leads to a large variety of lattice-gas energies as well as a much greater number of connectors, since the perpendicular "NN" spokes have different lengths (though NNN are still the same). However, the multiplicity can be reduced by sometimes neglecting some differences. We used 10 connectors (shown in Fig. 2.6) to characterize adatom interactions on Cu(110) [44], while TF used the first nine for Al(110).

For Cu(110) the CV scores are as good as those obtained using a dozen lateral interactions in the lattice-gas approach [44]. This agreement is plausible since it is often possible to establish linear relations between the connector and lattice-gas energies, e.g.,

$$C_6 = E_0 + \frac{E_1}{2} + \frac{E_2}{2} + \frac{E_3}{2} + \frac{E_{\mathrm{T1}}}{3} + \frac{E_{\mathrm{Q1}}}{4} \tag{2.13}$$

The sensitivity of multisite interactions to relaxation is not apparent from the connector energy values because each connector has contributions from adsorption energy (E_0 or C_1) and other pairwise interactions that dominate over contributions from multisite interactions; also, the contribution from a particular multisite interaction is divided by the number of participating adatoms (cf. (2.13), further decreasing the sensitivity of connector energies to adatom relaxations. However, the connector model incorporates such relaxation effects, as can be seen from the uniformly low CV scores for all relaxation schemes [44]. Evidently the connector model works well in the cases of Cu(110), Al(110), and Al(100). It remains to be seen whether the connector model provides an adequate solution, without the need for any ad hoc patches, to the overlayer problem. Relaxation effects become prominent during

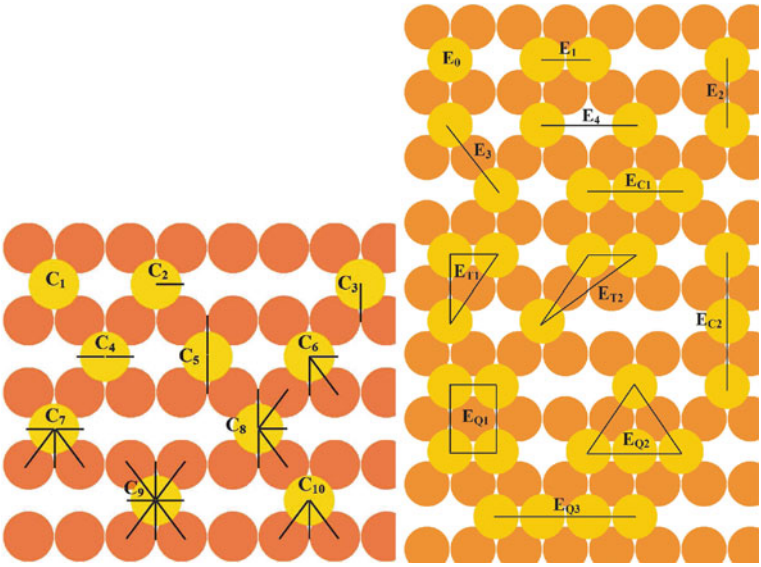

Fig. 2.6 *Left*: Connectors [24] used to characterize Cu adatom interactions on Cu(110). *Lighter* (*mustard*) *circles* represent adatoms and *darker* (*orange*) *circles* represent atoms in the substrate layer. *Right*: Lattice-gas interactions used to characterize Cu adatom interactions on Cu(110). Multisite interactions E_{T2}, E_{Q2}, and E_{Q3} were found to be insignificant. From [44], which also provides tables of the values of these energies

energy calculations of adatoms near step edges; in such calculations the simple lattice-gas model encounters problems [23, 60]. At the same time, accommodating the relaxation effects encountered in such calculations within the connector model might require the usage of connectors that account for the orientations of neighbor bonds, resulting in an undesirably large number of connectors in the model. A DFT-based study that compares these two models on a surface like Pt(111), where such lateral relaxation is known to complicate surface energy calculations [23], might elucidate this issue.

2.7 Interactions Between Organic Molecules

Understanding the interactions between and consequent self-assembly of organic molecules on metal surfaces has drawn much recent interest. The adsorption bond is roughly an order of magnitude weaker than for the chemisorbed systems considered above. Direct interactions between the organic molecules are often by way of hydrogen bonds, and there is always a van der Waals attraction which, for these systems, may play the dominant role. While the coupling to the substrate is relatively weak, the indirect electronic interactions between adsorbates may be important at long range when the substrate has metallic surface states.

Very recently we have considered the adsorption of benzene on Cu(111) [62], using a DFT approach with a van der Waals functional included. We can account for the two ordered submonolayer phases observed by Dougherty et al. [63]. The denser phase is due to direct van der Waals bonding between the benzenes while the less dense phase appears to be due to the surface-state-mediated interaction. We have not yet investigated the role of trio interactions in this system. Our ultimate goal is to explain the dramatic giant regular honeycomb structure formed by anthraquinone (AQ) molecules on this substrate [64]. In models that treat the admolecules as single "atoms," a repulsive trio interaction is crucial to prevent the formation of dense, unphysical overlayer regions (Kim and Einstein, Unpublished). Our belief is that the large, regular structure is related to interactions between AQ mediated by the metallic surface state. A variety of theoretical and experimental techniques are in progress to confirm this picture (Bartels and Einstein, Unpublished).

Acknowledgments Our research at Maryland was supported primarily by the NSF-MRSEC, Grant DMR 05-20471. Some aspects benefited from NSF Grant Chem 07-50334 and DOE-CMSN support. The Center for Nanophysics and Advanced Materials (CNAM) provided ancillary support. We thank T.J. Stasevich, P. Hyldgaard, K. Berland, E.D. Williams, L. Bartels, and K. Kim for fruitful collaboration and stimulating discussions on the topics discussed.

References

1. L.D. Roelofs, in *Chemistry and Physics of Solid Surfaces, IV*, ed. by R. Vanselow, R. Howe (Springer, Berlin, 1982), p. 219
2. B.N.J. Persson, Surface Sci. Rept. **15**, 1 (1992)
3. T.L. Einstein, in *Physical Structure of Solid Surfaces*, ed. by W.N. Unertl (Elsevier, Amsterdam, 1996), p. 577
4. A. Patrykiejew, S. Sokołowski, K. Binder, Surf. Sci. Rept. **37**, 207 (2000)
5. D.P. Landau, S.P. Lewis, H.-B. Schüttler (ed.), *Computer Simulation Studies in Condensed-Matter Physics*, vols. 1–19 (Springer Proceedings in Physics, Berlin, 1988–2008)
6. P.A. Rikvold, G. Brown, M.A. Novotny, A. Wieckowski, Colloids Surf. A: Physicochem. Eng. Asp. **134**, 3 (1998)
7. L.D. Roelofs, in *Physical Structure of Solid Surfaces*, ed. by W.N. Unertl (Elsevier, Amsterdam, 1996), p. 713
8. L. Österlund, M.Ø. Pedersen, I. Stensgaard, E. Lægsgaard, F. Besenbacher, Phys. Rev. Lett. **83**, 4812 (1999)
9. A. Bogicevic, S. Ovesson, P. Hyldgaard, B.I. Lundqvist, H. Brune, D.R. Jennison, Phys. Rev. Lett. **85**, 1910 (2000)
10. J.-S. McEwen, S.H. Payne, C. Stampfl, Chem. Phys. Lett. **361**, 317 (2002)
11. W. Luo, K.A. Fichthorn, Phys. Rev. B **72**, 115433 (2005)
12. C. Stampfl, Catal. Today **105**, 17 (2005); M. Borg et al., Chem. Phys. Chem. **6**, 1923 (2005)
13. G. Kresse, J. Hafner, Phys. Rev. B **47**, R558 (1993); **49**, 14251 (1994)
14. G. Kresse, J. Furthmüller, Comput. Mater. Sci. **6**, 15 (1996); Phys. Rev. B **54**, 11169 (1996)
15. T.L. Einstein, Langmuir **7**, 2520 (1991)
16. G. Ehrlich, F. Watanabe, Langmuir **7**, 2555 (1991)
17. S.-J. Koh, G. Ehrlich, Phys. Rev. B **60**, 5981 (1999)
18. Y. Zhang, V. Blum, K. Reuter, Phys. Rev. B **75**, 235406 (2007)
19. Y. Tiwary, K.A. Fichthorn, Phys. Rev. B **75**, 235451 (2007)

20. C. Lazo, F.J. Keil, Phys. Rev. B **79**, 245418 (2009)
21. W.A. Harrison, Phys. Rev. B **7**, 2408 (1973)
22. L.D. Roelofs, S.M. Foiles, M.S. Daw, M.I. Baskes, Surf. Sci. **234**, 63 (1990)
23. R. Sathiyanarayanan, T.J. Stasevich, T.L. Einstein, Surface Sci. **602**, 1243 (2008)
24. Y. Tiwary, K.A. Fichthorn, Phys. Rev. B. **78**, 205418 (2008)
25. T.L. Einstein, in *Chemistry and Physics of Solid Surfaces II*, ed. by R. Vanselow (CRC Press, Boca Raton, FL, 1979), p. 181
26. P.J. Feibelman, Ann. Rev. Phys. Chem. **40**, 261 (1989)
27. J.K. Nørskov, in *The Chemistry and Physics of Solid Surfaces*, vol. 6, ed. by D.A. King, D.P. Woodruff (Elsevier, Amsterdam, 1993), p. 1
28. S.P. Timoshenko, J.N. Goodier, *Theory of Elasticity*, 3rd edn. (McGraw-Hill, New York, NY, 1970)
29. T.L. Einstein, J.R. Schrieffer, Phys. Rev. B **7**, 3629 (1973)
30. C. Kittel, in *Solid State Physics*, ed. by F. Seitz, D. Turnbull, H. Ehrenreich (Academic, New York, NY, 1968), vol. 22, p. 1, and references therein.
31. P. Hyldgaard, M. Persson, J. Phys. Condens. Matter **12**, L13 (2000); P. Hyldgaard, T.L. Einstein, Europhys. Lett. **59**, 265 (2002)
32. P. Hyldgaard, T.L. Einstein, Surf. Sci. **532–535**, 600 (2003); J. Cryst. Growth **275**, e1637 (2005)
33. M.F. Crommie, C.P. Lutz, D.M. Eigler, Science **262**, 218 (1993)
34. B.N.J. Persson, Surf. Sci. **258**, 451 (1991)
35. A. Milchev, J. Chem. Phys **78**, 1994 (1983); Electrochem. Acta **28**, 941 (1983); A. Milchev, M. Paunov, Surface Sci. **108**, 25 (1981)
36. N.C. Bartelt, T.L. Einstein, E.D. Williams, J. Vac. Sci. Technol. A **2**, 1006 (1984)
37. M.N. Barber, J. Phys. A **15**, 915 (1982)
38. T.T. Tsong, R. Casanova. Phys. Rev. Lett. **47**, 113 (1981); T.T. Tsong, Mat. Sci. Eng. A **353**, 1 (2003)
39. F. Watanabe, G. Ehrlich, J. Chem. Phys. **96**, 3191 (1992)
40. R.B. Griffiths, comment during discussion, Conference on Phase Transitions on Surfaces, Orono, ME, Aug. 1981.
41. R. Najafabadi, D.J. Srolovitz, Surf. Sci. **317**, 221 (1994) (Cf., for steps)
42. T.J. Stasevich, T.L. Einstein, S. Stolbov, Phys. Rev. B **73**, 115426 (2006)
43. T. Mueller, G. Ceder, Phys. Rev. B **80**, 024103 (2009), use cross validation in the context of a Bayesian approach to cluster expansions
44. R. Sathiyanarayanan, T.L. Einstein, Surface Sci. **603**, 2387 (2009)
45. J. Shao, J. Am. Stat. Assoc. **88**, 486 (1993)
46. H.S. Johnston, C.A. Parr, J. Am. Chem. Soc. **85**, 2544 (1963); W.H. Weinberg, R.P. Merrill, Surface Sci. **33**, 493 (1972); C.Q. Sun, B.K. Tay, X.T. Zeng, S. Li, T.P. Chen, J. Zhou, H.L. Bai, E.Y. Jiang, J. Phys.: Condens. Matter **14**, 7781 (2002)
47. H.-C. Jeong, E. D. Williams, Surf. Sci. Rept. **34**, 171 (1999)
48. T.J. Stasevich, T.L. Einstein, R.K.P. Zia, M. Giesen, H. Ibach, F. Szalma, Phys. Rev. B **70**, 245404 (2004)
49. T.J. Stasevich, H. Gebremariam, T.L. Einstein, M. Giesen, C. Steimer, H. Ibach, Phys. Rev. B **71**, 245414 (2005)
50. H. Ibach, W. Schmickler, Phys. Rev. Lett. **91**, 016106 (2003) (This simple equivalency does not hold for stepped surfaces in an electrochemical system, where the electrode potential ϕ is fixed rather than the surface charge density conjugate to ϕ.)
51. C. Rottman, M. Wortis, Phys. Rev. B **24**, 6274 (1981)
52. J.E. Avron, H. van Beijeren, L.S. Schulman, R.K.P. Zia, J. Phys. A **15**, L81 (1982); R.K.P. Zia, J.E. Avron, Phys. Rev. B **25**, 2042 (1982)
53. J.W. Cahn, R. Kikuchi, J. Phys. Chem. Solids 20, 94 (1961)
54. S. Dieluweit, H. Ibach, M. Giesen, T. L. Einstein, Phys. Rev. B **67**, 121410(R) (2003)
55. N. Akutsu, Y. Akutsu, Surf. Sci. **376**, 92 (1997)

56. R. Van Moere, H.J.W. Zandvliet, B. Poelsema, Phys. Rev. B **67**, 193407 (2003)
57. H.J.W. Zandvliet, R. Van Moere, B. Poelsema, Phys. Rev. B **68**, 073404 (2003)
58. R.C. Nelson, T.L. Einstein, S.V. Khare, P.J. Rous, Surf. Sci. **295**, 462 (1993)
59. M. Giesen-Seibert, H. Ibach, Surf. Sci. **316**, 205 (1994); M. Giesen-Seibert, F. Schmitz, R. Jentjens, H. Ibach, Surf. Sci. **329**, 47 (1995)
60. T.J. Stasevich, T.L. Einstein, R.K.P. Zia, M. Giesen, H. Ibach, F. Szalma, Phys. Rev. B **70**, 245404 (2004)
61. Universal Connector Toy, United States Patent 6179681, now marketed by Superstructs. http://www.wikipatents.com/US-Patent-6179681/universal-connector-toy or http://www.freepatentsonline.com/6179681.html, 7 Sept, 2009
62. K. Berland, T.L. Einstein, P. Hyldgaard, Phys. Rev. B **80**, 155431 (2009)
63. D.B. Dougherty, P. Maksymovych, J. Lee, J.T. Yates, Jr., Phys. Rev. Lett. **97**, 236806 (2006)
64. G. Pawin, K.L. Wong, K.Y. Kwon, L. Bartels, Science **313**, 961 (2006)

Chapter 3
Wetting Layer Super-Diffusive Motion and QSE Growth in Pb/Si

M.C. Tringides, M. Hupalo, K.L. Man, M.M.T. Loy, and M.S. Altman

Abstract The unusual growth mode of uniform height islands discovered in Pb/Si was related to the electronic energy modulation with island height due to quantum size effects (QSEs). In addition to these energetic reasons provided by QSE, there is also the question of kinetics, i.e., how atoms move at relatively low temperatures (as low as 150 K) to build the islands in the short time of minutes. Controlled experiments with different techniques have shown the intriguing role of the dense wetting layer in transporting mass. STM experiments monitoring how unstable islands transform into stable islands have shown that the wetting layer between the islands moves selectively to the unstable islands, climbs over their sides, forms quickly rings of constant width $\sim$ 20 nm, and finally it completes the island top, but at a slower rate than the ring completion. This growth is independent of the starting interface, whether it is the amorphous wetting layer on the Si(111) (7×7) or the well-ordered Si(111)–Pb $\alpha(\sqrt{3}\times\sqrt{3})$ surface (except Pb diffusion on the latter interface is faster by a factor of $\sim$ 5). Real-time low-energy electron microscopy (LEEM) observations of mass transport phenomena have confirmed the fast mobility of the wetting layer in Pb/Si and in addition have revealed some unusual features that are unexpected from classical diffusion behavior. The experiment monitors the refilling of a circular vacant area generated by a laser pulse. The concentration profile does not disperse as in normal diffusion, the refilling speed $\Delta x/\Delta t$ is constant (instead of $\Delta x/\sqrt{\Delta t} = \text{constant}$), and the equilibration time diverges below a critical coverage, θ_c, as $1/\tau \sim (\theta_c - \theta)^{-\kappa}$. The absolute value of the refilling speed 0.05 nm/s at 190 K is orders of magnitude higher than what is expected from Pb diffusion on Pb crystals at higher temperatures. These results are compared with predictions of three candidate models: (i) a conventional diffusion model with a step-like coverage-dependent diffusion coefficient $D_c(\theta)$, (ii) a model with mass transport due to adatoms on top of the wetting layer with coverage-dependent adatom vacancy formation energy, and (iii) the carpet unrolling mechanism proposed for other systems. None of these

M.C. Tringides (✉)
Ames Laboratory-USDOE and Department of Physics and Astronomy, Iowa State University, Ames, IA 50011, USA
e-mail: tringides@ameslab.gov

M. Michailov (ed.), *Nanophenomena at Surfaces,* Springer Series in Surface Sciences 47,
DOI 10.1007/978-3-642-16510-8_3,

models can account for the unusual observations, which suggests that the wetting layer most likely enters a novel state of very high mobility for $\theta > \theta_c$, similar to a phase transition that needs to be better understood theoretically.

3.1 Diffusion Measurements with Externally Imposed Concentration Gradients

A standard method to measure surface diffusion is based on monitoring the time evolution of a non-equilibrium coverage profile when a coverage gradient is imposed initially [1]. The gradient provides the driving force for atoms to diffuse from high to low coverage regions, until a uniform equilibrium coverage distribution is attained everywhere. The evolution of the coverage $\theta(r, t)$ at location r and time t obeys the diffusion equation

$$\frac{\partial \theta}{\partial t} = \nabla \cdot (D \nabla \theta) \tag{3.1}$$

where $D_c(\theta)$ is the collective diffusion coefficient. For example, in 1-d step profile evolution experiments along a direction r the coverage has one value θ_1 in region $r < 0$ and a different value θ_2 in region $r > 0$. With time, atoms will move to equalize the surface coverage as shown schematically in Fig. 3.1. If there are no adatom interactions (except site exclusion) D_c is coverage independent, the evolving profile is described by

$$\theta(r, t) = \frac{(\theta_1 - \theta_2)}{2} \left(1 - \mathrm{erf}\left(r^2/\sqrt{2D_c t}\right)\right) \tag{3.2}$$

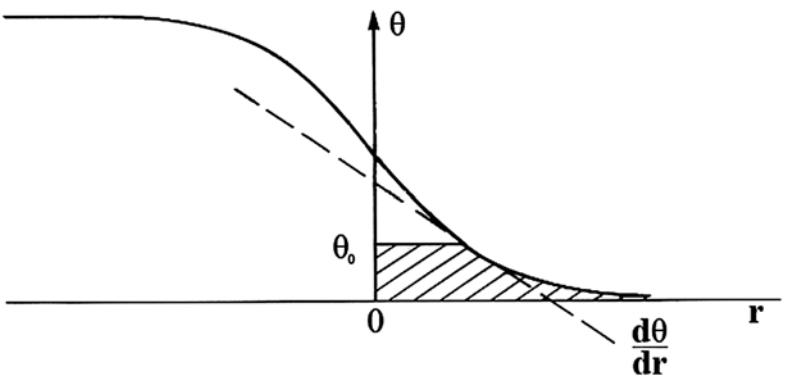

Fig. 3.1 Schematic showing the spreading of 1-d profiles as in classical diffusion. The scaled variable is $r/\sqrt{t}$, the integrated shaded area and the slope are used to determine the $D_c(\theta)$ coverage dependence in the Boltzmann–Matano analysis

and such profile shapes obtained at different t can be used to extract the constant D_c.

Analogous profile evolution experiments can be carried out with 2-d geometry [2, 3]: a circular depleted or vacant area is generated initially with one value of the coverage θ_2 within $r < r_0$ while in the outside region the coverage has a different value θ_1. Similar evolution will result in a uniform coverage over the whole area as in the 1-d case. The solution of (3.1) in this case for $N(t)$ (the total integrated amount that has diffused back to the area for constant D_c) at time t is given by

$$N(t) = N_\infty \left(1 - 2\int_0^\infty \frac{J_1(ur_0)}{u} e^{-D_c t u^2} du\right) \tag{3.3}$$

where $N_\infty = \pi r_0^2(\theta_2 - \theta_1)$ is the asymptotic value at long times and $J_1(ur_0)$ is the Bessel function. In addition to this case for sufficiently large r_0 (when compared to the spatial resolution of measuring the advancing edge profile at the vacant area), the profile can be also fitted by solving the diffusion equation in polar coordinates to deduce $D_c(\theta)$.

Because the diffusion equation is first order in time and second order in space, the profile evolution has certain general features that should be observable under all conditions: (a) the initial step profiles should become flatter with t since a profile component with spatial wavevector k relaxes faster (at a rate proportional to k^2), (b) as already seen in. (3.2) the solution can be written in terms of the scale variable $r/\sqrt{t}$, and (c) equivalently the width of the transition region where the profile changes from θ_1 to θ_2 grows in time as $\sqrt{t}$, which implies that the speed of the moving edge is not constant but decreases with time.

So far the discussion was in terms of constant D_c. If adatom interactions are present (besides site exclusion), this implies that the diffusion equation becomes coverage-dependent and the non-linear equation (3.1) applies. However, even under these conditions using the shape of the evolving profile, the coverage dependence $D_c(\theta)$ can be deduced by means of the Boltzmann–Matano (BM) method. Before applying the BM method to the experimental results, it is essential to show that the profiles scale (i.e., they can be written in the form $\theta(r, t) = \theta(r/\sqrt{t})$). If the scaling condition is met, then $D_c(\theta)$ is obtained for a range of coverages θ_0 ($\theta_2 < \theta_0 < \theta_1$) by using the measured scale-invariant shape

$$D_c(\theta_0) = \frac{1}{2t\left(\frac{d\theta}{dr}\right)_{\theta_0}} \int_{\theta_2}^{\theta_0} r\, d\theta \tag{3.4}$$

where the profile is integrated in the numerator and numerically differentiated to evaluate $d\theta/dr$ at θ_0 that is present in the denominator of (3.4). When interactions are present (depending both on their sign (whether repulsive or attractive) and their range, i.e., how many sites away they extend to) they result in very different

functional forms $D_c(\theta)$ [4]. This in turn implies different deviations of the profile shape from the ideal error function-based profiles of (3.2). Profiles which are steeper (than the error function) in the vacant region ($r < r_0$) lead to larger derivative in the denominator of (3.4) and therefore reduced $D_c(\theta)$ (such dependence indicates predominantly attractive interactions); while profiles which are flatter in the region $r < r_0$ have smaller derivative in the denominator of (3.4) and larger $D_c(\theta)$ (such dependence indicates predominantly repulsive interactions).

The features listed previously as characteristic of classical diffusion (i.e., the spreading of the initial steep profile, the dependence on the scaled variable $r/\sqrt{t}$, and the decreasing edge velocity) are also true for the case of coverage-dependent $D_c(\theta)$. They follow simply from the nature of the diffusion process that a more pronounced spatial variation (i.e., the second derivative $\partial^2\theta/\partial r^2$) causes weaker temporal variation (i.e., first derivative $\partial\theta/\partial t$). Concerning possible functional forms of $D_c(\theta)$ for classical diffusion, in general the coverage-dependent diffusion is a smooth function of θ. Only close to a phase transition can $D_c(\theta)$ have more structure (usually in the form of either maxima or minima with T or θ) as a result of changes in spatial and temporal correlations of the diffusing atoms in the system. Close to a second-order phase transition, critical fluctuations generated thermodynamically are so large ($\partial\mu/\partial\theta \rightarrow \infty$ as $T \rightarrow T_c$) that no diffusion currents can eliminate them. This effectively means that $D_c(T)$ goes to 0 as $T \rightarrow T_c$, known as critical slowing down [5]. Close to an order–disorder transition, the coverage dependence $D_c(\theta)$ (for fixed temperature $T < T_c$) can show maxima as the ideal coverage of the ordered phase $\theta \rightarrow \theta_c$ is approached, since at θ_c the perfect defect-free phase is least compressible (it costs large energy to generate adatoms out of this ideal structures, $\partial\theta/\partial\mu \rightarrow 0$ as $\theta \rightarrow \theta_c$). The amplitude of the diffusion maxima depends on the nature of the order parameter describing the phase transition; the maxima have larger amplitude when the order parameter is the coverage θ (i.e., for first-order phase transition in systems with attractive interactions). In all cases, these thermodynamic effects can produce narrow maxima or minima in $D_c(\theta)$ vs. θ, but not a sharp step-like jump at a critical coverage θ_c, within a very narrow transition region $\Delta\theta << 0.1$ ML such that D_c jumps from one value for $\theta < \theta_c$ to a different value that differs by orders of magnitude for $\theta > \theta_c$.

An unusual diffusion profile resembling somehow such θ dependence has been observed in multilayer diffusion (that involves at least two layers adsorbed on the surface with very different diffusion coefficients in each layer) [6]. If diffusion on top of a layer is fast while diffusion within the layer is slow, then the slow layer advances predominantly through the fast transfer of material from the top to the bottom layer. Over the timescale of the slow diffusion it seems that the lower layer moves at a constant speed, not the expected $\sqrt{t}$ scaling behavior. This is the so-called carpet unrolling mechanism and will be discussed in more detail below in connection with Li diffusion on metal surfaces. In essence, it is the simplest case of "reaction"-limited kinetics where diffusion is the fastest process but the timescale of the observations is set by a slow "reaction," i.e., mass transfer from a higher to a lower level. Even under these conditions the profile disperses and there is no critical dependence of the refilling time τ on θ.

3.2 Novel Low-Temperature Kinetic Pathways for the QSE-Driven Uniform Height Islands

After this short introduction to expectations from classical diffusion experiments, some basic results obtained during metal growth at low temperatures controlled by quantum size effects (QSEs) and in particular for the Pb/Si system will be reviewed. It has been a surprise that electron confinement can play a key role in the self-organization of metallic nanostructures [7]. Confinement becomes important when the structure dimensions are comparable to the Fermi wavelength λ_F, i.e., for metallic structures when the thickness is a few layers. Traditionally, spectroscopic techniques were used to map out the position of the energy levels of confined electrons as they shift with the change of the film thickness, high-quality spectra indicating the growth of good films [8, 9]. However film or island thickness was expected to change monotonically as the deposited amount was varied. In addition for typical confining potentials (at most a few tens of electron volts defined by the position of the valence band with respect to the vacuum) the difference in the energy level spacing between confining wells of adjacent thickness was considered too small ($\sim$ tens of millielectron volts) to have an effect in the grown film morphology.

However, in several metallic systems Ag/GaAs(100) [10], Ag/Si(111) [11], Pb/Si(111) [12], In/Si(111) [13], Ag/NiAl(100) [14], Ag/quasicrystals [15], Pb/Cu(111) [16], and Ag/Fe(100) [17, 18] uniform height selection was found. Different experimental techniques have been applied (STM, STS [19, 20], high-resolution electron diffraction [12], surface X-ray scattering [21], ARPES [22], in situ conductivity [23], etc.) and theoretical calculations using different approximation [24, 25] have been used to confirm that QSE is the reason for the observed height selection. Possibly Pb/Si(111) is the most widely studied system among these that exhibits QSE-induced morphology because of the ease in height selection (immediately after deposition) and the unusual sharpness of the height distribution. As reviewed in Chapter 4 by Jia et al. extensive work has been carried out both experimentally and theoretically to understand the role of QSE in film growth. Different theoretical techniques have been applied on different models (free electron model and first principles calculations) to calculate the observed stable heights in Pb/Si(111). In addition the chapter discusses the control of other film properties with height. It was found that several properties (lattice relaxation, work function, thermal expansion, superconductivity, and chemical reactivity) oscillate with height, as a result of how the electronic structure depends on changes; and in particular the variation of the density of states of the confined electrons with height. However, besides understanding how island stability relates to electron confinement, it is also essential to know how mass transport operates in the system that directs the randomly deposited atoms to ideal positions to build the defect-free islands.

QSE-driven height selection results from the dependence of the electronic energy on island height. The island height can increase only by multiples of the step height d while the electron wavefunction periodicity is defined by the Fermi wavelength λ_F. At the preferred heights, the leakage of the wavefunction outside the confining

well is reduced which generates energy minima in the total energy of the island vs. thickness. However, this condition is necessary but not sufficient for uniform height island formation. In most systems, the growth of QSE-induced island morphologies is carried out at relatively low temperatures (for Pb/Si(111) as low as 150 K [12]). At even lower temperatures high-quality homogeneous films have been observed macroscopically with strong diffraction oscillations [26, 27] and photoemission [28]. These results raise the question how mass transport in these systems is so efficient in building these islands relatively quickly (within a few minutes) at low temperatures. At least for Pb/Si(111) there must be other factors for the extraordinary height selectivity besides QSE-driven energetics. To what extent these kinetic effects are applicable to other systems already discovered with selectable heights or systems to be discovered is still an open question. For Pb/Si(111), several experiments to be discussed in detail below have shown a novel diffusion behavior at low temperatures which is unexpected based on the classical paradigm of diffusion described in Sect. 3.1. Although its origin is still unclear it results in unusually fast mass transport.

Initially, experiments that probe diffusion indirectly have revealed intriguing processes in Pb/Si(111) hinting that non-classical effects are present. Coarsening experiments in a mixture of stable and unstable islands (generated at high flux rates) were carried out with X-ray scattering and STM [21]. These experiments have shown that the coarsening time toward a lower density of uniform height stable islands is less at higher flux rates. Classically, no dependence on flux rate is expected since the final island size distribution and density is determined by the Gibbs–Thompson effect which leads to identical final state commonly referred to as Ostwald ripening [29]. The reason for the observed non-classical behavior in Pb/Si(111) is related to the extremely fast decay of smaller unstable height islands. (For example, three-layer Pb islands having the most unstable height of radius 7 nm decay within 2 min at 180 K which is orders of magnitude faster when compared to the decay of Pb islands at the top of Pb crystallites [30].)

QSEs influence not only island stability but kinetic barriers which become a strong function of island height (i.e., atom detachment that determines the timescale of island decay is very different for stable vs. unstable islands). It is also clear that the "sea" between the islands (which for classical coarsening [29] consists of monomers generated by atom evaporation from both large and small islands but at different rates) behaves very differently in Pb/Si(111) and is the key player for the way material is transferred to the stable islands [31, 32]. No monomers are present but the dense wetting layer resembles the movement of an actual sea: it incorporates quickly the mass released from the decay of unstable islands and the material "resurfaces" far away only at unstable islands transforming them into stable islands. The wetting layer moves in a novel collective way.

Modeling of these processes with rate equations that describe the rate of change of the number of islands n_h of height h in terms of their chemical potential μ_h has reproduced the evolution toward the final uniform seven-layer island height distribution [33]. Two main assumptions were needed: (i) the energy of an island of radius R and height h depends on both its radius and its height (where ε_b is the

bulk energy per atom, γ_t is surface energy of the top face, and γ_s is the surface energy of the side face)

$$E(R,h) = \pi R^2 h\varepsilon_b + \pi R^2\gamma_t(h) + 2\pi Rh\gamma_s \tag{3.5}$$

The first term is the bulk energy and the other two terms are the surface energies which include the standard Gibbs–Thompson term (that is determined by the island curvature $1/R$) and a term that depends on height because of QSE. The chemical potential of island of radius R and height h is given by

$$\mu(R,h) = \Omega(\varepsilon_b + \frac{\gamma_s}{R} + \frac{\gamma_t}{h}) \tag{3.6}$$

with Ω the unit volume per atom.

(ii) The dense wetting layer has chemical potential μ_{WL} higher than the chemical potential of stable islands $\mu_{WL} > \mu_{hs}$ (so material easily flows toward the stable islands) and below the chemical potential of unstable islands $\mu_{WL} < \mu_{hust}$ (so material easily flows from the unstable islands to the wetting layer). Besides island decay, other barriers (i.e., terrace diffusion [34], step edge barrier [35], nucleation rates [36], oxidation [37], etc.) were found to depend on height as a result of QSE.

3.3 Unusual Wetting Layer Mobility in Pb/Si(111)

3.3.1 STM Studies

The previous experiments have shown indirectly that the wetting layer was key for the transformation to stable height islands. More quantitative information was obtained from the time evolution of the rings after they form on the island top. Rings are observed both for islands grown on the amorphous wetting layer on top of the (7×7) surface as seen in Fig. 3.2 and for islands grown on top of the ordered $\alpha(\sqrt{3}\times\sqrt{3})$ and β-$(\sqrt{3}\times\sqrt{3})$ wetting layers as seen in Fig. 3.3a–c. Static images of the rings have been published before [32, 34, 38], but the main goal of this section is to describe the speed at which the rings move and how the top layer is completed. Such experiments carried out with STM rely on snapshots of sufficiently large areas with both stable and unstable islands, so changes on island heights and sizes can be seen directly, but not in real time. Direct observations of the motion of the wetting layer was seen only recently in diffusion experiments [3] with LEEM to be described in the next section. The unusually high wetting layer speeds at low temperatures seen in the STM and LEEM experiments are in good agreement with each other.

Rings form on both unstable and stable islands commonly above 200 K transforming them finally into superstable heights. Single layer rings are seen on unstable (even) height islands transforming into stable (odd) height islands. The height is measured from the wetting layer. Bilayer rings are also seen on stable (odd) height islands transforming them into (also odd height) islands of superstable height. For example, bilayer rings on top of five-layer islands transform, them into superstable

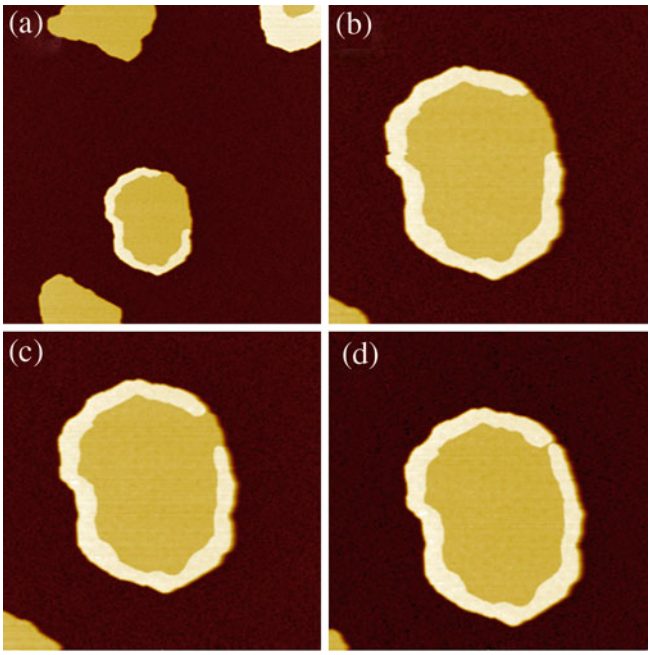

Fig. 3.2 Four images showing the evolution of a ring on top of a four-layer unstable island grown on the Si(7×7) at times 0, 9, 14, 25 min. *Top left image* is $500 \times 500\,\text{nm}^2$ and the other three images are $250 \times 250\,\text{nm}^2$. The temperature is $T = 180\,\text{K}$

seven-layer islands. This unusual growth morphology was also modeled [39] in detail to derive the potential energy surface that gives rise to single or bilayer rings. It was necessary to invoke QSE-driven height-dependent or site-dependent kinetic barriers (whether the center or the edge of the island) kinetic barriers. A major

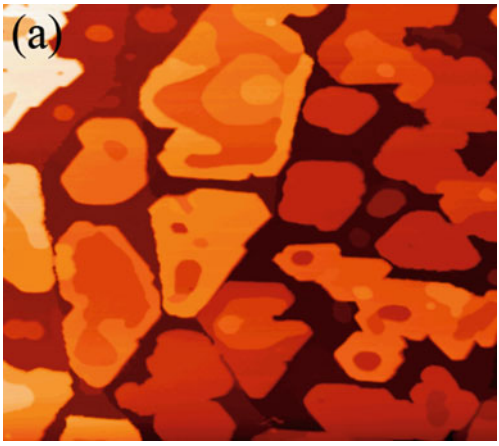

Fig. 3.3 (continued)

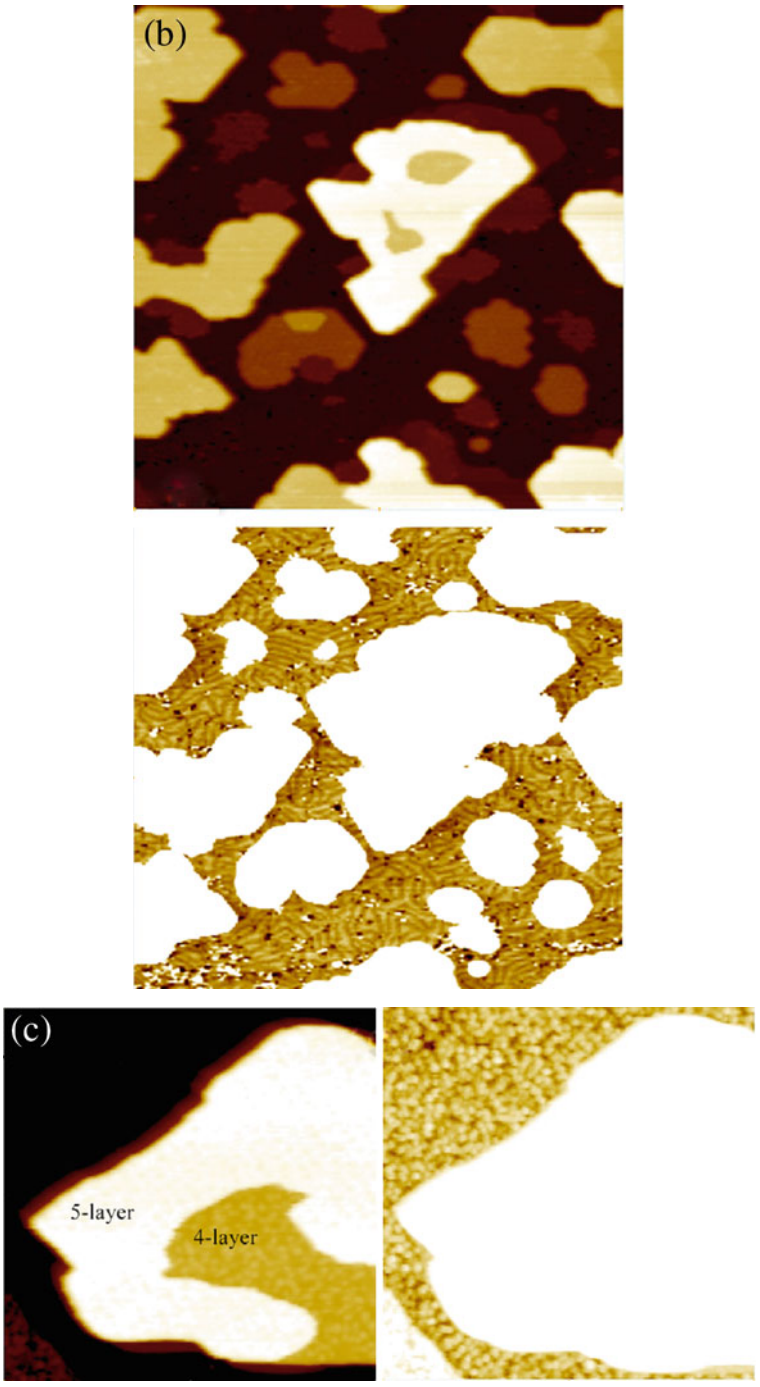

Fig. 3.3 (**a**) $500 \times 445\,\mathrm{nm}^2$ showing the growth of meandering four-layer islands on top of the Pb-$\alpha\sqrt{3} \times \sqrt{3}$ with rings. (**b**) $160 \times 180\,\mathrm{nm}^2$ area showing wetting layer on top of a two-layer island and the SIC phase intact between. (**c**) $67 \times 67\,\mathrm{nm}^2$ showing that rings are also grown on the Pb-$\beta(\sqrt{3} \times \sqrt{3})$ and the "granular" wetting layer

ingredient was the large diffusion anisotropy (i.e., fast azimuthal diffusion around the island perimeter as atoms arrive from the wetting layer vs. slower radial diffusion toward the island center). Some other intriguing non-classical characteristics of the rings are as follows: they form only on islands with radius larger than some minimum size 50 nm, their width is constant ∼20 nm (independent of the initial island radius), and the azimuthal speed is at least one order of magnitude faster than the radial speed toward the center. None of these characteristics are well understood. At higher temperatures ($T = 240$ K), multilayer height rings (four or five layers high) are seen [39] that indicate even higher mobility of the wetting layer.

A typical example of how rings form and how this is used to estimate the speed of the wetting layer is shown in Fig. 3.2a–d for the case of growth on the amorphous wetting layer on (7×7). First, several large (∼80 nm) four- or five-layer islands form at 240 K (because the stability difference between odd and even height islands is less for larger lateral sizes). The four-layer islands become five-layer (and eventually seven-layer) islands but over longer times than for smaller islands grown at lower temperature (∼180 K [12]). After growing the islands at 240 K, the surface is cooled to 180 K to be able to follow the ring evolution with the STM since the evolution is slower at this lower temperature. A four-layer island is shown in Fig. 3.2. The scale is $500 \times 500\,\text{nm}^2$ in Fig. 3.2a and $250 \times 250\,\text{nm}^2$ in Fig. 3.2b–d, which are obtained after 9, 14, 25 min, respectively, from the completion of Fig. 3.2a. The ring completes the perimeter with constant speed 0.05 nm/s. (A movie that was made from 18 successive images collected over an hour demonstrates that the ring advances at constant speed.) For such motion to be initiated it is necessary for the density of this amorphous wetting layer to be higher than the metallic density of Pb(111). The crucial role of the density is seen in stepwise coverage experiments (i.e., small depositions $\Delta\theta \sim 0.1$ ML increase the wetting layer density, then mass is transferred to the stable islands, and the density falls below the critical coverage but the next $\Delta\theta$ deposition restarts the transfer process). This speed of the rings is a lower bound to the speed of the wetting layer. As measured in SPA-LEED experiments [38] and as required by the model [39], the incoming wetting layer runs quickly over the facet planes of the Pb islands, but to move to the top it needs to overcome a barrier at the island edge. This barrier was measured to be 0.32 eV [38] and a barrier of similar magnitude was deduced from the simulations [39]. The combination of the rate to overcome this barrier and the intrinsic speed of the wetting layer defines the observed speed of the rings.

Figure 3.3a shows large Pb islands that have nucleated on top of the dense Pb $\alpha(\sqrt{3}\times\sqrt{3})$ phase (noted as α). The temperature is 180 K and a total amount 2.9 ML was deposited in two steps, 1.6 and 1.3 ML. The image scale is $500 \times 445\,\text{nm}^2$. The islands are bigger (than on the (7×7)) and resemble "continents" since they extend across the whole surface in irregular meandering shapes. Rings are seen on four-layer islands transforming them into five-layer islands, which is the preferred height for this interface [40]. The larger lateral extent of these islands and the greater number of rings at the perimeter confirm higher mobility of Pb on α noted before (than on the (7×7)). Figure 3.3b shows a smaller $180 \times 180\,\text{nm}^2$ area with smaller islands to illustrate that after the ring grows (bottom left island), the region between the islands is in the SIC phase with slightly less than $\approx 4/3$ ML. Figure 3.3c shows

a $67 \times 67\,\text{nm}^2$ stepped area with initially the low coverage $\beta(\sqrt{3} \times \sqrt{3})$ phase ($\theta = 1/3$ ML). This phase first transforms into a non-well-annealed version of the $\alpha(\sqrt{3}\times\sqrt{3})$ phase (4/3 ML) after the deposition of $\sim$ 1 ML and the ring transforms a four-layer island to a five-layer island which is the preferred height on this interface.

The presence of rings on top of metal islands has been noted in earlier growth experiments that have studied the static film morphology, but no association was made to the mobility of the surrounding wetting layer; or no measurements were made of the speed with which the rings are completed. Rings were seen during growth of Ag on Si(111) and the observation of island shape oscillations [41], although the rings were not discussed. These experiments were carried out at a relatively high temperature of 500 K. Rings were also seen in the same system at similar temperature, but the coadsorption of In to act as a surfactant speeds up the growth of the Ag islands to larger sizes and makes the rings on their top more distinct [42]. Large Pb(111) islands were grown on Si(100) at room temperature and imaged with LEEM and STM [43]. These larger islands have multiple height rings (up to 10 ML) with the inside of the island resembling a "depression" and at the sidewall the rings forming an ascending sequence of stepped terraces. These islands with "depressions" form after rapid diffusion and after an initial wetting layer of density 1.5 ML is present (as a $c(4 \times 4)$ superstructure). Both the rapid diffusion and the higher density of the $c(4 \times 4)$ are reminiscent of the conditions for the Pb/Si(111) wetting layer to become more mobile and build the islands. Ring morphologies on Pb/Si(111) have been seen with STM on large Pb islands at room temperature after they are completed and stop evolving [44, 45]. Rings were found on much taller islands of varying height (because these "mesas" were grown over several substrate steps). The islands have heights tens of monolayers so QSE differences between areas on the "mesa" of different heights are reduced, since the spacing and number of confined electronic levels become closer together as height increases). The current work, which was carried out at lower temperatures and for smaller height Pb islands, while the rings are forming, clarifies the crucial role of the wetting layer in building the islands. In addition in [44, 45] the ring formation was attributed to the interaction of the electric field between the tip and the substrate that apparently can trigger mass transport to the island top. The ring formation and the relative fractions of flat vs. ring areas of the island were discussed either in terms of energetics, i.e., the system phase separates into the two areas driven by QSE energy differences for stable vs. unstable heights [44], or purely in terms of kinetics (the faster process of moving atoms to the rings is triggered by the tip and the slower completion of the island top is controlled by vacancy diffusion [45]). The numerous differences between the current experiments and the previous work (i.e., lower temperatures, lower height islands, no tip effects, selective flow of Pb only toward unstable height islands, the role of the critical coverage θ_c of the wetting layer, and the similarity between ring morphologies on both interfaces (7×7) vs. α-phase) point to the intrinsic role the dense wetting layer plays in transferring efficiently the mass to the stable islands and not to extreneous effects due to the electric field.

Finally we note that this unusual control of the Pb film growth and the possibility to select the film morphology has also been exploited to answer questions in other physics problems, i.e., what is the nature of superconductivity in reduced

dimensions when tested in these uniform Pb films? SQUID measurements were performed in almost completed Pb films (with a few "defects," i.e., islands or vacancy islands for deposited amounts slightly above or slightly below the integer MLs) after they are cooled below the superconducting transition for bulk Pb [46]. The induced superconducting currents were pinned by the "defects" showing that classical superconductivity is robust even for film thickness as low as 5 ML and is similar on the nanoscale as in the bulk.

3.3.2 LEEM Studies

Although these STM experiments indicate unusual mobility of the wetting layer they do not measure directly its diffusion. This can be accomplished in simpler but real-time experiments when only the wetting layer is present [3]. A concentration profile is generated by desorbing Pb with a laser pulse within a circular area from an initially uniform layer. Then, the classical profile geometry of a vacant circular area described in Sect. 3.1 is generated. Mass within the undisturbed layer outside this vacant area moves to refill it. The refilling is monitored with LEEM with the contrast caused by the difference between the scattering factors of the dense layer outside the vacated hole and the layer inside the hole, which in practice has lower coverage (by $\sim$ 1 ML) but not completely vacated. No Pb islands are present in these experiments so the mobility of the wetting layer can be measured directly. Such experiments were carried out for both initial phases, i.e., the amorphous wetting layer on the (7×7) and the ordered $\alpha(\sqrt{3} \times \sqrt{3})$ wetting layer.

Since the specular intensity is measured in the LEEM experiment but in diffusion measurements what moves is mass, the LEEM intensity should be calibrated against coverage. For example, the initial profile $c(r, t = 0)$ within the hole was determined by re-depositing Pb at 120 K after cooling quickly from the temperature, 262 K, that the hole was generated. At this low temperature, the wetting layer "freezes" and there is no diffusion into the hole from outside, such that any changes that are observed during Pb deposition can be related to the known amount of deposited Pb. The coverage in the hole was increased and the LEEM image intensity was measured during continuous deposition at constant rate. A linear increase of the LEEM intensity with t at a given location r indicates that the LEEM intensity is proportional to $\theta(r, t)$. The LEEM intensity was measured at different distances r within the hole from its center as a function of t (from real-time video frames). A maximum in LEEM intensity is attained at all areas; but areas closer to the edge reach this maximum earlier because the amount desorbed and therefore the refilled amount is less. The maximum in the LEEM intensity at room temperature corresponds to 4/3 ML, the coverage of the SIC phase (the α-phase with 4/3 ML), that consists of small domains of the $(\sqrt{3} \times \sqrt{3})$ phase separated by meandering walls of the $(\sqrt{7} \times \sqrt{3})$ phase [46]. From the deposition time t_r to reach the LEEM intensity maximum and the known flux rate F, the coverage produced by laser desorption at position r is found from $\theta_r = 4/3 - (F \cdot t_r)$. From these measurements the concentration at any location r within the hole can be deduced. The bottom of the

hole is not flat; the coverage is lower at the center than at the edges. The structure of the film within the hole consists of the more strongly bound Pb $\gamma(\sqrt{3} \times \sqrt{3})$ ($\theta = 1/6$ ML) or $\beta(\sqrt{3} \times \sqrt{3})$ ($\theta = 1/3$ ML) phases in some proportion that depends upon the amount of Pb that was desorbed, which is controlled by the laser power. By varying the power, the radius of the hole r_0 can be also varied from 5 to 25 μm which at the same time increases the coverage difference between the center and the hole edge, $\Delta\theta_{\text{depth}}$, proportionally as $\Delta\theta_{\text{depth}} = kr_0$. The presented results were obtained for 17 μm $\leq r_0$; for 17 μm, the coverage difference between hole center and hole edge $\Delta\theta_{\text{depth}}$ is ~ 0.31 ML but the difference between the outside coverage and the coverage at the hole center is more than 0.75 ML. Because of this large gradient, the finite $\Delta\theta_{\text{depth}}$ and the non-flatness of the bottom of the profile should make no difference in the evolution of $\theta(r, t)$.

Although the diffusion of the α-phase wetting layer was studied and reported on more extensively [3], we focus here on the behavior of the amorphous wetting layer on the (7×7) surface to show the similarity between diffusion on the two interfaces and to make a closer link with the previously discussed STM experiments.

Figure 3.4 shows refilling of the hole in the amorphous layer at $\theta = 1.4$ ML on the Si(111)-(7×7) surface at 292 K. The surface prior to the application of the laser pulse is shown in Fig. 3.4a, followed by 11 images separated by 2.75 s for a total refilling time of ~30 s. The moving boundary divides the shrinking low coverage phase at the center (dark) and the surrounding brighter region. (The bright rim and the faint ring outside the hole do not change appreciably with time which indicates that a different phase is far away from the hole vs. at its edge.) Similar observations

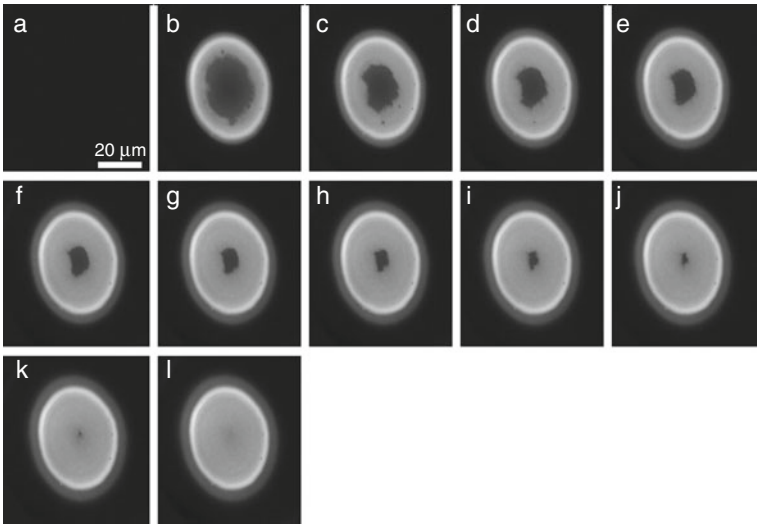

Fig. 3.4 Refilling of the initial hole generated by the laser pulse on Si(111)–(7×7). The temperature is 292 K and coverage 1.4 ML. The length scale is seen by the *white bar* in (**a**). The first image is before the application of the laser pulse and the time between each image is $\Delta t = 2.75$ s for a total time of 30 s. An outward almost stationary pulse is not related to the refilling of the hole

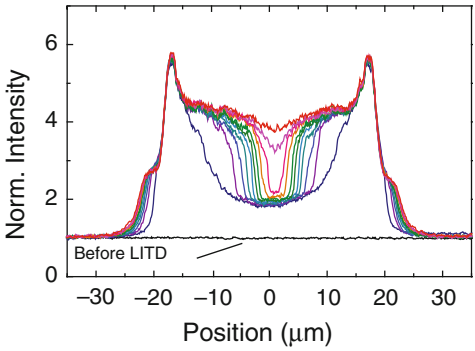

Fig. 3.5 Line profiles on the previous image of the Pb wetting layer on the Si(7×7) separated by $\Delta t = 2.75$ s showing the abrupt profile edge and constant refilling speed

for the α-phase wetting layer were reported in [3]. The unusual observations that are directly visible in these raw data are incompatible with classical diffusion without any analysis: (i) the profile edge moves without any dispersion, (ii) the moving speed is constant $\Delta x/\Delta t$ where Δx is the displacement of the edge position. Both these observations do not depend on the coverage calibration of the LEEM intensity. The constant refilling speed is also seen in Fig. 3.5 where 1-d radial intensity line profiles from the 12 frames of Fig. 3.4 are displayed. The bright rim at $r_0 = 17\,\mu$m in Figs. 3.4 and 3.5 is part of the wetting layer outside the hole. It appears bright because laser heating was sufficient to partially order the film structure but was not sufficient to desorb Pb. The film appears bright as it fills the hole because LITD has lifted the underlying (7×7) order and Pb that fills the hole converts the undesorbed Pb within the hole to the α-phase. The filling of the hole is initially fast in the first two frames following desorption, then settles to constant speed after the initial fast transient. Such a fast initial filling was also observed for the α-phase film in [3] (and Fig. 3.6 here), although this transient behavior was less pronounced.

The 1-d profiles for the refilling of the α-phase in Fig. 3.6 show the corresponding behavior for $\theta = 1.22$ ML and $T = 262$ K. The time interval between profiles is $\Delta t = 60$ s for a total refilling time ~12 min. These 1-d profiles also show non-dispersive profile shape and constant speed since the edge position moves the same distance for each interval Δt. The bottom of the profile in the hole is also non-flat as in

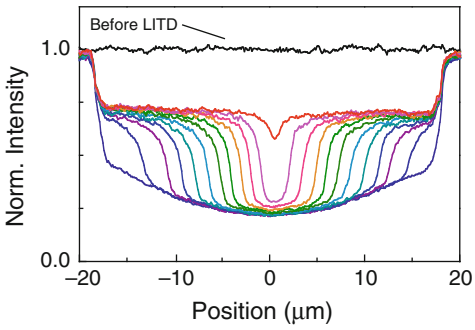

Fig. 3.6 1-d profiles for the refilling of the $\alpha(\sqrt{3}\times\sqrt{3})$ phase for $\theta = 1.22$ ML and $T = 262$ K. The time interval between profiles is $\Delta t = 60$ s for total refilling time of 12 min. The same unusual diffusion features as in Fig. 3.5 are observed irrespectively of the initial interface, whether it is (7×7) or $\alpha(\sqrt{3}\times\sqrt{3})$ phase

Fig. 3.5. Both conclusions about non-classical diffusion described before also hold for Fig. 3.6 which confirms the similar behavior of the wetting layer diffusion on the two interfaces. As will be discussed below, the laser pulse heats the surface within the hole and desorbs partially Pb to a local coverage ~0.7 ML less than the coverage outside. This initial phase generated by the pulse is the same for both Pb-(7 × 7) and α-phases. As Pb enters to refill the hole it generates the same sequence of phases with θ: first the (1 × 1) at $\theta \approx 1$ ML followed by the SIC phase at $\theta \approx 4/3$ ML. For the wetting layer on the (7 × 7), this means that although the phases outside and inside the hole have the same θ, their structure is different: outside the hole the structure is the initial amorphous layer with 4/3 ML and inside the hole is a weakly ordered SIC phase with 4/3 ML.

Another unusual observation about these experiments already discussed in [3] for the α-phase layer is the existence of a sharp transition of the refilling time τ vs. θ (of the initial wetting layer outside the hole) at fixed T. There is a critical coverage θ_c that was estimated in [3] to be 1.3 ML (close to the coverage of the SIC phase) below which there is dramatic increase of the refilling time. This divergence can be described by power law reminiscent of critical phenomena $1/\tau \sim (\theta_c - \theta)^{-\kappa}$ for $\theta < \theta_c$. (More detailed recent measurements have identified from the diffraction patterns the numerous "devil's staircase" phases that are known to form in this system in the range $1.2 < \theta < 4/3$ ML and have located with higher precision the exact value of θ_c [47].) Although the nature of this dependence is not fully understood, such a critical sensitivity of τ or $D_c(\theta)$ with small changes of θ as low as 0.01 ML is unique to the Pb wetting layer.

Figure 3.7 shows the results of several refilling experiments on the two interfaces. The refilling time is plotted as a function of hole radius at the same four temperatures. (As described before the hole radius is changed by adjusting the laser power.) Figure 3.7a corresponds to the refilling on the Pb-$\alpha(\sqrt{3}\times\sqrt{3})$ layer and Fig. 3.7b on the Pb-(7×7) layer. The four temperatures shown are 286, 276, 264, and 259 K from

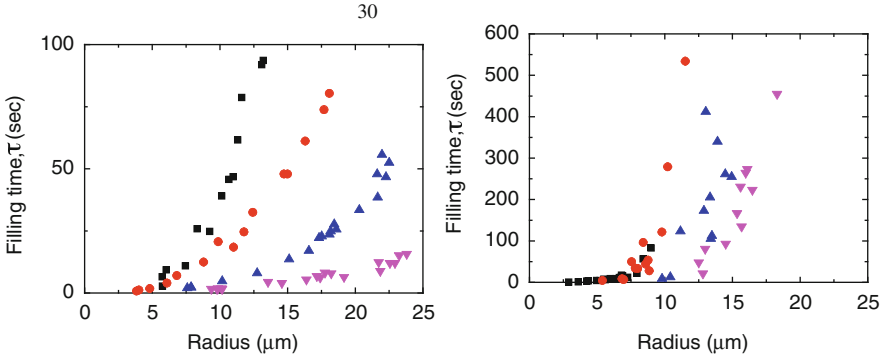

Fig. 3.7 (**a**) Refilling on the $\alpha(\sqrt{3} \times \sqrt{3})$ for $\theta = 1.22$ ML (below θ_c) for 286 K (▼), 279 K (▲), 269 K (●), 262 K (■) and (**b**) on the (7×7) for $\theta = 1.6$ ML (above θ_c) for 286 K (▼), 276 K (▲), 264 K (●), 259 K (■). Note: the ordinate axis scales for the (7×7) and the $\alpha(\sqrt{3}\times\sqrt{3})$ differ by a factor of 6

bottom to top. The coverages are 1.22 ML in Fig. 3.7a and 1.6 ML in Fig. 3.7b which are lower and higher than θ_c, respectively. It is important to notice that the ordinate axis scale is six times larger (0–600 s) for the (7×7) than for the $\alpha(\sqrt{3} \times \sqrt{3})$ (0–100 s). This by itself shows that the mobility is higher on the $\alpha(\sqrt{3} \times \sqrt{3})$ since τ increases as θ is reduced below θ_c; in particular, τ is higher on the (7×7) than on the $\alpha(\sqrt{3} \times \sqrt{3})$ despite $\theta < \theta_c$ in the latter case. The purpose of Fig. 3.7 is not to compare the exact values of τ for the same T and θ on the two phases (since this requires very fine control of the coverage to show it is the same in the two experiments), but simply to conclude which refilling speed and mobility is larger. The faster speed on the α-phase is in good agreement with the STM observations discussed earlier (namely, the interconnected "continents" on the $\alpha(\sqrt{3} \times \sqrt{3})$ vs. separate individual islands on the (7×7) for the same θ). In addition, Fig. 3.7 shows the dependence of τ on the hole radius r_0 especially for the α-phase because the data follow a more clear noise-free dependence. They can be fitted to a power law dependence $\tau \sim r_0^n$ with the exponent n close to 2.8. This is another illustration of the constant refilling speed because from the LEEM intensity calibration it was found that increasing the hole radius (with laser power) also increases the depth of the profile hole, $\Delta\theta_{\text{depth}} \approx kr_0$, so the total amount desorbed is proportional to r_0^3 and therefore the measured exponent is very close to the expected $n = 3$ exponent.

For completion, the results of earlier SPA-LEED experiments that explored the phase transformations in Pb/Si(111) after Pb deposition at low temperatures are shown in Fig. 3.8. In these experiments, a uniform 2-d phase exists over the whole

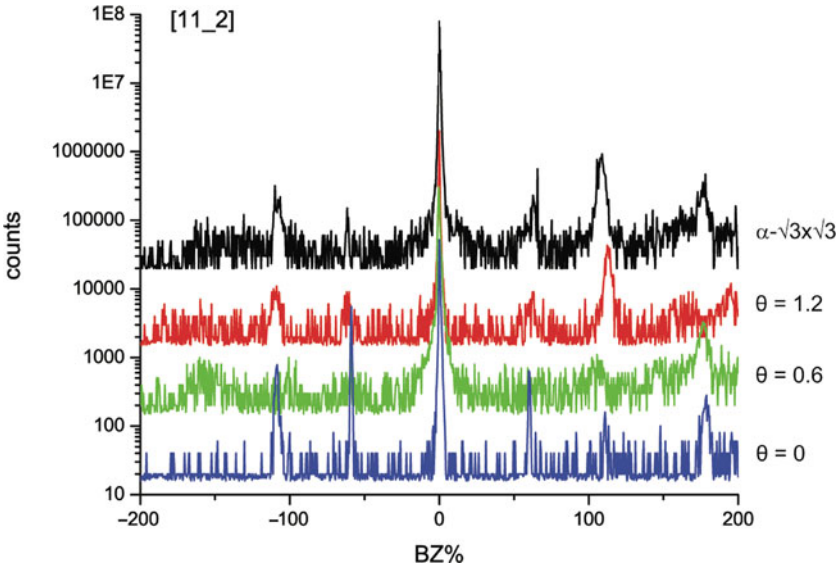

Fig. 3.8 1-d diffraction profiles along the [11 $\bar{2}$] direction at 190 K. Initially the surface is prepared in the $\beta(\sqrt{3} \times \sqrt{3})$ with $\theta = 1/3$ ML (*bottom curve*), phase with 1 × 1 diffraction pattern after ~2/3 ML (second curve), $\alpha(\sqrt{3} \times \sqrt{3})$ phase after ~1 ML (third curve), well-annealed $\alpha(\sqrt{3} \times \sqrt{3})$ (after heating 1.7 ML to 500 K)

surface which transforms to a different 2-d phase during deposition without annealing. In Fig. 3.8 1-d diffraction patterns along the [11 $\bar{2}$] direction are shown at 190 K. Initially the surface is prepared in the $\beta(\sqrt{3} \times \sqrt{3})$ phase with $\theta = 1/3$ ML (bottom of Fig. 3.8). After the addition of $\sim 2/3$ ML the surface transforms to a phase with (1×1) diffraction pattern (the second curve). With the addition of a total of ~ 1 ML the pattern changes to a pattern characteristic of the α-phase (with the 2/3, 2/3 spot stronger than the 1/3, 1/3 spot, the third curve). This phase is comparable to the phase that is obtained after thermal annealing of an initial amount 1.7 ML at 500 K (top pattern in Fig. 3.8). It has lower intensity because the domains are smaller and there is a large network of domain walls. The sequence of phases is the same as the phases observed during hole refilling, by the diffusion of the outside layer on both interfaces. They showed that the same ordered patterns are observed once the correct coverage of Pb is present in the hole irrespective of how the atoms arrive, by deposition or diffusion. As discussed below in detail this shows that the unusual kinetics are not reaction front limited.

3.4 Modeling of the LEEM Experiments

3.4.1 Coverage-Dependent Coefficients

In the 1-d diffusion geometry of Fig. 3.1, different profile shapes can be used to deduce the coverage-dependent coefficient $D_c(\theta)$ by the BM method if the scaling condition $c(r, t) = c(r/t^{1/2})$ is met. In the LEEM experiments, the geometry of the vacant circular hole is 2-d, so the BM can still be used if the change of the profile shape is small compared to the hole radius r_0. However, since the scaling condition is clearly not met (because of the constant speed $\Delta x/\Delta t$) the more fundamental question was whether a still coverage-dependent coefficient $D_c(\theta)$ can reproduce the novel features described earlier.

The non-linear diffusion equation (3.1) in 2-d can be written as

$$\frac{\partial \theta}{\partial t} = D_c(\theta)\left(\frac{1}{r}\frac{\partial \theta}{\partial r} + \frac{\partial^2 \theta}{\partial r^2}\right) + \frac{\partial D_c(\theta)}{\partial \theta}\left(\frac{\partial \theta}{\partial r}\right)^2 \tag{3.7}$$

By applying the physical argument described before in connection with (3.4) (that a flat profile implies fast diffusion and a steep profile implies slow diffusion) the Boltzmann function is a possible functional form

$$D_c(\theta) = \frac{D_1 - D_2}{1 + \exp\left(\frac{\theta - \theta_c}{w}\right)} + D_2 \tag{3.8}$$

This coverage-dependent $D_c(\theta)$ is shown in Fig. 3.9a. D_c increases rapidly from a small value at low θ to a high value at high θ to reflect the observations: the wetting layer moves rapidly outside the hole where the coverage is high, but once it enters

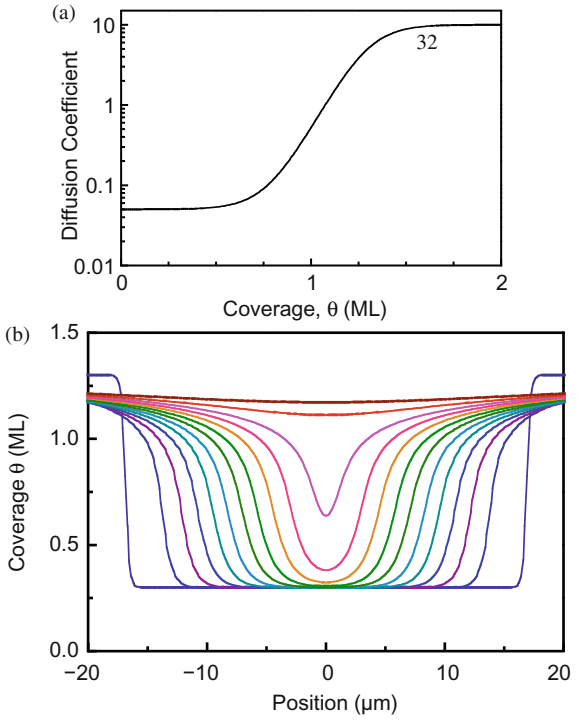

Fig. 3.9 (**a**) $D_c(\theta)$ according to (3.8). The model has four parameters: D_1 the value at low θ, D_2 the value at high θ, θ_c the critical coverage above which D_2 is valid, and w the coverage width of the transition from the low to the high value. (**b**) Simulated profiles for the previous $D_c(\theta)$ dependence by numerically solving the diffusion equation (3.8) in excellent agreement with the profiles observed in Figs. 3.5 and 3.6

the hole it slows down by orders of magnitude (to account for the absence of edge dispersion). The model has four parameters: D_1 the value at low θ, D_2 the value at high θ, θ_c the critical coverage which is the inflection point between the two limiting values of D, and w the coverage width of this transition. Comparison was made between the numerical solution of (3.7) using (3.8) and the data of Figs. 3.5 and 3.6. The solution is shown in Fig. 3.9b for the following optimal parameters: $D_1 = 0.05$, $D_2 = 10$, $\theta_c = 1.3$ ML, and $w = 0.1$ ML. The D_c's are expressed in terms of r_0^2/τ units for $r_0 = 17\,\mu$m and $\tau = 44$ s, corresponding to the experimentally observed filling time for this r_0 in the α-phase at $T = 269$ K and $\theta = 1.22$ ML, but clearly the parameters can be rescaled to fit any of the other measured profiles. As initial conditions for the calculation of the profile evolution in Fig. 3.9b, it was assumed that $\theta(r < r_0) = 0.3$ ML and $\theta(r > r_0) = 1.3$ ML so the large gradient $\Delta\theta = 1$ ML ensures similar profile shapes even with slight shifts in θ_c or the initial conditions.

It is seen that a coverage-dependent $D_c(\theta)$ can produce an invariant profile shape and constant filling speed. However, despite the apparent good agreement between the calculated and measured profiles, there are concerns. For cases where the outside coverage $\theta(r > r_0, t = 0)$ is below the critical coverage $\theta < \theta_c$, the profile shape will not be dispersionless and appreciable edge spreading will be seen. The reason is the sudden drop of $D_c(\theta)$ for $\theta < \theta_c$ (and therefore the smaller difference between diffusion outside and diffusion inside the hole). This implies that the outside atoms will not enter the hole much faster than diffusion within the hole and therefore the

edge will not remain so abrupt and the moving edge speed will not be constant. This deviation from experimental observation will become more apparent for larger coverage deficits ($\theta_c - \theta$). Although it should be accessible in the coverage range that has been examined experimentally, no such change of profile shape evolution or non-constancy of speed was observed for coverages as low as 0.09 ML below θ_c. A similar criticism for this model applies if instead of θ the temperature is changed. Depending on the activation energies of D_c above and below θ_c the ratio D_1/D_2 in the model will change with temperature. This implies that the shape of the profile will be different at different temperatures and it will not remain dispersionless. This has not been observed experimentally. Only if the activation energies above and below θ_c are the same will the non-classical features be preserved with changes of temperature. Temperature-dependent measurements below θ_c are in progress.

3.4.2 Adatom Vacancy Model

Another model that has been considered [3] and possibly can account for these unusual observations is based on an adatom–vacancy diffusion mechanism that at the minimum can provide a phenomenological explanation, but at the cost of introducing a number of assumptions and energy barriers. Vacancy generation can be energetically possible since the wetting layer is dense and considerable strain can develop, even for the amorphous layer on the (7×7) surface. If we define the local variables, $c_a(r, t)$ the adatom concentration, $c_v(r,t)$ the vacancy concentration, and $\theta(r,t)$ the coverage that remains in the wetting layer, then we can write rate equations describing how these local concentrations change with t:

$$\frac{\partial c_a(r,t)}{\partial t} = D_a \nabla_r^2 c_a(r,t) + [R_G \theta(r,t) - R_R c_a(r,t) c_v(r,t)] \tag{3.9a}$$

$$\frac{\partial \theta(r,t)}{\partial t} = -\frac{\partial c_v(r,t)}{\partial t} = -[R_G \theta(r,t) - R_R c_a(r,t) c_v(r,t)] \tag{3.9b}$$

where R_G, R_R are temperature-dependent rates that describe how adatoms and vacancies are thermally generated and D_a is the adatom diffusion coefficient on top of the wetting layer. This set of equations assumes that only adatoms diffuse and that vacancies are immobile. The first equation states that a change in $c_a(r, t)$ is due to either adatom diffusion, adatom generation from the wetting layer, or elimination of adatoms by recombination with static vacancies. The second equation states that vacancies are generated simultaneously with the thermally excited adatoms from the wetting layer or are lost by recombination. Since a vacancy cannot move, by mass conservation if a vacancy is generated at (r, t) then the coverage at this location must decrease correspondingly.

As initial condition, one assumes the experimental situation where a circular hole has lower coverage ($c_v(r < r_0, t = 0) > 0$) compared to the coverage outside the hole. In [3], $c_v = 0.5$ was assumed. The adatom concentration $c_a(r, t)$ is determined

by the activation energy of R_G to match the measured refilling times. The rate of change of the vacancy, $\partial c_v(r,t)/\partial t$, and wetting layer coverage $\partial\theta(r,t)/\partial t$ are exactly complementary to each other. There is no difference between the initially imposed vacancies in the hole and vacancies generated thermally in the wetting layer outside. Adatoms (which are assumed to be on top of the wetting layer) move to the edge of the hole where the concentration of vacancies is large and they are eliminated. If there are no holes the wetting layer is at equilibrium and has a small but equal number of vacancies and adatoms, again determined by R_G and R_R.

To account for the constant refilling speed (given that the adatom concentration must be small), all the adatoms from far away outside the hole should be collected at a constant rate irrespective of how far they originate from. This number can be estimated: for $r_0 = 17\,\mu$m, there are 7.2×10^9 sites in the hole to be filled for a 1 ML deficit. Using a value of $c_a = 10^{-3}$ ML as the thermally generated adatom density outside the hole that was determined in the modeling [3] and $1\,\text{ML} = 7.84 \times 10^{14}$ atoms/cm^2 as the density of Si(111) this implies that adatoms should be collected from an area 0.009 cm^2. This collection area has a linear radius 600 μm or $35r_0$, i.e., diffusion must be "instantaneous" on the wetting layer. The adatoms must arrive at the edge of the hole in time shorter than the LEEM acquisition time, 500 ms in these experiments, so the apparent arrival rate as seen in Fig. (4) of [3] is constant: the refilling is not limited by the diffusion from the outside (for thermally activated diffusion the time to arrive increases with the square root of the distance the atoms travel). Using this it means the adatom diffusion barrier E_a of $D_a = D_0 \exp(-E_a/kT)$ must be effectively zero. The best fit to the model requires a very low diffusion barrier 0.05 eV [3] consistent with the calculated Pb on (crystalline) Pb(111) terrace diffusion barrier [34].

The unperturbed edge of the profile is built in the model since only at the edge of the hole are adatoms and vacancies eliminated. Or to express this mathematically, the right-hand side of (3.9(a)) above is zero far away from the perimeter of the hole because the thermally excited adatoms and vacancy holes obey detailed balance $R_G\theta(r,t) \approx R_R c_a(r,t)c_v(r,t)$, i.e., there is local equilibrium. Only at the edge of the hole is the second term $R_R c_a(r,t)c_v(r,t)$ large (because a large $c_v(r,t)$ is imposed at $r < r_0$ externally by laser desorption and $c_a(r,t)$ is relatively larger at $r > r_0$ than it is at $r < r_0$). The first term of 3.9(b) can be neglected because $R_R >> R_G$ (or the corresponding activation energies must be chosen so $E_G > E_R$). Under these conditions, 3.9(b) becomes $\partial\theta(r,t)/\partial t =$ constant only at the edge, i.e., the edge of the profile is unperturbed and moves at a constant speed.

There is one more important observation to be accounted by the model, i.e., the existence of a critical coverage θ_c; below this coverage the refilling becomes increasingly slow with exponential dependence on the coverage deviation $(\theta_c - \theta)$. To account for this, the number of thermally generated adatoms that cause the refilling and the elimination of the vacancies must be suppressed so the "refilling rate" $R_R c_a(r,t)c_v(r,t)$ becomes smaller (because the term $c_a(r,t)$ goes to zero). To accomplish this one more assumption is needed, that the recombination activation energy E_R is constant but the generation activation energy increases linearly as the

coverage falls below θ_c, $E_G = E_g(\theta_c) + \varepsilon(\theta_c - \theta)$ with $\theta < \theta_c$. Preliminary fits to account for the increase of the refilling time by four orders of magnitude as θ decreases by 0.1 ML below θ_c require $\varepsilon = 0.6$ eV/0.1 ML [3].

The adatom–vacancy model is based on numerous assumptions that independently are added to account for the unusual observations. It is not clear how these assumptions are physically justified: the very low diffusion barrier, the absolute values of $E = 0.35$ eV, $E_G = 0.2$ eV in preliminary fits [3] (for such a soft metal as Pb), and the most unintuitive assumption being the increasing cost to generate a vacancy by 0.6 eV/0.1 ML as the layer is diluted minutely. These assumptions have not yet been justified by DFT or even heuristic arguments. In addition, if the model is matched at one temperature then the fit will not be as good at a different temperature since all rates R_R, R_G are a strong function of temperature and they will change their value. The (7×7) wetting layer is amorphous so it is even harder to envision how vacancies are generated and how the energy cost increases dramatically with decreasing θ.

3.5 Comparison with Other Pb Diffusion Experiments

How do the magnitudes of these unusual mobilities of the different wetting layers on Si(111) compare with the diffusion of Pb on Pb macroscopic crystals? As can be seen from Fig. 3.7, which compares the refilling time for different hole radii on the two interfaces within the temperature range $\sim 262\,\text{K} < T < 285\,\text{K}$, one can conclude that the refilling speeds are in the range 20–1000 nm/s on the (7×7) and 150–5800 nm/s on the $\alpha(\sqrt{3} \times \sqrt{3})$ for comparable hole radii in the range 5–20 μm. The coverages of the two phases in Fig. 3.7 were (approximately) 1.6 ML on the (7×7) and 1.22 ML on the $\alpha(\sqrt{3} \times \sqrt{3})$. The quoted values are not meant for direct comparison because the refilling times as discussed previously are sensitive functions of θ especially for $\theta < \theta_c$ but they set up the scale of the speed (to be compared with the STM and other results in the literature). From the STM experiments on the (7×7) and at the much lower temperature of 190 K, the speed of the ring growth around the top of islands is 0.05 nm/s as seen in Fig. 3.2; but, at higher temperature of 242 K [31], the speed is at least 20 nm/s, which is comparable to the refilling speed shown in Fig. 3.7b, although direct coverage comparison is not easy. In making this comparison, the ring speed on top of an island might be expected to be lower than the wetting layer hole filling speed because there is the additional barrier [38] to overcome at the island edge during transport of atoms to the island top.

In [49], Pb "neck" formation was studied of the top layer on Pb crystals at higher temperature 318 K (so the top layer is in a "liquid" state due to surface "melting"). The neck forms as a result of the tip–surface interaction and the high electric field. Pb is mobile, moving toward the area under the tip making a "neck" and bridging the tip surface gap with a speed which depends on temperature. This shorts the gap and leads to a higher current for the same tip–surface voltage. By retracting the tip over a certain distance Δz within a time interval Δt, the connection can be broken which increases the gap resistance as sensed from the abrupt decrease of

the current. The tip retraction speed depends on the speed of the moving Pb layer and the tip–surface separation. If the tip is close to the surface the "neck" breaking should not depend on the retraction speed since for faster retractions it is easier to break the "neck." At the minimum distance the retraction speed $\Delta z/\Delta t$ matches the speed of the wetting layer. At this speed the break point becomes independent of the tip–surface separation. When the break point separation is plotted vs. tip retracting speed (at fixed T), the curve has an open hyperbola-like shape. The speed at the corner of the hyperbola (the point where the retraction speed is independent of separation) is the speed of the moving Pb. For example, at the lowest temperature of [49] 318 K, the tip retracts $\Delta z = 60$ nm and over $\Delta t = 240$ s. This implies that the speed of Pb toward the tip is $\Delta z/\Delta t = 0.25$ nm/s.

This speed is low when compared to the speed of the wetting layer as measured by LEEM or by STM. Already the speed is less by two orders of magnitude although the temperature in the "neck" experiment (318 K) is higher than the lower temperature shown in Fig. 3.7 (∼260 K). The comparison can be made more quantitative by using the speed at 318 K and the activation energy 1 eV measured in [49], to extrapolate to the lower temperature of the LEEM or STM experiments. If the extrapolation is done at 262 K, then the speed is 0.000095 nm/s, which is seven orders of magnitude lower than the LEEM experiment at this temperature. This shows that the unusual wetting layer mobility is a novel effect not related to the thermal diffusion on top of bulk crystalline Pb. This possibility is even more plausible since the experiments in [49] were compared to earlier He scattering experiments of Pb on Pb(110) [50] which also gave a slow diffusion coefficient and a relatively high activation energy of 0.65 eV. Even the terrace diffusion barriers measured on the Pb islands at low temperatures $T \sim 200$ K [32, 34] where QSEs are important in controlling the kinetics gave a much smaller barrier (0.05 eV), as noted before in connection with the modeling of the adatom–vacancy model. This also supports the hypothesis that these unusual mobilities have non-classical but yet to be understood origin.

3.6 Comparison with Other Step Profile Evolution Experiments

Experiments for different coverages were carried out in Li/Mo(112) at 300 K [6] that, as noted in Sect. 3.1, were attributed to the carpet unrolling mechanism. However, these results do not have the intriguing novelties of the current experiments and besides they were carried out at higher θ where (up to 3.5 ML) additional layers are present. The evolving step profile was measured with a Kelvin probe that records the local workfunction change $\Delta\phi(r,t)$ which is related monotonically to the local coverage, $\theta(r,t) = F(\Delta\phi(r,t))$ (with coverage calibration usually established from the known coverage of a 2-d ordered phase). The spatial resolution of the method is ∼1 μm. Although a moving step profile was observed, it moved at increasingly slower speed as mass was transferred from the upper layers to the layer in contact

with the substrate. During the time that atoms from the upper layers hop across the profile edge into the lowest layer, mass at the edge is replenished quickly by fast diffusion on top of this layer. The advancing profile shape does not change because diffusion in the upper layers is fast compared to diffusion within the lower layer. The coverage profile shows two unperturbed edges: the receding edge in the upper layer serves as the source of atoms that are incorporated at the unperturbed edge of the layer in contact with the substrate. The speed of the lower advancing edge decreases as its distance from the upper source edge increases with time. This clearly shows a film that does not behave as Pb/Si of Figs. 3.5 and 3.6 where the motion of a single edge with constant speed demonstrates that the whole layer moves collectively.

The BM method was used for the analysis in [6] with $r/\sqrt{t}$ the scaled variable so the profile speed was decreasing with t. Since diffusion of the second layer was higher than diffusion in the first layer, the derived coverage dependence $D_c(\theta)$ showed a gradual jump starting from 0.5 ML in the first layer to a value five orders of magnitude larger in the second layer; but the coverage width of the transition region between these two values, 0.3 ML, is much larger than essentially discontinuous jump (that was assumed in the modeling of profile evolution in Pb/Si (Sect. 3.4.1). Finally, for Li/Mo(112) there is no critical region and critical coverage θ_c where the diffusion coefficient decreases with an exponential or power law dependence on the coverage difference $(\theta_c - \theta)$ for $\theta < \theta_c$.

Concentration profiles that do not disperse with t have been also observed with LEEM in a more complicated system, Au/Si(111) [51], but at much higher temperature 910 K and with smaller spreading speeds 7×10^{-2} nm/s than that observed in Pb/Si(111). The Au/Si(111) is complex because from the dense 1 ML high coverage phase on one side to zero coverage (i.e., the clean Si(111) (7×7)) on the other side of the profile edge, two superstructures form, the Au($\sqrt{3} \times \sqrt{3}$) and Au(5×1). The system is not homogeneous as in the current work. In the experiment of [51], additional edges were identified separating the 1 ML from the $\sqrt{3}$ phase, the $\sqrt{3}$ from the (5×1) phase, and the (5×1) from the (7×7) phase (even the (5×1) phase had two distinct phases with coverages differing by 0.1 ML). Only the edge separating the (5×1) from the (7×7) phase was moving at a constant speed. In this system the time measured for the edge to diffuse to a given location is the time to arrive at the location and the time to convert from the random atom position to the ordering of the local phase. The data were accounted quantitatively if diffusion on top of the (5×1) was the fastest process and the measured diffusion time was determined by the time for these atoms to move from the top of the (5×1) to the layer below and expand the (5×1) domain area, analogous to the carpet unrolling mechanism. Besides these inhomogeneities, the higher temperature, and the lower advancing speed, no critical coverage θ_c was identified in [51].

No such inhomogeneities exist in the Pb/Si(111) system and if the same local coverage θ within the hole is realized, the same phase forms irrespective of whether it was added by deposition as in Fig. 3.8 or by diffusion from the edge. There is only one boundary observed and the speed across the moving layer is the same.

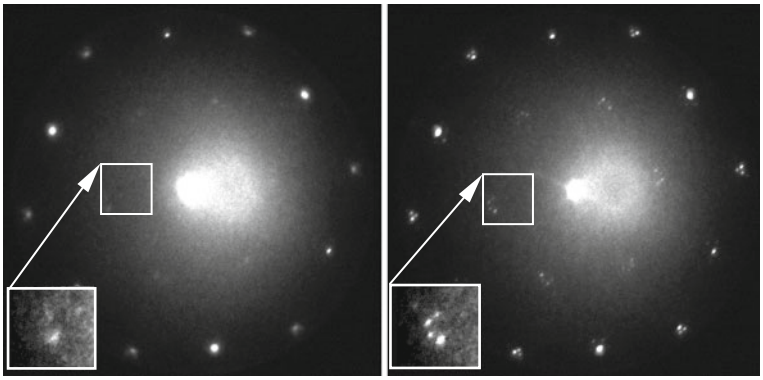

Fig. 3.10 μ-LEED patterns obtained (**a**) inside the hole after refilling and (**b**) outside the hole for the α-phase layer. They show similar Pb α-phase film structure and coverage (but the outside one of higher intensity because of the initial annealing). The same α-phase is seen inside and outside the hole, with a single moving boundary which does not support reaction front kinetics

Figure 3.10 shows a comparison of μ-LEED patterns outside the laser-induced hole and inside the hole after the refilling at 320 K. The pattern outside the hole in Fig. 3.10b indicates that the α-phase film has well-ordered HIC structure [47] with coverage in the range 1.25–1.30 ML. The pattern in Fig. 3.10a shows that a less ordered α-phase HIC structure with comparable coverage is formed upon refilling. A similar pattern is observed on both interfaces (7×7) and α-phase following refilling which indicates the same sequence of phases are produced irrespective of initial surface conditions or the source of Pb, deposited and annealed or diffused from the edge of the hole. This cannot be caused by a carpet unrolling mechanism since in the diffusion experiments the phases outside the hole are so different and since in the SPA-LEED experiment (Fig. 3.8) the atoms are arriving from the gas phase.

Finally we mention a very puzzling study of truly liquid Pb film adsorbed on Si at higher temperature ($T = 673$ K). The film was studied with X-ray scattering [52] at the solid–liquid interface. From reflectivity measurements it was found that the liquid Pb close to the Si was in a compressed state with density few percent higher than bulk Pb density. At the very least, this demonstrates that a compressed liquid phase is possible in the Pb/Si system although it is not clear if it is related to the compressed state and its unusual mobility at the much lower temperatures of the current studies.

3.7 Conclusions

From both the STM and LEEM experiments it is clear that the wetting layer plays an unusual role in transporting material to generate the sharp height island distribution in Pb/Si. The transfer at a constant speed is a far more efficient way to move mass

than normal diffusion since distance is linear with time; furthermore, because of the higher density of the wetting layer (10% compressed above bulk Pb(111)) the motion is collective instead of the diffusion of individual atoms. The absolute value of the refilling speed (0.05 nm/s at 190 K on the (7×7)) is also much higher than what was expected from Pb thermal diffusion on macroscopic crystals. None of these results are well understood theoretically and the models discussed have severe limitations. The existence of a critical coverage θ_c is the least understood result except that it is related to the compressed state of the system.

Despite the need for a better theoretical understanding of these phenomena they point out to the importance of the behavior of the wetting layer especially at low temperatures. Growth at low temperatures is usually ignored (because thermal diffusion is expected to be suppressed) or in the cases when it results in smooth crystalline films (seen with diffraction intensity oscillations), the initial mobility of the wetting layer is neglected. Clearly for Pb/Si(111) this is not the case and the system provides the best benchmark to exploit QSE in generating novel kinetic pathways to build the uniform height metal islands extremely fast. A still widely open question is whether this unusual mobility is unique to Pb/Si or other metal/semiconductor systems display similar behavior. Understanding better the kinetics in Pb/Si will facilitate the search of other systems with QSE-driven self-organization.

Acknowledgments This work was supported in part by the Office of Science, Basic Energy Sciences, Materials Science Division of the U.S. Department of Energy–USDOE under Contract No. DE-AC02-07CH11358 through the Ames Laboratory and in part by the Hong Kong Research Grants Council under grant HKUST600106.

References

1. M.C. Tringides (ed.), *Surface Diffusion: Atomistic and Collective Processes* (Plenum, New York, NY, 1998)
2. C.M. Yim, K.L. Man, X. Xiao, M.S. Altman, Low-energy electron microscopy of CO/Pt(111) surface diffusion by nonequilibrium coverage profile evolution. Phys. Rev. B **78**, 155439 (2008)
3. K.L. Man, M.C. Tringides, M.M.T. Loy, MS. Altman, Anomalous mass transport in the Pb wetting layer on the Si(111) Surface. Phys. Rev. Lett. **101**, 226102 (2008)
4. M.C. Tringides, M. Hupalo, edts J. Karger, P. Heitjans, R. Haberlandt, *Fluctuations and Growth Phenomena in Surface Diffusion in Diffusion in Condensed Matter* (Viwweg, Braunschweig/Wiesbaden, 2003)
5. L. Cai, M.S. Altman, E. Granato, T. AlaNissila, S.C. Ying, X. Xiao, Surface diffusion anomaly near a substrate phase transition. Phys. Rev. Lett. **88**, 226105 (2002)
6. A.T. Loburets, A.G. Naumovets, Yu.S. Vedula, in *Surface Diffusion: Atomistic and Collective Processes*, ed. by M.C. Tringides (Plenum, New York, NY, 1998)
7. M.C. Tringides, M. Jalochowski, E. Bauer, Quantum size effects in metallic nanostructures. Phys. Today **60**(4), 50 (2007)
8. N.V. Smith, Phase analysis of image states and surface states associated with nearly-free-electron band gaps. Phys. Rev. B **32**, 3549 (1985)
9. T.C. Chiang, Photoemission studies of quantum well states in thin films. Surf. Sci. Rep. **39**, 181 (2000)

10. A.R. Smith, K.J. Chao, Q. Niu, C.K. Shih, Formation of atomically flat silver films on GaAs with a 'silver mean' quasiperiodicity. Science **273**, 226 (1996)
11. L. Gavioli, K.R. Kimberlin, M.C. Tringides J.F. Wendelken, Z. Zhang, Quantum growth of Ag islands on Si(111): Plateaus with magic height. Phys. Rev. Lett. **82**, 129 (1999)
12. K. Budde, E. Abram, V. Yeh, M.C. Tringides, Uniform self-organized 7-step height Pb/Si(111)-(7x7) islands at low temperatures and quantum size effects. Phys. Rev. Rap. Com. B **61**, 10602 (2000)
13. J. Chen, M. Hupalo, M. Ji, C.Z. Wang, K.M. Ho, M.C. Tringides, Crystallographic phase transition and island height selection in In/Si(111) growth. Phys. Rev. B **77**, 233302 (2008)
14. Y. Han, B. Unal, F. Qin, D. Jing, C.J. Jenks, D.-J Liu, P.A. Thiel, J.W. Evans, Kinetics of facile bilayer island formation at low temperature: Ag/NiAl(110). Phys. Rev. Lett. **100**, 116105 (2008)
15. V. Fournée, H. Sharma, M. Shimoda, A. Tsai, B. Unal, A. Ross, T. Lograsso, P.A. Thiel, Quantum size effects in metal thin films grown on quasicrystalline substrates. Phys. Rev. Lett. **95**, 155504 (2005)
16. R. Otero, A.L. Vázquez de Parga, R. Miranda, Observation of preferred heights in Pb nanoislands: A quantum size effect. Phys. Rev. B **66**, 115401 (2002)
17. H. Hong, C.-M. Wei, M.Y. Chou, L. Basile, H. Chen, M. Holt, T.-C. Chiang, Alternating layer and island growth of Pb on Si by spontaneous quantum phase separation. Phys. Rev. Lett. **90**, 076104 (2003)
18. K.L. Man, Z.Q. Qiu, M.S. Altman, Kinetic limitations in electronic growth of Ag films on Fe(100). Phys. Rev. Lett. **93**, 236104 (2004); Y.Z. Wu, A.K. Schmid, M.S. Altman, X.F. Jin, Z.Q. Qiu, Spin-dependent Fabry-Pérot interference from a Cu thin film grown on fcc Co(001). Phys. Rev. Lett. **94**, 027201 (2005)
19. W.B. Su, S.H. Chang, W.B. Jian, C.S. Chang, L.J. Chen, T.T. Tsong, Correlation between quantized electronic states and oscillatory thickness relaxations of 2D Pb islands on Si(111)-(7 × 7) Surfaces. Phys. Rev. Lett. **86**, 5116 (2001)
20. M. Hupalo, V. Yeh, L. Berbil-Bautista, S. Kremmer, E. Abram, M.C. Tringides, Uniform height island growth of Pb on Si(111)-Pb ($\sqrt{3}x\sqrt{3}$) at low temperatures. Phys. Rev. B **64**, 155307 (2001)
21. C. Joeffrey, R. Feng, E.H. Conrad, M. Hupalo, P. Ryan, C. Kim, P.F. Miceli, M.C. Tringides, Infuence of quantum size effects on island coarsening. Phys. Rev. Lett. **96**, 106105 (2006)
22. M.H. Upton, C.M. Wei, M.Y. Chou, T. Miller, T.C. Chiang, Thermal stability and electronic structure of atomically flat uniform Pb films on Si(111). Phys. Rev. Lett. **93**, 026802 (2004)
23. M. Jalochowski, M. Hoffmann, E. Bauer, Pb layer-by-layer growth at very low temperatures. Phys. Rev. B **51**, 7231 (1995)
24. C.M. Wei, M.Y. Chou, Theory of quantum size effects in thin Pb(111) films. Phys. Rev. B **66**, 233408 (2002)
25. Z.Y. Zhang, Q. Niu, C.K. Shih, Electronic growth of metallic overlayers on semiconductor substrates. Phys. Rev. Lett. **80**, 5381 (1998)
26. M. Jalochowski, E. Bauer, Rheed intensity and electrical resistivity oscillations during metallic film growth. Surf. Sci. **213**, 556 (1989)
27. A. Petkova, J. Wollschlager, H.L. Gunter, M. Henzler, Order and disorder in ultrathin Pb films grown on Si(111) 7 × 7 substrates at low temperatures. Surf. Sci. **482**, 922 (2001)
28. M.H. Upton, T. Miller, T.C. Chiang, Appl. Absolute determination of film thickness from photoemission: Application to atomically uniform films of Pb on Si. Phys. Lett. **85**, 1235 (2004)
29. M. Zinke-Allmang, L.C. Feldman, M.H. Grabow, Clustering on surfaces. Suf. Sci. Rep. **16**, 377 (1992)
30. K. Thurmer, J.J. Reutt-Robey, E.D. Williams, M. Uwaha, A. Emundts, H.P. Bonzel, Step dynamics in 3D crystal shape relaxation. Phys. Rev. Lett. **87**, 186102 (2001)
31. C. Rye, M. Yakes, M. Hupalo, M.C. Tringides, Novel coarsening of Pb nanostructures on Si(7 × 7). J. Undergrad. Res. **7**, USDOE 82 (2007)

32. M. Hupalo, M.C. Tringides, Ultafast kinetics in Pb/Si(111) from the collective spreading of the wetting layer. Phys. Rev. B **75**, 235443 (2007)
33. M. Li, J.W. Evans, C.Z. Wang, M. Hupalo, M.C. Tringides, T.L. Chan, K.M. Ho, Strongly-driven coarsening of height-selected Pb islands on Si(111). Surf. Sci. Lett. **601**, 140 (2007)
34. T.-L. Chan, C. Z. Wang, M. Hupalo, M.C. Tringides and K.M. Ho, Quantum size effect on the diffusion barriers and growth morphology of Pb/Si(111). Phys. Rev. Lett. **96**, 226102 (2006)
35. Y. Han, M. Hupalo, M.C. Tringides and Feng Liu, Quantum modulation of island nucleation on top of a metal nanomesa. Surf. Sci. Lett. **602**, 62 (2008)
36. S.M. Binz, M. Hupalo, M.C. Tringides, Height-dependent nucleation and ideal layer by layer growth in Pb/Pb(111)/Si(111). Phys. Rev B **78**, 193407 (2008)
37. X. Ma, P. Jiang, Y. Qi, J. Jia, Y. Yang, W. Duan, W.X. Li, X. Bao, S.B. Zhang, Q.K. Xue, Experimental observation of quantum oscillation of surface chemical reactivities. PNAS **104** (22), 9204 (2007)
38. A. Menzel. M. Kammler, E.H. Conrad, V. Yeh, M. Hupalo, M.C. Tringides, Kinetics measurements of Pb island growth on Si(111). Phys. Rev. B **67**, 165314 (2003)
39. Z. Kuntova, M. Hupalo, Z. Chvoj, M.C. Tringides, Bilayer ring second layer nucleation morphology in Pb/Si(111)-7 $\times$ 7. Phys. Rev. B **75**, 205436 (2007)
40. V. Yeh, L. Berbil Bautista, C.Z. Wang, K.M. Ho, M.C. Tringides, Role of the metal/semiconductor interface in quantum size effects: Pb/Si(111). Phys. Rev. Lett. **85**, 5158 (2000)
41. J. Tersoff, A.W. Denier van der Gon, R. Tromp, Shape oscillations in growth of small crystals. Phys. Rev. Lett. **70**, 1143 (1993)
42. K.L. Man, W.X. Tang, H. Huang, M.S. Altman, Kinetic limitations in two- and three-dimensional growth. Mater. Res. Soc. Symp. Proc. **849** (Materials Research Society, Warrendale, Pa., 2005) KK5.3
43. L. Li, C. Kozio, K. Wurm, Y. Hong, E. Bauer, I.S.T. Tsong, Surface morphology of Pb overlayers grown on Si(100)-(2 $\times$ 1). Phys. Rev. B **50**, 10834 (1994)
44. H. Okamoto, D. Chen, T. Yamada, Competing classical and quantum effects in shape relaxation of a metallic island. Phys. Rev. Lett. **89**, 256101 (2002)
45. C.-S. Jiang, S.-C. Li, H.-B. Yu, D. Eom, X.-D.Wang, Ph. Ebert, J.-F. Jia, Q.-K. Xue, C.-K. Shih, Building Pb nanomesas with atomic-layer precision. Phys. Rev. Lett. **92**, 106104 (2004)
46. M.M. Ozer, Y. Jia, Z. Zhang, J.R. Thompson, H.H. Weitering, Tuning the quantum stability and superconductivity of ultrathin metal alloys. Science **316**, 1594 (2007)
47. S. Stepanovsky, M. Yakes, V. Yeh, M. Hupalo, M.C. Tringides, The dense $\alpha-\sqrt{3} \times \sqrt{3}$ Pb/Si(111) phase: a comprehensive STM and SPA-LEED study of ordering, phase transitions and interactions. Surf. Sci. **600**, 1417 (2006)
48. K.L Man et al., Collective super-diffusive motion in the Pb wetting layer on the Si(111) surface to be published
49. L. Kuipers, J.W. Frenken, Jump to contact, neck formation, and surface melting in the scanning tunneling microscope. Phys. Rev. Lett. **70**, 3907 (1993)
50. J.W.M. Frenken, B.J. Hinch, J.P. Toennies, Ch. Woll, Anisotropic diffusion at a melting surface studied with He-atom scattering. Phys. Rev. B **41**, 938 (1990)
51. J. Slezak, M. Ondrejcek, Z. Chvoj, V. Chab, H. Conrad, S. Heun, Th. Schmidt, B. Ressel, K.C. Prince, Surface diffusion of Au on Si(111): A microscopic study. Phys. Rev. B. **61**, 16121 (2000)
52. H. Reichert, M. Denk, J. Okasinki, V. Honkimaki, H. Dosch, Giant metal compression at liquid-solid (Pb-Si, In-Si) schottky junction. Phys. Rev. Lett. **98**, 116101 (2007)

Chapter 4
Quantum Size Effects in the Growth and Properties of Ultrathin Metal Films, Alloys, and Related Low-Dimensional Structures

Y. Jia, M.M. Özer, H.H. Weitering, and Z. Zhang

Abstract This chapter addresses the quantum mechanical nature of the formation, stability, and properties of ultrathin metal films, metallic alloys, and related low-dimensional structures, with Pb as a primary elemental example. The emphasis is on the contribution to the overall energetics from the electronic degrees of freedom of the low-dimensional systems. As a metal film reduces its thickness, the competition between quantum confinement, charge spilling, and Friedel oscillations, *all of electronic origin*, can dictate whether an atomically smooth film is marginally, critically, or magically stable or unstable against roughening during the growth of such metal films. The "electronic growth" mode as emphasized here serves as an intriguing addition to the three well-established classic modes of crystal growth. In exploring electronic growth, Pb(111) films represent a particularly compelling example, not only because their stability exhibits unusually strong quantum oscillations but also because their physical and chemical properties can be tuned with great precision by controlling the film thickness or the chemical composition. Recent advances and the perpectives in this active area of film growth will be reviewed, with results from both theoretical and experimental studies.

4.1 Historical Review

Low-dimensional materials have been an important platform for the discovery of novel quantum phenomena, such as the quantized conductance and quantum Hall effects in semiconductor heterostructures [1] and giant magneto-resistance in metallic magnetic superlattices [2]. In these examples, fabrication of the low-dimensional medium was accomplished via classical thin film growth; yet the emerging properties are clearly quantum mechanical in nature. More recently, it has been shown that the size quantization of itinerant electrons in an ultrathin metal film also plays a decisive role in the early formation stages and kinetic stability of the films [3–9].

Y. Jia (✉)
School of Physics and Engineering, Zhengzhou University, Zhengzhou, Henan 450052, China;
Materials Science and Technology Division, Oak Ridge National Laboratory, Oak Ridge, TN 37831, USA
e-mail: jiayu@zzu.edu.cn

M. Michailov (ed.), *Nanophenomena at Surfaces,* Springer Series in Surface Sciences 47,
DOI 10.1007/978-3-642-16510-8_4,

The ability to exploit quantum mechanical principles while tuning and assembling nanostructures offers a whole new range of opportunities for exploring the physical and chemical properties of functional nanomaterials with precisely controlled dimensions [10–15].

Atomically flat metal thin films on a proper substrate, such as Ag/GaAs(110), Pb/Si(111), Pb/Ge(111), Al(110)/Si(111), In/Si(111), and Mg(0001)/Si(111) films, have been the model systems for exploring electronically driven self-assembly, a process dubbed "electronic growth" or "quantum growth" [4]. In these systems, the interplay between the quantum size effect and the morphological evolution of the films received considerable attention following the discovery of "magic thicknesses" or "critical thicknesses" and perferred island heights in ultrathin metal films grown at moderately low tempertures. In particular, Pb is a soft metal and hence electronic effects in the formation stages of the film could easily overwhelm lattice strain contributions to the total free energy of the film [16]. An added consideration is that the Fermi wavelength λ_F is nearly commensurate with the interatomic layer spacing d along the $\langle 111 \rangle$ direction, which amplifies the role of quantum size effects and Friedel oscillations on the growth mode of the Pb films.

Studies of the quantum size effect (QSE) in thin films date back to the 1970s. Jaklevic and Lambe first observed the QSE by means of tunneling experiments in metal–oxide–metal junctions [17]. Schulte carried out self-consistent studies of thin films and showed that the work function oscillates with the thickness of the films [18]. Such oscillations were also confirmed beyond the jellium model by Feibelman [19], who also found oscillations in the surface energy.

In the 1990s, researchers found that atomically smooth metal films on semiconductors are sometimes formed at low temperatures, under growth conditions that seem to be far away from thermodynamic equilibrium [3]. However, because the adatom diffusion still appears to be significant in this growth regime, thermodynamic considerations can still be applied at least locally. This novel growth mode is qualitatively different from the three well-established classical growth modes [20] and appears to be related to quantum size effects that provide a non-trivial thickness-dependent contribution to the free energy of the film, one that easily overwhelms the strain contributions due to lattice mismatch. This has led to the surprising observation that smooth film growth in the quantum regime is possible only *above* a certain critical thickness [8, 21, 22]. Qualitatively, this newly defined critical thickness is just the inverse of the transition at the critical thickness defined in the classic Stranski–Krastanov (SK) growth mode [23].

The first striking example of the quantum growth mode of Ag on GaAs was revealed in a two-step process [3], deposition at low temperature and subsequent annealing to room temperature. At very low temperature, since the mobility is very low, only tiny grains or "nanoclusters" are formed as opposed to smooth films or large 3D clusters. Upon heating the sample to room temperature, the atoms acquired sufficient mobility to self-organize into an atomically smooth film with a thickness of six monolayers (ML). If the nominal deposition amount is slightly less, then the film contains large holes exposing the bare GaAs substrate. Evidently, the "underdosed" Ag film phase separates into a 6 ML thick Ag film and holes exposing the

bare substrate. This indicates that the atomically flat 6 ML thick Ag film constitutes a particularly stable morphology.

Similar behavior has been observed in both Ag and Pb films grown on Si(111) at low temperature [7, 8]. Scanning tunneling microscopy (STM) and spot profile analysis low energy electron diffraction measurements of Pb/Si(111) revealed the presence of large islands with flat-tops, steep edges, and strongly preferred heights [24, 25]. Budde et al. have observed that Pb islands of seven monolayers are preferred to form on the Si(111)–(7×7) substrate at low temperatures with low energy electron diffraction (LEED) [21]. Su et al. [24] confirmed this observation with STM. The existence of competing 4 or 5, 7 and 9 ML island heights was summarized in a "kinetic phase diagram" for nominal coverages up to 10 ML and temperatures between 120 and 250 K [25]. Hong et al. [22] studied the same system using real-time in situ X-ray diffraction, and their results show that the growth switches to a layer-by-layer mode for films of over five monolayers. Özer et al. performed a comprehensive STM study of Pb films on three different semiconducting substrates, Si(111)–7×7, Si(111)– $\sqrt{3}\times\sqrt{3}R30^\circ-\alpha$, and Ge(111)– $\sqrt{3}\times\sqrt{3}-\alpha$. It is found that Pb films have the same re-entrant bilayer-by-bilayer growth mode on these three different substrates.

Remarkably, the quantum stability of the meal films, derived from single or nearly free electron pictures, also influences a wide variety of physical and chemical properties. In this chapter, we will first discuss the role of the quantum size effect in the stability of thin metallic films from both the free electron model and the density functional theory perspectives, and we will highlight some of the key experimental observations for mostly Pb and Mg. The second part of this review will be devoted to the structural, physical, and chemical properties of the films, specifically lattice relaxations and work functions, superconductivity, and surface chemical reactivity. We refer to the chapter by Tringides and Altman in this volume [pp. XX–XX] with regard to QSE on growth kinetics, particularly the various atomistic rates on different metal films and flat-top nanoislands. We also refer to a somewhat related recent review from our collaborative team [26], which emphasized more on the experimental aspects of the subjects.

4.2 The Quantum Size Effect

4.2.1 Quantum Size Effect and Electronic Growth

When a metal film becomes very thin, there will be three central ingredients that can influence the stability of the film on the supporting substrate, namely quantum comfinement, charge spilling, and interface-induced Friedel oscillations [4]. Electronic confinement within the metal overlayer can mediate an effective repulsive force between the interface and the surface. Electron transfer from the overlayer to the substrate leads to an attactive force between the two interfaces, acting to distabilize the overlayer [16]. Interface or surface-induced Friedel oscillations in

electron density can further impose an oscillatory modulation onto the two previous interactions.

Generally, for most metals, the Fermi wavelength is comparable to the lattice spacing in a given direction. This means that if a metal film is only several atomic layers thick, the motion of the nearly free electrons perpendicular to the film will resemble that of the famous "particle-in-a-box" in introductory quantum mechanics. When the "free" electrons are squeezed into a box with hard wall barriers (referring to one dimension for simplicity), the momentum wave vector should become quantized such that an integer multiple of half-wavelengths can fit inside the box. In a very thin film the wave function of an itinerant electron is expected to obey the same quantization condition along the film normal, the total phase difference accumulated by the reflections must be a number of 2π according to the Sommerfeld–Bohr quantization rule:

$$2k_z d + \Phi_1 + \Phi_2 = 2\pi n \tag{4.1}$$

here k_z is the allowed wave vector component normal to the surface, n takes on integer values, d is the thickness of the films, and Φ_1 and Φ_2 are the phase terms that account for wavefunction leakage beyond the potential steps at the film boundaries, for the vacuum films on both sides, the Φ_1 and Φ_2 are taken to be π. Furthermore we have $k_z = n\pi/d$ or, equivalently, $d = n\lambda/2$, where n is a non-zero, positive integer. The parallel momentum states, however, are still represented by two-dimensional (2D) Bloch waves with a free electron-like dispersion, $E\left(\vec{k}_0\right) = \hbar^2 k_0^2/2\,m^*$, where m^* is the effective mass. In turn, the discretization of the electronic energy band can lead to an oscillatory dependence of the film's total energy on its thickness, instead of the linear dependence on thickness for very thick films. This oscillatory behavior implies that a thin film of certain layers may be energetically favored over other layers, opening a window of opportunity that an atomically flat film will form upon annealing [4, 16, 27] (see Figs. 4.1 and 4.2).

A more accurate analysis of quantum size effect physics requires first-principles electronic structure calculations as a function of the film thickness. Such first-

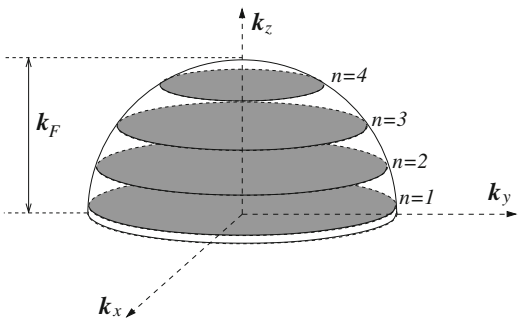

Fig. 4.1 Energy subbands of a metallic thin film

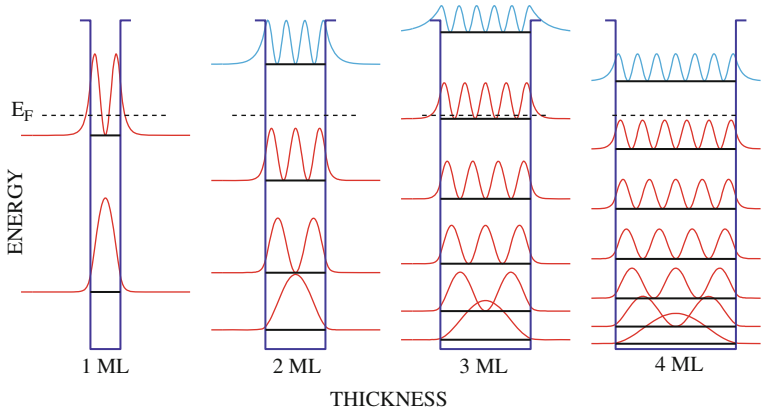

Fig. 4.2 Sketch of confinement of electrons in ultrathin metallic films

principles calculations confirm the qualitative predictions from the nearly free electron model. The thickness-dependent surface energy and work function also follow from such calculations and exhibit damped oscillations as a function of the film thickness, with periods depending on the specific systems.

4.2.2 Surface Energy and the Stability of Films

We first discuss the criterion of stablity, that is, how to use the total energies to determine the stability of a metallic film or the possible outcome of an annealing experiment. As a given amount of a certain material is deposited on a substrate, many different morphologies may result. The case of continuous film is illustrated in Fig. 4.3. During annealing at certain temperatures, the film will likely change its morphology. The system always tends to seek a morphology of lower energy when it is allowed by growth kinetics. The configuration that is a local minimum in the system energy is relatively stable and will likely be the outcome of annealing.

The total energy $E_t(L)$ of a thin metallic film can be obtained, within the free electron model, by summing over the single particle energies E_n (k_0, L) below the

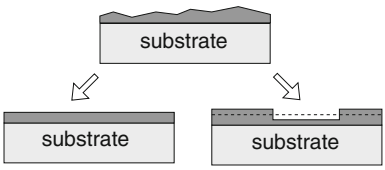

Fig. 4.3 Morphological evolution of continuous thin films. The *top* is a rough film before annealing; after annealing, the film may become atomically flat (*bottom left*) or develop into a film with two different heights (*bottom right*). In these cases, the contact area between the film and the substrate is conserved during the morphological evolution [27]

Fermi level $E_t(L)$ of the film [27]. Here, n represents the subband index and L is the film thickness in monolayers ($d = Ld_0$, d_0 being the interlayer spacing). This total energy determines the thermodynamic stability of the film at low temperatures. One usually subtracts the bulk energy to obtain the surface energy $E_s(L)$ per unit area. A thin film of L monolayers is (meta) stable if the electronic compressibility $\partial^2 E_s/\partial L^2 > 0$. Under this condition, small-scale roughness in the film will be suppressed, provided that the atom mobility is high enough. A film is unstable if $\partial^2 E_s/\partial L^2 < 0$, in which case the system can achieve a lower energy state by developing a mixed phase of different film thicknesses. A critical thickness L_c can be defined if the film is stable for $L \geq L_c$ and unstable for $L < L_c$ or the other way around. A magic thickness L_m can be defined if $E_s(L)$ has a downward cusp at L_m, meaning that the film is unstable on both sides of L_m [4].

For discrete layer thicknesses, this criterion is sometimes recast as a criterion for the discrete "second difference" of $E_s(L)$:

$$\mathrm{d}^2 E_s(L) = E_s(L+1) + E_s(L-1) - 2E_s(L) \tag{4.2}$$

which should also be positive for a stable film of thickness $L\mathrm{d}_0$. This criterion should be viewed as a criterion for the local stability of the film. It does not rule out phase separation into film regions with a thickness of $L \pm 2$. Global stability of a closed film morphology requires that $E_s(L)$ is convex (or $\partial^2 E_s/\partial L^2 > 0$) over a wide coverage range. This is indeed the case for the nearly free electron model if one ignores the small quantum oscillations arising from the band discretization. These small quantum oscillations could make the function $E_s(L)$ locally convex, which in turn should lead to phase separation into preferred thicknesses, a phenomenon that is sometimes referred to as "quantum phase separation" [22].

4.3 Understanding the QSE Within Nearly Free Electron Models

4.3.1 Nearly Free Electron Model

To illustrate the basic physics of how quantum size effects can affect the growth and stability of a metal film, we focus on the total electronic energy as a function of layer thickness starting with non-interacting electrons that are *vertically* confined by a square well potential, this is the so-called nearly free electron model. In this model, a metal film can be described with a free electron gas confined to an infinte quantum well. In general, the total energy E_t of a freestanding metallic thin film with thickness d determines the thermodynamic stablity. It can be shown that [27]

$$E_t = \frac{m_e S}{2\pi\hbar^2} \sum_{n \leq N} \left(E_F^2 - E_n^2 \right) \tag{4.3}$$

And the surface energy E_s is

$$E_s(d) = \frac{k_F^2 E_F}{4\pi} \left\{ \sum_{n \le N} \frac{E_F^2 - E_n^2}{E_F^2} - \frac{4}{5} \frac{dk_F}{\pi} \right\} \tag{4.4}$$

where E_F, E_f, and k_F are the Fermi level, Fermi energy, and Fermi wave number, respectively. S is the surface area of the films.

According to (4.3) and (4.4), one noticeable result for such a nearly free electron model is that the Fermi energy of a free electron slab is pushed to higher energy as the film thickness decreases, which is due to the increase of the kinetic energy (Fig. 4.4a and b) [4, 27–29]. In addition, the film's Fermi energy oscillates as a function of thickness, as marked by a series of cusps that are separated by a thickness interval of $\lambda_F/2$. This is related to the fact that the level spacing decreases with increasing thickness. As the film thickness increases, the Fermi energy exhibits a cusp when an empty subband begins to shift through the Fermi level. At the Fermi

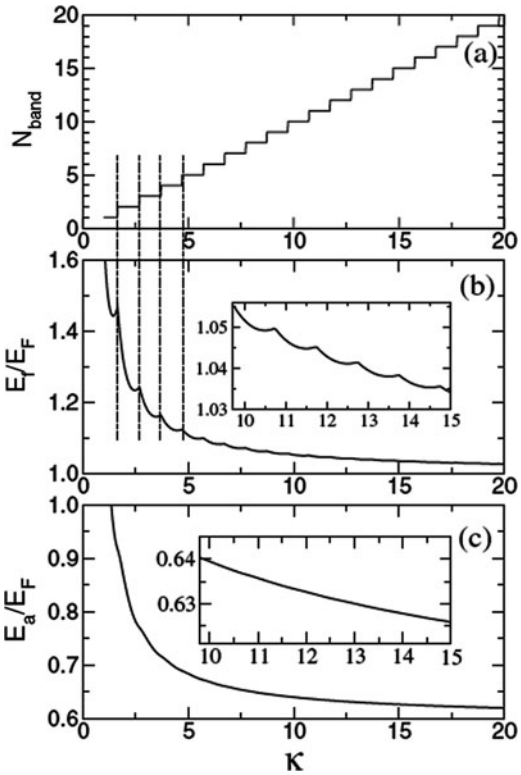

Fig. 4.4 (**a**) Number of subbands below the Fermi energy. (**b**) Fermi energy E_f and (**c**) surface energy per electron *Ea* as a function of a metallic thin film. The interfaces are modeled as infinite energy barriers, showing the increase of the Fermi energy at low film thicknesses as well as the superimposed oscillations with a period of $\lambda_F/2$. The film thickness is labeled by the dimensionless number $\kappa = dk_F/\pi$. Reproduced from [27]. Insets show the enlarged portions of E_f and E_a. The *dashed lines* indicate the correspondence between the emergence of a new subband and a cusp

level, the general quantization condition $d = n\lambda/2$ becomes $d = n\lambda_F/2$ and, consequently, the cusps in $E_F(d)$ are separated by a thickness $\lambda_F/2$. Because of the $\lambda_F/2$ oscillations of the Fermi level, the cohesive energy of the slab oscillates as well.

To be specific, the five different metallic films which represent three different types of stability, with their second differences are shown in Fig. 4.5, revealing that

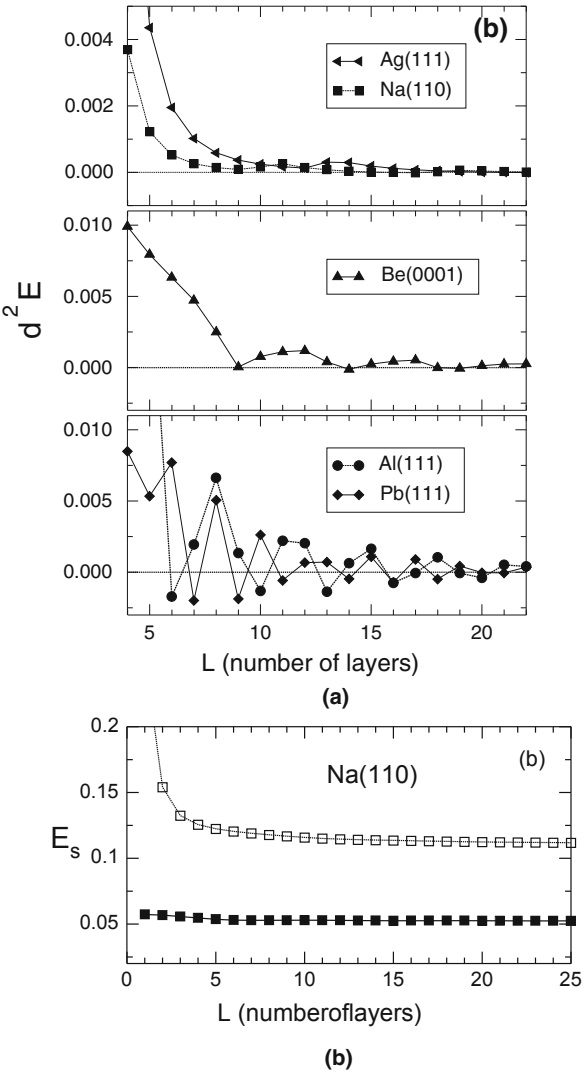

Fig. 4.5 Surface energy and discrete second differences: (**a**) The infinite potential well captures the qualitative differences in the local stability of Ag(111), Na(110), Be(0001), Al(111), and Pb(111) films. **(b)** Freestanding Na(110) films exhibit a dramatic reduction of the kinetic energy when using finite energy barriers (black squares) as opposed to infinite barriers (open squares). The kinetic energy lowering is due to charge spilling and is especially profound at small thicknesses. Reproduced from [27]

the films are very different from each other. The alkali metal Na(110) and transition metal Ag(111) films are the first type of stability, their surface energy become bulk-like very quickly: beyond five monolayers ($L > 5$), their $d^2 E_s$ is already very small. Another type is alkaline earth metal films, such as Mg(0001) and Be(0001) films; the surface energy of Be(0001) films decays into bulk slower; despite the apparent oscillations, Be(0001) films of different monolayers are stable since its second difference $d^2 E_s$ is almost always positive. Even its second difference $d^2 E_s$ becomes negative at a few thicknesses, its absolute value is very small and does not indicate a strong instability. This implies that, according to the computation, it is very hard to grow atomically flat Be(0001) of any thickness in experiments. However, Al(111) and Pb(111) films are very different from the above two types of films. First, their second difference $d^2 E_s$ decays even slower. Second, their $d^2 E_s$ oscillates around zero with $d^2 E_s$ possibly being negative. For example, Al(111) films have negative $d^2 E_s$ at $L = 5$, 10, 13, and 16 monolayers, which means that Al(111) films are unstable at these thickness. In other words, unlike Be(0001), the oscillations here in $d^2 E_s$ imply oscillations in the film stability for Al(111) and Pb(111) films. Besides the apparent similarity, Al(111) and Pb(111) films have different oscillation patterns in the film stability. The stability of Pb(111) films oscillates in an even–odd fashion interrupted by crossovers. This is exactly the oscillation pattern observed in the stability of Pb(111) film in [15], although there exists difference in which layers are stable due to the substrate effects in the experimental studies. Considering how crude the present model is, the agreement is quite amazing. Moreover, the amplitude of the oscillations in $d^2 E_s$ matches well with the ab initio calculations in. [10, 15, 30, 33] and, more importantly, in thin film growth experiments [8, 31]. The oscillation pattern in film stability is determined by the ratio between the Fermi wavelength λ_F and the layer spacing d_0 as we will discuss in the following sections. For Pb(111) films, we have $\lambda_F/2 : d_0 = 1 : 1.44 \approx 2 : 3$; for Al(111) films, we have $\lambda_F/2 : d_0 = 1 : 1.3 \approx 3 : 4$.

The model can be improved by changing the infinite potential barriers with finite barriers, taking into account the lattice potential, allowing the electron wave function to spill into the vacuum and substrate regions [27, 30]. Figure 4.6 presents the Fermi energy of a Pb(111) film as a function of thickness with different boundaries. In the infinite well model, when the thickness of the films is exactly equal to Nd_0, $E_F(d)$ rises drastically as the film thickness decreases to compensate for the areas of electron depletion near the film boundaries. However, with a finite well, as the energy barrier decreases, the less confinement felt by the free electrons and the electrons can spill out of the film more easily, so such compensation is unnecessary. Therefore, the Fermi energies E_f of the film decrease accordingly to its bulk value. At the same time, the slopes of the energies decreasing with thickness become less steep as finite well decreases. This makes the oscillations in Fermi energy E_f to appear more pronounced. On the other hand, in the infinite well but allowing the electron density to allow to spill out the classical film boundaries, the result is very similar to the case of finite well. In addition, as indicated by the dashed line in Fig. 4.6, the barrier height of the well shifts the cusp positions, which is known as phase shift [32].

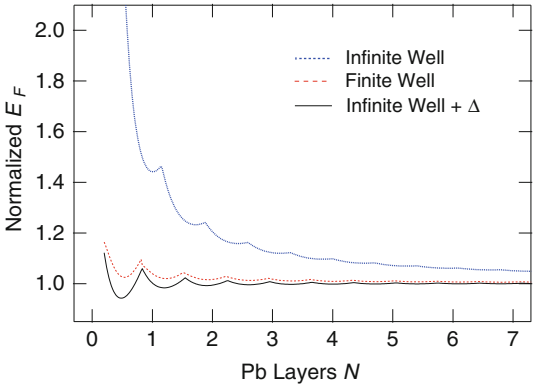

Fig. 4.6 The Fermi energy of Pb(111) films as a function of the thickness, normalized to its bulk free electron value. Reproduced from [29]

4.3.2 Beyond the Nearly Free Electron Model

The next step is to include exchange and correlation effects within the density functional theory (DFT) formalism. From Schulte's calculations [18] it is evident that the main feature, such as the $\lambda_F/2$ oscillation of the Fermi level remains preserved in DFT. However, in these calculations the oscillation of the Fermi energy is caused primarily by a corresponding variation in the effective potential, whereas the variation in the kinetic energy with thickness is very small. This has implications for the interpretation of the calculated work function oscillations. The latter are caused primarily by the oscillations in the surface dipole as a function of the layer thickness, not by periodic variations of the Fermi energy.

The effective potential in DFT is computed self-consistently and contains the electrostatic potential and the local exchange-correlation potential. Interestingly, the electrostatic potential in the jellium calculations reveals significant oscillations or Friedel oscillations in the electron density, due to the presence of two surfaces. The oscillations in the electrostatic potential are partially offset by corresponding oscillations in the exchange correlation potential so that the oscillations in the effective potential are weaker than those of the electrostatic potential. As we will show, however, Friedel oscillations can still play a decisive role in the thin film stability.

It should be noted that the properties (e.g., work function, potentials, total energy) of a jellium slab are derived from universal curves that only scale with the electron density or value of r_s. To assess the predictive capability for real materials, the universal curves must be sampled with the discrete atomic-layer spacing of each material. It is not a priori obvious whether the $\lambda_F/2$ quantum oscillations can be observed experimentally. For instance, if the atomic layer spacing d_0 was perfectly commensurate with $\lambda_F/2$, then there would be no oscillations at all.

Nowadays it is possible to go beyond jellium calculations and extract the properties from advanced DFT calculations that include the fully relaxed atomic coordinates [6, 9]. The predictive capabilities of these calculations are amazingly accurate.

However, this benefit of accuracy does not necessarily imply a higher level of transparency of the underlying physical principles. Simple model calculations remain invaluable in assessing the basic principles of thermodynamic stability in the thin film quantum regime.

Finally, it has been shown that the oscillations become more profound if one reduces the confinement by lowering the potential barriers at both interfaces [4, 5, 27]. As expected, the effects of charge spilling are most profound in the thinnest films, say less than 5 ML. This effect is likely to be very important for thin metal films on semiconductors where the confinement at the interface arises from the Schottky barrier height. The latter is usually much smaller than the potential barrier on the vacuum side (i.e., work function) and, hence, the stability criterion for a freestanding metal slab and that of a metal on a semiconductor could be qualitatively different. Indeed, whereas the quantum mechanically confined electron motion produces an energy contribution that helps to stabilize the film against roughening, charge spilling results in a contribution that potentially destabilizes the metal film. The latter contribution is roughly estimated from the charge transfer across the metal/semiconductor interface, which also increases with increased confinement. The balance between these two energy contributions defines the new critical thickness below which smooth film growth should be impossible [4, 27]. The argument can only be qualitative, however, because it lacks self-consistency.

4.4 Quantum Size Effects in Pb(111) Films

4.4.1 Re-entrant Bilayer-by-Bilayer Growth Behaviors of Pb Films: Experimental Results

When ultrathin Pb films grow on a semiconductor or metal substrate, such as Si(111), Ge(111), and Cu(111), the quantum size effect prevails over the strain effect, despite the large lattice mismatch that always exists. Experimentally, the bilayer oscillations were first identified with helium atom scattering (HAS) [33] and had been correctly attributed to the bilayer-by-bilayer growth of Pb(111) although later an alternative explanation was offered by the same group in which the bilayer oscillations in HAS were attributed to bilayer oscillations in the charge spilling during layer-by-layer growth [34].

Comprehensive and comparative STM studies of Pb growth on three different types of Ge(111) and Si(111) substrates, namely Si(111) $\sqrt{3} \times \sqrt{3}$, Si(111) 7×7, and Ge(111) $\sqrt{3} \times \sqrt{3}$, respectively, have been carried out [8]. The results show that quantum growth can be exploited to produce atomically smooth Pb films over mesoscopic length scales on all three substrates. The minimum coverage for smooth film growth or critical thickness $t_C = 5$ ML. In the smooth growth regime, there exists an intriguing re-entrant bilayer-by-bilayer (RBBB)_mode, characterized by strong preference of bilayer growth with periodic interruption of monolayer or trilayer growth.

Figure 4.7a shows a 500 × 500 nm STM image of a Pb film on Si(111) substrate. Flat-topped islands rising 4 or 5 ML above the wetting layer can be seen; no other island heights have been observed. In this coverage range, Pb islands never merge to form a continuous film. Figure 4.7b shows a 500 × 500 nm image of an almost

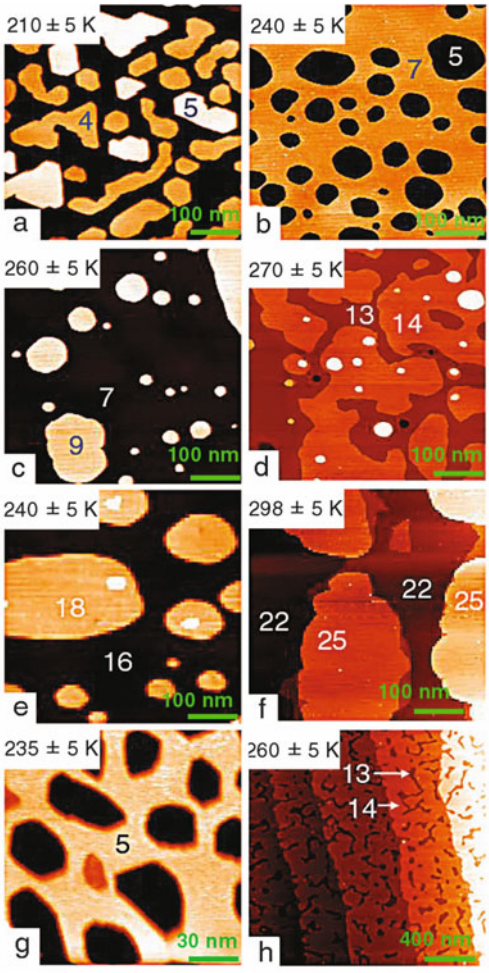

Interface	Observed Layer Thickness										
Si(111)7x7-Pb	5	7	9	11	13	14	16	18	20		
Si(111)(√3×√3)-α	5	7	9	11	13	14	16	18	20	22	25
Ge(111)(√3×√3)-α	5	7	9	11	13	14	16	18	20		

Fig. 4.7 STM images of Pb on (**a–f**) Si(111) $\sqrt{3} \times \sqrt{3}$-*R*30°-Pb, (**g**) Ge(111)-$\sqrt{3} \times \sqrt{3}$-*R*30°-Pb, and (**h**) Si(111)-7 × 7. Layer thicknesses are indicated in each panel and are measured with respect to the wetting layer. The table summarizes the observed thicknesses for each interface with even–odd crossovers indicated in *bold italics*. Image sizes and postannealing temperatures are also indicated in **a**–**h**. From [8]

continuous 7 ML Pb film with 2 ML deep voids. It is clear that in this coverage regime, the 5 ML film is atomically flat and continuous on a mesoscopic length scale while the larger part of the 5 ML surface is covered with an additional bilayer of Pb, making the total film thickness to be 7 ML. The 5 and 7 ML terraces neither possess single monolayer steps nor single monolayer voids, thus confirming the onset of perfect bilayer growth on top of the closed 5 ML film. Figure 4.7c reveals 2 ML high islands on the 7 ML films. Again, the absence of voids or monolayer high islands on the 7 ML film shows that the growth proceeds in a perfect bilayer-by-bilayer mode. Bilayer growth continues until the coverage reaches 13 ML. Figure 4.1d shows a 13 ML high film with monatomic layer high islands (14 ML) residing on top and tiny amounts of 16 ML high islands. After this intermission, near-perfect bilayer growth resumes at 14 ML, ending at 22 ML. Figure 4.7e shows the bilayer height steps on a 16 ML film. Figure 4.7f shows 3 ML high steps on top of a 22 ML high film, indicating a *trilayer* intermission. In all, Pb grows in a perfect bilayer-by-bilayer mode from 5 to 13 ML and from 14 to 22 ML. The stable thicknesses are 5, 7, 9, 11, 13*14, 16, 18, 20, 22*25 ML. This layer count excluded the wetting layer. The odd-numbered layers are favored between 5 and 13 ML while even-numbered layers are favored between 14 and 22 ML, which averages to a beating wavelength $\lambda_{\text{beat}} = 9$ ML. As we will discuss below, this RBBB growth mode is a manifestation of the QSE, and the even–odd crossover phenomenon is the result of a beating of the interlayer spacing $d_0 = 2.86$ Å and the Fermi wavelength.

For the Ge(111) substrate, Figure 4.7g shows a smooth 5 ML film of Pb on Ge(111) with 5 ML deep voids. Upon subsequent deposition, the voids close before bilayer growth commences. The even–odd crossovers also occur at the same location as for Si(111), indicating that the smaller band gap for electron confinement on Ge does not alter the bilayer growth and stability crossovers of the films.

In Pb(111) thin films, the $\lambda_F/2$ oscillations interfere with the periodicity of the atomic layer spacing along the growth direction so that the (possible) oscillation pattern in the thin film stability is determined by the relation between λ_F and atomic layer spacing d_0 [8, 9]. Pb(111) films are particularly interesting in this regard because each bilayer increment of the film thickness accommodates three additional antinodes of the Fermi wavefunction or $3\lambda_F/2 \approx 2$ ML. This accidental near commensurability causes quasi-bilayer oscillations in the thin film stability.

Besides the Pb growth on Si substrate, Pb growth on Cu(111) substrates has also been studied [35]. Three-dimensional islands of various heights were grown on the Cu surface at the temperature of 300 K and above. The heights of 6, 8, 10–11, and 15 ML were found, but not of 5, 9, 12, or 16 ML.

4.4.2 First-Principles Calculations

In ab initio calculations, the surface energy of a Pb film is computed using the following formula:

$$E_s = \frac{1}{2}[E^{\text{tot}}_{\text{film}}(n) - nE_{\text{bulk}}] \tag{4.5}$$

$E_{\text{film}}^{\text{tot}}(n)$ is the total energy of the film with n layers and E_{bulk} is the total energy per layer of the bulk. As a result, these total energies should increase linearly with the film thickness modulated by some small fluctuations. By fitting the data with a linear function and subtracting the linear part from the total energies, the desired surface energies E_{s} can be obtained.

Shown in Fig. 4.8 are the surface energies of freestanding Pb films and their discrete second derivatives. The surface energy oscillates mostly with film thickness in a bilayer fashion. However, this bilayer pattern is interrupted at least twice by crossovers at films of 8 layers and 17 layers, as seen in Fig. 4.8. The separation between the neighboring crossovers is nine monolayers. Clearly, the oscillation with film thickness persists for films as thick as 26 monolayers. From Fig. 4.8b, the films of 4, 6, 9, 11, 13, 15, 18, 20, and 22 layers are stable. These results agree well with experimental investigations [8].

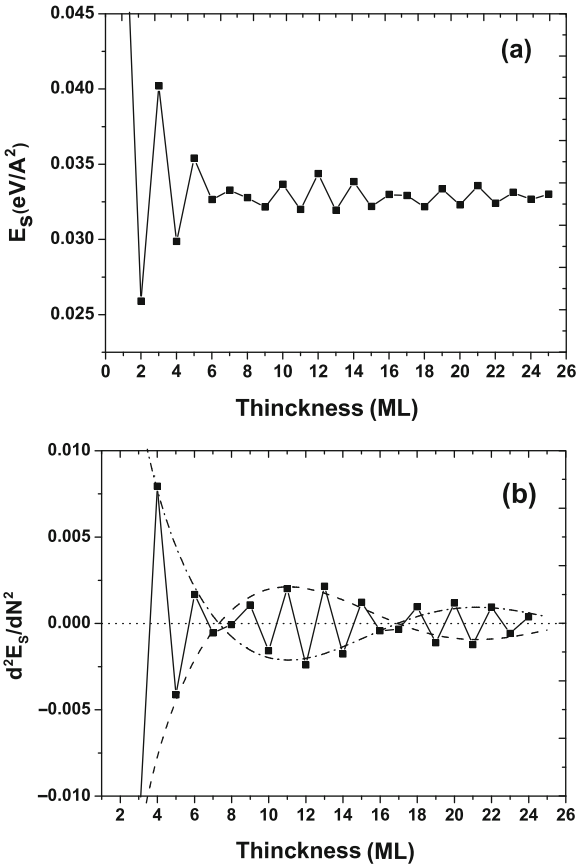

Fig. 4.8 (**a**) Surface energies of freestanding Pb films. (**b**) The discrete second derivative of surface energy of freestanding Pb films

For Pb films on the Ge(111) substrate, there is a 11% mismatch between the lattice constants (Ge, 5.76 Å; Pb, 5.04 Å). This large mismatch makes it impossible to carry out directly first-principles calculations for the Pb(111) and Ge(111) interfaces. A technical trick to overcome this obstacle is to rotate the substrate by 30° and place a 2×2 Pb unit cell on a bulk truncated Ge(111)- ($\sqrt{3}\times\sqrt{3}R30°$) surface. Such a method enables to accommodate the lattice mismatch between Ge and Pb and the substrate remains semiconducting. Another way adopted is to artificially compress the substrate to match the lattice constants, such as for Si(111) substrate in [35]. But in this approach, the substrate may become metallic and change its conducting nature, which is not desirable.

The surface energies of Pb films on the Ge(111) substrate and their discrete second derivatives are plotted in Fig. 4.9. Similar to the freestanding films, there are bilayer oscillations interrupted by crossovers. The separation between the crossovers is about nine monolayers but the crossovers are located at 5 monolayers, 13 mono-

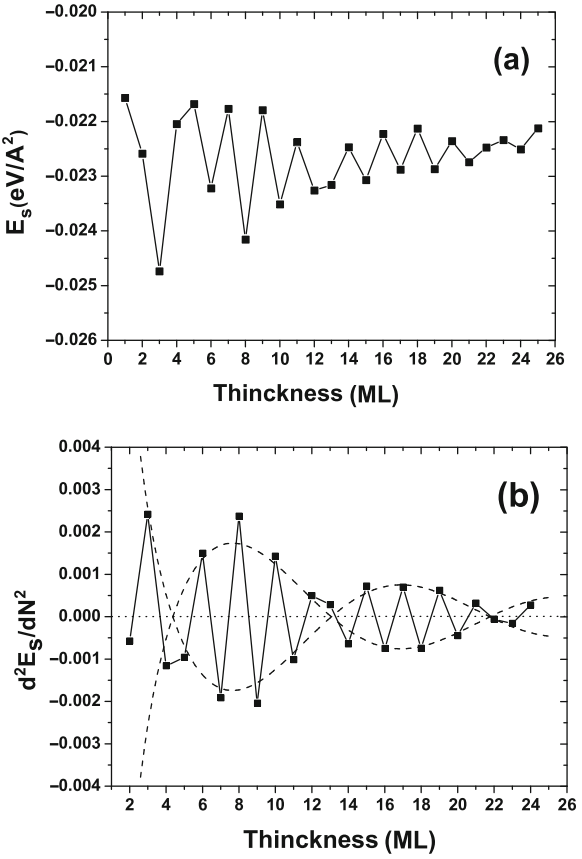

Fig. 4.9 **(a)** Surface energies of Pb(111) films on a Ge(111) substrate. **(b)** The second derivative of surface energy of Pb(111) films on a Ge(111) substrate

layers, and 23 monolayers, which are different from the freestanding case. From Fig. 4.9b it can be inferred that the films are stable at 3, 6, 8, 10, 12, 15, 17, 19, and 21 layers. This agrees almost perfectly with a recent experiment of Pb film growth on the Ge(111) substrate [8]. This indicates that our first-principles calculations have captured the essential physics.

4.4.3 Band Structure and Beating Phenomena of Pb(111) Films

To understand the magic stability of the Pb films, including the unique growth behaviors discussed above, the band structure of Pb films with different thickness is shown in Fig. 4.10. For s–p metals, the QWS is often described by (4.1). For a film with a thickness of N monolayer and interlayer spacing d (4.1) becomes

$$2kNd + 2\phi_s = 2n\pi \tag{4.6}$$

Using (4.6), one can calculate the periodicity for the QW states crossing the Fermi level, $\Delta N = \frac{\pi}{k_F d}$, where k_F is the Fermi wave vector. We use the value of $k'_F = 1.596\text{Å}$, which was obtained from the de Hass–van Alphen measurement [36, 37]. Since the energy band comes from band folding from the second Brillouin zone, we have $k_F = 2k_{BZ} - k'_F = 0.61\ \text{A}^{-1}$ and $\Delta N = 1.8$ ML, indicating the QWS crossing the Fermi level for every incremental increase in the film thickness of about 1.8 layers, which is consistent with the experimental finding of bilayer stability.

There exists a small difference between the $2k_F$ and the k_{BZ}, and this difference will accumulate as the film grows thicker, leading to the "beating effect." The beating period of the crossovers is then given by

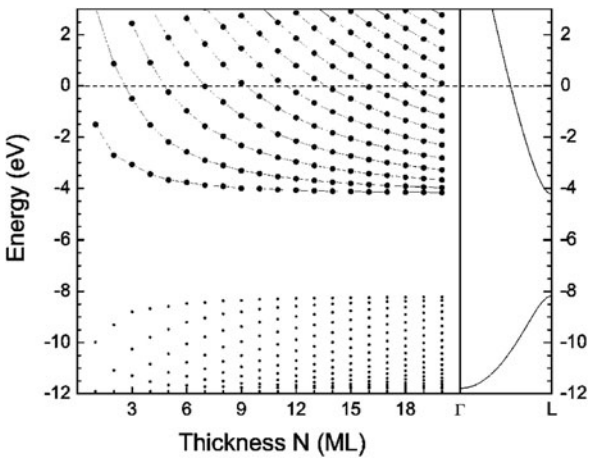

Fig. 4.10 Quantum well state energies as a function of Pb(111) layer thickness calculated at $\bar{\Gamma}$ using the local density approximation to density functional theory. The bulk energy dispersion is also shown. The *horizontal dashed line* indicates the Fermi level. Reproduced from [6]

$$\lambda_{\text{beat}} = \frac{\pi}{2k_{\text{F}} - k_{\text{BZ}}} \approx 9\,\text{ML} \tag{4.7}$$

The salient features of the re-entrant bilayer-by-bilayer mode are attributed to the quantum nature of the film stability, as confirmed quantitatively in DFT calculations disscussed above.

4.4.4 Transition from Smooth Film to Island Regime

The island morphologies can never be formulated as a unique, reversible, and path-independent function of deposition temperature, annealing temperature, and deposition amount, even though 2D flat-top objects do form at low deposition temperatures because of size quantization effects. The contact area between the islands and the substrate changes upon annealing whereas for a continuous film, the contact area remains preserved during the morphological evolution. Reduction of the surface energy upon creating taller islands should ultimately lead to 3D clusters in thermodynamic equilibrium [38]. Hence, the stability arguments presented for the case of a closed 2D morphology cannot be used here. At low temperatures, on the other hand, one can think of a local equilibrium concept where a number of nearby local energy minima may be accessible within the "attempt range" of the system. From this perspective, the gradual evolution of taller islands can be thought of as successive jumps over multiple energy barriers, each time reaching a lower point in the global energy landscape.

The demarcation between the low temperature quantum growth region and the high temperature thermodynamic limit is a delicate one. For the quantum regime, the local stability concept is better suited whereas at high temperature the global energy landscape must be used [21]. It is well known that deposition of Pb(111) at 150–220 K produces flat-top islands with fairly uniform heights [25]. The selected height can be tuned by changing the deposition or post-annealing temperature: the lower the temperature, the lower the average island height. The first selected height turns out to be 5 ML, then comes the 7 and 9 ML islands at elevated temperatures. Once the 5 (or 7 or 9 ML) high islands cover the whole surface, the growth continues in layer-by-layer or bilayer-by-bilayer fashion depending on the temperature [8]. This new growth mode, i.e., the initial formation of flat-top islands followed by 2D layer growth, has been explained in terms of *quantum phase separation* [22].

The roughening of initially flat continuous films (grown at very low temperature) upon warming is closely connected to this quantum phase separation: films deposited at 110–150 K exhibit some surface roughness because of the limited surface diffusion at low temperature. As the temperature is raised, the film first becomes smooth and then upon further annealing it will develop deep holes that go all the way down to the interfacial wetting layer (see Fig. 4.11). The ejected material from these holes accumulates around the holes, thus creating local areas of higher film thicknesses. Figure 4.11 shows the evolution of an initially 6.5 ML thick Pb deposit (wetting layer +5.5 ML) on a Si(111) 7×7 substrate, as seen with STM. Snapshots

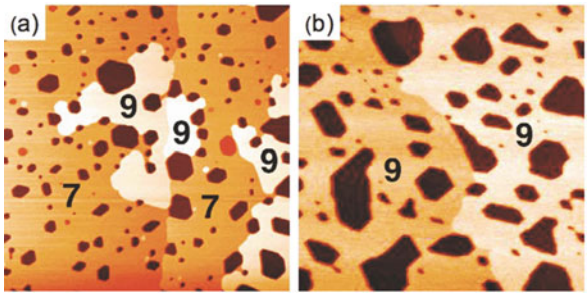

Fig. 4.11 $500 \times 500\,\text{nm}^2$ images showing the evolution of a predominantly 7 ML film into a 9 ML film upon thermal annealing. The nominal coverage is fixed. The initial deposition of 6.5 ML was done at 150 K. Both images show a substrate terrace passing through middle of the frames. (**a**) Image recorded at 225 K during the evolution. The 7 and 9 ML tall areas are indicated. Very few 5 ML speckles can be seen. (**b**) At 250 K, all the holes are 9 ML deep; the 5 and 7 ML tall areas no longer exist

were taken as the film thickness evolves from 7 to 9 ML. These thicknesses are measured from the wetting layer. While the 7 ML thick film evolves into a 9 ML thick film at 225 K, see Fig. 4.11a, the 9 ML film is still stable at 250 K (Fig. 4.11b). Also, it is known that the 5 ML film is significantly unstable compared to the 7 ML film on Si(111) 7×7 in close resemblance to reference [21]. In Fig. 4.11a, only a few small 5 ML thick speckles are left whereas they have totally disappeared in Fig. 4.11b. Although the films shown in these images are not closed, the enormous lateral size of the connected pieces validates the use of thin film stability arguments. The general trend is that thinner films break up at lower temperature as compared to the thicker films.

The above picture emphasizes once more the irreversible approach toward thermodynamic equilibrium, starting from quantum growth regime. This transition is a very complex issue and at this point we can only speculate as to how this might happen, as we will do in the following paragraphs. In this context, one report particularly caught our attention [39]: the authors of this study deposited 11 ML Pb onto the Si(111) $(\sqrt{3} \times \sqrt{3})R30^\circ$ − Pb surface (which can be viewed as a bulk truncated Si(111) surface terminated with 1/3 ML of Pb) at 110 K and monitored the film morphology with X-ray diffraction as they increased the sample temperature. The authors reported that at some particular temperature (280 K) the film reaches a particular local equilibrium at which the discrete second derivative of the thickness distribution, obtained from the X-ray data, correlates with the thickness-dependent surface energy. Figure 4.12 is replicated from this work and shows the fractional surface area covered with N monolayers. Based on the above discussion, the presence of a thickness less than 11 ML should not be expected, nonetheless their weight in the spectrum is significant. However, the statistical analysis given in this work, which correlates the height distribution to the surface energy, may be questionable because the authors used a local equilibrium (low temperature) argument at high temperature where mass transport takes place over several hundreds of nanometers.

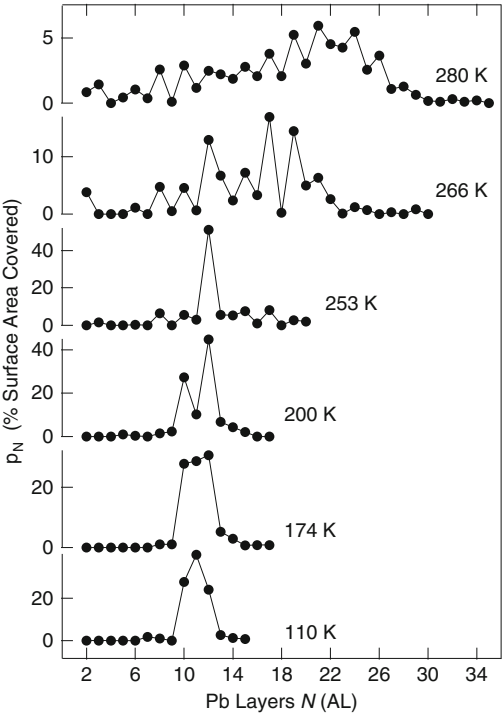

Fig. 4.12 Evolution of the Pb thickness distribution as a function of annealing temperature. Initial low temperature deposition of 11 ML Pb produces a narrow width distribution. The thickness distribution broadens at elevated temperatures [39]

Instead, it can be argued that one should consider the global energy landscape which includes the surface free energy of the island facets and that of the exposed wetting layer. Thus, one probably cannot expect to find a particular temperature where the calculated surface energy and experimental thickness distribution correlate over a nearly 30 ML wide thickness window. The explicit assumption that each particular film thickness is in local equilibrium with its neighboring thicknesses $N \pm 1$ may not be valid. This would imply that, e.g., 5-6-7 ML and 19-20-21 ML thick areas maintain their local equilibrium at the same temperature. However, the STM data indicate that once the tall 19-20-21 ML mesas come into being, the 5-6-7 ML thick areas are no longer in local equilibrium and do not exist. Instead, the statistical analysis should have indicated a trend toward 3D cluster formation.

4.5 Role of Friedel Oscillations in Thin Film Stability

So far QSE-related oscillations in film stability are reasonably well understood, some quantitatively, some still at a qualitative level. One particular question is why QSEs are so robust in Pb(111) films, affecting a thickness range more than 20 ML

in both experiments and first-principles calculations. Also, why is it not that robust in other crystal orientations of Pb, in Cu and Al films?

Vacuum and substrate interfaces at the thin film boundaries introduce steep discontinuity of the positive background charge. The collective screening response of the electron gas against this sharp discontinuity creates the well-known Friedel oscillations [18]. Nearly free electron calculations considered before have been carried out against a constant background and completely ignore the presence of the Friedel oscillations [27]. The wavelength of these oscillations is $\lambda_F/2$, which is incidentally the same key parameter in the free electron QSE. So, it is far from obvious how to extract the role of the Friedel oscillations in QSE .

To be more specific, according to free electron calculations, QSE should be washed out beyond 10–15 ML [27]. On the other hand, both experiments and first-principles calculations suggest that stability oscillations of the Pb(111) films last up to 25 ML or more [8]. The reason for this robustness of the apparent quantum size effect has remained a mystery for a very long time.

Conventionally Friedel oscillations decay according to $1/z^2$, where z is the depth measured from the interface. Recent DFT calculations [40] confirm this behavior for freestanding films of Pb(110), Pb(100), and Al(111). Pb(111) films, however, exhibit an unusual $1/z$ decay law. This guarantees the persistence of the $\lambda_F/2$ charge corrugation up to 25 ML or more. We also note that there are two sets of Friedel oscillations emanating from the two interfaces of the film. Direct evidence for the role of Friedel oscillations (at the DFT level) comes from the extraordinarily large lattice relaxation at the center of the film [40].

The $1/z$ decay law is expected only for quasi-1D electron systems, or equivalently flat Fermi surface segments. Indeed, recent DFT calculations show convincingly such Fermi surface nesting features along the Pb[111] direction [35, 40, 41], an intriguing property which merits further exploration.

4.6 Structural, Electronic, Physical, and Chemical Properties of Quantum Films

Thorough study of QSE is essential in understanding the various physical and chemical properties of thin metal films of few atomic layers thick and other nanostructures of comparable size. Furthermore, this detailed understanding makes it possible to use the QSE as a tuning knob to adjust some of the physical and chemical properties of quantum systems. In the rest of this work, we will give a brief overview of the QSE on lattice relaxations, work functions, superconductivity, and chemical reactivity. We will also briefly describe how such properties can be tunned via metal alloying in the quantum regime.

4.6.1 Lattice Relaxation

Abrupt termination of the crysal at the vacuum interface causes the well-known Friedel oscillations of the electronic charge density with the period of $\lambda_F/2$ or,

equivalently, $2k_F$, perpendicular to the film [20]. That means, the charge density close to the surface does not share the same periodicty with the crystal along the direction normal to the film. Hence, one would expect the ion cores at the top few layers to be displaced slightly with respect to bulk equilibrium positions [22, 42, 43]. This behavior is observed as bilayer oscillations in the atomic layer spacing d_{12} and d_{23} in Pb(111) films via LEED-IV (intensity versus electron energy) studies [42]. There it was shown that for a few selected Pb thicknesses the first layer spacing d_{12} (as counted from the surface) is contracted compared to its bulk value (d_{12} is negative) while the second layer spacing d_{23} is slightly expanded. Actually, these results are very similar to the relaxation of the top few layers of bulk Pb as expected from Friedel oscillations [43, 44]. On the other hand, QSE might add a thickness-dependent variation in the layer spacing to this picture due to confinement. This effect, however, turns out to be quite small and cannot be detected by LEED method due to limited probing depth.

Much larger relaxations have been reported based on HAS [34, 45, 46] and STM [24] measurements, with values up to -30% for d_{12} and $+15\%$ for d_{23} around the bulk equilibrium spacing [45]. Due to the nature of these techniques, however, the observed relaxations should be attributed to the strong electronic charge density variations around the vacuum boundary of the quantum well instead of the actual ion core displacemets.

Floreano et al. [46] have measured the atomic layer relaxations inside thin films with X-ray diffraction and X-ray reflectivity methods and concluded that the outermost layer d_{12} exhibits much smaller oscillations (about 5%) compared to those given by HAS measurements. Large number of parameters used in the fitting of their rod scans introduce limited confidence on the results. Czoschke et al. [42] have reduced the number of the parameters employing a theroretical model. They have calculated the derivative of the charge density $\partial\rho/\partial z$ inside the film using free electron model. Assuming the lattice displacements should be proportional to this gradient, they have obtained a displacement pattern to which the X-ray reflectivity data is to be fitted. The result obtained in this fashion for a 10 ML Pb film on Si(111) $\sqrt{3}\times\sqrt{3}R30^\circ-$Pb gave a d_{12} contraction of 9% (a 5% contraction was found for a 9 ML film (Chiang, Private Communication)). So, this model ends up with smaller relaxations compared to HAS and STM measurements, although 9% relaxation is still quite large. Although this model is physically intuitive and seemingly relevant, it is probably too simplistic. Not only the charge density in the film is model dependent but also the linear response of the ion cores to the charge density gradient is presumably not valid for the large relaxations obtained.

DFT calculations of ultrathin Pb(111) slabs on a variety of substrates confirmed the oscillatory nature of the interlayer spacing due to the $2k_F$ modulation of the charge density propagating into the bulk, as well as the superimposed oscillations as a function of thickness [9]. Figure 4.13 shows the interlayer relaxations Δd_{12} and Δd_{23} as a function of the Pb film thickness on a Ge(111) substrate [9]. The interlayer relaxation in a film of N monolayer is defined as $\Delta d_{m,m+1} = \frac{d_{m,m+1}-d_0}{d_0}\times 100$ ($d_{m,m+1}$ is the interlayer spacing between the m and the $m+1$ layers). The by now familiar oscillation pattern including the even–odd crossovers is clearly reproduced. DFT results show that the first interlayer spacing d_{12} is contracted by about 5.5%

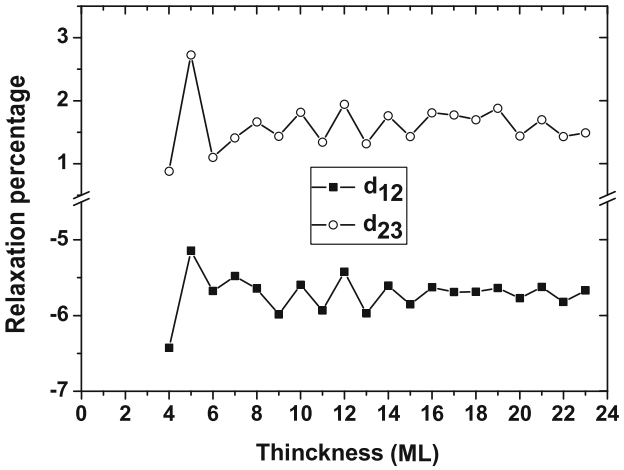

Fig. 4.13 Interlayer spacings Δd_{12} and Δd_{23} of Pb(111) films on Ge(111) substrate relative to bulk spacing. Reproduced from [9]

relative to the bulk value of the lattice constant while the second interlayer spacing d_{23} is expanded by about 1.5%. These results are in good agreement with the LEED measurements [47]. Note that the crossover positions of Δd_{12} and Δd_{23} are not the same as that of surface energy. Interestingly, the location of the even odd crossovers has shifted by a half beating period as compared to the even–odd crossovers in the corresponding surface energy $E_s(L)$, suggesting that the lattice relaxation depends on the thickness according to $\mathrm{d}E_s(L)/\mathrm{d}L$. This property is not yet fully understood.

4.6.2 Work Function

The work function (WF) is defined as the minimum energy required to remove an electron from the surface (see Fig. 4.14). The theoretical and experimental studies on the work function exhibit changes due to the alkali metal adsorption [48], crystallographic orientation [49], and the surface steps [50] and reveal that WF is related to the local density of states near the Fermi level. As we have discussed, the presence of QWS dramatically modulates the density of states at the Fermi level when the film thickness is varied. Therefore, one would expect to see thickness-dependent variations in the work function also.

Based on DFT calculations, Wei and Chou showed that, similar to the surface energy, the WF of freestanding Pb(111) films also reveals bilayer oscillations as a function of the film thickness [6]. Work function calculations for films on a Ge substrate have also been performed [9] and shown in Fig. 4.15. Bilayer oscillations are evident and even–odd crossovers exhibit ~9 ML periodicity similar to surface energy results. However, the location of the crossover points is phase shifted by half of a beating wavelength, similar to the behavior of the lattice relaxations.

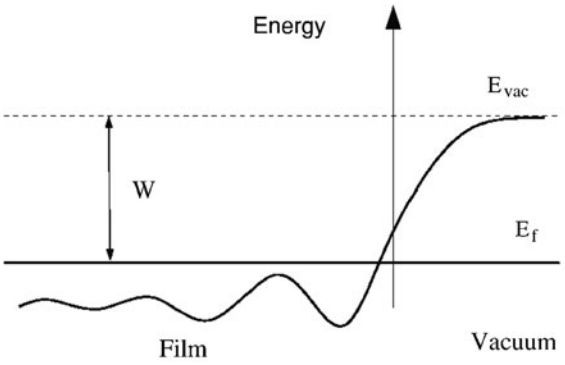

Fig. 4.14 Schematic drawing of energies at a film surface. The *solid curve* represents the electrostatic potential across the film surface. The oscillations in the potential are caused by the Friedel oscillations of the surface electron density. Its value deep in the vacuum side is usually called the vacuum energy

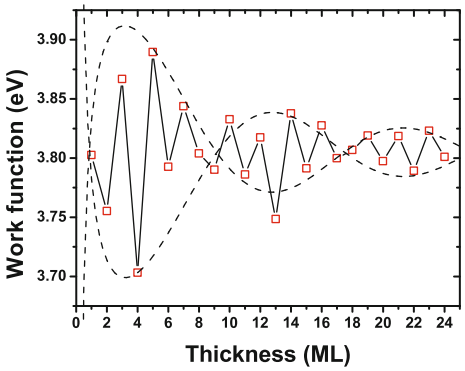

Fig. 4.15 The work function of Pb films as a function of thickness on Ge(111) $\sqrt{3} \times \sqrt{3}$ substrate

Experimentally, WF oscillations have been measured with scanning tunneling spectroscopy. Qi et al. [51] have investigated the thickness dependence of the WF on flat-top-wedged Pb islands using the STM and STS measurements. Figure 4.16a shows the STM image of a flat-top Pb island with thickness increasing from left (11 ML) to right (15 ML). The inset shows the atomically resolved STM image of the top (111) plane. Fig. 4.16b shows the cross-sectional profile along the line

Figure 4.16a, c, d shows the topographic and WF images of the island taken simultaneously. From the WF image, we can clearly see that even layers (12 and 14 ML) have larger work functions compared to odd layers (11, 13, and 15 ML). The tunneling current strongly depends on the tip–sample distance because of its dependence on the image potential. However, it can be shown that the quantity $\mathrm{d} \ln I / \mathrm{d}s$ is a constant to first approximation [52]. Hence, the work function can be determined from

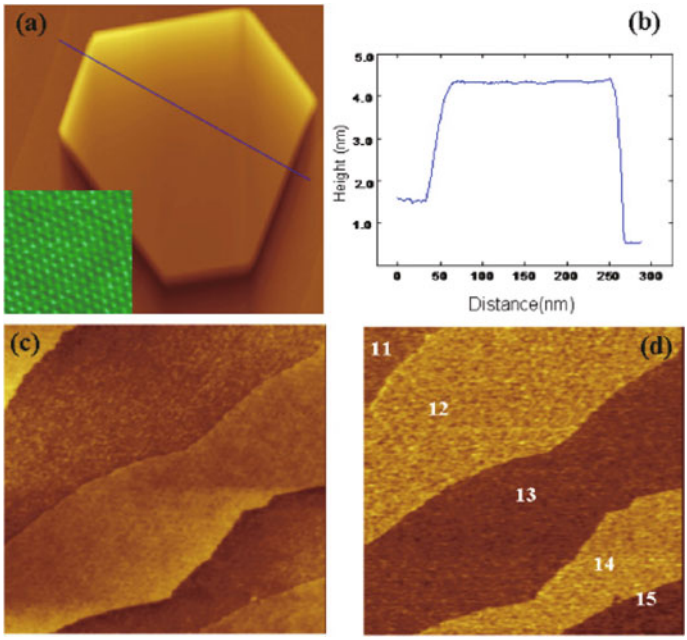

Fig. 4.16 **(a)** The STM image of a Pb island taken at $V = -0.8\,\mathrm{V}$ and $I = 0.1\,\mathrm{nA}$. Image size: $500 \times 500\,\mathrm{nm}^2$. Inset is a $5 \times 5\,\mathrm{nm}^2$ atomic resolution image $V = 0.4\,\mathrm{V}$, $I = 0.1\,\mathrm{nA}$. **(b)** A line plot along the *blue line* in **(a)** to show the height profile. **(c)** The topographic and **(d)** local work function images taken simultaneously $V = -2\,\mathrm{V}$, $I = 0.1\,\mathrm{nA}$. The *bright area* has a larger work function than the *dark area*. Image size: $337 \times 337\,\mathrm{nm}^2$

$$\phi \approx 0.95 \left(\frac{\mathrm{d} \ln I}{\mathrm{d}s} \right)^2 \tag{4.8}$$

and experimentally obtained via modulated tip sample distance.

Figure 4.17 shows the WF obtained by this method for a thickness range from 11 to 34 ML. As seen in this figure, the WF is larger for the even layers compared to the odd layers when N is between 11 and 17 ML, whereas the reverse occurs when N is between 19 and 26 ML and so on. Overall, the bilayer oscillations of the WF are concomitant with an envelope function of beating at approximately 9 ML. The measured oscillatory periodicity and beating behavior show quite reasonable agreement with theoretical prediction [9].

Here we note that the similarity between the thickness dependences of the work function and the calculated lattice relaxation. They both exhibit even–odd crossover points at similar thicknesses. This behavior can be understood based on the charge spilling from the quantum well: higher the dipole moment because of the larger charge spill, higher the work function. This larger charge spill would also reduce the d_{12} layer contraction as compared to the d_{12} contraction of a bulk Pb(111) crystal.

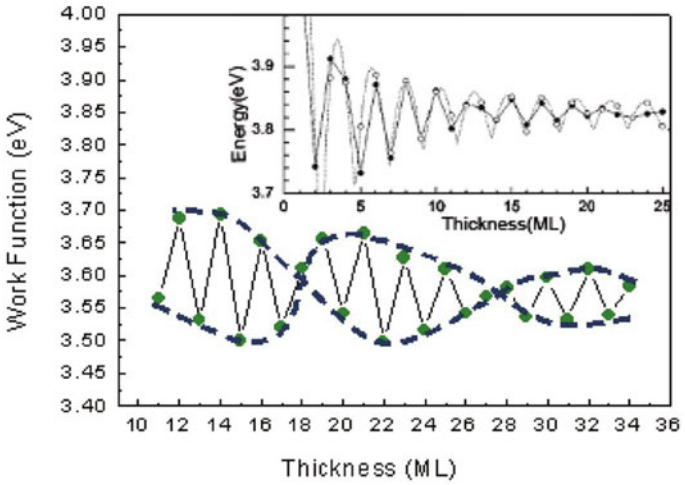

Fig. 4.17 Work function of Pb(111) films measured as a function of film thickness. Reproduced from [51]

So, the connection between work function and surface relaxation is established (Fig. 4.18).

Why the surface energy exhibits a different beating pattern compared to work function and lattice relaxations is not that transparent. According to Jellium calculations by Schulte, the charge spilling is minimum when a 2D subband is just touching the Fermi sphere and it exhibits a maximum when the Fermi level is located in the middle of the highest occupied and the lowest unoccupied subbands at Γ [18]. This largest charge spilling case coincides with a local minimum of $E_s(L)$. Therefore one tentatively would expect $E_s(L)$ and work function to oscillate in phase. However, the Fermi energy also oscillates as well as the dipole strength. So, these two phenomena are entangled to each other and the physics of the beating would be revealed after a self-consistent treatment of the problem. Apparently, the result of such an analyses turns out to be a phase shift of about 4–5 ML, i.e., half of a beating wavelength.

Very recently, Miller, Chou, and Chiang presented an analytic derviation and numerical examples for the phase relations and the beating functions in terms of subband crossing of the Fermi level. Based on the standard quantum well model [33, 54, 55], one can derive the following central equations for the chemical potential μ and surface energy per unit area E_s:

$$\frac{1}{N^2}\frac{d}{dN}(N^2\mu) = \frac{3\rho}{ND(\mu)} \tag{4.9}$$

$$\frac{1}{N^4}\frac{d}{dN}(N^4 E_s) = \frac{3}{2}\rho(\mu - \mu_{\text{bulk}}) \tag{4.10}$$

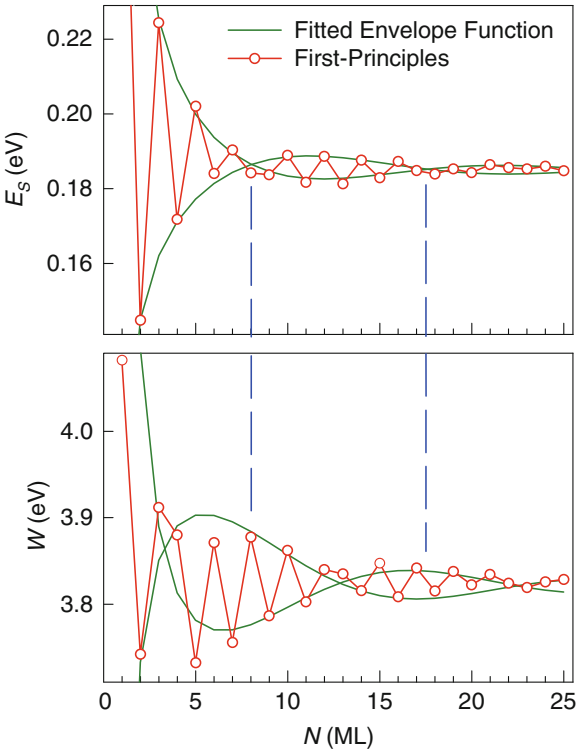

Fig. 4.18 Surface energy E_s per surface atom and work function W as a function of thickness N of freestanding Pb(111) films from a first-principles calculation. Also shown are envelope functions derived from a model fit to highlight the beating patterns. The two *vertical lines* are lined up with two adjacent nodes in E_s and highlight the out of phase relationship between the envelope functions of E_s and W. Reproduced from [53]

where N, ρ, and $D(\mu)$ are the film thickness, the electron density, and the density of states per unit volume at the chemical potential, respectively. μ_{bulk} is the bulk chemical potential. Equations (4.8) and (4.9) indicate that the rate of change of the chemical potential for increasing N is related to the inverse of the density of states at the chemical potential, and the rate of change of the surface energy is related to the chemical potential.

The numerical results for Pb(111) are shown in Fig. 4.19. The top panel shows the evolution of the quantized electron structure E_n. The subbands cross μ with a period of $\Delta N = 0.7\,\text{ML}$; the crossings are marked by the vertical dashed lines. The second panel shows $D(\mu)$. Each subband has a constant density of states, and the total density of states is a series of steps. Upon normalizing by the volume, it becomes a series of diminishing sawteeth. The third panel is $D(\mu)^{-1}$. The next panel displays the work function relative to the bulk limit: $\Delta W = -\Delta\mu \equiv \mu_{\text{bulk}} - \mu$. The bottom panel displays E_s. Clearly, the oscillations in surface energy lead the oscillations in the work function by 1/4 of a thickness period.

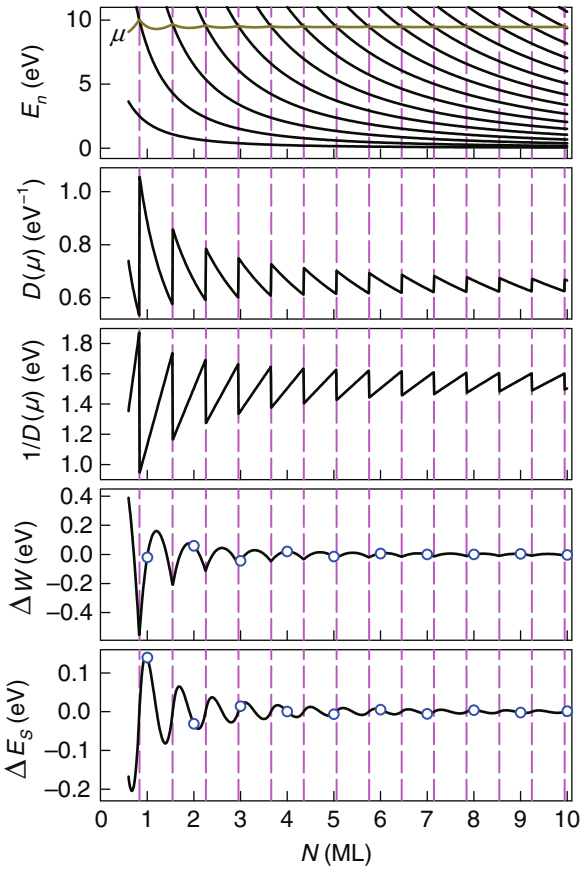

Fig. 4.19 The numerical results of surface energy and work functions from a quantum well model calculations. Reproduced from [53]

4.6.3 Localized Surface Phonons and Electron–Phonon Interaction

Electron–phonon coupling is an important factor that determines the superconductivity of a material. For a conventional superconductor such as Pb, the effective electron–electron attraction necessary for the binding of cooper pairs is ultimately governed by electron–phonon coupling [56]. The formation of QWS strongly modifies the mechanical stability of the films, as reflected by the expansion and shrinkage of interlayer spacing [57]. Both of the factors speak directly to the possibility of modulating electron–phonon coupling and thus superconductivity of the Pb films.

Zhang et al. studied the interaction of electron–phonon coupling in Pb films with different thickness by using the variable temperature ARPES spectra and temperature-dependent PES [58]. The temperature-dependent PES for the 23 and

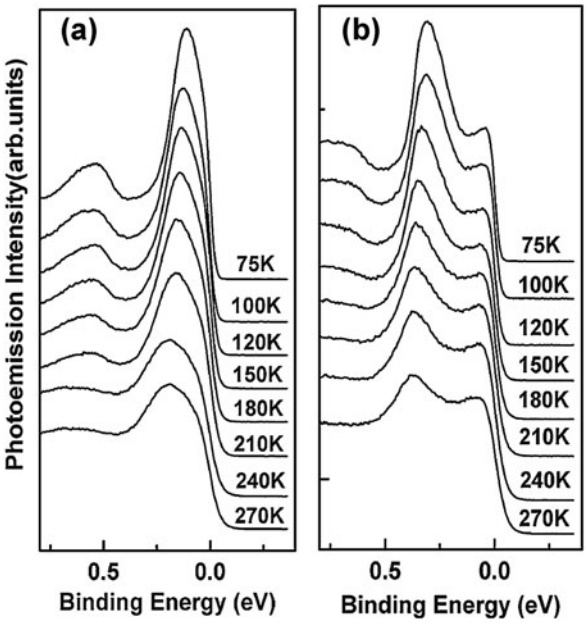

Fig. 4.20 Temperature-dependent photoemission spectra of Pb films for **(a)** 23 ML and **(b)** 24 ML collected within a temperature range of 75–270 K. The *vertical dashed lines* reveal the variation of the QWS binding energy as the film temperature is changed [58]

24 ML films is shown in Fig. 4.20a and b. These results show that, with increasing substrate temperature, the peak position of the QWS shifts toward higher binding energies while the peak widths broaden. To find out the exact relation between the line width (ΔE) of the QWS and the temperature, a curve fitting by Voigt line shape was made. The fitting results are plotted in Fig. 4.21a for the films of 22 and 23 ML, where ΔE increases linearly with increasing temperature and exhibits prominent different slopes for the adjacent layers. The relation between this slope and the electron–phonon coupling strength, λ, is

$$\lambda = \frac{1}{2\pi k_{\mathrm{B}}} \frac{\mathrm{d}\Delta E}{\mathrm{d}T} \tag{4.11}$$

The λ values derived from the QWS peaks for different thicknesses are shown in Fig. 4.21b (triangles), where only the values for stable layers (15, 17, 19, 21, 22, 23, and 24 ML) are plotted. Besides an overall gradual increase of λ toward the bulk value (1.55), an oscillation of λ with a period of 2 ML is clearly noted from 21 to 24 ML.

Theoretically, Yndurain and Jigato [59] recently do the DFT calculations to investigate the surface phonons and electron–phonon interaction. Zero parallel momentum phonon modes for Pb(111) freestanding slabs of widths ranging from

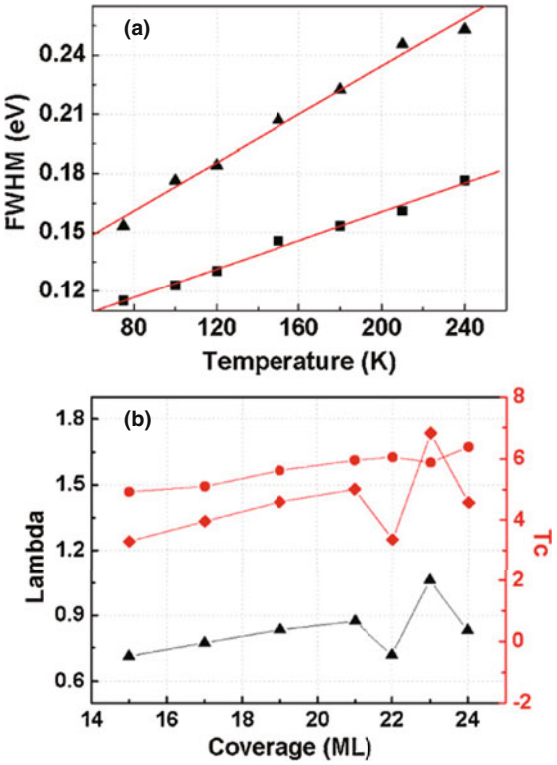

Fig. 4.21 **(a)** Lorentzian peak widths of the QWS of the 22 ML (*square*) and 23 ML (*triangle*) films plotted as a function of temperature. **(b)** Measured λ (*triangles*) and calculated superconductivity transition temperature (*diamonds*). Reproduced from [58]

3 to 14 layers are calculated and the results are shown in Fig. 4.22. From Fig. 4.22, one can see that both longitudinal and transverse surface modes take place at energies above the corresponding bulk values due to a 6% contraction of the surface layer (see Fig. 4.13). A bilayer oscillatory variation of both surface states is found, being more pronounced for the longitudinal modes than in the transverse ones as expected due to their different characters. It is expected that, like the surface energy, there should be one crossover among these layers with a beating period of 9 ML. However, the beating effect is not found in the DFT calculations. More theoretical studies are needed to reconfirm this.

4.6.4 Thermal Expansion

Temperature dependence of the PES spectra width was used to investigate many-body effects with regard to electron–phonon coupling. The peak positions, i.e., the binding energies of the QWS in the temperature-dependent spectra, could be used to understand the thermal expansion behavior of the thin films. From this dependence,

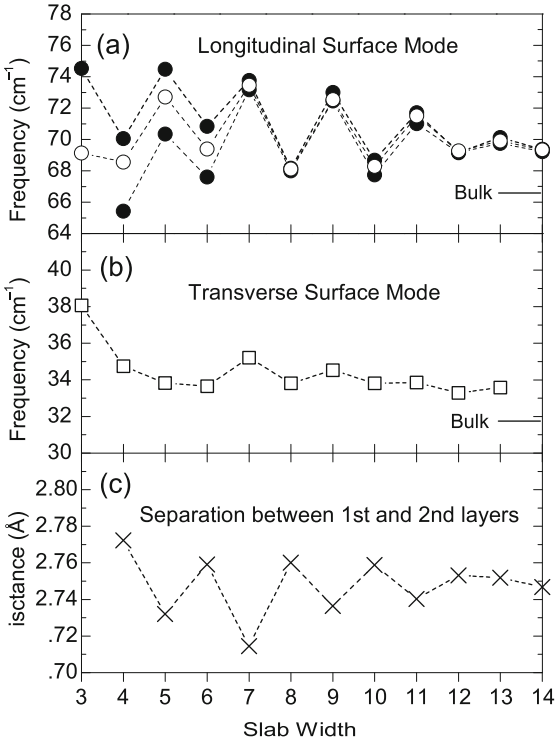

Fig. 4.22 Frequencies of localized surface phonon modes at $k_{\parallel} = 0$ for different slab thicknesses. Panels (**a**) and (**b**) stand for longitudinal and transverse modes, respectively. In both cases the highest corresponding bulk mode frequency is indicated. In panel (**a**) the results considering the cases of both slab's ends free (*bold symbols*) and fixing one while leaving the other one free (*open symbols*) are shown. Panel (**b**) stands only for the case of one slab's ends fixed. Panel (**c**) shows the contraction of the outermost layer

one could deduce the thermal expansion coefficients of the Pb films of different thicknesses along the film normal direction.

Shown in Fig. 4.20 are the temperature-dependent photoemission spectra of 23 ML (Fig. 4.20a) and 24 ML (Fig. 4.20b) Pb films by Zhang et al. [58]. From the spectra, the film morphology assumes an atomically flat surface over a macroscopic scale. Again, the strongest peaks correspond to the highest occupied QWS. Note that for both films including other films studied, the QWS peaks shift always toward higher binding energy with increasing substrate temperature. Furthermore, a dramatic difference between even and odd Pb layers can be clearly detected.

To quantify the results, the temperature dependence of the QWS binding energy for several Pb films is fitted linearly and shown in Fig. 4.23a. While the increased binding energy of the QWS in Ag/V(100) system was explained as that the energy of the QWS decreases more than the Fermi energy of the substrate, it could be attributed to a different reason, namely the thermal broadening of the confinement

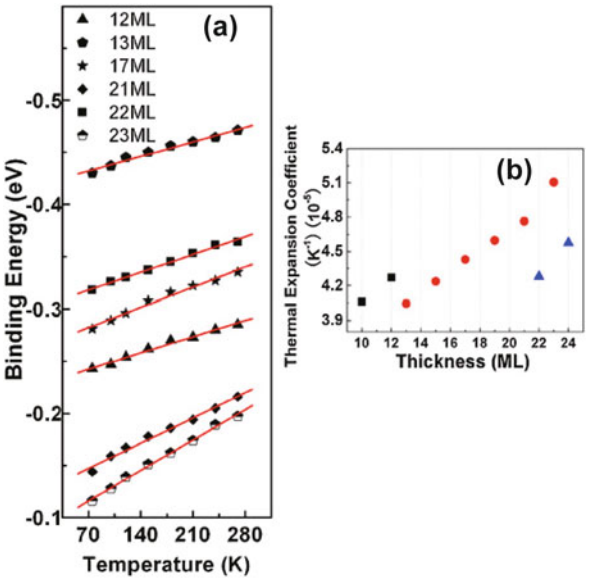

Fig. 4.23 (*Color online*) **(a)** Binding energy of the QWS plotted as a function of temperature. The *dots* and *lines* indicate the experimental data and linear fits, respectively. (**b**) Thermal expansion coeients of the Pb films along the confined direction calculated with the proposed model

well width, in addition to variation of the Fermi level of Pb films. For Pb/Si(111), when temperature (T) increases, E_F of the Pb film drops much more than E_F of Si does due to the dramatic difference in their thermal expansion coefficients, so there is a charge transfer from Si to the Pb film. These charges only stay at the Pb–Si interface (no charge is expected in the Pb film), which shift up all energy levels equally of the Pb film until $E_F(\text{Pb}) = E_F(\text{Si})$ is satisfied. Therefore, the Fermi energy of Si and its change have minor effect on the relative shift of the QWS in the Pb film. Within a simple free electron approximation, the temperature-dependence of the Fermi energy of a bulk material is described as

$$\frac{dE_F}{dT} = -2E_F\alpha_r \tag{4.12}$$

where α_r is the linear thermal expansion coefficient of the material, and E_F is its Fermi energy relative to the bottom of valence band. For the thermal-induced shift of the substrate Fermi level, α_r can be selected as $2.8 \times 10^{-6}\,\text{K}^{-1}$ (the bulk value). As for the thermal-induced shift of the QWS energy, such approximation should be reasonable regarding to the fact that the QWS energies of the Pb films involved are within a small energy window of 0.6 eV below the Fermi level, which has been successfully used to determine the Pb band structure. The thermal-induced shift of the QWS energy (E_{QW}) with respect to the bottom of valence band has the following form where α_Z is the linear expansion coefficient along the confined direction:

$$\mathrm{d}E_{\mathrm{QW}} \big/ \mathrm{d}T = -2E_{\mathrm{QW}}\alpha_{\mathrm{Z}} \tag{4.13}$$

The linear thermal expansion coefficients of the Pb films in the confined direction were calculated by the experimental thermal shift of QWS binding energy in terms of (4.11) and (4.12), and the results are shown in Fig. 4.23b. Several observations can be made as follows: (1) the thermal expansion coefficients in the film normal direction are greatly enhanced compared to the bulk Pb; (2) there is a 2 ML oscillation for the Pb films from 21 to 24 ML; (3) the overall trend is that a lower expansion coefficient corresponds to a film with a higher QWS binding energy. Since the thickness of the Pb films is very small, the linear expansion coefficient in the film plane (*xy*-plane) should be very closed to that of bulk Si, while in *z*-direction, a great enhancement can be expected because of what called Poisson effects and that the linear expansion coefficient of Si ($2.8 \times 10^{-6}\,\mathrm{K}^{-1}$) is one order of magnitude lower than that of Pb($2.89 \times 10^{-5}\,\mathrm{K}^{-1}$). To understand the global enhancement of the linear thermal expansion coefficient along the confined direction, we use α_{r}, α_{P}, and α_{Z} to describe the linear expansion coefficient of the freestanding film, the confined film in the film plane, and the film normal (z) direction, respectively. α_{Z} can be expressed as

$$\alpha_{\mathrm{Z}} = \alpha_{\mathrm{r}} + \frac{2(\alpha_{\mathrm{r}} - \alpha_{\mathrm{P}})\eta}{1 - \eta} \tag{4.14}$$

where η is the Poisson ratio. Substituting α_{r} and α_{P} by the linear expansion coefficients of bulk Pb and bulk Si, respectively, and taking η as the Poisson ratio of bulk Pb(0.44), we obtain α_z that equals $2.414\alpha_{\mathrm{r}}$. That means, in an ideal case, the thermal expansion in *z*-direction should be enhanced by 2.414 times of the bulk value, which is adequate to explain the global enhancement of the experimental data in Pb/Si(111).

4.6.5 Superconductivity

Advances in the thin film growth via QSE also prove to be essential to study the superconductivity in 2D geometry. Because the normal state resistance is a critical factor in destruction of the superconductivity, excellent film quality is required to investigate the inherent physics of low-dimensional superconductors [60]. For example, when the normal state resistance reaches the quantum resistance for the Cooper pairs, the superconductivity disappears [61]. While the normal state resistance was the control knob in the earlier studies of the thin film superconductivity, atomically smooth films achieved in the quantum growth regime render the film thickness as the well-controlled fundamental parameter [12–14]. Indeed, it is already known that the boundary scattering sets the limit of the resistivity at low temperatures [62, 63].

Various groups have measured the superconducting transition temperature T_{C} of Pb films and Pb islands employing various methods such as contactless mag-

netization [14], DC transport [12], and superconducting gap measurements [13]. Macroscopic coherence is obtained from the first two methods (Fig. 4.24), whereas the gap measurements give the local character of the superconductivity (Fig. 4.25).

Ozer et al. [14, 15] employed the superconducting quantum interference device (SQUID) to measure the superconductivity. This method eliminates the electrical contact issues because the measurements are performed inductively. On the other

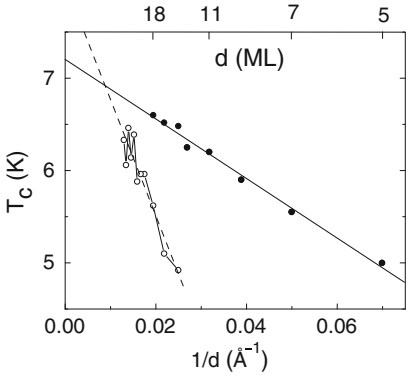

Fig. 4.24 T_C of Pb(111) films as a function of inverse film thickness. *Filled dots* show the magnetic measurements [14]; *open circles* correspond to transport measurements [12]

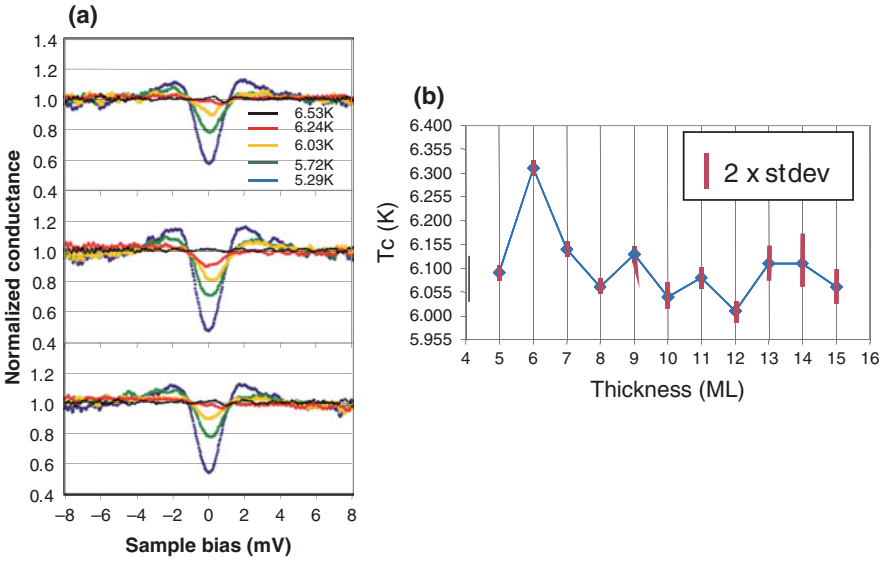

Fig. 4.25 T_C measurements from the opening of the superconducting gaps in scanning tunneling spectroscopy. (**a**) Gap of 5, 6, and 7 ML thick Pb films at various temperatures. (**b**) T_Cs obtained from the gap measurements in panel (**a**). Reproduced from [13]

hand, these measurements have to be carried out ex situ. This requires a protective cap layer to be deposited, which potentially can affect the superconducting properties. Also, in order to pick up a measurable magnetic signal, the macroscopic coherence must be established over all sample. DC transport measurements, however, detect the onset of the superconductivity via establishement of a single filamentary supercurrent.

Magnetic data in Fig. 4.24 exhibit a clear $1/d$ dependence of T_C, which can be explained in terms of the suppressed order parameter close to the film boundaries according to Simonin's theory [64]. Possible bilayer T_C oscillations cannot be seen in this data set because only the stable thicknesses dictated by QSE and separated by 2 ML have been prepared. T_C values extrapolate to 7.2 K in the bulk limit which is the true bulk value. Same $1/d$ thickness dependence of T_C is observed also for Pb–Bi alloys films. $Pb_{89}Bi_{11}$ and $Pb_{80}Bi_{20}$ films exhibit extrapolated bulk T_C values of 7.69 and 8.05 K, respectively [31, 65]. Same figure also shows the transport measurements with monolayer resolution indicating that most of these films were grown in the classical layer-by-layer growth regime. In this data set, bilayer oscillations of T_C are evident and it can be explained by oscillating density of states and/or electron–phonon coupling due to QSE [12].

We note that the magnetic and transport data show significantly different slopes in these T_C versus $1/d$ plots. Only the magnetic data extrapolate to the correct bulk value. Metalic Au protective layer employed for transport data may cause this difference because of a possible proximity effect. Note that amorphous Ge layer was used to protect the samples prepared for magnetic measurements. In situ superconducting gap measurements [13] shown in Fig. 4.25 exhibit another contrast quite different in character: this time T_C does not exhibit a significant thickness dependence and bilayer oscillations depicted in the figure are much smaller than those observed in transport measurements. This radically different behaviors may be due to the fact that magnetic and transport measurements rely on the establishement of the macroscopic coherence, i.e., they are sensitive to both amplitude and phase of the order parameter. On the other hand, *local* scanning tuneling spectroscopy (STS) measurements detect only the amplitude of the order parameter.

A recent study reported superconducting gap opening in 2 ML thick Pb films [66, 67]. This is interesting because in a 2 ML Pb film, only one 2D subband is allowed to exist due to the relation $3\lambda_F/2 \approx 2$ ML. Also, this work reports two different T_C values for 2 ML films residing on phase separated $\sqrt{3} \times \sqrt{3}$ and 1×1 substrate reconstructions. This last point shows the effect of the interface on the thin film superconductivity.

Film morphology obtained by quantum growth also allows the incorporation of nanostructures into the picture providing a control knob of some superconducting parameters [15]. STM images of 9 ML thick Pb films are shown in Fig. 4.15. In these images, slight overdose of Pb causes 2 ML tall mesas (a) and slight underdose of Pb creates 2 ML deep voids (b) as dictated by QSE (see Sect. 4.4.1). Pb is a type I supeconductor in bulk form; however, it becomes type II character below a crtitical thickness of ~250 nm [68]. As a result, magnetization loops show strong hysteresis as shown in Fig. 4.15c, d. Wide-open loops, belonging to the films with

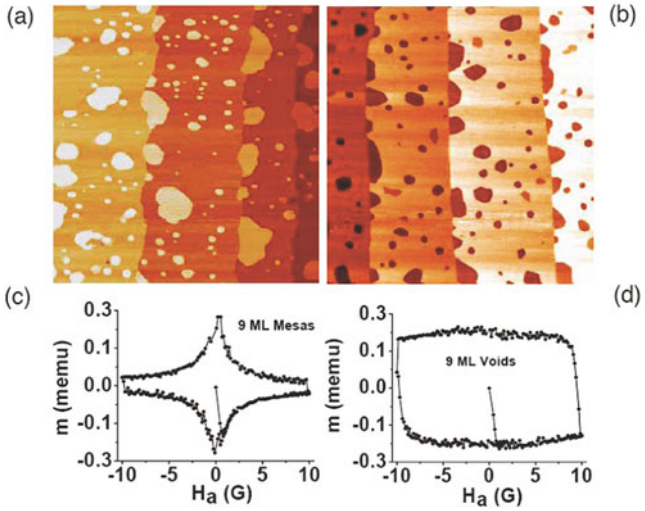

Fig. 4.26 $700 \times 700\,\text{nm}^2$ STM images of Nano-patterned 9 ML Pb(111) films and the corresponding hysteresis loops. **(a)** Film with 2 ML tall mesas, **(b)** film with 2 ML deep voids, **(c)** hysteresis loop of film with mesas, and **(d)** hysteresis loop of film with voids. For both samples, the lateral area is $3 \times 3\,\text{mm}^2$ and the magnetic data are taken at 2 K. Reproduced from [15]

voids, are due to strong flux pinning inside these blind holes and directly related to roboust superconducting current density, J_C, which reaches as high as 10% of the theoretical depairing density. Also, this reference gives a simple model to calculate J_C based on pinning properties of the voids (Fig. 4.26).

4.6.6 Surface Reactivity

QSE also plays an important role in the surface reactivity. Au is the most nobel element, still it becomes reactive at the nanometer scale [69]. In recent years, many experimental results have been published showing strong QSE modulations on ultrathin metal films [10, 11, 30, 70–73]. For example, Bartynski et al. reported thickness-dependent oscillations in the CO desorption from Cu films [11]. These oscillations were correlated with 2D subbands crossing the Fermi level periodically. Similarly, oxidation rate of ultrathin Mg(0001) exhibits oscillations as the film thickness is varied (Fig. 4.27) [10]. Maximum oxidation rate is achieved when a new quantum well state crosses the Fermi energy with increasing film thickness. These strong oscillations are related to the oscillatory decay lengths of the quantum well states, which affects the work function and electron transfer between the metal substrate and the anti-bonding orbitals of the incoming O_2. Hence, the dissociation barrier and initial oxidation rate are ultimately controlled by QSE. Also, first-principles calculations were supplied to verify the validity of this basic mechanism [10].

Recently, STM observations of an oxidized Pb mesa in the quantum regime brought the most direct proof of the thickness modulated adsorption and reactivity

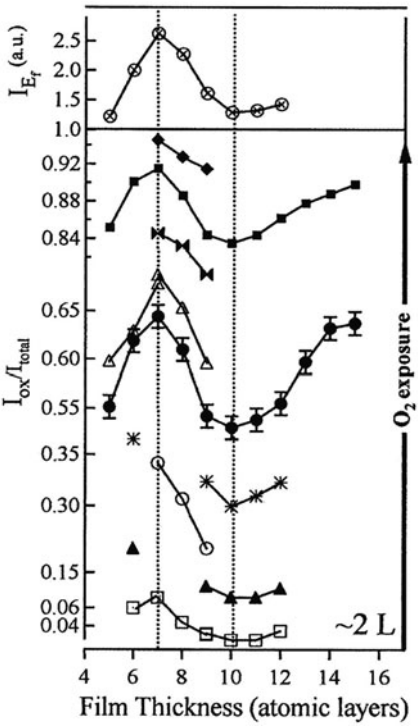

Fig. 4.27 *Lower panel*: plots of the Mg 2p oxide component in X-ray photoemission spectroscopy (XPS) as a function of film thickness obtained in several experimental runs. Data with the same symbol correspond to the same O_2 exposure. *Upper panel*: photoemission intensity at the Fermi level. The observed tuning of the oxidation rate is directly correlated with the oscillations in the density of states at the Fermi level, due to the QSE. The oscillatory reactivity has been attributed to oscillatory dissociation barriers [10]

[30]. Fig. 4.28a shows the STM image of a flat-top Pb mesa grown on Si(111) 7×7 surface which accomodates Pb thicknesses between 10 and 16 ML due to stepped substrate structure ($600 \times 600\,\text{nm}^2$ image). Panel (b) shows the cros section of this mesa. Panel (d) shows the STM image of the thickness-dependent contrast developed after 60 L oxygen exposure at 100 K substrate temperature. From 9 to 12 ML thick regions are labeled on the image. Bright spots are the chemisorbed oxygen clusters with a typical size of 1.2 nm. Although the crystal orientation is the same Pb(111) for all the thicknesses, oxygen adsorption on even layers is clearly larger than that on the odd layers. This behavior is consistent with the aforementioned quantum electronic struture and local work function of the mesa [51]. Oxidation occurs at room temperature with additional oxygen exposure of 120 L. This process again turns out to be thickness dependent and shown in panel (e). Panel (f) is a close up to the PbO nanocrystals.

So, both adsorption and oxidation are strongly enhanced when the Pb thickness is an even number of atomic layers. Quantitative analyses of the adsoption coverage

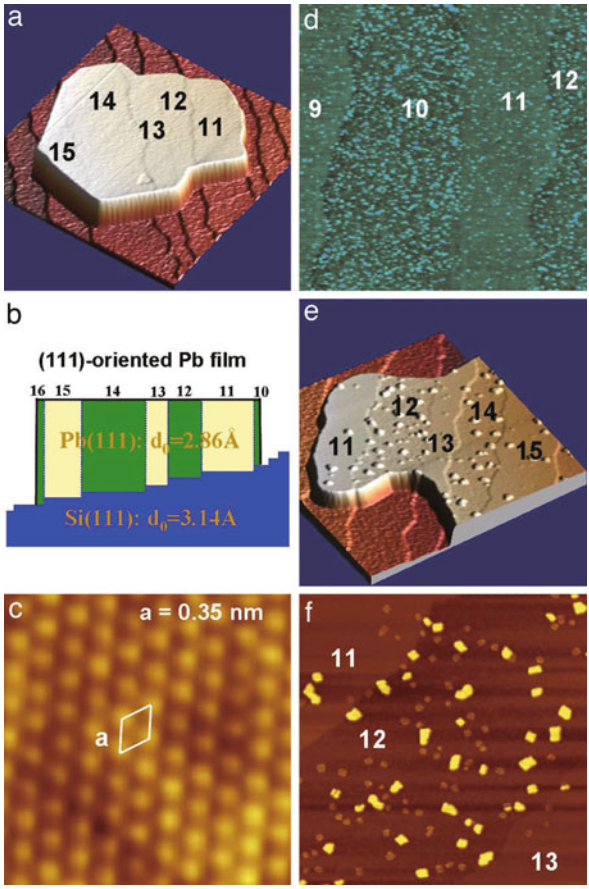

Fig. 4.28 (**a**) STM image of an atomically flat Pb mesa on a stepped Si surface. The *numbers* indicate the local thickness of the mesa in atomic layers. (**b**) Schematic cross section of the mesa. (**c**) Atomic resolution image on top of the mesa, revealing a Pb(111) orientation. (**d**–**f**) STM images during the various stages of adsorption and oxidation, as described in the text. Notice the contrasting behavior of the even and odd layers. Reproduced from [30]

indicate that the adsorption energy differs by about 9 meV between 10 and 11 ML films. In temperature scale this correspond to about 100 K difference between two adjacent thicknesses.

Local density of states (LDOS) and adsorption are shown to correlate in Fig. 4.29. The familiar crossover between even and odd layers takes place at around 17 ML as expected from the same behavior of charge spill and work function. The correlation between the thickness-dependent LDOS and adsorption is explained in the framework of Newns–Anderson adsorption model [30, 74]: the chance of hybridization between the s–p band of the Pb surface and the antibonding π^* state of O_2 is increased if the LDOS is higher. An STS study of quantum well states is also supplied by this reference. However, the correlation between the location of quantum

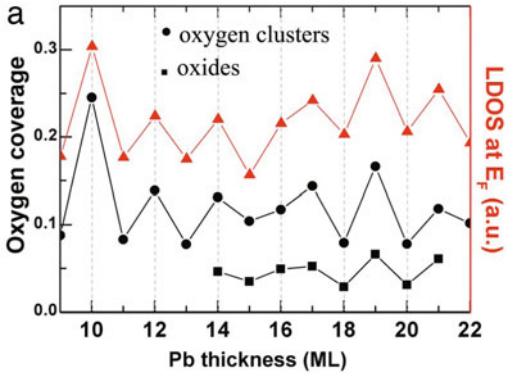

Fig. 4.29 Oxygen coverage in relation to local density of states at the Fermi level. *Black dots* show the oxygen clusters and *black squares* show the oxide coverage as defined in [30]. *Red triangles* show the local density of states. Reproduced from [30]

well states with respect to Fermi level and LDOS shown in Fig. 4.18 does not agree with the first-principles calculations given by [13].

4.7 Tuning the Quantum Stability Via Alloying

4.7.1 Stability of PbBi Alloy Films

In Pb(111) films, the periodic interruption of the bilayer growth follows a well-defined beating pattern with 9 ML, which is due to the fact that λ_F and d are not exactly commensurate (see Sect. 4.3). This suggests the possibility of altering the quantum growth mode by tuning the Fermi wave vector k_F via doping [31]. According to the free electron model, the Fermi wave vector is given by $k_F = (3\pi^2 n)^{1/3}$, where n is the electron density. Bi has five valance electrons whereas Pb has four. Therefore, the free electron density of a $Pb_{0.89}Bi_{0.11}$ alloy film increases by about 3% compared to pure Pb. This in turn increases the Fermi wave vector by 0.9% and, consequently, the associated beating period becomes 12.7 ML. The strong dependence of the beating wavelength on carrier density is due to the fact that k_F is very close to the middle of the second Brillion zone.

Figure 4.30 shows the STM images of $Pb_{0.89}Bi_{0.11}$ thin film alloys for various thicknesses. The alloy films exhibit a re-entrant bilayer-by-bilayer growth mode [31]. The observed stable thickness sequence is 4-6*7-9-11-13-15-17-19*20 . . . ML, where * indicates the even–odd crossover (this and all layer counts exclude a 1 ML thick wetting layer; see [24]), the period of the even–odd crossovers is ∼13 monolayers. Alloy films with higher Bi concentration ($Pb_{0.80}Bi_{0.20}$) do not exhibit quantum growth anymore and simply follow classical layer-by-layer growth throughout the entire thickness range. This indicates that excessive scattering washes out the QSE.

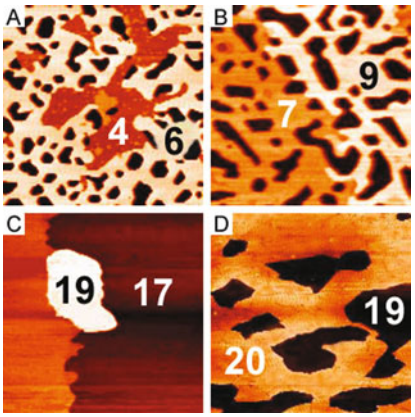

Fig. 4.30 STM images revealing the quantum growth mode of $Pb_{0.89}Bi_{0.11}$ alloy films, with bilayer growth (**a**) for 4 and 6 ML thicknesses and (**b**) for 7 and 9 ML thicknesses. In these images, the *black pores* are uncoated regions extending down to the substrate; in films used for study of superconductive properties, we verified the films to be simply connected and fully covering the substrate. Image (**c**) shows bilayer growth in a thicker film (also with a 1 ML terrace from the substrate), while (**d**) illustrates single layer growth near the even–odd crossover thickness. Reproduced from. [31]

DFT calculations for different Bi doping concentrations of $Pb_{1-x}Bi_x$ alloy films have been carried out [31, 75]. Figure 4.31 shows the surface energy of Pb_{89} Bi_{11} alloy films as a function of thickness for both freestanding films and films on a rotated Si(111) substrate. Note that for calculations performed on the substrate, both the beating periodicity and the location of the even–odd crossovers are in excellent agreement with the experimental result. Further calculations have been carried out

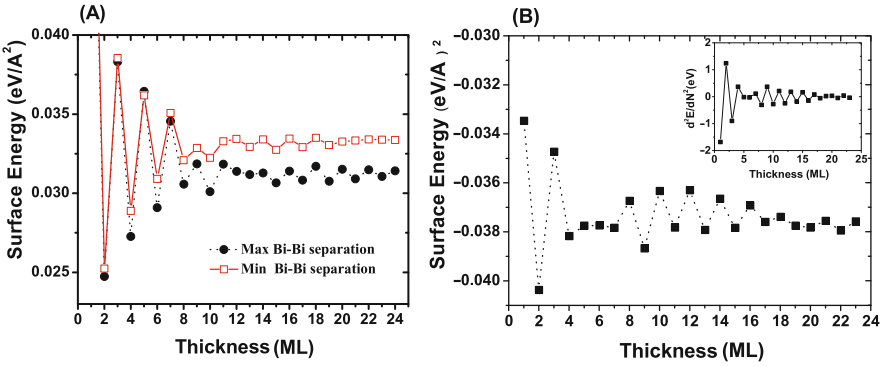

Fig. 4.31 (**a**) Surface energy of a $Pb_{0.89}Bi_{0.11}$ freestanding alloy slab obtained from first-principles DFT calculations. The *black curve* (*circles*) represents the surface energy for maximum Bi–Bi separation (within the constraints of a supercell calculation). The *red curve* (*squares*) represents the surface energy of a slab in which Bi atoms all have Bi nearest neighbors in the adjacent (111) layers; (**b**) surface energy of a $Pb_{89}Bi_{11}$ thin film alloy on a Si(111) substrate together with the second-order derivation of surface energy as a function of thickness (inset). Reproduced from [31]

for different Bi concentrations [75]. $Pb_{0.86}Bi_{0.14}$ and $Pb_{0.75}Bi_{0.25}$ alloys yield 15 and 17 ML beating periods, respectively. The QSE effect, however, gets weaker with increasing Bi content in agreement with the experimental results of $Pb_{0.8}Bi_{0.2}$ [31].

4.7.2 Tuning the Superconductivity Via Alloying

As reported earlier for clean Pb [14], the upper critical field $H_{c2}(T)$ markedly flattens near T_c, resulting in a characteristic "hockey stick" profile that is particularly noticeable for the thinner films [31]. This feature becomes much more pronounced for the $Pb_{89}Bi_{11}$ and $Pb_{80}Bi_{20}$ quantum alloys compared to pure Pb. The strong curvature near T_c marks a profound departure from the anisotropic Ginzburg–Landau theory, which predicts that $H_{c2} \propto (1 - T/T_c)$. The upper critical field resumes Ginzburg–Landau-like behavior below a characteristic temperature T_c^*, which is defined by extrapolating the linear part of the low temperature H_{c2} curve to zero dc field [31](see Fig. 4.32).

Although a rounding of $H_{c2}(T)$ near T_c is often attributed to structural inhomogeneities in conjunction with the boundary conditions for the pair wave function, the

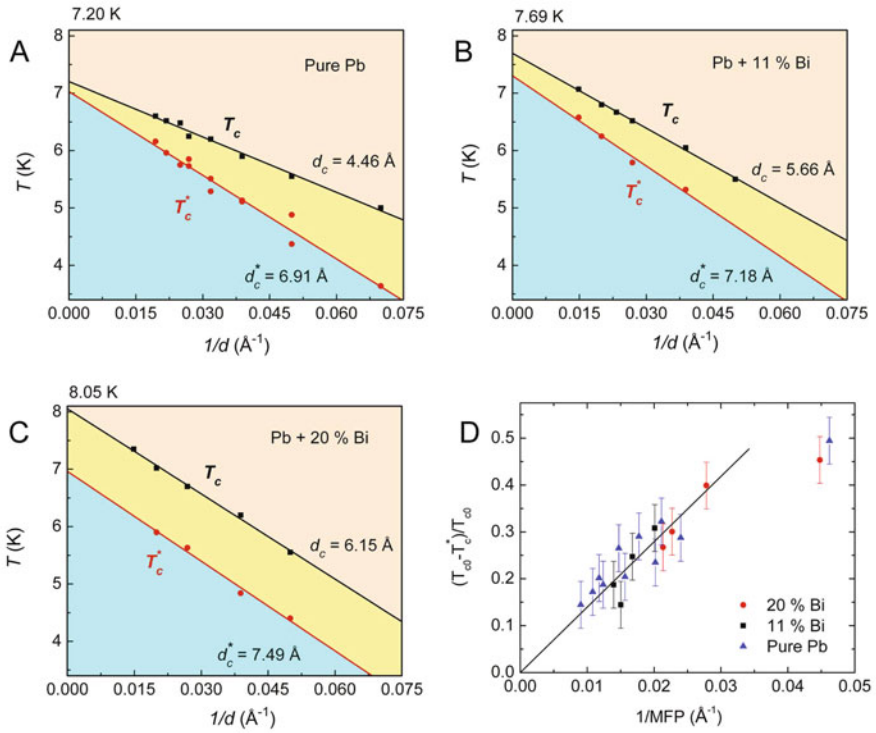

Fig. 4.32 Characteristic temperatures T_C and T_C^* values versus inverse film thickness (**a**) for pure Pb, (**b**) for $Pb_{0.89}Bi_{0.11}$, and (**c**) for $Pb_{0.80}Bi_{0.20}$ alloys. Reproduced from [31]

rounding here changes systematically with the fundamental nanoscale dimension d, because both T_c and T_c^* vary linearly with $1/d$ while the low temperature slopes $dH_{c2}/dT \propto (d - d_c^*)^{-1}$ also vary systematically with thickness [42]. On the other hand, the separation between T_c and T_c^* *increases* with Bi content, and T_c^* does *not* extrapolate to the T_c of the corresponding bulk alloys. This indicates that the thickness of the quantum alloy films is not the only parameter controlling T_c^*.

It is interesting that the "hockey stick" profile of the upper critical field and breakdown of the anisotropic Ginzburg–Landau theory could signal multi-gap superconductivity related to the existence of multiple 2D subbands in the quantum alloys, where each band has its own intrinsic coherence length. This interpretation is based on an intriguing analogy with MgB_2, where the slope of $H_{c2}(T)$ near T_C is determined primarily by intraband scattering in the "clean" σ band and where a similar upturn in the upper critical field below T_C has been attributed to intraband scattering in the "dirty" band channel [76, 77]. In the PbBi alloy film, the H_{c2} upturn would reflect a similar crossover phenomenon, possibly involving several orthogonal subband channels that are coupled via off-diagonal electron–phonon coupling and weak interband scattering [76, 77]. Because the intraband scattering relaxation time decreases with increasing subband index, the clean channel might be associated with the lowest subband. This conjecture could in principle be verified with low-temperature, ultrahigh-resolution scanning tunneling spectroscopy. In contrast to bulk MgB_2 – one of the very few known multi-gap superconductors – such a low-dimensional superconductor would be fully tunable, which opens up new possibilities for experimental and theoretical studies of multi-gap superconductivity in the quantum regime.

4.8 Concluding Remarks and Perspectives

In this review, we attempted to highlight a novel type of "quantum engineering" in which quantum mechanics plays an essential role in defining the kinetic and thermodynamic parameters of metallic thin films as well as the preferred mode of growth of a variety of metallic nanostructures on semiconductor substrates. The impact of this new concept clearly lies in its enabling role. It provides the basis on which quantum size effects can be exploited to precisely control the formation of metallic structures; such structures formed in the quantum regime, in turn, are bound to serve as appealing platforms for elucidating intriguing quantum properties.

In the past 10 years, this field has evolved from the confirmation of the quantum stability concept in a wide variety of materials' systems to the discovery of their novel properties, which include magnetism [78], transport, superconductivity, work function, and surface chemical reactivity. Despite these significant advances, many challenging issues remain. For example, it is still not fully understand how the QWS formed in the normal direction affect the in-plane atomic motion in the film, particularly at the electronic and atomistic levels and the coupling between the two length scales. Further theoretical and experimental studies are needed for fully

understanding the observed phenomena for precise structural control and exploring and designing noval physical properties in the quantum regime.

Further research efforts may also prove fruitful in the directions of optical adsorption, nano friction, catalysis, and reflectivity, all of which with clear relevance for sustainable energy applications. For example, it is expected that the QSE would have an strong modulation to the friction coefficient on Pb(111) and other ultrthin films, similar to the experimental observations showing that the electron friction can play a key role in the systems of N_2 on the Pb substrate [79, 80].

It is also expected that future research in this area will shift toward synthesis of more complex metallic systems such as the quantum stabilization of "nano alloys" that are immiscible in bulk form [81, 82], as well as applications in other areas of chemistry, physics, and engineering. Intriguing possibilities include pushing the robustness of the superconducting state to even smaller length scales so as to obtain unprecedented insights into the emergence of collective quantum phenomena in structures containing the fewest number of atom [3]. As another example, conceptual advances in plasmonics could involve the tailoring of resonant frequencies and Landau damping in metallic nanoparticles with precisely controlled morphology (Özer et al., unpublished). Finally, molecular adsorption, decomposition, and chemical reactions on quantum mechanically confined metals and nano-alloy catalysts may lead to catalysis via quantum design. The authors hope that this review will contribute to the necessary cross-fertilization between the various research disciplines so that the enabling concept of quantum growth may find its way from traditional surface science to the broader science and engineering domain.

Acknowledgments During the course of this line of research we have benefited from many of our collaborators and colleagues in the field. In particular, we thank C. K. Shih, Q. Niu, J. H. Cho, A. R. Smith, J. R. Thompson, B. Wu, and E. J. Moon for their valuable contributions to the main findings and advances presented in this review. YJ acknowledges financial support from NSF of China (Grant No. 10574113, 10974182), HHW and ZYZ acknowledge financial support from NSF under contract No. DMR 06-06485 and DMR 0906025 and the US-DOE Office of Basic Energy Sciences, Division of Materials Sciences and Engineering.

References

1. D.C. Tsui, H.L. Stormer, A.C. Gossard, Two-dimensional magnetotransport in the extreme quantum limit. Phys. Rev. Lett. **48**, 1559 (1982)
2. M.N. Baibich, J.M. Broto, A. Fert, F. Nguyen Van Dau, F. Petroff, P. Etienne, G. Creuzet, A. Friederich, J. Chazelas, Giant magnetoresistance of (001)Fe/(001)Cr magnetic superlattices. Phys. Rev. Lett. **61**, 2472 (1988)
3. A.R. Smith, K.-J. Chao, Q. Niu, C.-K. Shih, Formation of atomically flat silver films on GaAs with a "silver mean" quasi periodicity. Science **273**, 226 (1996)
4. Z.Y. Zhang, Q. Niu, C.-K. Shih, "Electronic growth" of metallic overlayers on semiconductor substrates. Phys. Rev. Lett. **80**, 5381 (1998)
5. V. Yeh, L. Berbil-Bautista, C.Z. Wang, K.M. Ho, M.C. Tringides, Role of the metal/semiconductor interface in quantum size effects: Pb/Si(111). Phys. Rev. Lett. **85**, 5158 (2000)

6. C.M. Wei, M.Y. Chou, Theory of quantum size effects in thin Pb(111) films. Phys. Rev. B **66**, 233408 (2002)
7. M.H. Upton, C.M. Wei, M.Y. Chou, T. Miller, T.C. Chiang, Thermal stability and electronic structure of atomically uniform Pb films on Si(111). Phys. Rev. Lett. **93**, 026802 (2004)
8. M.M. Özer, Y. Jia, B. Wu, Z.Y. Zhang, H.H. Weitering, Quantum stability and reentrant bilayer-by-bilayer growth of atomically smooth Pb films on semiconductor substrates. Phys. Rev. B **72**, 113409 (2005)
9. Y. Jia, B. Wu, H. H. Weitering, Z.Y. Zhang, Quantum size effects in Pb films from first principles: the role of the substrate. Phys. Rev. B **74**, 035433 (2006)
10. L. Aballe, A. Barinov, A. Locatelli, S. Heun, M. Kiskinova, Tuning surface reactivity via electron quantum confinement. Phys. Rev. Lett. **93**, 196103 (2004)
11. A.G. Danese, F.G. Curti, R.A. Bartynski, Quantum size effect induced modification of the chemisorption properties of thin metal films. Phys. Rev. B **70**, 165420 (2004)
12. Y. Guo, Y.F. Zhang, X.Y. Bao, T.Z. Han, Z. Tang, L.X. Zhang, W.G. Zhu, E.G. Wang, Q. Niu, Z.Q. Qiu, J.F. Jia, Z.X. Zhao, Q.K. Xue, Superconductivity modulated by quantum size effects. Science **306**, 1915 (2004)
13. D. Eom, S. Qin, M.Y. Chou, C.K. Shih, Persistent superconductivity in ultrathin Pb films: a scanning tunneling spectroscopy study. Phys. Rev. Lett. **96**, 027005 (2006)
14. M.M. Özer, J.R. Thompson, H.H. Weitering, Hard superconductivity of a soft metal in the quantum regime. Nat. Phys. **2**, 173 (2006)
15. M.M. Özer, J.R. Thompson, H.H. Weitering, Robust superconductivity in quantum-confined Pb: equilibrium and irreversible superconductive properties. Phys. Rev. B **74**, 235427 (2006)
16. Z.G. Suo, Z.Y. Zhang, Epitaxial films stabilized by long-range forces. Phys. Rev. B **58**, 5116 (1998)
17. R.C. Jakleic, J. Lambe, M. Mikkor, W.C. Vassell, Observation of electron standing waves in a crystalline box. Phys. Rev. Lett. **26**, 88 (1971)
18. F.K. Schulte, A theory of thin metal films: electron density, potentials and work function. Surf. Sci. **55**, 427 (1976)
19. P.J. Feibelman, Static quantum-size effects in thin crystalline, simple-metal films. Phys. Rev. B **27**, 1991 (1983)
20. A. Zangwill, *Physics at Surfaces* (Cambridge University Press, Cambridge, 1998)
21. M. Hupalo, V. Yeh, L. Berbil-Bautista, S. Kremmer, E. Abram, M.C. Tringides, Uniform-height island growth of Pb on Si(111)-Pb($\sqrt{3}\times\sqrt{3}$) at low temperatures. Phys. Rev. B **64**, 155307 (2001)
22. H.W. Hong, C.M. Wei, M.Y. Chou, Z. Wu, L. Basile, H. Chen, M. Holt, T.C. Chiang, Alternating layer and island growth of Pb on Si by spontaneous quantum phase separation. Phys. Rev. Lett. **90**, 076104 (2003)
23. van N. Stranski, L. Von Krastanow, *Abhandlungen der Mathematisch-Naturwissenschaftlichen Klasse. Akademie der Wissenschaften und der Literatur in Mainz*, **146**, 797 (1939)
24. W.B. Su, S.H. Chang, W.B. Jian, C.S. Chang, L.J. Chen, T.T. Tsong, Correlation between quantized electronic states and oscillatory thickness relaxations of 2D Pb islands on Si(111)-(7×7) surfaces. Phys. Rev. Lett. **86**, 5116 (2001)
25. M. Hupalo, S. Kremmer, V. Yeh, L. Berbil-Bautista, E. Abram, M.C. Tringides, Uniform island height selection in the low temperature growth of Pb/Si(111)-(7×7). Surf. Sci. **493**, 526 (2001)
26. M.M. Özer, C.-Z. Wang, Z. Zhang, H.H. Weitering, Quantum size effects in the growth, coarsening, and properties of ultra-thin metal films and related nanostructures. J. Low Temp. Phys. **157**, 221 (2009)
27. B. Wu, Z. Zhang, Stability of metallic thin films studied with a free electron model. Phys. Rev. B **77**, 035410 (2008)
28. M.C. Tringides, M. Jalochowski, E. Bauer, Quantum size effects in metallic nanostructures. Phys. Today **60**, 50 (2007)
29. P. Czoschke, H. Hong, L. Basile, T.-C. Chiang, Quantum size effects in the surface energy of Pb/Si(111) film nanostructures studied by surface x-ray diffraction and model calculations. Phys. Rev. B **72**, 075402 (2005)

30. X. Ma, P. Jiang, Y. Qi, J. Jia, Y. Yang, W. Duan, W.-X. Li, X. Bao, S.B. Zhang, Q.-K. Xue, Experimental observation of quantum oscillation of surface chemical reactivities. Proc. Natl. Acad. Sci.**104**, 9204 (2007)
31. M.M. Özer, Y. Jia, Z.Y. Zhang, J.R. Thompson, H.H. Weitering, Tuning the quantum stability and superconductivity of ultrathin metal alloys. Science **316**, 1594 (2007)
32. T.C. Chiang, Photoemission studies of quantum well states in thin films. Surf. Sci. Rep. **39**, 181 (2000)
33. B.J. Hinch, C. Koziol, J.P. Toennies, G. Zhang, Evidence for quantum size effects observed by helium atom scattering during the growth of Pb on Cu(111). Europhys. Lett. **10**, 341 (1989)
34. J. Braun, J.P. Toennies, Observation of a quantum size effect in the surface electron density of thin lead films. Surf. Sci. **384**, L858, (1997)
35. R. Otero, A. L. Vázquez de Parga, R. Miranda, Observation of preferred heights in Pb nanoislands: a quantum size effect. Phys. Rev. B. **66**, 115401 (2002)
36. J.R. Anderson, A.V. Gold, Fermi surface, pseudopotential coefficients, and spin-orbit coupling in lead. Phys. Rev. **139**, A1459 (1965)
37. M. Jalochowski, H. Knoppe, G. Lilienkamp, E. Bauer, Photoemission from ultrathin metallic films: quantum size effect, electron scattering, and film structure. Phys. Rev. B **46**, 4693 (1992)
38. J.C. Heyraud, J.J. Méois, Equilibrium shape and temperature; lead on graphite. Surf. Sci. **128**, 334 (1983)
39. P. Czoschke, H.W. Hong, L. Basile, T.C. Chiang, Quantum beating patterns observed in the energetics of Pb film nanostructures. Phys. Rev. Lett. **93**, 036103 (2004)
40. Y. Jia, B. Wu, C. Li, T. Einstein, H.H. Weitering, Z.Y. Zhang, Strong quantum size effects in Pb(111) thin films mediated by anomalous friedel oscillations. Phys. Rev. Lett. **105**, 066101 (2010)
41. I.B. Altfeder, V. Narayanamurti, D.M. Chen, Imaging subsurface reflection phase with quantized electrons. Phys. Rev. Lett. **88**, 206801 (2002)
42. P. Czoschke, H.W. Hong, L. Basile, T.C. Chiang, Quantum oscillations in the layer structure of thin metal films. Phys. Rev. Lett. **91**, 226801 (2003)
43. J.H Cho, Ismail, Z.Y. Zhang, E.W. Plummer, Oscillatory lattice relaxation at metal surfaces. Phys. Rev. B **59**, 1677 (1999)
44. M.W. Finnis, V. Heine, Theory of lattice contraction at aluminium surfaces. J. Phys. F. Met. Phys. **4,** L37–L41 (1974)
45. A. Crottini, D. Cvetko, L. Floreano, R. Gotter, A. Morgante, F. Tommasini, Step height oscillations during layer-by-layer growth of Pb on Ge(001). Phys. Rev. Lett. **79**, 1527 (1997)
46. L. Floreano, D. Cvetko, F. Bruno, G. Bavdek, A. Cossaro, R. Gotter, A. Verdini, A. Morgante, Quantum size effects in the low temperature layer-by-layer growth of Pb on Ge(001). Prog. Surf. Sci. **72**, 135 (2003)
47. A. Mans, J.H. Dil, A. R. H. F. Ettema, H.H. Weitering, Quantum electronic stability and spectroscopy of ultrathin Pb films on Si(111)7×7. Phys. Rev. B **66**, 195410 (2002)
48. M. Breitholtz, T. Kihlgren, S.-A. Lindgren, L. Wallden, Condensation of Na metal on graphite studied by photoemission. Phys. Rev. B **67**, 235416 (2003)
49. C.J. Fall, N. Binggeli, A. Baldereschi, Work functions at facet edges. Phys. Rev. Lett. **88**, 156802 (2002)
50. K. Besocke, B. Krahl-Urban, H. Wangner, Dipole moments associated with edge atoms; A comparative study on stepped Pt, Au and W surfaces. Surf. Sci. **68**, 39–46 (1977)
51. Y. Qi, X. Ma, P. Jiang, S.H. Ji, Y.S. Fu, J.F. Jia, Q.K. Xue, S.B. Zhang, Atomic-layer-resolved local work functions of Pb thin films and their dependence on quantum well states. Appl. Phys. Lett. **90**, 013109 (2007)
52. C.-S. Jiang, S.C. Li, H.B. Yu, D. Eom, X.D. Wang, Ph. Ebert, J.F. Jia, Q.K. Xue, C.K. Shih, Building Pb nanomesas with atomic-layer precision. Phys. Rev. Lett. **92**, 106104 (2004)
53. T. Miller, M.Y. Chou, T.C. Chiang, Phase relations associated with one-dimensional shell effects in thin metal films. Phys. Rev. Lett. **102**, 236803 (2009)

54. F.J. Himpsel, J.E. Ortega, G.J. Mankey, R.F. Willis, Magnetic nanostructures. Adv. Phys. **47**, 511 (1998)
55. M. Milum, P. Pervan, D.P. Woodruff, Quantum well structures in thin metal films: simple model physics in reality. Rep. Prog. Phys. **65**, 99 (2002)
56. B. Allen, R.–C. Dynes, Transition temperature of strong-coupled superconductors reanalyzed. Phys. Rev. B **12**, 905 (1975)
57. A. Crottini, D. Cvetko, L. Floreano, R. Gotter, A. Morgante, F. Tommasini, Step height oscillations during layer-by-layer growth of Pb on Ge(001). Phys. Rev. Lett. **79**, 1527 (1997)
58. Y.F. Zhang, J.F. Jia, T.Z. Han, Z. Tang, Q.T. Shen, Y. Guo, Z.Q. Qiu, Q.K. Xue, Band structure and oscillatory electron-phonon coupling of Pb thin films determined by atomic-layer-resolved quantum-well states. Phys. Rev. Lett. **95**, 096802 (2005)
59. F. Yndurain, M.P. Jigato, First principles calculation of localized surface phonons and electron-phonon interaction at Pb(111) thin films. Phys. Rev. Lett. **100**, 205501 (2008)
60. J. Kosterlitz, D. Thouless, Ordering, metastability and phase transitions in two-dimensional systems. J. Phys. C **6**, 1181 (1973)
61. D.B. Haviland, Y. Liu, A.M. Goldman, Onset of superconductivity in the two-dimensional limit. Phys. Rev. Lett. **62**, 2180 (1989)
62. I. Vilfan, M. Henzler, O. Pfennigstorf, H. Pfnür, Anomalous thickness dependence of the hall effect in ultrathin Pb layers on Si(111). Phys. Rev. B. **66**, 241306 (2002)
63. I. Vilfan, H. Pfnür, Charge-carrier transport properties of ultrathin Pb films. Eur. Phys. J. B. **36**, 281 (2003)
64. J. Simonin, Surface term in the superconductive Ginzburg-Landau free energy: application to thin films. Phys. Rev. B **33**, 7830 (1986)
65. R.C. Dynes, J.M. Rowell, Influence of electrons-per-atom ratio and phonon frequencies on the superconducting transition temperature of lead alloys. Phys. Rev. B **11**, 1884 (1975)
66. S. Qin, J. Kim, Q. Niu, C.K. Shih, Superconductivity at the two-dimensional limit. Science **324**, 1314 (2009)
67. H.H. Weitering, The world's thinnest superconductor. Chem. Phys.Chem. **10**, 1 (2009)
68. G.J. Dolan, J. Silcox, Critical thicknesses in superconducting thin films. Phys. Rev. Lett. **30**, 603 (1973)
69. M. Valden, X. Lai, D.W. Goodman, Onset of catalytic activity of gold clusters on titania with the appearance of nonmetallic properties. Science **281**, 1647 (1998)
70. M.S. Chen, D. Kumar, C.-W. Yi, D.W. Goodman, The promotional effect of gold in catalysis by palladium-gold. Science **310**, 291 (2005)
71. M.S. Chen, Y. Cai, Z. Yan, D.W. Goodman, On the origin of the unique properties of supported Au nanoparticles. J. Am. Chem. Soc. **128**, 6341 (2006)
72. M.S. Chen, D.W. Goodman, Structure-activity relationships in supported Au catalysts. Catal. Today **111**, 22–23 (2006)
73. N. Binggeli, M. Altarelli, Surface reactivity and quantum-size effects on the electronic density decay length of ultrathin metal films. Phys. Rev. Lett. **96**, 036805 (2006)
74. J.K. Norskov, Chemisorption on metal surfaces. Rep. Prog. Phys. **53**, 1253 (1990)
75. N. Trivedi, N.W. Ashcroft, First-principles study of quantum size effects in ultrathin Pb-Bi metal alloy films. Phys. Rev. B. **38**, 12298 (1988)
76. A. Gurevich, S. Patnaik, V. Braccini, K.H. Kim, C. Mielke, X. Song, L.D. Cooley, S.D. Bu, D.M. Kim, J.H. Choi, L.J. Belenky, J. Giencke, M.K. Lee, W. Tian, X.Q. Pan, A. Siri, E.E. Hellstrom, C.B. Eom, D.C. Larbalestier, Very high upper critical fields in MgB_2 produced by selective tuning of impurity scattering. Supercond. Sci. Tech. **17,** 278 (2004)
77. M. Mansor, J.P. Carbotte, Upper critical field in two-band superconductivity. Phys. Rev. B **72**, 024538 (2005)
78. Z.Q. Qiu, N.V. Smith, Quantum well states and oscillatory magnetic interlayer coupling. J. Phys Condens. Matter **14**, R169 (2002)
79. A. Dayo, W. Alnasrallah, J. Krim, Superconductivity-dependent sliding friction. Phys. Rev. Lett. **80**, 1690 (1998)

80. M. Highland, J. Krim, Superconductivity dependent friction of water, nitrogen, and superheated He films adsorbed on Pb(111). Phys. Rev. Lett. **96**, 226107 (2006)
81. E.J. Moon, M. M. Özer, R.J. Thompson, H.H. Weitering, submitted
82. A. Khajetoorians, W.G. Zhu, J.S. Kim, S. Qin, H. Eisele, Z.Y. Zhang, C.-K. Shih, Adsorbate-induced restructuring of Pb mesas grown on vicinal Si(111) in the quantum regime. Phys. Rev. B **80**, 245426 (2009)

Chapter 5
Surface Electromigration and Current Crowding

R. Yongsunthon, C. Tao, P. Rous, and E.D. Williams

Abstract Steps on macroscopic surfaces provide a useful model system for quantifying electron scattering at defects in nanostructures, where the large surface/volume ratio will cause surface effects to dominate. Here, the effects of electron scattering at surface steps are quantified using thin silver films with (111) surface orientation. Using real-time scanning tunneling microscopy (STM) measurements while large current densities are applied to the films, changes in step fluctuations and island motion are observed and quantified. Applying the tools of the continuum step model, the observations are analyzed in terms of step free energies and kinetics, yielding quantitative values of the electromigration force driving the observed mass displacements. The derived magnitudes are surprisingly large in comparison with classical calculations of the force due to electron scattering at the internal surface of a conductor. This result indicates that the specific atomistic characteristics of the scattering sites, in this case kinks at the step edge, may greatly enhance the electromigration force. Within the classical ballistic picture of ballistic momentum transfer, specific mechanisms for such enhancement include enhanced geometric "blocking" at the kinked step edges, changes in carrier density near kinks, and current crowding. Quantum transmission effects at atomic-scale defect sites may also be responsible for the observed enhancement. The nature of classical current crowding as a function of the shape and size of defect was characterized using magnetic force microscopy (MFM) of fabricated micron-scale model structures. Techniques were developed to remove the effects of instrumental broadening using deconvolution, so that full three-dimensional maps of the magnetic fields above the current line are determined. A Green function inversion technique is then used to invert the field distribution to determine the spatial variations in the current density in the sample. Current enhancement is highly localized near defects and is maximized by sharp variations in geometry that require strong deflections of the current path. Current enhancements up to a factor of 4 are found at the most strongly deflecting defects, while small notches of various shapes typically cause local enhancements

R. Yongsunthon (✉)
Corning Incorporated, Corning, New York, NY, USA
e-mail: YongsuntR@corning.com

M. Michailov (ed.), *Nanophenomena at Surfaces,* Springer Series in Surface Sciences 47,
DOI 10.1007/978-3-642-16510-8_5,

of tens of percent to a factor of 2. The perpendicular component of the current flow around defects forms a dipole pattern with length scale determined by the length of the defect along the direction of the current flow. The shape and localization of the dipole pattern vary with the sharpness and symmetry of the defect. The current crowding affect alone is not sufficient to explain the greatly enhanced electromigration force observed for scattering at kink sites at steps.

5.1 Introduction

Electromigration is the mass transport of atoms in or on an electrically conducting material, where the transport is driven by applied electric fields and the resulting current flow. Study of the mechanisms of electromigration has yielded deep physical insights about the mechanisms of electron scattering, and in particular the special characteristics (e.g., surface resistivity) of surfaces and interfaces [1–3]. As the size scale of electrical interconnects shrinks, and as interest in nanoelectronic grows, the role of electron scattering at surfaces, and thus at surface defects and non-uniformities, becomes more important [4–6]. Electromigration failure can arise from a surface diffusion flux that is driven by competition between the electromigration and healing capillary forces. These surface processes may couple constructively along a void surface [7, 8], with increased effect due to anisotropic surface diffusion to drive catastrophic void formation [9, 10]. In addition, current crowding [9–12] in the vicinity of a defect may also have a great role in its evolution by increasing the local magnitude of the electromigration force.

The tools of surface science opened the study of electromigration to atomic scale characterization [13], and the surprising and complex behavior in the electromigration-induced evolution of Si surface structure [14–18] led to deep theoretical investigations [19] of the development of kinetic instabilities in the presence of an electromigration force. In the same time frame, fundamental scattering calculations [20, 21] have made it possible to quantify the electromigration forces acting on surface atoms including different defect sites. More recently, there has been renewed interest, focused on nanoscale structures, in fundamental issues of current flow at constrictions and interfaces [22, 23]. The combination of theoretical and experimental advances in the understanding of electromigration opens the possibility for using nanoscale structures to tailor surface resistivity [21, 24–26] and to control structure as in nanogap formation [27–29], for driving dopants into nanowires [30], for coupling electrical signals to atomic fluctuations [25, 31] and even the possibility of driving nanoscale rotational motion [32].

In the following, we will review an example of the use of direct imaging (STM) to follow the evolution of structure during electromigration. Analysis of the observations using the continuum step model approach [33] reveals an unexpectedly large electromigration force, which we will argue indicates a substantial effect of nanoscale current crowding. We will then present a parallel set of investigations, carried out on micron-scale structures, which demonstrate the direct observation of non-uniform current flow around defects. Because the classical laws of

electromagnetism that govern the current flow are scale invariant, experimental micron-scale observations can be used to illuminate nanoscale phenomena.

5.2 Direct Observation of Surface Electromigration

The nature of electron scattering at the internal surfaces of a conductor is illustrated in Fig. 5.1 [34]. The specular scattering expected for perfectly flat surfaces will lead to electromigration forces on any atoms that are free to diffuse on the surface. In addition, the presence of defects, which have different scattering cross sections and different local electric fields, can enhance scattering leading to an enhanced surface resistivity. In the following we will describe the use of direct observations of diffusion biased by an applied current to quantify the magnitude of the electromigration force, and thus the underlying charge scattering characteristics of the defects.

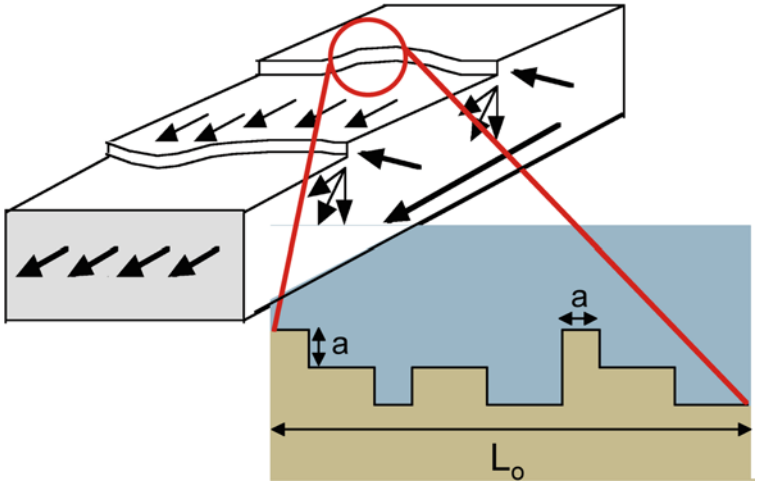

Fig. 5.1 Schematic illustration of current flow adjacent to a surface with defects in the form of steps. Enhanced scattering from step sites at the surface is suggested by the *arrows* that represent the direction of motion of the charged carriers. The inset illustrates a lattice model of kinked (thermally roughened) step edge segments of horizontal extent $L_o = 13a$, with six single and one double height kinks [34]

5.2.1 Surface Electromigration and Surface Resistivity

The presence of the electromigration force introduces a small bias in the diffusion of atoms on the surface, parallel to the current (and field). By convention, this bias can be expressed as an energy difference between atoms diffusing parallel or anti-parallel to the current $\Delta U = Z^* e \mathbf{E} a$, where $\mathbf{E}$ is the electric field applied to the sample, Z^* is the effective valence of a diffusing atom, and a is the atomic lattice

spacing. A typical estimate of the bias of $\sim 10^{-5}$ eV/unit cell at a current density of 10^7 A/cm^2 [35] is so small that it may result in a directional bias in fewer than one in a hundred thousand diffusion steps. However, at large current densities, $\sim 10^8$ A/cm^2, the cumulative effects of this small bias can generate micron-scale voids in conductors [3, 13, 36], and observable atomic-scale rearrangements in nanoscale, electromigration structures [27, 30, 31, 34] occur at current densities 2–3 orders of magnitude smaller.

The effective valence, Z^*, is a convenient notation that encompasses the underlying physics of electron scattering. This can be quantified using a simple description of the electromigration force in terms of ballistic scattering [2]. A local electron flux j/e, with electron mass m and speed v_F, the Fermi velocity, impinging on an atom with scattering cross section σ, will impart an average force F equal to the product of the momentum transfer per collision and the number of collisions per time, $F = mv_F\sigma j/e$. Relating the current density j to the field through the resistivity ρ, $j = \rho E$, yields an expression for the effective valence $Z^* = mv_F\sigma\rho/e$. Theoretical difficulty arises in this simple picture because the macroscopic current density depends on the charge density n, drift velocity v_d, and electron scattering time τ ($j_{bulk} = nev_d = ne^2\tau E/m = E/\rho$, with ρ the bulk resistivity), where the quantities n and τ are known for the bulk [37] but poorly understood for electrons near surfaces and interfaces [20, 21]. Despite these issues, the effective valence is a useful metric for quantifying and comparing electromigration effects in different materials and structures. As an example, the predicted effective valence of an isolated Ag adatom on Ag(111) is $Z^* = -19$ [20]. For atoms in a close-packed site along a step edge, with a current direction perpendicular to the step edge, the direct force per step atom may be two times higher than the force on an adatom [38, 39], which would yield a predicted valence of $Z^* \sim 38$.

One consequence of electron scattering from surface defects is a change in the resistivity of the material. The change in the surface resistivity ρ_s resulting from a wind force F_w acting on a scattering site density n_k is [20]

$$t_f \frac{\partial \rho_s}{\partial n_k} = -\frac{1}{en_c J}\left(F_w^k + \sum_j \delta F_w^j\right) \tag{5.1}$$

where t_f is the material thickness, n_c is the local carrier density, F_w^k is the wind force acting per defect site, and F_w^j are additional changes in force on the carriers due to the perturbation of atomic structure in the immediate vicinity of the surface defect sites.

5.2.2 Experimental Observation of Electromigration Effects

One approach to assess the electromigration force is to observe the biased mass transport that it causes. To do this in a way that can be interpreted in terms of

fundamental interactions, observations at the atomic scale are needed. This can be accomplished using direct STM imaging of surfaces of a current-carrying conductor, with extreme care to address the issues of temperature and drift that arise with a large current density.

Single-crystal thin-film Ag samples with (111) surface orientation were prepared by thermal evaporation of 100–350 nm of Ag onto a freshly cleaved mica substrate [40–42]. The samples were then transferred into a treatment chamber. After several Ar^+ sputtering and annealing cycles, atomically clean Ag(111) surfaces were obtained. To modify the surface morphology for experiments on Ag island motion, gentle sputtering without annealing was used. The types of surface structures that can be controllably achieved are illustrated in Fig. 5.2. After these procedures, the samples were loaded onto an STM stage designed to heat-sink the mica substrates. Following application of direct current, 30–40 min is needed for thermal stabilization. To measure the structural evolution or motion of defects, time-lapse imaging is used. To assess step displacement, repeated one-dimensional scans are made across the step at a scan rate of ∼9 pixels/ms. To assess island motion, the fastest scan speed is 60 s per 256 × 256 pixel image and 120 s per 512 × 512 pixel image. The typical tunneling parameters are ∼50 pA at sample bias ∼1.6 V. Under these tunneling conditions the tip–sample interactions can be negligible for Ag surfaces [40, 43].

Two methods were used to determine the temperature of the sample under applied current. The temperature was measured using an alumel–chromel thermocouple, which was spot-welded to a tiny Ta tab (strip) and brought into direct contact with the film surface in a calibration performed after the electromigration measurements [40]. In addition, the sample temperature was calibrated via a thermocouple in a separate chamber (base pressure $\sim 4 \times 10^{-8}$ torr) using the same heater system as in the UHV system. The thermocouple wire diameter was 0.001″, and a simple analysis shows that the heat-sinking effect of the thermocouple results in less than 1 K temperature change.

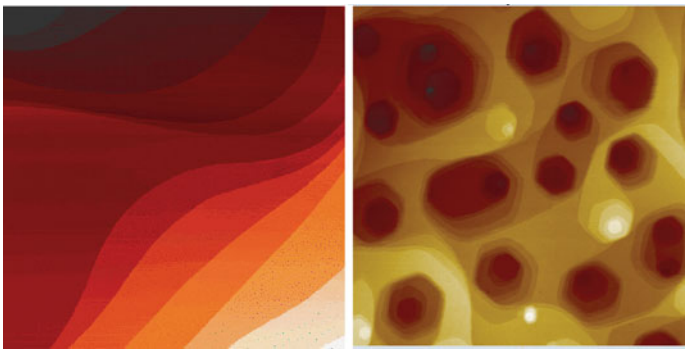

Fig. 5.2 STM images of clean Ag(111) films grown on mica in UHV. *Left*: 800 × 800 nm^2 STM image of structure achieved by annealing during sputtering. *Right*: 500 nm × 500 nm STM image of structure achieved by sputtering at room temperature [79]

5.2.3 Experimental Assessment of the Electromigration Force on Steps

Two distinctly different measurements were performed that allowed an independent assessment of the electromigration force acting on atoms at step edges on the Ag(111) surface. The first experiment measured fluctuations of independent steps under an electromigration force oriented parallel and anti-parallel to the step normal. The second experiment addressed the biased motion of islands, which are of course bounded by steps, under a biasing current.

5.2.3.1 Step Fluctuations

At temperatures where thermal diffusion is possible, the steps on a solid surface fluctuate via motion of the atoms at their edges. This fluctuation involves excitation of kinks at the step edge, diffusion of atoms along the step edge, atomic detachment from the step edge, diffusion on terraces, and atomic attachment from terraces to the step [33]. The fluctuations can be quantified via repeated STM scans perpendicular to the edge, as shown in Fig. 5.3, and analyzed in terms of their temporal correlation functions. For steps on Ag(111), such analysis has shown that the steps fluctuate at

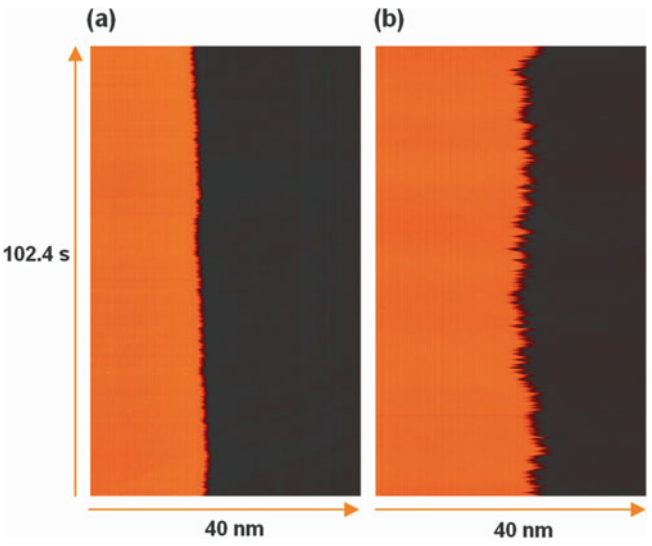

Fig. 5.3 Fluctuation measurement of a close-packed step edge on Ag(111). STM temporal pseudoimages obtained by scanning the STM tip over a fixed position on the step edge in the direction perpendicular to the step orientation. For both images, the line scan length is 40 nm, a line scan time is 51.2 ms, and total time is 102.4 s with 2000 lines. The step orientations are along a close-packed direction. The images are obtained at 300 K (**a**) and at 460 K (**b**). The average step width $w = \sqrt{\langle [x(t) - \bar{x}]^2 \rangle}$ is 0.136 ± 0.007 nm at 300 K and about seven times larger, 0.908 ± 0.043 nm at 460 K [46]

and above room temperature with diffusion along the step edge being the dominant mechanism [40, 44–46].

The temporal correlation function of a step in thermal equilibrium, for the case where fluctuations are dominated by step edge diffusion, is

$$G(t) = \left\langle (x(t) - x(0))^2 \right\rangle = \left(\frac{2\Gamma\,(1 - 1/4)}{\pi} \right) \left(\frac{kT}{\tilde{\beta}} \right)^{\frac{3}{4}} (\Gamma_n t)^{\frac{1}{4}} = g_{\mathrm{eq}}(t) t^{1/4} \quad (5.2)$$

where $x(t)$ is the experimentally measured step edge position, Γ_n is the step mobility, and $\tilde{\beta}$ is the step stiffness. Given a measurement or calculation [47] of the step stiffness, the step mobility and thus the time constant for step edge diffusion can be extracted from fits to (5.2). For close-packed steps on Ag(111), the resulting hopping time constant is $\sim$31 μs at room temperature. For misoriented steps, the hopping time constant is much larger $\sim$704 μs [41].

The addition of an electromigration force creates a biasing effect on the atoms diffusing along the step edge, which can be understood by analogy to the Bales–Zangwill fingering instability that occurs during growth [48]. In this case, a diffusional bias perpendicular to the step edge results in spontaneous increased deviations from the equilibrium wandering when the bias favors diffusion in the step-downhill direction. For an uphill bias, an anomalous straightening of the step edge occurs. This effect is quantified in a modified step continuum model that includes the effect of an electromigration force acting perpendicular to a step that is fluctuating via step edge diffusion [49]. The correlation function deviates from the equilibrium result as

$$G(t) = g_{\mathrm{eq}}(t) t^{1/4} \left[1 \pm 0.3487 \left(\frac{t}{\tau_{\mathrm{EM}}} \right)^{1/2} \right] \quad (5.3)$$

where the $+$ and $-$ signs correspond to a downhill and uphill direction of force, respectively. The electromigration force gives rise to an additional time constant, τ_{EM}, which is the time when the time correlation function begins to deviate significantly from its equilibrium behavior:

$$\tau_{\mathrm{EM}} = \frac{(k_{\mathrm{B}} T) \left(\tilde{\beta} a_x \right)}{(F a_x)^2} \left(\frac{a_x}{a_y} \right) \tau_h \quad (5.4)$$

Because the electromigration force is weak, the time constant τ_{EM} is expected to be much longer than the fundamental time constants of step motion.

The experimental test of the prediction of (5.3) is shown in Fig. 5.4 [25]. Deviations from the pure $t^{1/4}$ behavior of the equilibrium fluctuations were observed as the current direction was switched from the uphill to downhill direction. The deviations occur at shorter times than expected based on the expected value of the effective valence, $Z^* \sim 38$ for steps on Ag(111). A quantitative analysis using (5.3) and the approximate expression for the electromigration force, $F = Z^* \rho j$, using

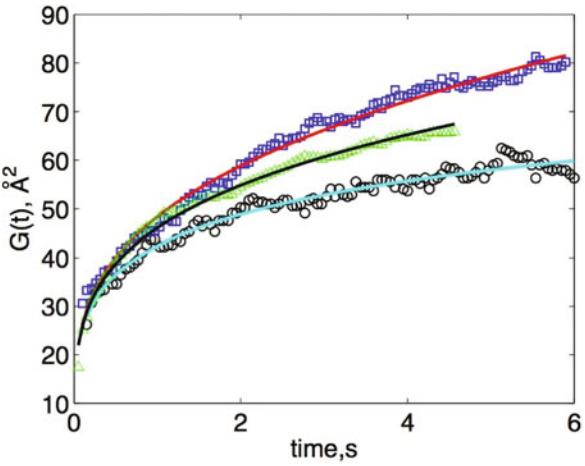

Fig. 5.4 Time correlation functions, $G(t)$, for the step fluctuations ($x(t)$ data) extracted from repeated measurements. The data for the step-down current (*open circles*) are the average over 10 separate measurements; for the step-up current (*open squares*) the average is over 9. Fits to (5.3) are shown as the *solid lines* for each data set. Also shown is the measured correlation function (average of 19 separate measurements) for an unstressed sample (*open triangles*) fit to a single power law [25]

the bulk current densities and the bulk resistivity of Ag, which is approximately $1.8 \times 10^{-6}\,\Omega\,\mathrm{cm}$ at 325 K and $2.2 \times 10^{6}\,\Omega\,\mathrm{cm}$ at 370 K, respectively [50, 51], confirms the surprising character of the result. Taking into account all possible measurement biases, the *lower limit* on the effective valence required to explain the observation is $Z^* = -(2 \pm 1) \times 10^2$, which is *at least* a factor of 5 higher than expected [25, 34].

5.2.3.2 Island Motion

As shown in Fig. 5.2, it is possible to tailor the surface to contain a substantial density of monolayer island stacks. Slightly above room temperature, the top layer island in each stack shrinks because the small radius of curvature increases the local chemical potential (Gibbs–Thompson effect) relative to lower islands in the stack [52]. In addition the islands, particularly the top layer island, move in a fashion similar to Brownian motion [53, 54] as a result of atomic motion at their edges. In the presence of an electromigration force, the atomic diffusion underlying the island motion will be biased, with concomitant effects on the motion of the island [55, 56].

Island diffusion can occur due to motion of free atoms on the terraces (D_T) or on the island edges (D_L). If the island moves because the electromigration force induces a drift velocity ($v_\mathrm{EM} = D_\mathrm{T}F/kT$) of atoms on the terrace onto (or away from) the front (or back) island edge, then the island motion will be in the direction opposite the electromigration force. Alternatively, if the island moves because the force preferentially moves atoms along its edges in one direction, then the island

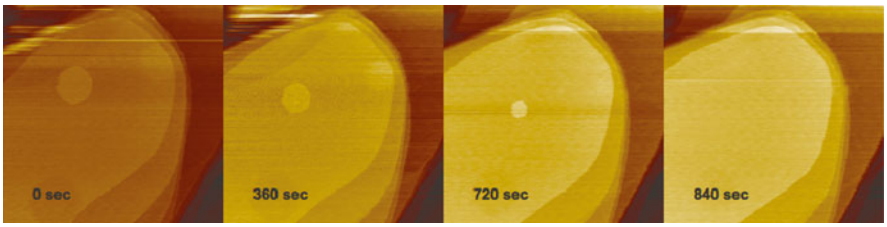

Fig. 5.5 Time-lapse STM images ($400 \times 400\,\text{nm}^2$) of a silver island simultaneously decaying in size and moving under a current density $\sim 6.7 \times 10^9\,\text{A/m}^2$ with the current direction upward in the images as shown and thus a wind force direction downward [79]

motion will be in the same direction as the electromigration force [55]. The results in Fig. 5.5 clearly show the island displacement occurring in the opposite direction to the current and thus in the same direction as the electromigration wind force. Thus the electromigration-induced motion for Ag islands on Ag(111) is the result of biased diffusion along the step edges (Fig. 5.5).

The theoretical prediction for the velocity of the island motion due to biased step edge diffusion is [55]

$$V = \frac{a D_{\text{L}} F}{k_{\text{B}} T R_0} \tag{5.5}$$

where a the lattice constant, D_{L} the macroscopic step diffusion constant, F the wind force, and R_0 the island radius can now be used to determine the magnitude of the force biasing edge diffusion. The decay of the islands as they are moving provides a natural mechanism to determine the velocity as a function of island radius. By quantifying the island center of mass positions, the velocity can be determined as shown in Fig. 5.6 (top panel) with values of 0.02–0.12 nm/s for island radii from 55 nm down to 15 nm. The decay rate is independent of island size, at $-5.5\,\text{nm}^2/\text{s}$, and combining this information yields the velocity vs. radius plot of the bottom panel of Fig. 5.6, which yields an excellent fit (solid line) to the inverse radius prediction of (5.5).

To determine the electromigration force from (5.5), it is necessary to evaluate the edge diffusion constant, which is related to the step stiffness and step mobility defined in (5.2). Because the island exposes all step orientations, it is necessary to consider how these quantities vary with orientation. For straight step edges, $\theta = 0$, $\tilde{\beta}$ is (equation 23 in [47])

$$\frac{k_{\text{B}} T}{\tilde{\beta}(0) a_{//}} = \frac{3(y-1)}{2y\sqrt{y^2 - 2y - 3}} \tag{5.6}$$

with $y = \sqrt{\frac{1+3z}{z(1-z)}}$ and $z = \text{e}^{-2\varepsilon_k / k_{\text{B}} T}$. The kink energy ε is 0.117 eV, so the resulting $\tilde{\beta}(0) = 4.52\,\text{eV/nm}$ at 318 K. For rough step edges ($\theta \neq 0$), we can calculate an average value of $\tilde{\beta}$ using (equation 18 in [47])

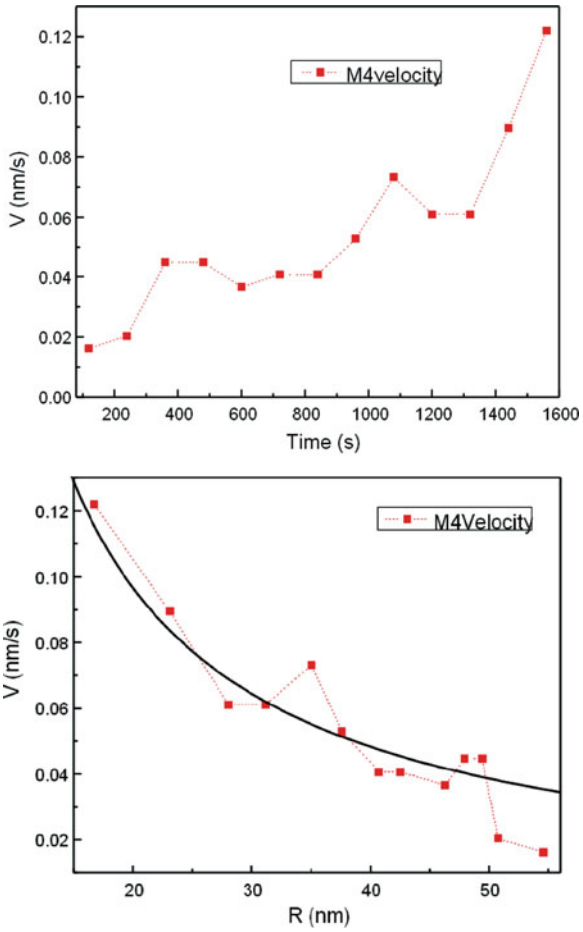

Fig. 5.6 *Top panel*: velocity vs. time determined from the position of the center of mass of a moving island. *Bottom panel*: using the measured island size as a function of time, the velocity is determined as a function of radius. The *black solid line* is a one-parameter fit of the experimental data to $v = C/R$ yielding $C = 1.93 \pm 0.09\,\mathrm{nm}^2/\mathrm{s}$

$$\frac{k_\mathrm{B}T}{\tilde{\beta}(\theta)} = \frac{\sin(3\theta)}{2\sqrt{3}} \tag{5.7}$$

By averaging θ from 5° to 30°, we obtain the average value for rough step edges of 0.51 eV/nm at 318 K.

The edge diffusion constant D_L is related to the step edge mobility Γ_h as $D_\mathrm{L} = a_{//}^2 c_\mathrm{st} D_\mathrm{st} = \frac{\Gamma_\mathrm{h}}{a_\perp^2 a_{//}}$, where $a_{//} = 0.29\,\mathrm{nm}$ and $a_\perp = 0.25\,\mathrm{nm}$. The step edge mobility is determined by direct measurement of the equilibrium fluctuations of the steps, quantified by the prefactor G_0 of the time correlation function via [41]

$$\Gamma_h = G_0^4 \left(\frac{2\Gamma(3/4)}{\pi} \right)^{-4} \left(\frac{k_B T}{\tilde{\beta}} \right)^{-3} \tag{5.8}$$

At 300 K, the measured average values of G_0 are 0.04 and 0.08 $nm^2/s^{1/4}$ for straight step edges and rough step edges, respectively [41]. The standard deviation on these measured values is ~10% of the value, which by standard error propagation yields ~40% uncertainty on the mobility value. The corresponding G_0 values at 318 K are obtained by applying an interpolation based on the measured value of G_0 at 460 K, which is 0.93 $nm^2/s^{1/4}$. The resulting G_0 values at 318 K are 0.07 $nm^2/s^{1/4}$ for straight step edges and 0.14 $nm^2/s^{1/4}$ for rough step edges.

Using G_0 and $\tilde{\beta}$, now it is straightforward to calculate the step edge mobility Γ_h. The resulting values are 323.7 and 7.4 nm^5/s for straight and rough step edges, respectively. The corresponding values of the edge diffusion are $D_L = 1.8 \times 10^4$ nm^2/s for straight edges and $D_L = 4.1 \times 10^2$ nm^2/s for rough edges. A reasonable estimate of the uncertainty for these values is ~40% as noted above.

Combining these results and using the values in (5.5) yield a lower limit on the effective values of $Z^* \sim 750$. Once again, the biased diffusion resulting from the applied current leads to a surprisingly large estimate of the underlying electromigration force.

5.2.4 Kink-Enhanced Scattering

The unexpectedly strong force, measured in these two very different approaches, may arise from the highly kinked environment at the step edge as suggested in Fig. 5.1. Because diffusion is parallel to the step edge, only the component of the electromigration force tangential to the local step orientation will bias the step edge diffusion. The largest impact of the electromigration force will thus occur for the most highly kinked step regions. There have been no calculations of the electromigration force acting on low-symmetry kink sites. However, such sites have enhanced valence charge density [57] and also present anomalous barriers to step edge diffusion [58].

The surprisingly large magnitude in this case arises from at least three effects: current crowding, changes in scattering cross section, and changes in local electron density. Current crowding, the variation of local current density near constrictions in flow path (which will be discussed in detail in the following section), can cause local increases up to about a factor of 4 in extreme geometries [37]. However, the constriction due to current flow around the island edge is likely to be more modest, as discussed in the following section. The steps or the edges of the island themselves can act as reflecting barriers, increasing the cross section for scattering compared with a free atom on the surface by about a factor of at least 1.5 for Al(001) [38, 39]. Finally, atomic relaxation at step edges causes redistribution of local charge density [59], with especially strong enhancement, up to a factor of 10 on Cu(532), near kink sites [57]. The combination of these three effects therefore may account for about a

factor of 30 increase in the force on kink site atoms at the island edge compared to a free Ag atom. Using a quantum perspective rather than a classical perspective will be important in fully quantifying the nature of such nanoscale defects [2, 60–62].

5.3 Direct Observation of Current Distribution

As noted above, current crowding near defect structures is expected to play an important role in determining the nature of electron scattering and the electromigration force. At the nanoscale, the direct characterization of current distributions is difficult. However, the classical electrostatic principles governing current flow are independent of scale. Thus observations of current crowding at the micron scale can be used to assess the classical limits of behavior at the nanoscale.

Here we demonstrate quantification of spatial distributions of current flow by measurement of the magnetic fields above current-carrying structures using magnetic force microscopy (MFM). The effects of defect shape and size are characterized by systematically fabricating different structural defects using lithography and focused ion beam milling. The structures were chosen to represent typical defects observed in technological electromigration failures and to provide an evaluation of the effects of defect aspect ratio, pitch, and rounding on the patterns of deflected current.

5.3.1 Magnetic Force Measurements

In AFM [63, 64] and all related techniques (MFM, EFM, LFM, etc.), properties of the sample are deduced from the behavior of a small tip–cantilever system interacting with the sample. A tip, typically some etched silicon or silicon nitride pyramidal structure (see Fig. 5.7a), is attached to a cantilever, typically between 50 and 200 mm in length, that has a reflective coating on the top surface. The behavior of this cantilever may be tracked by monitoring the position of a laser beam reflected off the top reflective side of the cantilever, usually with some photodiode-based detector.

The tapping (also known as “intermittent contact” or “non-contact”) AFM technique involves tracking the amplitude of the cantilever, driven in oscillation on (or near) resonance, as its tip passes over the sample under study. As the cantilever is brought near to a sample, its tip eventually begins to tap the surface, dissipating energy and changing the vibrational amplitude of the tip. As the tip is scanned over the sample surface, the feedback loop changes the height of the tip–cantilever to keep this oscillation amplitude fixed. This tip height is recorded as a function of position generating the topography of the sample. Tapping AFM is less damaging and more sensitive than earlier contact AFM techniques, where a passive tip is dragged across the surface and the deflection of the cantilever is the feedback

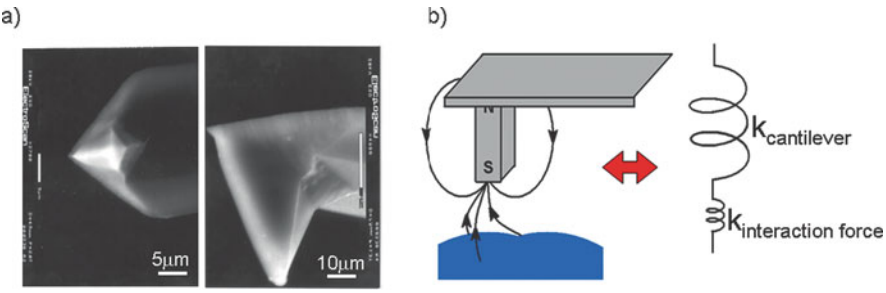

Fig. 5.7 (**a**) Scanning electron micrograph of MESP-HM magnetic tips, which are etched silicon probes coated in Co/Cr and magnetized along the pyramid axis, perpendicular to the sample. (**b**) Schematic illustration of the interaction between the magnetic tip and the sample that perturbs the effective spring constant of the cantilever

element. More importantly, the oscillation of the cantilever is necessary for the phase imaging which sets the foundation for the magnetic detection mechanism described below.

Standard phase shift techniques, such as MFM and EFM, extract information from the phase response of the oscillating cantilever, driven at fixed frequency, as its tip passes over the sample. Near the surface, the interaction force between the tip and the sample changes the effective spring constant of the cantilever, shown schematically in Fig. 5.7b, changing its natural resonance frequency and thus forcing the phase to change. The phase shift detected depends on the interaction force as

$$\mathrm{d}\varphi = -\frac{Q}{k}\,\frac{\partial F_{\mathrm{tip-sample}}}{\partial z} \tag{5.9}$$

where the quality factor, Q, and the spring constant, k, are constants dependent upon the individual tip–cantilever system used. The phase will shift in response to the presence of any interaction force between the tip–cantilever system and the sample, and an appropriate expression for the shift can be derived for a specific interaction force.

In MFM phase imaging the interaction force depends on the gradient of the scalar product of the tip magnetization, m, and the sample magnetic field, B:

$$\vec{F}_{\mathrm{tip-sample}} = \vec{F}_{\mathrm{magnetic}} = \vec{\nabla}(\vec{m}\cdot\vec{B}) \tag{5.10}$$

For MFM tip magnetization perpendicular to the sample (vertical magnetization), the MFM phase shift is proportional to the curvature of the vertical component of the magnetic field, B_z, and the vertical magnetization of the tip, m_z:

$$d\varphi = -\frac{Q}{k} m_z \frac{\partial^2 B_z}{\partial z^2} \tag{5.11}$$

The influence of the size of the magnetic tip on the measured signal will be discussed in Sect. 5.3.3.

As is apparent in (5.9), the phase of the oscillating cantilever will shift in response to any existing force(s) between the tip and the sample. Because the magnetic force gradients are weak, it is important to eliminate the effects of topographic and electrostatic structure in imaging. To eliminate topographic interactions, phase data are generally taken at a significant lift height from the sample. To do so, a lift mode is used, in which the tip makes two line scans over the sample for each recorded line. During the first scan, topography is recorded. During the second scan, the tip is lifted at a constant height above a specific baseline calculated by the data acquisition software and held at that level during the entire pass. To exclude phase response due to electrostatic forces, the potential between the tip and the sample may be nulled by an external voltage divider [65, 66], thereby eliminating any electrostatic component in the total phase response.

5.3.2 Experimental Implementation

The magnetic signal generated by current-carrying wires is much smaller than that of magnetic samples for which early MFMs were designed. Therefore, our optical head contains a special low noise laser (Digital Instruments part no. 226-000-0004), which is specified to have minimized mode hopping, a phenomenon that can result in artifacts and noise in the images. The magnetic tips used are commercially available Co/Cr-coated MESP (magnetic etched silicon probe) tips or their higher moment counterparts (MESP-HM), magnetized along the tip axis, perpendicular to the sample surface. Sample holders are electrically isolated from the conducting cap on the scanner piezo. To allow current biasing, they have two or three large contact pads that are connected by thin 40-gauge wires to external electronics. Care was taken to protect the scanner's piezo element from overheating which can cause the scanner's lateral distance calibration to fail by as much as 30%.

Samples were fabricated with controlled geometries to implement and measure the effects of current stressing by standard photolithography/liftoff created on thermally grown SiO_2 by photolithography, followed by thermal evaporation of 20 nm Cr and 110 nm Au. The metallic line widths were 10–12 μm and the fabricated defects were generally 1–7 μm in size, as shown in Fig. 5.8a. MFM measurements were made with typical currents in the individual lines of about 33 mA, corresponding to current densities on the order of $3–4 \times 10^6$ A/cm^2. Simulated defect structures were fabricated using a combination of standard photolithography/liftoff and focused ion beam (FIB) milling techniques. The FIB milling allowed for defect dimensions as small as 0.5 μm with the sharpest corners and apexes having a 50 nm radius of curvature. Ion milling was performed with 50 kV Ga^+ ions using a Micrion 2500 FIB machine with a 5 nm beam column. A serpentine beam scanning

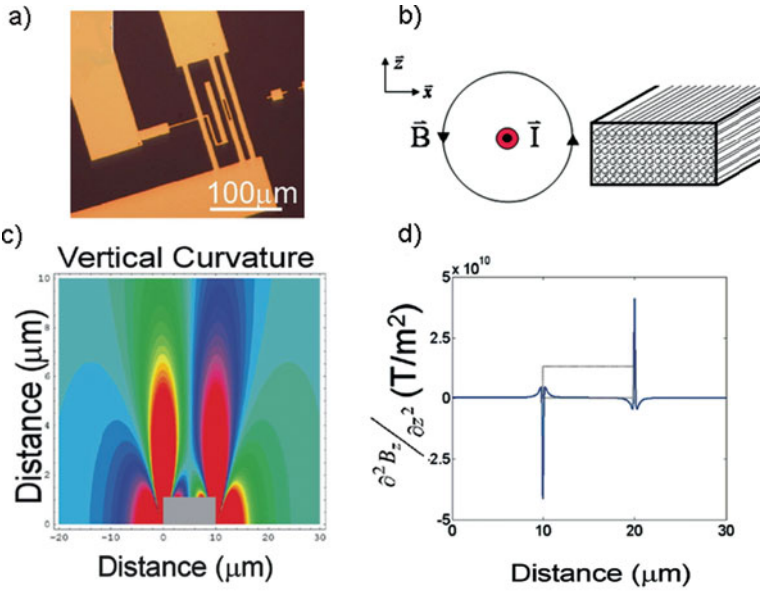

Fig. 5.8 (**a**) Optical photograph of a sample containing a 3 μm × 40 μm slot, created by photolithography, thermal evaporation, and liftoff. (**b**) Schematic of the circular field around a single wire and a cartoon of a rectangular metal line being modeled as bundle of infinitesimally thin wires. (**c**) Contour plot of the curvature of the vertical component of the magnetic field from a wire of rectangular cross section, modeled as shown in (**a**). (**d**) Line scan from the contour plot in (**c**), taken 100 nm above the wire top surface

procedure and relatively low ion current (∼30 pA) were chosen to provide better control of slit shape.

5.3.2.1 Demonstrating MFM Current Detection

For the purposes of intuitively understanding the MFM phase images, we may perform a simple analytical calculation of the expected vertical field curvature, where the metal lines are modeled as bundles of infinitely long, infinitesimally thin wires, as shown in the schematic of Fig. 5.8b. Such systems possess two-dimensional symmetry and may be easily integrated. For simple systems where the current flows along lengths that are long compared to characteristic tip dimensions, this model is quite accurate. We may therefore solve for the magnetic field around the conductor, by integrating the magnetic field contributions of infinitesimally thin, infinitely long wires over the cross-sectional area of the conductor. The expected MFM phase signal can then be calculated by taking the second vertical spatial derivative of the magnetic field. The resulting magnetic field lines must curve around the current lines, and the vertical component of the magnetic field thus varies greatly across the width of the wire, from zero along the middle of the line to a maximum at the edges,

as shown in Fig. 5.8c, d. Since two spatial derivatives are involved, the relative variation in magnetic field curvature near edges and surface defects is even larger than that in the actual field and is responsible for the high MFM resolution around small structures. Note that since the MFM signal is proportional to the vertical magnetic field curvature, we expect the contrast to be maximum at edges parallel to the current flow and, given a homogenous current density, this contrast should be symmetric (equal in magnitude but opposite in polarity). This illustrative analysis is a good approximate method for determining the nature of current crowding. For more quantitative analysis and for lines containing rather complicated defect structures, a finite-element calculation may be used to determine the expected current density, resulting field, and MFM signal.

A tapping AFM image and the corresponding MFM phase image for the 1 μm × 1 μm notch are shown in Fig. 5.9. Given the vertical tip magnetization, there is MFM contrast only at the line edges where the magnetic field must curve into or out of the sample plane. In the presence of a uniform current density, the MFM signal at the line edges must be symmetrical. This behavior is observed for lines of constant width [65, 67] and in the present lines for measurements away from the notch. There is significantly higher contrast at the notch edge than at the line edge on the side opposite the notch. The bold gray line profile in Fig. 5.9b, averaged over a 0.5 μm segment (12 out of 512 line scans) along the symmetry point of the notch, shows high asymmetry in the MFM peak heights. As a reference for comparison, the thin line profile of Fig. 5.9b, which shows the signal averaged along a 0.5 μm segment away from the notch, has the typical symmetry of a line with uniform current density. This reference profile was used to determine the non-uniform background, which was fixed by requiring that the reference line peaks have identical heights. After background subtraction, the asymmetry in the peak heights at the notch is found to be 1.5.

Although a rigorous inversion can be performed on the MFM, understanding of the current crowding phenomena can be obtained from the simple model described above. To introduce the effect of current crowding, these infinitesimally thin wires were divided into groups as shown in the inset of Fig. 5.9c. The current density in each group was assigned with higher values closer to the notch. For our calculations, five conductor segments were used: four of width 2 μm and one of width 1 μm. The curvature of the vertical component of the magnetic field was calculated for each segment, the field curvatures from the segments were added together, and the result was convolved with the estimated instrumental phase response [68] to account for tip dimensional effects. Calculations using current densities with constant or gently increasing gradients yielded near-unity asymmetries about 20% lower than observed. A current density distribution that is much more localized to the notch yields the calculated signal shown in the curve of Fig. 5.9c, more consistent with what was measured. The current distribution that yielded the calculated curve puts about 70% of the current displaced by the 1 μm notch into the 1 μm adjacent segment. The observed asymmetry in the MFM signal is consistent with a highly localized current crowding effect and is qualitatively similar to the numerical analysis of Artz et al. [10, 69].

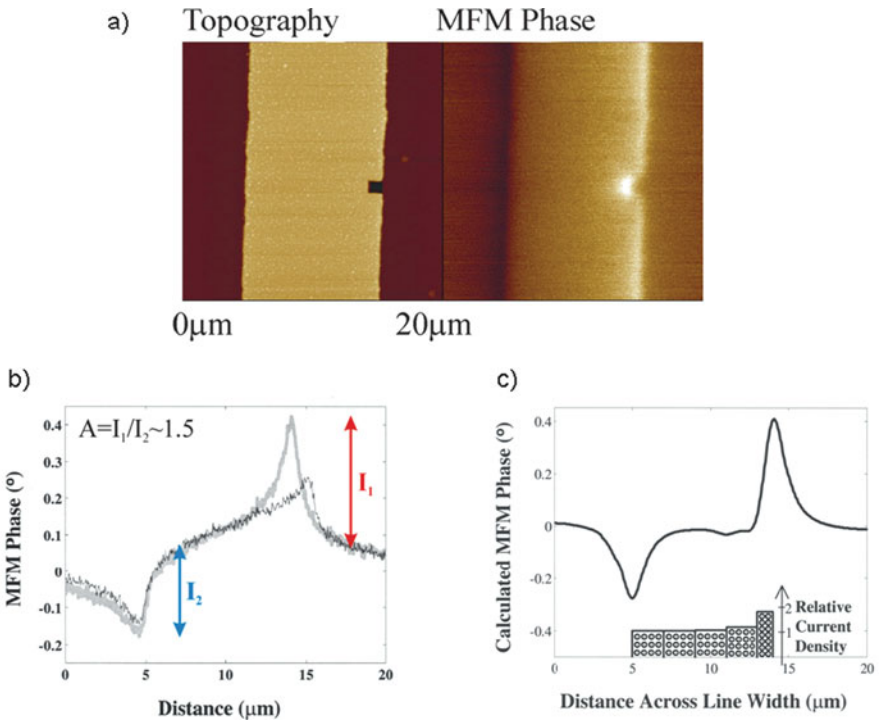

Fig. 5.9 (**a**) Topography and MFM phase of line containing 1 μm × 1 μm notch: 20 μm × 20 μm image of a 10 μm line with a 1 μm × 1 μm notch on one side. This line is carrying a 33 mA current, corresponding to a 3.3×10^6 A/m^2 current density. *Left*: AFM topography (z-range: 350 nm). *Right*: Corresponding MFM phase measured with 200 nm linear lift height (z-range: 1.0°). (**b**) MFM phase line scans from line containing 1 μm × 1 μm notch. The *bold gray line* is an MFM scan measured perpendicular to the line and across the notch center, averaged over a 0.5 μm segment (12 out of 512 line scans), while the *thin dark line* is an MFM reference away from the notch. (**c**) Model of current distribution in line containing 1 μm × 1 μm notch. *Bottom inset bar graph*: model current density profile along the conductor width, normalized to the base uniform current in a normal, homogenous line; the 10 μm line width is divided into five segments, each a bundle of infinitesimally thin, infinitely long wires. *Graphed curve*: calculated MFM signal at the notch center, using the current density distribution shown in the inset. The calculated peak asymmetry is about 1.5

5.3.3 Deconvolution Procedure

Analysis of the MFM signals to determine the current distributions around defects requires that the instrumental broadening effect due to the tip size is removed. Since the tip is a real physical object, often in the form of an etched silicon pyramid with a magnetic Co/Cr coating, the three-dimensional tip response function tends to be narrow close to the tip apex and broadens higher up, toward the tip base. The three-dimensional response function can be reduced to an effective two-dimensional tip response. The measured MFM signal, $D(x, y, z)$, obtained at tip height z is a three-dimensional (3D) instrumental convolution

$$D(x, y, z) = \iiint A(x - x', y - y', z - z') f(x', y', z') \mathrm{d}x' \mathrm{d}y' \mathrm{d}z' = \iiint A(x', y', z') f(x - x', y - y', z - z') \mathrm{d}x' \mathrm{d}y' \mathrm{d}z' \tag{5.12}$$

over the instrumental response function $A(x, y, z)$ and the unknown true signal $f(x, y, z)$.

In either dipole or monopole models, the phase is dependent upon the interaction of the tip with the magnetic field of the sample. Due to the boundary conditions of the sample system, there is a degree of freedom in the vertical displacement of field strengths that allows the three-dimensional instrumental response to be rigorously reduced to a two-dimensional (2D) effective instrumental response, through integration of the vertical z-dependence. Since $\nabla \times \mathbf{H}$ vanishes above the sample, we may identify H with the gradient of a scalar potential function, Ψ, satisfying Laplace's equation:

$$\nabla^2 \Psi = 0 \tag{5.13}$$

According to the extended dipole model, $f(x, y, z + \Delta z)$ is proportional to the curvature of the magnetic field and the third vertical derivative of Ψ and can thus be written as a convolution over $f(x, y, z)$ (an analogous relation holds for the monopole model):

$$f(x, y, z + \Delta z) = \int G(x - \bar{x}, y - \bar{y}, \Delta z) f(\bar{x}, \bar{y}, z) \mathrm{d}\bar{x} \mathrm{d}\bar{y} \tag{5.14}$$

where the two-dimensional (2D) Green's function has the form

$$G(x, y, z) = \frac{z}{2\pi} \left(\frac{1}{x^2 + y^2 + z^2} \right)^{3/2} \tag{5.15}$$

Knowledge of $f(x, y, z)$ everywhere on a line $\mathrm{z} = \mathrm{z}_0$ thus determines $f(x, y, z)$ on every line where $z > z_0$. Thus the instrumental convolution along the vertical direction may be replaced by an effective response that is only dependent upon the relative tip height and it follows that

$$A_{\mathrm{eff}}(x, y, z_{\mathrm{tip}}) = \iint G(x - \bar{x}, y - \bar{y}, \Delta z) A_{\mathrm{eff}}(\bar{x}, \bar{y}, z_{\mathrm{tip}} + \Delta z) \mathrm{d}\bar{x} \mathrm{d}\bar{y} \tag{5.16}$$

Data can be taken at a small tip and sample separation, where the signal-to-noise ratio is optimized and the peaks are narrow relative to the tip response and propagated to a higher height where the signal peaks broaden and the tip response narrows (doing the reverse would involve a deconvolution rather than a convolution). The effective instrument response can be evaluated at this height, given knowledge of the true signal $f(x, y, z_{\mathrm{tip}} + \Delta z)$. A similar broadening convolution can then be performed on the tip response, bringing the narrow effective tip response obtained

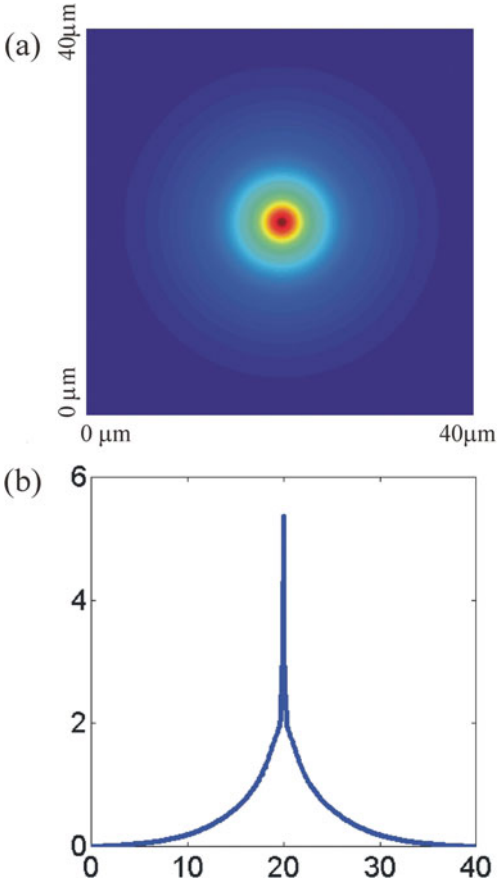

Fig. 5.10 Two-dimensional instrumental response function determined by iterative fitting. (**a**) The two-dimensional response function is shown on a 40 μm scale. (**b**) A slice of the two-dimensional response function shown in (**a**). The general broad features are similar to the one-dimensional response function found earlier. The spike was added to allow sufficient resolution in the vicinity of the small defect structures

at a large tip–sample separation to the lower separation of interest, where it is broader.

Thus, given data from a sample where the true signal is known, as is the case for regions from a straight wire far from the defect, the deconvolution algorithm may be used to determine the instrumental response. An example of an instrumental response function determined in this way is shown in Fig. 5.10. In the following, we will discuss the determination of current distributions from MFM data from which the instrumental broadening has been removed via deconvolution.

5.3.4 Image Inversion

Following deconvolution to remove the instrumental broadening, it is possible to quantify the distribution of currents underlying the MFM images by inverting the data. Techniques of inversion from the magnetic field have been well developed

for two-dimensional current distributions [70–72] and can be extended to inversion from MFM phase signal, which is proportional to the curvature of the magnetic field.

The magnetic field, $\mathbf{B}(\mathbf{r})$, at an observation point $\mathbf{r}$, is related by the Biot–Savart law to the current density, $\mathbf{J}(\mathbf{r}')$, at all source points $\mathbf{r} = (\mathbf{x}', \mathbf{y}', \mathbf{z}')$. We assume that the current lies in a thin sheet of depth d in the xy-plane, the magnetization is along the z-axis and that $J_z = 0$. For standard MFM images, the magnetic field component of interest is B_z so the Biot–Savart law simplifies to

$$B_z(r) = \frac{\mu_0}{4\pi} \iiint \frac{(y - y')J_x(x', y') - (x - x')J_y(x', y')}{|\mathbf{r} - \mathbf{r}'|^3} \mathrm{d}x'\mathrm{d}y'\mathrm{d}z' \tag{5.17}$$

From (5.1), it may appear as though we are trying to retrieve two components of the current density (J_x and J_y) from a single measurement of the magnetic field, but at steady state, we may use the continuity equation, $\nabla \cdot J = 0$, to relate the two current components. The continuity equation is automatically satisfied if we write $J = \nabla \times M$.

For a current sheet of finite thickness, d,

$$J_x(x, y) = \frac{1}{2\alpha} \iint \left[\frac{k_y}{k^2} \mathrm{e}^{+k|z|} (\mathrm{e}^{kd} - 1)^{-1} \right] \mathrm{d}(k_x, k_y, z) \mathrm{e}^{-\mathrm{i}k_x x} \mathrm{e}^{-\mathrm{i}k_y y} \mathrm{d}k_x \mathrm{d}k_y \tag{5.18}$$

$$J_y(x, y) = \frac{1}{2\alpha} \iint \left[\frac{k_x}{k^2} \mathrm{e}^{+k|z|} (\mathrm{e}^{kd} - 1)^{-1} \right] \mathrm{d}(k_x, k_y, z) \mathrm{e}^{-\mathrm{i}k_x x} \mathrm{e}^{-\mathrm{i}k_y y} \mathrm{d}k_x \mathrm{d}k_y \tag{5.19}$$

The components of the current density inside the sample can be obtained by digitally filtering the MFM signal in Fourier space, a numerical procedure that is readily performed using standard fast-Fourier transform (FFT) algorithms. We have empirically found that this filter tends to remove the random, high-frequency noise intrinsic to MFM phase data and that it is relatively insensitive to error in the tip–sample separation, z (changes in z on the order of 25% do not seem to change the result noticeably).

5.3.5 Inversion Results for Prototypical Structures

The shape of a void defect, or any other current-deflecting structure, plays a significant role in determining the rate of electromigration-driven morphological evolution because of its effect on the degree of current crowding near the defect. Measurements were performed on a series of model structures designed to enhance understanding of current crowding and to define the limitations of the experimental technique. The first two structures, the slit-like defect and the 90° bend, were inspired by real-world defects, while the latter structures were chosen to isolate crowding dependence on specific geometric properties.

5.3.5.1 Effect of a Diagonally Oriented Slit-Like Defect

Electromigration-driven failure sites in interconnects in integrated circuits often assume the shape of a wedge or slit [73]. A slit-like form is the more aggressive of the two prototypical shapes and was thus chosen to represent current crowding in real-world defects. The topography and corresponding MFM phase of a 45°-slanted slit defect are shown in Fig. 5.11a, b. The greatly enhanced MFM contrast near the end of the slit is clear evidence of current crowding, as discussed previously in the context of the 1 μm × 1 μm notch defect in Fig. 5.9. These data were deconvolved and inverted using the methods described above, to obtain a quantitative image of the current density variations, as shown in the three panels of Fig. 5.11b. These panels show the parallel current density component, the perpendicular current density component, and the total current density. Since the raw MFM data are normalized to the signal from a uniform reference region far from the defect, the inversion is composed of relative values (that can be scaled by the known current density in the reference region, if so desired).

As expected, in regions far from the defect, the current is uniformly distributed across the line and there is no current flow perpendicular to the line ($J_x = J_{\text{perp}} = 0$). In the vicinity of the defect, the current is highly localized at the inner edge of the slit, with the current density a factor of 3.9 times larger than the reference current density far from the defect. This crowding region extends approximately 1 μm from the slit inner edge, as measured by the full-width at half-maximum of the maximum current density. The component of the current density parallel to the line edges decreases significantly in the 10 μm region leeward of the slit (upper half of the line, as seen in Fig. 5.11b and correspondingly increases on the other side of the slit. The non-vanishing component of the current density perpendicular to the line is confined to within 5 μm of the slit and takes the form of a current dipole. Due to the constrictive effect of the slit defect, the current must deviate to the right, yielding positive J_{perp}, on one side of slit and to the left, yielding negative J_{perp}, on the other side.

The results of an a priori finite-element calculation of the sheet current density for the conducting structure, as defined by the AFM topography image (Fig. 5.11c) of the line containing the slanted slit, are shown in Fig. 5.11d. From left to right, the panels correspond to the AFM topography of the sample, the parallel current density component, the perpendicular current density component, and the total current density. The color scale in each panel is equivalent to that in the corresponding panel in Fig. 5.11b. The basic features of the inverted current density behavior are consistent with the finite-element calculation. The spatial extent of the current crowding region in the inversion is within 1 μm of that in the calculation. The maximum current density is 4.4 times greater than that of the reference current density far from the defect, 10% higher than the 3.9 factor increase seen in the inversion. Compared to the calculated current density, the maximum measured current density and sharpness of the current crowding are slightly diminished. The blurring and attenuation of the measured current crowding are due, in part, to the incomplete recovery of the magnetic field curvature from the deconvolution. Incomplete recovery of the

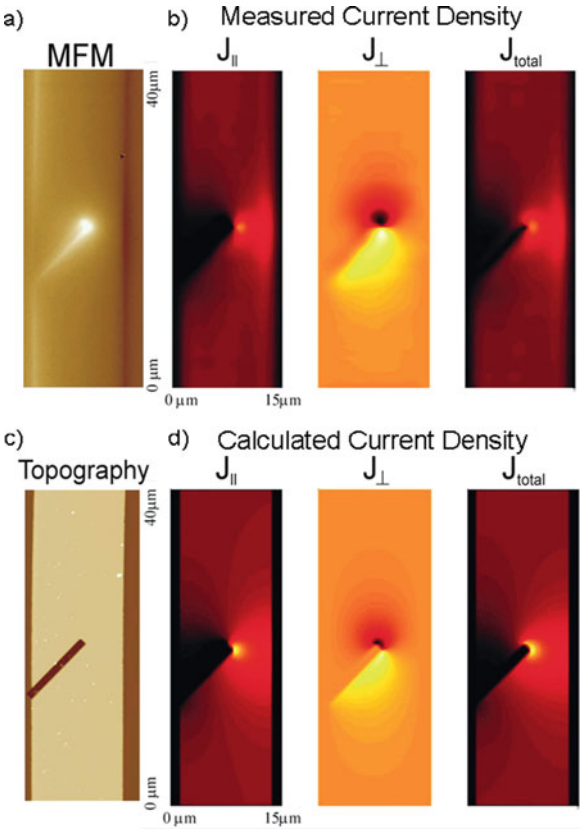

Fig. 5.11 (**a**) MFM image of (1×9) μm^2 45°-slanted slit defect. (**b**) Inverted current density, calculated from the MFM measurement in (**a**). From *left* to *right*, the panels correspond to the AFM topography of the sample, the parallel current density component, the perpendicular current density component, and the total current density. In the image of J_{total}, the color scale was chosen so that the brightest color corresponds to 3.9, the darkest to 0 (in units of current density that have been normalized to the reference current density far from the slit); the scale for the vertical component $J_y = J_{par}$ is similar (since to lowest order, the current flow is parallel to the line); the scale for the horizontal component $J_{perp} = J_x$ is such that the brightest (darkest) color corresponds to 1.6 (−1.6). Since the raw MFM data is normalized to the signal from a uniform reference region far from the defect, the inversion is composed of relative values (that can be scaled by the known current density in the reference region, if so desired). (**c**) Topography of the slit defect. (**d**) Finite-element calculation of the expected current density, based on the topography in (**c**). The color scale of each panel is equivalent to that of the corresponding panel in the inversion of (**b**). The maximum (normalized) calculated current density is 4.4

"true" signal would suggest that our results should be interpreted as a lower bound of the extent of the current crowding behavior. Errors associated with imperfect deconvolution will tend to make our results systematically low, but the −10% discrepancy between the inversion and the calculation for the slanted slit is also due to the physical issues associated with a real sample. In particular, the "softer," more

rounded line/defect edges are not accurately described by the present calculation, which assumes perfectly sharp edges; there is also a 50–100 nm skin of ion beam-damaged, higher resistance material surrounding the defect which should physically reduce the sharpness of the crowding.

Various structural characteristics of the slit defect contribute to its influence on local current. To better understand the current crowding effect, we may qualitatively decouple the structure's effects into a current direction changing component and a geometric component, which are discussed in the following sections.

5.3.5.2 Effect of Change of Current Direction

Conductive structures which induce large changes in current direction, such as interconnect vias and bends, are likely to exhibit significant current crowding, even though they are not defects per se. This effect is particularly important for industrial applications because all integrated circuits incorporate many bends and vias to increase the device density on chips. To illustrate this crowding effect, topography and MFM measurements were performed on a metallic line with a 90° bend, as shown in Fig. 5.12a, b. Once again, there is clear evidence of spatial variation in the current density, specifically strong variations in the MFM signal near the corners of the structure. These data were deconvolved and inverted using the methods described above, to obtain a quantitative image of the current density variations, as shown in Fig. 5.12c. From left to right, the panels correspond to the current density y-component, the current density x-component, and the total current density.

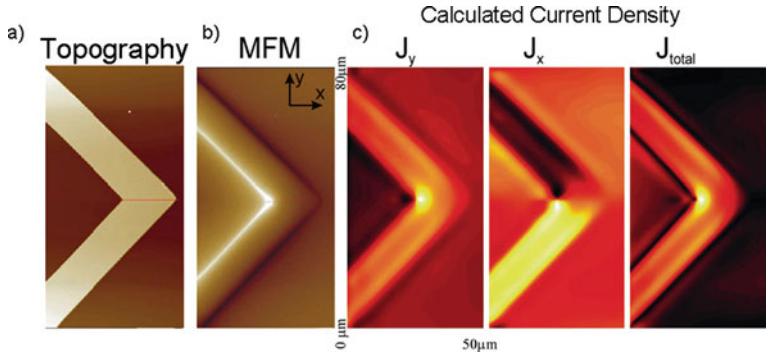

Fig. 5.12 90° bend in metallic line. (**a**) Topography of the 90° corner. (**b**) Corresponding MFM image. (**c**) Inverted current density, calculated from the MFM measurement in (**a**). From *left* to *right*, the panels correspond to the parallel current density component, the perpendicular current density component, and the total current density. In the image of J_{total}, the color scale was chosen so that the brightest color corresponds to 1.74, the darkest to 0 (in units of current density that have been normalized to the reference current density far from the corner); the scale for J_y (where the line is oriented at ±45° with respect to the y-axis) is similar; the scale for J_x is such that the brightest (darkest) color corresponds to $J_{\max} \sin 45°$ ($-J_{\max} \sin 45°$). The inversion is composed of relative values (that can be scaled by the known current density in the reference region, if so desired)

The results shown in Fig. 5.12 provide clear evidence for current crowding in the vicinity of the inner corner of the 90° bend, where the maximum current density is 1.74 as compared to regions far from the bend. There is a corresponding current depletion in the vicinity of the outer corner of the bend. The total normalized current density, J_{total}, across the line connecting the two corner edges (shown as a dotted red line in Fig. 5.12a) varies as 1.74 ± 0.05 at $x = 0$ (inner corner), 1.41 at $x = L/4$, 0.76 at $x = L/2$, 0.45 at $x = 3L/4$, and 0 at $x = L$, where $L = \sqrt{2}w$ (the line width). The vertical current density component, J_y, is essentially a $\cos(\pm 45°)$ projection of the total current density. The horizontal current density component, J_x, is the $\sin(\pm 45°)$ projection of the total current density, and we can therefore see the horizontal current direction change at the bend (where J_x changes sign).

The results can be compared with the results of an a priori finite-element calculation of the sheet current density for the conducting 90° bend that has been published previously [11]. The difficulty of this calculation lies in the mathematical divergence at the bend, which formally results in a current density divergence near the inner corner. As a result, the calculated maximum current density at the inner corner varies, depending on the computational step size from 2 to 4.5 [11], making comparison with experiment dubious. However, this difficulty does not affect the calculated values away from the corner, which show an estimated normalized current density, J_{total}, variation: 1.36 ± 0.05 at $x = L/4$, 0.77 at $x = L/2$, 0.41 at $x = 3L/4$, and 0 at $x = L$, where $L = \sqrt{2}w$ (the line width). The measured current density variation is in excellent ($< 10\%$) agreement with this calculation.

Current crowding can be qualitatively described as electrons following the path of least resistance, that is the shortest path available, and collectively crowding along this path, e.g., at the inner corners of bends. This kind of current crowding is particularly important for the semiconductor industry, because all integrated circuits necessarily incorporate changes in current path into their design. The degree of crowding can be mitigated by creating gentler transitions and directional changes, but this constrains designs that must also be optimized for device density and manufacturing efficiency.

5.3.5.3 Effects of Defect Shape and Size

The effects of the shape of a constriction, i.e., how rapidly the change occurs, and of the length (parallel to the current path) of the constriction are both of interest in assessing the effect of defects on current crowding in an electromigration context. Therefore a series of structures of systematically varying shapes were fabricated on a single current line for direct comparison. Here we illustrate the effects of taper and extent of the constriction.

Pang et al. have shown that the use of slowly tapering transition segments, between the contact pads and the lines of interest in a sample, will tend to increase the conducting lifetime of the sample [74], over the lifetime of samples that use square transitions with strong bottleneck effects. Such results would suggest that the current behavior is more severe in regions where the current density must change abruptly. To observe the dependence of current crowding on how abruptly the cur-

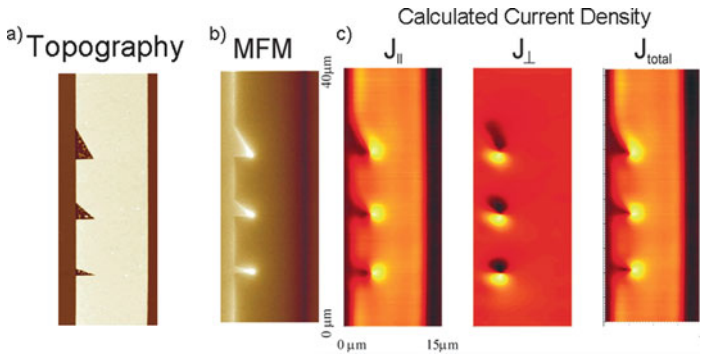

Fig. 5.13 Effect of current density gradient: (**a**) The sample topography shows three triangles that are 3-μm wide with base lengths of 4.9, 2.6, and 1 μm. (**b**) Corresponding MFM image. (**c**) Inverted current density, calculated from the MFM measurement in (**a**). From *left* to *right*, the panels correspond to the parallel current density component, the perpendicular current density component, and the total current density. In the image of J_{total}, the color scale was chosen so that the brightest color corresponds to 2.0, the darkest to 0 (in units of current density that have been normalized to the reference current density far from the defects); the scale for the horizontal component $J_{\text{perp}} = J_x$ is such that the brightest (darkest) color corresponds to 0.7 (−0.7)

rent density changes, we fabricated a series of right-triangular notches, each with the same 3 μm width but with base lengths (parallel to the line) varying from 1 to 10 μm, in 12-μm-wide lines. Since the apex of each triangle is limited by the 50 nm FIB spatial resolution, any differences in current crowding between the defect structures are due to the length of the triangle base, rather than the sharpness of triangle apex (which is ∼50 nm for each triangle). The AFM topography and MFM phase image of these samples are shown in Fig. 5.13a, b. The MFM phase for the three structures does increase with the current gradient near the defects but the correlation is somewhat weak. Thus the crowding appears to be dominated by the abrupt change in current direction where the metallic line resumes its nominal width, a scenario which is qualitatively similar to the 90° bend discussed above.

The inverted current densities for this sample, calculated from the MFM phase data in Fig. 5.13b, are shown in Fig. 5.13c. Similar to the defects discussed above, there is significant crowding at the point where the electron path is shortest, i.e., at the triangle apex. Effects of current density gradient are particularly visible in the perpendicular component of the current density, where the gentlest gradient (longest triangle base) structure results in the lowest deviation from parallel current flow. The three triangles, of base length, of 4.9, 2.6, and 1 μm, have respective maximum (normalized) current densities of 1.63, 2.00, and 1.98. The lower crowding for the largest base triangle is consistent with the expectation for a more gradual taper in the constriction. For the two steeper tapers, the differences are smaller than the sensitivity of our measurement.

These results for tapered structures can be contrasted with results for current blocking structures of identical shape but variable length along the current path, as illustrated in Fig. 5.14. The topography and MFM phase of (2×2) μm^2, (0.5×2)

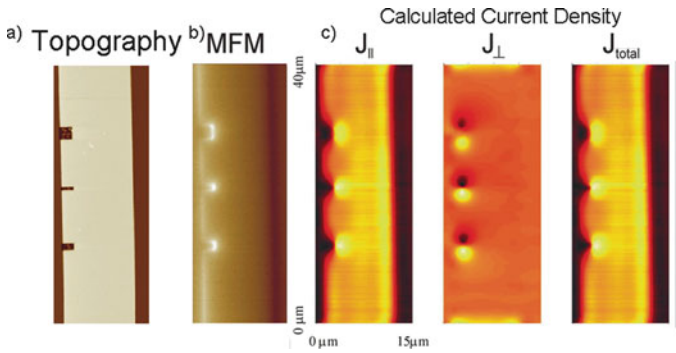

Fig. 5.14 Rectangular defects of variable width. (**a**) The sample topography includes notches 2-μm wide, with lengths of 1, 0.5, and 2 μm. (**b**) Corresponding MFM image. (**c**) Inverted current density, calculated from the MFM measurement in (**a**). From *left* to *right*, the panels correspond to the parallel current density component, the perpendicular current density component, and the total current density. In the image of J_{total}, the color scale was chosen so that the brightest color corresponds to 1.3, the darkest to 0 (in units of current density that have been normalized to the reference current density far from the defects); the scale for the horizontal component $J_{\text{perp}} = J_x$ is such that the brightest (darkest) color corresponds to 0.1 (−0.1)

μm^2, and (1×2) μm^2 rectangular notches of 12-μm-wide lines are shown in Fig. 5.14a, b. The corresponding inverted current density of this sample is shown in Fig. 5.14c, with respective maximum (normalized) current density of 1.10, 1.29, and 1.29. The value of 1.1 is less than expected, which is likely due to incomplete deconvolution. The current density for both the 1 and 0.5 μm notches is clearly higher than that of the 2 μm notch, as expected. For the two shorter notches, the dipole-like appearance of the perpendicular component of the current density also appears to be sharper than the longer notch, which indicates that the change in current path is more abrupt. The inverted current density of the shortest 0.5 μm notch is equivalent to that of the larger 1 μm notch. The similarity of the current density around the two defects occurs because their crowding behaviors are dominated by the defect edges.

5.3.5.4 Effect of Feature Sharpness

As noted above, the lack of abrupt boundaries in physical structures may account for reduced current crowding in physical structures as compared with calculations for perfectly sharp boundaries. To address such effects, a set of (6×2) μm^2 notches with corners of varying radii of curvature was fabricated in a current line. The notch corners were fabricated with radii of curvature $R = 1.0$ and 0.05 μm, as shown in Fig. 5.15. The inverted current density of the sample containing the notches with radii of curvature of $R = 1.0$ and $R = 0.05$ μm yields respective maximum normalized current densities of 1.94 and 1.97. The current density at the rounded corner is not distinguishable from that at the sharp corner, above the random noise intrinsic to the measurement, and the systematic error introduced by the analysis techniques. Since any focused ion beam damage corresponding to the dosage

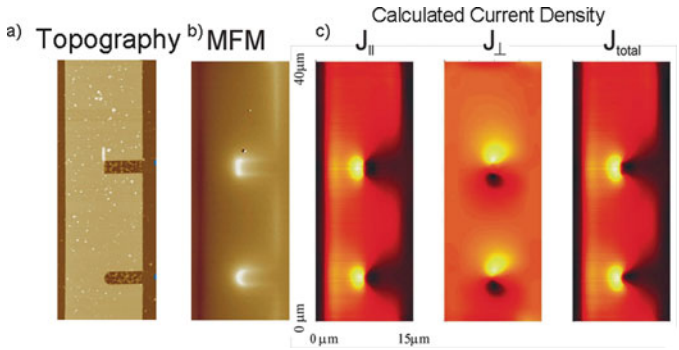

Fig. 5.15 Notches with different radii of curvature. (**a**) The sample topography shows $(2\times6)\ \mu m^2$ notches with corners of radius of curvature $R = 0.050$ and $R = 1.0\,\mu m$. (**b**) Corresponding MFM image. (**c**) Inverted current density, calculated from the MFM measurement in (**a**). From *left* to *right*, the panels correspond to the parallel current density component, the perpendicular current density component, and the total current density. In the image of J_{total}, the color scale was chosen so that the brightest color corresponds to 2.0, the darkest to 0 (in units of current density that have been normalized to the reference current density far from the slit); the scale for the horizontal component $J_{perp} = J_x$ is such that the brightest (darkest) color corresponds to 1.6 (−1.6)

parameters used will only penetrate to ∼50–100 nm, damaged-induced effects do not sufficiently account for the lack of a significant difference between the $R = 0.05$ and $R = 1.0\,\mu m$ corners. It is thus likely that the similarity between measured current densities is a real geometric effect, where crowding is dominated by the steep angle at which both structures deflect current flow, somewhat analogous to the 90° bend and tapered structures discussed earlier.

5.3.6 Current Crowding Effects

The MFM phase measurement, deconvolution, and inversion technique presented here allows quantification of spatially variable current density with sub-micron resolution. Although the analytical methodology involved may introduce systematic error into the final results, this technique remains highly suited for current density measurements on scales relevant to electromigration studies. The measurements are generally in good agreement with theoretical calculations which exclude discontinuities due to the (unphysical) infinitely sharp edges modeled.

For all the structures examined, the magnitude of current crowding is primarily determined by the abruptness of current deflection. However, the pattern of current crowding, and in particular the dipolar behavior of the perpendicular displacements, is strongly dependent on the size and sharpness of the structures. Since electromigration-driven diffusion is highly dependent upon local current density, current-deflecting defects will be particularly susceptible to nonlinearities, which accelerate mass flux and line failure. Similar behavior should be observed in nanoelectronic devices, with increasing impact as even atomic-scale structural defects will become a significant part of the cross section of a nanostructure.

5.4 Conclusions

Experimental quantification of electron scattering effects in nanoscale structures is in its infancy. Steps on macroscopic surfaces provide a useful model system for quantifying defect scattering in nanostructures, where the large surface/volume ratio will cause surface effects to dominate. The effects of defects can be documented via observations of local surface resistivity [24] and potential drops [26] related to surface steps, which provide direct electrostatic information with limited spatial resolution. In addition, direct measurements of current flow via MFM, as discussed above, can be scaled from micron-scale structures to assess the relative magnitudes of behavior likely at nanoscale structures. Direct measurements of electromigration-induced mass flow provide another window into the nature of electron scattering at defects. In this case, the observations can be interpreted in terms of atomic-scale mass transport, yielding structure-specific values of the electromigration force [75, 76].

The observations presented above represent the two extremes of high-resolution observations of electromigration-induced transport and low-resolution direct measurements of the electrostatic effects of surface scattering at defects. Analysis of the electromigration-induced transport on Ag(111) surfaces allowed identification of an atomically specific force, specifically acting at kink sites. The analysis of the force yielded a surprisingly large value, which in the ballistic electron scattering model may arise from a combination of geometric blocking at the kink sites, changes in electron density due to the lower coordination at the kink sites, and current crowding. The blocking effect is likely to yield an enhancement up to a factor of 2 at step edges compared with free adatoms on the surface [38, 39]. The direct measurements of current crowding at the micron scale show, for small aspect ratio structures analogous to kink sites, that the scale of the enhancement is more typically some tens of percent [77]. These classical effects thus do not predict the large enhancements measured. However, recent atomistic calculations including non-equilibrium transport explicitly may provide an explanation in terms of quantized conductance at the atomic-scale resistivity dipole created by current flow around kink sites [78]. Further experiments to assess the electromigration force for different metals and different types of scattering sites will be needed to test this exciting possibility.

Acknowledgments This work has been supported by the University of Maryland NSF MRSEC under grant # DMR 05-20471, including use of the Shared Experimental Facilities. Infrastructure support is also provided by the UMD NanoCenter and CNAM.

References

1. R.S. Sorbello, Electromigration and the local transport field in mesoscopic systems. Phys. Rev. **B39**, 4984 (1989)
2. R.S. Sorbello, Theory of electromigration. Solid State Phys. **51**, 159–231 (1997)
3. P.S. Ho, T. Kwok, Electromigration in Metals. Rep. Prog. Phys. **52**, 301–348 (1989)

4. A.A. Baski, K.M. Saoud, K.M. Jones, 1-D nanostructures grown on the Si(5512) surface. Appl. Surf. Sci. **182**, 216–222 (2001)
5. G. Gardinowski, J. Schmeidel, H. Pfnur, T. Block, C. Tegenkamp, Switchable nanometer contacts: Authrathin Ag nanostructures on Si(100). Appl. Phys. Lett. **89**, 063120 (2006)
6. K. Midori, P. Neelima, C. Vasily, V. Bert, Nanowires and nanorings at the atomic level. Phys. Rev. Lett. **91**(9), 096102 (2003)
7. Z. Suo, W. Wang, M. Yang, Electromigration instability: Transgranular slits in interconnects. Appl. Phys. Lett. **64**, 1944–1946 (1994)
8. D. Maroudas, Dynamics of transgranular voids in metallic thin films under electromigration conditions. Appl. Phys. Lett. **67**(798–800) (1995)
9. M.R. Gungor, D. Maroudas, Nonlinear analysis of the morphological evolution of void surfaces in metallic thin films under electromigration conditions. Surf. Sci. **415**, L1055–1060 (1998)
10. O. Kraft, E. Arzt, Numerical simulation of electromigration -induced shape changes of voids in bamboo lines. Appl. Phys. Lett. **66**, 2063–2065 (1995)
11. K.N. Tu, C.C. Yeh, C.Y. Liu, C. Chen, Numerical simulation of current crowding phenomena and their effects on electromigration in very large scale integration interconnects. J. Appl. Phys. **76**, 988–990. (2000)
12. E.C.C. Yeh, K.N. Tu, Numerical simulation of current crowding phenomena and their effects on electromigration in very large scale integration interconnects. J. Appl. Phys. **88**, 5680–5686 (2000)
13. H. Yasunaga, A. Natori, Electromigration on semiconductor surfaces. Surf. Sci. Rep. **15**, 205–280 (1992)
14. A.V. Latyshev, A.L. Aseev, A.B. Krasilnikov, S.I. Stenin, Transformations on Clean Si(111) stepped surface during sublimation. Surf. Sci. **213**, 157–169 (1989)
15. A. Yamanaka, K. Yagi, H. Yasunaga, Surface electromigration of metal atoms on Si(111) surface studied by UHV reflection electron microscopy. Ultramicroscopy **29**, 161–167 (1989)
16. Y. Homma, R. McClelland, H. Hibino, DC-resistive-heating-induced step bunching on Vicinal Si(111). Jpn. J. Appl. Phys. **29**, 2254–2256 (1990)
17. J.-J. Métois, and M. Audriffen, An experimental study of step dynamics under the influence of electromigration: Si(111). Int J Mod. Phys B **11**, 3691 (1997)
18. Y.-N. Yang, E.S. Fu, E.D. Williams, An STM study of current-induced step bunching on Si(111). Surf. Sci. **356**, 101–111 (1996)
19. C. Misbah, O. Pierre-Louis, Y. Saito, Crystal surfaces in and out of equilibrium: A modern view. Rev. Mod. Phys. **82**, 981 (2010)
20. M.F.G. Hedouin, P.J. Rous, Relationship between adatom-induced surface resistivity and the wind force for adatom electromigration: A layer Korringa-Kohn-Rostoker study. Phys. Rev. B **62**, 8473 (2000)
21. H. Ishida, Semiclassical derivation of the surface resistivity formula. Phys. Rev. B. **60**, 4532–4534 (1999)
22. T.N. Todorov, Spatial distribution of the electric current and field in atomic scale conductors. Philos. Mag. B **79**, 1577–1590 (1999)
23. Z. Yang, M. Chsiev, M. Zwolak, Y.-C. Chen, M. Di Ventra, Role of heating and current-induced forces in the stability of atomic wires. Phys. Rev. B, **71**, 041402R (2005)
24. I. Matsuda, M. Ueno, T. Hirahara, R. Hobara, H. Morikawa, C.H. Liu, S. Hasegawa, Electrical resistance of a monatomic step on a crystal surface. Phys. Rev. Lett. **93**(23), 236801 (2004)
25. O. Bondarchuk, W.G. Cullen, M. Degawa, E.D. Williams, T. Bole, P.J. Rous, Biased surface fluctuations due to current stress. Phys. Rev. Lett. **99**, 206801 (2007)
26. J. Homoth, M. Wenderoth, T. Druga, L. Winking, R.G. Ulbrich, C.A. Bobisch, B. Weyers, A. Bannani, E. Zubkov, A.M. Bernhart, R.R. Kaspers, R. Möller, Electron transport on the nanoscale: Ballistic transmission and Ohm's law. Nano Lett. **9**, 1588–1592 (2009)
27. H. Park, A.K.L. Lim, A.P. Alivisatos, J. Park, P.L. McEuen, Fabrication of metallic electrodes with nanometer separation by electromigration. Appl. Phys. Lett. **75**, 301–303 (1999)
28. G. Essen, M.S. Fuhrer, Break Junction monitoring. Appl. Phys. Lett. **87**, 263101 (2005)

29. T. Taychatanapat, K.I. Bolotin, F. Kuemmeth, D.C. Ralph, Imaging electromigration during the formation of break junctions. Nano Lett. **7**(3), 652–656 (2007)
30. S. Heinze, N.-P. Wang, J. Tersoff, Electromigration forces on ions in carbon nanotubes. Phys. Rev. Lett. **95**, 186802 (2005)
31. O. Pierre-Louis, Dynamic correlations of macroscopic quantities. Phys. Rev. E, **76**, 062601 (2007)
32. D. Dundas, E.J. McEniry, T.N. Todorov, Current-driven atomic waterwheels. Nat. Nanotechnol. **4**, 99–102 (2009)
33. H.-C. Jeong, E.D. Williams, Steps on surfaces: Experiment and theory. Surf. Sci. Rep. **34**, 171–294 (1999)
34. E.D. Williams, O. Bondarchuk, C.G. Tao, W. Yan, W.G. Cullen, P.J. Rous, T. Bole, Temporal step fluctuations on a conductor surface: Electromigration force, surface resistivity and low-frequency noise. New J. Phys. **9**, 387 (2007)
35. M. Rusanen, P. Kuhn, J. Krug, Kinetic Monte Carlo simulations of oscillatory shape evolution for electromigration-driven islands. Phys. Rev. B. **74**, 245423 (2006)
36. T. Sun, B. Yao, A.P. Warren, K. Barmak, M.F. Toney, R.E. Peale, K.R. Coffey, Dominant role of grain boundary scattering in the resistivity of nanometric Cu films. Phys. Rev. B, **79**, 041402 (2009)
37. J. Hoekstra, A.P. Sutton, T.N. Todorov, A. Horsfield, Electromigration of vacancies in copper. Phys. Rev. B **62**, 8568–8571 (2000)
38. P.J. Rous, Electromigration wind force at stepped Al surfaces. Phys. Rev. **B59**, 7719–7723 (1999)
39. P.J. Rous, Multiple-scattering theory of the surface resistivity of stepped Al surfaces. Phys. Rev. B **61**, 8484–8488 (2000)
40. O. Bondarchuk, D.B. Dougherty, M. Degawa, M. Constantin, C. Dasgupta, S. Das Sarma, Correlation Time for Step Structural Fluctuations. Phys. Rev. B. **71**, 045426 (2005)
41. C. Tao, T.J. Stasevich, T.L. Einstein, E.D. Williams, Step Fluctuations on Ag(111) surfaces with C_{60}. Phys. Rev. B **73**, 125436(1–7) (2006)
42. A.A. Baski, H. Fuchs, Epitaxial growth of silver on mica as studied by AFM and STM. Surf. Sci. **313**, 275 (1994)
43. M. Giesen, C. Steimer, H. Ibach, What does one learn from equilibrium shapes of two-dimensional islands on surfaces? Surf. Sci. **471**, 80–100 (2001)
44. F. Mugele, A. Rettenberger, J. Boneberg, P. Leiderer, The influence of tip–sample interaction on step fluctuations on Ag(111). Surf. Sci. **400**, 80–86 (1998)
45. M. Giesen, Step, Island Dynamics at solid/vacuum and solid/liquid interfaces. Prog. Surf. Sci. **68**, 1–153 (2001)
46. C. Tao, W.G. Cullen, E.D. Williams, C. Dasgupta, Generalized survival in step fluctuations. Phys. Rev. E **76**, 021601 (2007)
47. T.J. Stasevich, H. Gebremariam, T.L. Einstein, M. Giesen, C. Steimer, H. Ibach, Low-temperature orientation dependence of step stiffness on {111} surfaces. Phys. Rev. B. **71**, 245414 (2005)
48. G.S. Bales, A. Zangwill, Morphological instability of a terrace edge during step-flow growth. Phys. Rev. **B41**(9), 5500–5508 (1990)
49. P.J. Rous, T.W. Bole, Temporal evolution of step-edge fluctuations under electromigration conditions. Phys. Rev. B 2007. **76**, 125435 (1970)
50. B.S. Verma, H.J. Juretschke, Strain dependence of the resistivity of silver films. J. Appl. Phys. **41**, 4732–4735 (1970)
51. R.A. Matula, Resistivity of Noble Metals. J. Phys. Chem Ref. Data **8**, 1260 (1979)
52. K. Thürmer, J. Reutt-Robey, E.D. Williams, A. Emundts, H. Bonzel, M. Uwaha, Step dynamics in crystal shape relaxation. Phys. Rev. Lett. **87**, 186102–186104 (2001)
53. J.-M. Wen, S.-L. Chang, J.W. Burnett, J.W. Evans, P.A. Thiel, Diffusion of large two-dimensional Ag Clusters on Ag(100). Phys. Rev. Lett. **73**, 2591–2594 (1994)
54. K. Morgenstern, G. Rosenfeld, B. Poelsema, G. Comsa, Brownian motion of vacancy islands on Ag(111). Phys. Rev. Lett. **74**, 2058–2061 (1995)

55. O. Pierre-Louis, T.L. Einstein, Electromigration of single layer clusters. Phys. Rev. **B62**, 13697–13706 (2000)
56. P. Kuhn, J. Krug, F. Hausser, A. Voigt, Complex shape evolution of electromigration-driven single-layer islands. Phys. Rev. Lett. **94**(16) (2005)
57. F. Mehmood, A. Kara, T.S. Rahman, First principles study of the electronic and geometric structure of Cu(532). Surf. Sci. **600**, 4501–4507 (2006)
58. J. Ikonomov, K. Starbova, M. Giesen, Island coalescence and diffusion along kinked steps on Cu(001): evidence for a large kink Ehrlich-Schwoebel barrier. Surf. Sci. **601**, 1403–1408 (2007)
59. Y. Mo, W. Zhu, E. Kaxiras, Z.Y. Zhang, Electronic nature of step-edge barriers against adatom descent on transition-metal surfaces. Phys. Rev. Lett. **101**, 216101 (2008)
60. R.S. Sorbello, Residual Resistivity dipole in electron transport and electromigration. Phys. Rev. **B23**, 5119 (1981)
61. N.D. Lang, Resistance of atomic wires. Phys. Rev. **B52**, 5335–5342 (1995)
62. B.G. Briner, R.M. Feenstra, T.P. Chin, J.M. Woodal, Local transport properties of thin bismuth films studied by scanning tunneling potentiometry. Phys. Rev. **B54**, R5283–5286 (1996)
63. B. Binnig, H. Rohrer, Scanning tunneling microscopy – from birth to adolescence. Rev. Mod. Phys. **59**, 615–625 (1987)
64. C.F. Quate, The atomic force microscope as a tool for surface imaging. Surf. Sci. **299/300**, 980 (1994)
65. R. Yongsunthon, J. McCoy, E.D. Williams, Evaluation of MFM for quantification of electromigration processes. ULSI Metrol. Conf. Proc. **550**(1), 630–634 (2001)
66. R. Yongsunthon, J. McCoy, E.D. Williams, Calibrated MFM Measurement of Current-carrying Lines. J. Vacuum Sci. Technol. **19**(4), 1763–1768 (2001)
67. R.D. Gomez, A.O. Pak, A.J. Anderson, E.R. Burke, A.J. Leyendecker, I.D. Mayergoyz, Quantification of magnetic force microscopy images using combined electrostatic and magnetostatic imaging. J. Appl. Phys. **83**, 6226–6228 (1998)
68. R. Yongsunthon, A. Stanishevsky, J. McCoy, E.D. Williams, Observation of current crowding near fabricated voids in Au lines. Appl. Phys. Lett. **78**, 2661–2663 (2001)
69. E. Arzt, O. Kraft, W.D. Nix, J.E. Sanchez, Electromigration failure by shape change of voids in bamboo lines. J. Appl. Phys. **76**, 1563–1571 (1994)
70. B.J. Roth, N.G. Sepulveda, J.J.P. Wikswo, Using a magnetometer to image a two-dimensional current distribution. J. Appl. Phys. **65**, 362–382 (1989)
71. S. Chatraphorn, E.F. Fleet, F.C. Wellstood, L.A. Knauss, T.M. Elles, Scanning SQUID microscopy of integrated circuits. Appl. Phys. Lett. **2000**, 2304–2306 (2000)
72. J.J.P. Wikswo. The magnetic inverse problem for NDE in NATO ASI: SQUID Sensors: Fundamentals, fabrication and applications. 1996. Acquafredda di Maratea, Italy: NATO ASI Series
73. M.R. Gungor, D. Maroudas, Electromigration with current crowding. J. Appl. Phys. **85**, 2233 (1999)
74. X. Pang, A.M. Kriman, G.H. Bernstein, Electromigration in nanometer Al-Cu Interconnect Lines. J. Electrochem. Soc. **149**, G103-G1.8 (2002)
75. J. Krug, H.T. Dobbs, Current-Induced Faceting of Crystal Surfaces. Phys. Rev. Lett. **73**, 1947–1950 (1994)
76. O. Pierre-Louis, Local Electromigration Model for Crystal Surfaces. Phys. Rev. Lett. **96**(13), 135901 (2006)
77. R. Yongsunthon, E.D. Williams, A. Stanishevsky, P. Rous, J. Mccoy, R. Pego, Magnetic force microscopy signatures of defects in current-carrying lines. Mater. Res. Soc. Symp. Proc. **699**, 107–112 (2002)
78. K.H. Bevan, H. Guo, E.D. Williams, Z.Y. Zhang, First-principles quantum transport theory of the enhanced wind force driving electromigration on Ag(111). Phys. Rev. **B81** (23), 235416 (2010)
79. C. Tao, Doctoral Dissertation: Fluctuations on metal surfaces and molecule/metal interfaces, Department of Physics, University of Maryland: College Park, MD, 2007

Chapter 6
Classification Order of Surface-Confined Intermixing at Epitaxial Interface

M. Michailov

Abstract The self-organization phenomena at epitaxial interface hold special attention in contemporary material science. Being relevant to the fundamental physical problem of competing, long-range and short-range atomic interactions in systems with reduced dimensionality, these phenomena have found exacting academic interest. They are also of great technological importance for their ability to bring spontaneous formation of regular nanoscale surface patterns and superlattices with exotic properties. The basic phenomenon involved in this process is surface diffusion. That is the motivation behind the present study which deals with important details of diffusion scenarios that control the fine atomic structure of epitaxial interface. Consisting surface imperfections (terraces, steps, kinks, and vacancies), the interface offers variety of barriers for surface diffusion. Therefore, the adatoms and clusters need a certain critical energy to overcome the corresponding diffusion barriers. In the most general case the critical energies can be attained by variation of the system temperature. Hence, their values define temperature limits of system energy gaps associated with different diffusion scenarios. This systematization imply classification order of surface alloying: blocked, incomplete, and complete. On that background, two diffusion problems, related to the atomic-scale surface morphology, will be discussed. The first problem deals with diffusion of atomic clusters on atomically smooth interface. On flat domains, far from terraces and steps, we analyzed the impact of size, shape, and cluster/substrate lattice misfit on the diffusion behavior of atomic clusters (islands). We found that the lattice constant of small clusters depends on the number N of building atoms at $1 < N \leq 10$. In heteroepitaxy, this effect of variable lattice constant originates from the enhanced charge transfer and the strong influence of the surface potential on cluster atomic arrangement. At constant temperature, the variation of the lattice constant leads to variable misfit which affects the island migration. The cluster/substrate commensurability influences the oscillation behavior of the diffusion coefficient caused by variation in the cluster shape. We discuss

M. Michailov (✉)
"Rostislaw Kaischew" Institute of Physical Chemistry, Bulgarian Academy of Sciences, 1113, Sofia, Bulgaria
e-mail: mike@ipc.bas.bg

M. Michailov (ed.), *Nanophenomena at Surfaces,* Springer Series in Surface Sciences 47,
DOI 10.1007/978-3-642-16510-8_6,

the results in a physical model that implies cluster diffusion with size-dependent cluster/substrate misfit. The second problem is devoted to diffusion phenomena in the vicinity of atomic terraces on stepped or vicinal surfaces. Here, we develop a computational model that refines important details of diffusion behavior of adatoms accounting for the energy barriers at specific atomic sites (smooth domains, terraces, and steps) located on the crystal surface. The dynamic competition between energy gained by mixing and substrate strain energy results in diffusion scenario where adatoms form alloyed islands and alloyed stripes in the vicinity of terrace edges. Being in agreement with recent experimental findings, the observed effect of stripe and island alloy formation opens up a way regular surface patterns to be configured at different atomic levels on the crystal surface. The complete surface alloying of the entire interface layer is also briefly discussed with critical analysis and classification of experimental findings and simulation data.

6.1 Introduction

The problem of surface diffusion and surface-confined intermixing is of fundamental importance for contemporary material science [1–5]. Besides the purely academic challenge, the attention to this phenomenon is inspired by the strong dependence of basic physical properties of electronic devices on the sharpness at atomic level of the interface between materials. That is why detailed knowledge of the fine atomic structure and thermodynamic properties of the epitaxial layer is crucial for design and fabrication of interfaces with preferred exotic features. Since surface diffusion is basic phenomenon controlling nanostructure formation on surfaces, this study deals with a variety of diffusion scenarios that cause 2D pattern formation on epitaxial interface. Accounting for energy barriers at specific sites on the crystal surface, the computational model presented opens up a way the entire interface to be manipulated at atomic level in great detail [4]. In this case the fine-tuning of the adatom energy through temperature variation can direct the basic mass-transport mechanisms in a way that promotes or restricts the evolution of specific nanoscale surface patterns. In the next sections we will review and analyze the diffusion energy barriers and the resulting diffusion processes on atomically smooth domains and stepped (vicinal) interfaces.

6.2 Surface Imperfections and Diffusion Energy Barriers on Epitaxial Interface

Detailed analysis of the general picture of surface morphology on atomic scale reveals different types of surface diffusion barriers E_{DB} for adsorbed particles [4, 6–8]. Being caused by surface imperfections as steps, kinks, domain boundaries, defects, or vacancies, these barriers involve a variety of activation energies which control diffusion on flat, atomically smooth surface domains; diffusion in the vicinity of steps of atomic terraces; and diffusion inside the outermost surface

layer, Fig. 6.1. Hence, the migration of adatoms is confined in specific energy gaps imposed by the dominant surface morphology. Determined by the site-dependent values of E_{DB}, the diffusion in each of the above scenarios could generate completely different, stable atomic arrangements of the epitaxial interface. That is why, detailed analysis of the specific energy barriers for atomic migration on the crystal surface might reveal new mechanisms for fine-tuning of diffusion processes and for generation of nanoscale surface patterns with variable size and geometry [4]. The native interface structure consists of islands and terraces with steps and smooth domains. Therefore, a random walking adatom with energy $E^{\mathrm{D}}_{\mathrm{ATOM}}$ meets different energy barriers shown in Fig. 6.1: (i) $E^{\mathrm{DB}}_{\mathrm{SMOOTH}}$ – the barrier for diffusion on top of smooth domains; (ii) $E^{\mathrm{DB}}_{\mathrm{DIRECT}}$ – the barrier for direct incorporation inside the substrate; and (iii) $E^{\mathrm{DB}}_{\mathrm{STEP}}$ – the barrier for diffusion inside the terrace for atoms passing through the steps. On that physical background we consider diffusion scenarios in specific energy regions. Being correlated with the system temperature, these regions are defined by the following equations:

$$E^{\mathrm{D}}_{\mathrm{ATOM}} < E^{\mathrm{DB}}_{\mathrm{STEP}} < E^{\mathrm{DB}}_{\mathrm{DIRECT}} \tag{6.1}$$

(i) The diffusion behavior in this energy region is typical for low temperatures at which the adatom energies are below the diffusion barriers for direct incorporation into the substrate, as well as for penetration in the terrace by passing through the steps. This case is relevant to a simple random walk of adatoms exclusively on top of the interface layer (the yellow atoms in Fig. 6.1). It will be considered as atomic diffusion at blocked surface intermixing.

$$E^{\mathrm{DB}}_{\mathrm{STEP}} \leq E^{\mathrm{D}}_{\mathrm{ATOM}} < E^{\mathrm{DB}}_{\mathrm{DIRECT}} \tag{6.2}$$

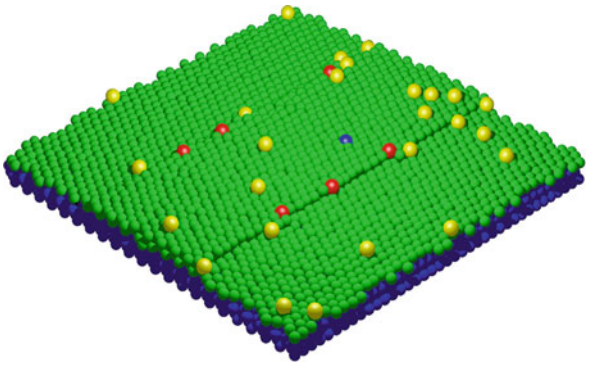

Fig. 6.1 Principal view of basic types of energy barriers for surface diffusion on stepped or vicinal epitaxial interface: (i) the barrier for diffusion on top of smooth domains – $E^{\mathrm{DB}}_{\mathrm{SMOOTH}}$ (*yellow balls*), (6.1); (ii) the barrier for diffusion into the terrace across the atomic steps – $E^{\mathrm{DB}}_{\mathrm{STEP}}$ (*red balls*), (6.2); (iii) the barrier for diffusion into the terrace or substrate by direct incorporation, $E^{\mathrm{DB}}_{\mathrm{DIRECT}}$ (*black balls*), (6.3)

(ii) Here, the diffusion scenario is realized in a temperature window where the energy of adatoms is above the barrier for diffusion across the atomic steps, but below the barrier for direct embedding (the red atoms at the terrace edges in Fig. 6.1). In this energy gap the atomic diffusion causes incomplete surface intermixing.

$$E_{\mathrm{ATOM}}^{\mathrm{D}} > E_{\mathrm{STEP}}^{\mathrm{DB}} \geq E_{\mathrm{DIRECT}}^{\mathrm{DB}} \tag{6.3}$$

(iii) In this high-temperature region, the adatom energies exceed all existing surface diffusion barriers on the interface. This case reflects surface-confined intermixing which is spread over the entire outermost epitaxial layer. It will be considered as atomic diffusion at complete surface intermixing.

In the next sections we will discuss in detail the diffusion behavior for the energy regions (i–iii), as defined by (6.1), (6.2), and (6.3).

6.3 Atomistic Simulations of the Interface Layer: Computational and Physical Models

The fine atomic structure of epitaxial interface evolves as a result of subtle competition of long-range and short-range interactions. In view of that, the interface is considered as a rather complex physical system [6–8]. The variety of interactions implicated in this scenario and the presence of imperfections on the real surfaces including atomic terraces, steps, kinks, vacancies, defects, grain boundaries makes the problem of atomic arrangement at epitaxial interface generally not amenable to pure theoretical treatment. Getting over these difficulties, the atomistic simulations treat successfully the problem of complicated interface structure. Let us point here the essential advantage of computer simulations, i.e., to isolate simultaneously acting physical effects and, therefore, to evaluate separately their contribution to specific behavior of the real systems, [9]. Applying appropriate interacting potentials, the computer modeling straightens out the experimental findings and, moreover, it reveals and predicts non-expecting phenomena at epitaxial interface [10]. Hence, the physical experiment might be conducted and extended in a right direction.

The present computational model implies classical canonical Monte Carlo (MC) sampling [9] with tight binding second moment approximation of electron density of states (TB SMA) many-body potential between interacting atoms [11, 12]. This semi-empirical TB SMA potential has been extensively applied in contemporary atomistic simulations of transition metals and intermetallic alloys [4, 10, 13–15]. Its advantage relates to the ability of reproducing real physical properties of surfaces and interfaces including point defects, dislocations, vacancies, grain boundaries.

The total cohesive energy for an atom i that belongs to the system being simulated in TB SMA approach is defined as

$$E_i = E_i^{\mathrm{r}} + E_i^{\mathrm{b}} \tag{6.4}$$

where E_i^{r} is the repulsive energy term

$$E_i^{\mathrm{r}} = \sum_{j, r_{\alpha\beta} < r_{\mathrm{c}}} A_{\alpha\beta} \exp\left[-p_{\alpha\beta} \left(\frac{\mathbf{r}_{ij}}{\mathbf{r}^0_{\alpha\beta}} - 1 \right) \right] \tag{6.5}$$

and E_i^{b} is the band energy term obtained by the second-moment approximation of the electron density of states, expressed as

$$E_i^{\mathrm{b}} = -\sqrt{\sum_{j, r_{ij} < r_{\mathrm{c}}} \xi^2_{\alpha\beta} \exp\left[-2q_{\alpha\beta} \left(\frac{\mathbf{r}_{ij}}{\mathbf{r}^0_{\alpha\beta}} - 1 \right) \right]} \tag{6.6}$$

The indexes α and β indicate the chemical nature of atoms, $\mathbf{r}_{\alpha\alpha}$ is the first-neighbor atomic distance of the pure substance, $\mathbf{r}^0_{\alpha\beta} = \left(\mathbf{r}_{\alpha\alpha} + \mathbf{r}_{\beta\beta}\right)/2$ if $\alpha \neq \beta$, $\mathbf{r}_{ij}$ is the distance between atoms i and j, $\mathbf{r}_{\mathrm{c}}$ is the cutoff distance for the interaction. The quantity ξ is an effective hopping integral and q describes its dependence on the relative interatomic distance. In the most general case, the band energy term in (6.6) is a functional expression representing a sum over the local electronic charge density induced at site i from atoms at site j. The hopping integral ξ originates from quantum mechanical TB models and its value directly relates to the overlapping of electron tight-binding wave functions of neighboring atoms [11, 12]. This is the reason for ξ to be strongly influenced by the local atomic environment and therefore to be coverage dependent. This refinement is essential for simulation of epitaxial interfaces, since the local atomic arrangement is entirely different at low concentration of adatoms and at complete monolayer [13, 15]. It has been shown that accounting for the coverage dependence of ξ, the atomistic simulations generate system behavior in complete accordance with the real physical experiment: (i) formation of lattice gas; (ii) surface intermixing; (iii) formation of c(2×2), p(4×1), and p(5×1) 2D superstructures; (iv) critical behavior and Ising-type order–disorder transition of the c(2×2) phase, etc. [4, 10]. The values of the hopping integral ξ and all related parameters A, p, and q in the interacting potential, (6.5) and (6.6), are taken from [11]. These values are consistent with the overall thermodynamic properties of the real system since they reproduce basic physical characteristics as melting point, evaporation energy, elastic constants, etc.

The physical model is designed to allow description of wide-ranging surface morphology including atomic terraces, steps, kinks, large flat domains, vacancies. The system, constructed as a 3D continuum space, is limited to sizes $L_x = 38$, $L_y = 22$, and $L_z = 5$ lattice units in the corresponding space directions. The initial configuration is Cu(111) stepped crystal surface with random adsorption of Pb atoms. The coverage is kept constant throughout the simulation experiment. The large atomic terraces allow random migration of single atoms and compact clusters on top surface layer as well as diffusion into the substrate by way of direct incorporation. In contrast to smooth domains, the presence of steps tolerates diffusion through the periphery of atomic terraces. Hence, all possible mass transfer processes are feasible in the model. The interface energy, pair distribution function (PDF) analysis, and series successive snapshots of system configurations reveal the time

evolution of atomic structure of the interface. The simulations are done on canonical ensemble, i.e., system with constant number of particles at constant temperature. Full lattice dynamics for all atoms in adsorbed and substrate layers is applied for complete spatial relaxation of the system. The final equilibrium state is realized after an average Monte Carlo time of 5×10^5 MC steps per atom. At that state, for a fixed temperature, the total system energy is minimal and fluctuates around a constant value. All simulation details are described elsewhere [10].

As a model for studying surface diffusion and surface-confined intermixing we chose Pb/Cu interface. An important reason for this preference is the large number of experimental data collected for this system, which provides a reliable point of reference for the computational model [2, 16–25]. Extensive studies in the last two decades demonstrated variety of Pb/Cu mixed equilibrium phases. Although Pb and Cu are volume-immiscible substances, it was shown that the formation of 2D surface alloy on the interface is an energetically favorable process [10, 18–23]. Hence, in the framework of present computational and physical models, we will discuss in detail the surface diffusion on this epitaxial interface.

6.4 Surface Diffusion on Smooth Epitaxial Interface: Blocked Surface Alloying

We have already defined the basic energy regions (6.1), (6.2), and (6.3), where essential variation of surface diffusion mechanisms is expected. Being directly related to the system temperature, these regions determine the thermal energy of adatoms and atomic clusters for migration on epitaxial interface. The atoms in their random walk have to overcome a variety of energy barriers originating from the specific surface morphology. At low temperature, the adatom energy does not exceed the energy barriers for direct embedding inside the substrate, (6.1). In that case the interface structure evolves as a result of atomic migration exclusively on top of the surface layer. The exchange of atoms with substrate is strongly suppressed and, therefore, the diffusion generates isolated clusters or large ordered assemblies following the trend to minimize the interface energy. As shown in Fig. 6.2, attachment and detachment to the steps and kinks of atomic terraces are also feasible.

Being well worn, the diffusion of single atoms at low temperatures and the resulting decoration of steps and kinks are phenomena studied in great detail both theoretically and experimentally [6–8]. That is the reason, in the energy gap defined by (6.1), to focus our attention exclusively on diffusion of 2D atomic assemblies on smooth epitaxial interface, where fine details of the mechanisms of islands migration are still an open task. These details relate to the questions (i) How the diffusion coefficient of an atomic cluster is influenced by cluster size and geometry? (ii) Does the lattice constant of an atomic cluster on foreign substrate depend on the number of atoms building the cluster? (iii) How does the variation of cluster/substrate misfit affect the general cluster diffusion behavior?

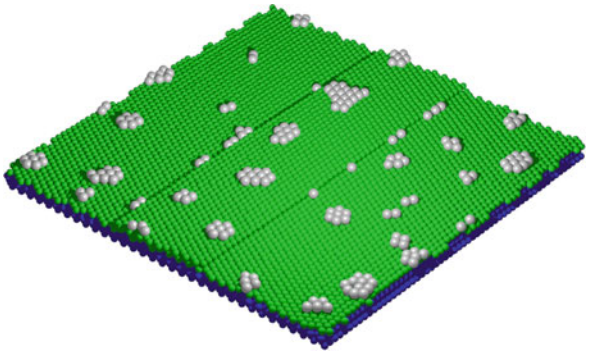

Fig. 6.2 Atomic configuration of smooth epitaxial interface at low temperature. Since the adatom energy does not exceed the energy barriers for direct incorporation inside the substrate, the surface alloying is entirely blocked, (6.1). The interface structure evolves by diffusion of adatoms exclusively on the outermost substrate layer resulting in formation of 2D islands and attachment to the steps of terraces

6.4.1 Size and Shape Effects in Cluster Diffusion on Smooth Domains

In the last decade, extensive theoretical and experimental studies revealed that the diffusion coefficient D of clusters scales with the number N of atoms in them as $D \propto N^{-\alpha}$. Being dependent on the dominant mass-transport mechanism, the exponent α takes values $\alpha = 3/2$ for periphery diffusion (PD), $\alpha = 1$ for terrace diffusion (TD), and $\alpha = 1/2$ for evaporation/condensation mechanism [7, 26–28]. Unfortunately, the values of the above scaling exponents reflect highly simplified cases. In fact, cluster migration is a quite complex phenomenon influenced by simultaneously acting diffusion mechanisms. The transport process is found to be also timescale dependent, because of the long-time behavior of edge and step fluctuations [6, 8]. As a result the terrace diffusion dominates at long times whereas the edge diffusion plays a key role at short times. That is why, the experimentally observed non-universal scaling exponents reflect the contribution of competing mass-transport processes. The experimental evidence of exotic oscillatory behavior of the surface diffusion coefficient of clusters as a function of their size is another challenge [29–35]. The effect of "magic clusters" mobility mostly relates to different geometric configurations (compact or non-compact structures) of atomic assemblies. In some specific cases of heteroepitaxial systems, a soliton or dislocation mechanism could be essential for island diffusion, too [32–35]. In the next section, we will demonstrate that besides the above effects, the commensurability between overlayer and substrate has to be taken into account of diffusion behavior of 2D islands.

In the present model, the diffusion on smooth epitaxial interface was evaluated by the trace of the center of mass of N-atomic cluster. As seen in Fig. 6.3, this center follows Einstein random walk behavior. The computational data are collected for six-atomic cluster at $T = 400\,\mathrm{K}$ over 1×10^6 MC steps.

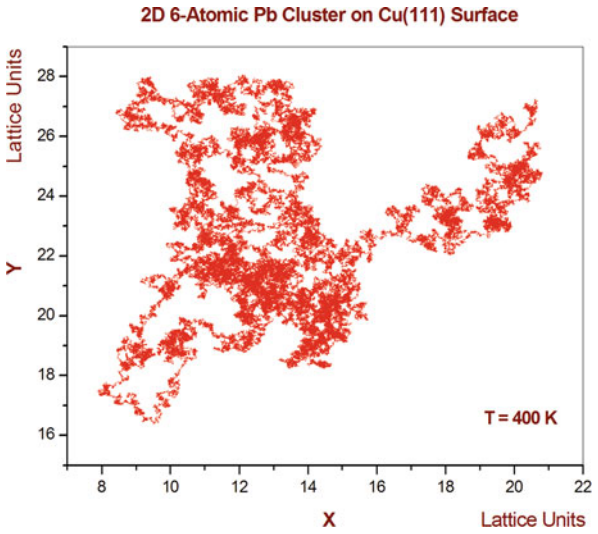

Fig. 6.3 The center of mass diffusion trace of six-atomic Pb cluster on Cu(111) at 400 K

The atomistic simulations reveal well-defined size effect of diffusion coefficient for clusters consisting $1 < N \leq 10$ atoms, Fig. 6.4. The size dependence of D, presented in Fig. 6.4, manifests clear oscillations increasing the number of atoms in the cluster. The observed variation of D does not follow the $D \propto N^{-\alpha}$ scaling and could be explained by the model of open and closed geometrical shapes of islands [29, 30]. As expected, the seven-atomic cluster, having compact shape because of fcc(111) symmetry, has lower mobility compared to the open six-atomic cluster.

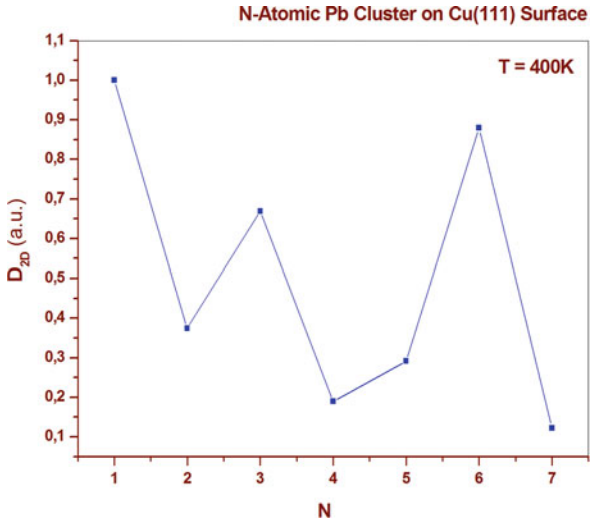

Fig. 6.4 Size-dependent oscillations at $T = 400$ K of diffusion coefficient D_{2D} of N-atomic Pb cluster on Cu(111) surface (from Michailov and Vladkov [32], Copyright © 2007 Elsevier B.V.)

This behavior is consistent with experimental findings for Rh/Rh(100) [29] and simulations for Cu on Cu(100) [30] where compact clusters of four and six atoms on fcc(100) surface demonstrate lower mobility. Therefore, the shape of clusters may change dramatically the mass-transport mechanism and even more may dominate over the dependence on the cluster size.

6.4.2 Impact of the Lattice Misfit on Cluster Diffusion Behavior

Having established the size- or shape-dependent oscillations of D, we explore the impact of cluster/substrate commensurability, too. The commensurability was evaluated by the value of lattice misfit m defined as the ratio $m = L_{CL}/L_{SUB}$. The quantities L_{CL} and L_{SUB} are the lattice constants of the cluster and the substrate, respectively. The influence of lattice misfit on the surface diffusion of clusters, assuming different thermal expansion of substrate and overlayer in heteroepitaxial systems, has been previously studied by Hamilton in the approximation of simple Frenkel–Kontorova model [33, 34]. Here, applying continuum-space Monte Carlo simulations, we extend this model to the case of 2D island migration on epitaxial interface. The simulation experiments demonstrate clear dependence of the misfit on the cluster size for $1 < N \leq 10$ [32]. Let us point here that at fixed temperature, L_{SUB} for large substrate has a constant value and therefore the variation of m is a result of variation of L_{CL}.

The PDF analysis of the lattice parameter L_{CL} of 2D foreign island deposited on fcc(111) surface shows a gradual increase of lateral inter-atomic distance with island size at 400 K and 500 K. The first dramatic change is observed between two- and three-atomic clusters where nearest-neighbor interatomic distance increases by about 5%, Fig. 6.5. The physical explanation of this effect can be related to the intensive charge density redistribution between two- and three-atomic clusters and substrate. The enlargement of L_{CL} is less pronounced, but clear for islands containing three, four, five, and six atoms. It continuously increases and has a relative jump at seven-atomic cluster. This jump coincides with the formation of a closed island shape. Subsequent increase of N does not produce significant change of the cluster lattice constant. Our simulation data show that above 12 atoms the function $L_{CL} = L_{CL}(N)$ is practically constant. At values of $N > 12$ the L_{CL} attains the bulk lattice constant. The increase of the cluster lattice constant with N is caused by atomic accommodation (rearrangement) and force balance in the specific 2D configuration. On the other hand, the cluster lattice constant is also affected by the substrate potential which contributes to the overall system atomic arrangement.

Experimental evidence for size-dependent lattice parameter of Ag clusters deposited on Si(100) surface and 10% variation of the lattice constant of metal nanoparticles of different size and shape was recently reported [36, 37]. In heteroepitaxial systems, coverage-dependent lattice constant of Pb islands on Cu(111) surface has been also observed many years ago [16]. In a low-coverage range, at Pb atom concentrations less than 37.5%, the adlayer exhibits important expansion,

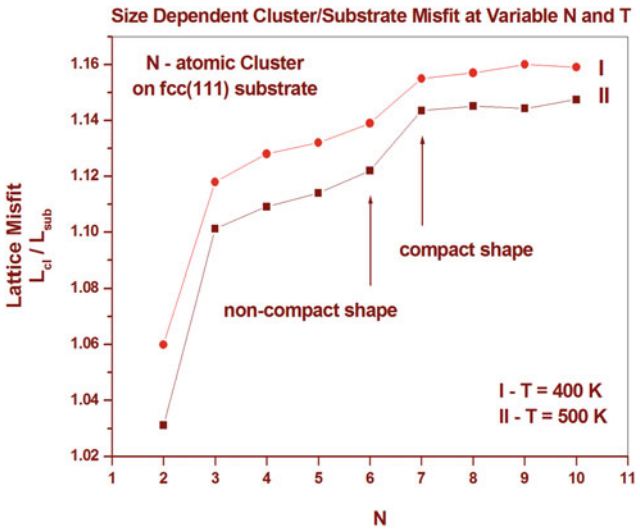

Fig. 6.5 Cluster/substrate lattice misfit as a function of the number N of atoms in the cluster at 400 K (data from [32]) and 500 K. The cluster lattice constant attains the bulk value at $N > 10$

while at a given critical coverage of 56.3% compressed Pb islands are formed with lattice constant reduced by 2.65% with respect to that of the bulk Pb phase [16, 38]. This effect reveals dramatic change in the magnitude of lateral interactions from low- to high-coverage range and reflects the environment-dependent character of the interactions at the interface layer [10, 13, 15]. The observed size-dependent cluster/substrate misfit variation affects the general diffusion behavior. This is demonstrated for three-atomic island by variation of the lateral Pb–Pb interactions through the value of the hopping integral ξ, (6.6). Hence, keeping constant the cluster/substrate normal interaction, we generate variable misfit in the system, Fig. 6.6. Since the number of atoms in the cluster is fixed, the shape effect is eliminated and therefore the oscillations of the diffusion coefficient are caused exclusively by the misfit variation. In all cases for islands with specific number of four, five, six, and seven atoms, D varies non-monotonically, oscillating with the misfit value, Fig. 6.6. It is essential to note that if the misfit does not affect the cluster diffusion, we would observe monotonic dependence of D with increasing the lateral bonding. The simulation results also suggest that the contribution of cluster misfit is more pronounced at small N up to 10 atoms. Above this value the misfit is nearly constant with cluster size and the shape effect dominates the diffusion behavior. For three-atomic clusters D changes between 0.2 and 0.7, while for seven-atomic clusters this variation is smaller, being between 0.04 and 0.2. All values of D are normalized to the diffusion coefficient of single atom. The above results stand for essential contribution of the lattice misfit to the island diffusion behavior.

Because of the quite general physical origin of the misfit variation with cluster size (broken crystal symmetry and periodicity, small number of interacting atoms,

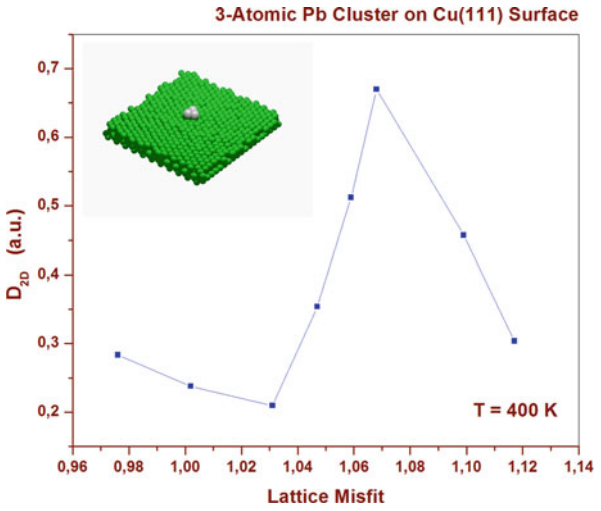

Fig. 6.6 Misfit-dependent diffusion coefficient D_3 of three-atomic Pb cluster on Cu(111) surface at 400 K. A significant increase of D_3 is observed at specific values of misfit. The value of D is normalized to the diffusion coefficient of single atom (from Michailov and Vladkov [32], Copyright © 2007 Elsevier B.V.)

strong peripheral atom contribution, confined electron density distribution, reduced space dimension, etc.) the misfit effect on the cluster mobility is expected to be also valid for homoepitaxial systems. Our analysis of pair distribution function suggests that the misfit variation with the number of atoms in the cluster is more pronounced in large-misfit heteroepitaxial systems such as Pb/Cu. The different electronic structure of overlayer and substrate leads to enhanced charge transfer and therefore the influence of surface potential on the overlaying cluster is increased. For homoepitaxial system, our results on surface diffusion of Cu islands on Cu(111) demonstrate a noticeably weaker $L_{\mathrm{CL}} = L_{\mathrm{CL}}(N)$ dependence. In that case no oscillations are observed and D decreases monotonically with cluster size. The extracted scaling exponent $\alpha = 1.38 \pm 0.048$ and the time evolution snapshot analysis suggests that surface diffusion should be related to entire cluster gliding as a result of concerted motion of several atoms. Similar results based on molecular dynamics and kinetics Monte Carlo simulations with embedded atom interaction potential have been reported [39].

Evidently, the real cluster migration is influenced by a number of simultaneously acting effects. Considering their subtle competition, it could be expected that oscillations, originating from cluster/substrate misfit found here, have to be added to the oscillations due to shape effects. In the case of periphery diffusion mechanism or entire cluster gliding, the misfit variation should modulate the $D \propto N^{-\alpha}$ dependence. The experimental verification of this prediction is still an open task. In the framework of the present model, it could also be concluded that incommensurate clusters migrate faster than commensurate clusters. Commensurability implies stronger bonding of island with substrate, i.e., relatively tight "locking" of

the cluster to the substrate potential. In contrast, the incommensurate clusters exhibit floating solid behavior and therefore, faster migration on the surface.

6.5 Surface Diffusion on Stepped Epitaxial Interface: Incomplete Surface-Confined Intermixing

In the energy regions defined by system temperature below T_L (blocked alloying, (6.1)) and above T_H (complete alloying, (6.3)), the simulation results for the diffusion of single adatoms do not reveal any unusual behavior. The system completely follows experimental findings of entirely phase separated at $T < T_L$ or entirely mixed ordered or disordered interface at $T > T_H$. [18, 19]. Opportunely, this is not the case of atomic diffusion in the temperature gap $T_L \leq T \leq T_H$, where the atomistic model reveals a number of fine effects. These effects come out by the variety of energy barriers that the adatom with fixed energy meets at specific sites on the crystal surface. Consequently, the initial atomic-scale surface morphology moulds the final equilibrium interface structure. In this section we will discuss diffusion scenarios at the most common types of surface morphology: epitaxial interface with large, atomically smooth domains and epitaxial interface with terraces having variable width, edged by different steps and kinks.

6.5.1 Diffusion in the Vicinity of Steps of Atomic Terraces

In the temperature region $300\,\mathrm{K} \leq T \leq 500\,\mathrm{K}$ the energy of migrating atoms is below the barrier for direct embedding inside the substrate, (6.2). The simulations at 400 K show lack of any atomic exchange between adsorbed and substrate atoms on large terraces or smooth, step-free surface areas. This behavior is consistent with recently reported rather high diffusion energy barrier of 1.17 eV for direct embedding of Pb atoms inside the Cu(111) terrace [17]. On the other hand, the low activation energy of 0.03 eV for adatom surface diffusion favors the atomic transport on top of the substrate. Hence, in specific temperature window $T_L \leq T \leq T_H$, the suppressed direct alloying $\left(E^{D}_{ATOM} < E^{DB}_{DIRECT}\right)$ in the outermost surface layer assists the atoms to attach the steps of the atomic terraces, Fig. 6.7.

We have already pointed out that adatoms have different ability for embedding, depending on the sites they inhabit on the epitaxial interface. As a result of different elastic strain in complete surface layer and in terrace with finite size, the energy barriers for diffusion into the smooth substrate by direct atomic exchange, E^{DB}_{DIRECT}, and for diffusion across the step of terraces, E^{DB}_{STEP}, are expected to be different. Indeed, at equilibrium, close to step edges, the simulations show very distinct Pb adatom diffusion inside the Cu matrix, Fig. 6.8. Following initial intensive process of intermixing in the vicinity of step, the diffusion within the terrace significantly decreases and the concentration of foreign Pb atoms dramatically falls down after the third atomic row of the Cu terrace. Approaching equilibrium, the system

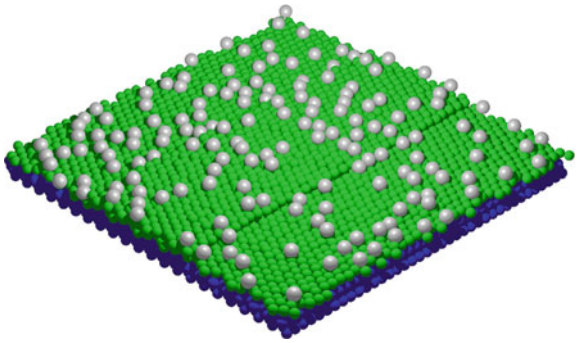

Fig. 6.7 Non-equilibrium configuration of Pb adatoms on Cu(111) interface in the temperature region $T_L \leq T \leq T_H$. Going to equilibrium the adatoms form alloyed stripes in the vicinity of terrace edges shown in Fig. 6.8

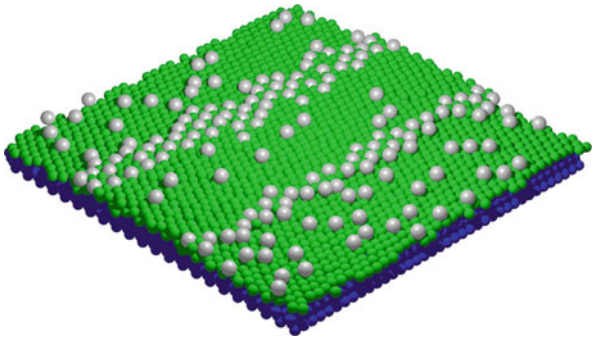

Fig. 6.8 Snapshot of random atomic configuration of 0.1 ML Pb (*light gray balls*) at 300 K on Cu(111) stepped surface with initial Cu terrace width of 16 atoms. The formation of 2D stripes due to Pb diffusion across the atomic steps is seen. No surface alloying takes place on a smooth, step-free surface area

generates thermodynamically stable configuration of finite-size alloyed stripes and pure terrace areas, shown in Fig. 6.8. The stripes have characteristic width L_S which depends on temperature and step anisotropy. It is essential to note that in the configuration presented in Fig. 6.8, the interface energy has already reached minimum and fluctuates around a constant value as seen from the time evolution of the system, Fig. 6.9. This behavior indicates a system state in absolute or deep local energy minimum. Therefore, in a specific temperature range, $T_L \leq T \leq T_H$, we can block completely the direct atomic exchange and open an energy window for diffusion exclusively trough the steps. Similar diffusion scenario generated by the present computational model has been observed experimentally by STM on the Pb/Cu(111) system, [17, 18]. Molecular Dynamics study also confirms easier penetration of Ni adatom in the vicinity of terrace edges on the substrates Cu(100) and Cu(111), [40]. In that case, it has been observed additionally direct embedding of Ni atoms very close to steps of the Cu(111) terrace.

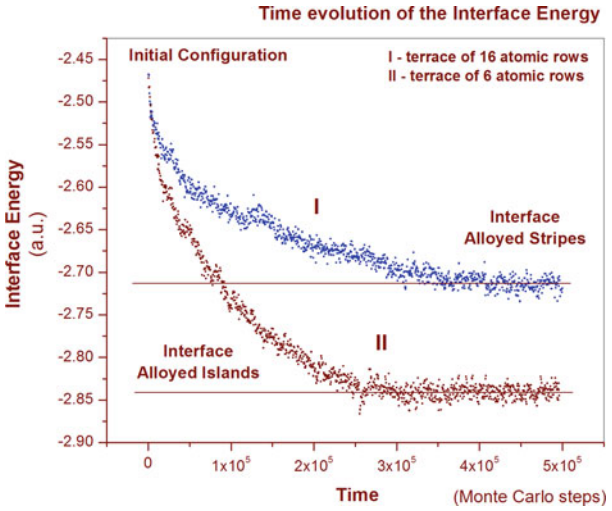

Fig. 6.9 The interface energy dependence on Monte Carlo time. After formation a constant width stripes I (data from [4]) or alloyed islands II, the energy fluctuates close to a constant value

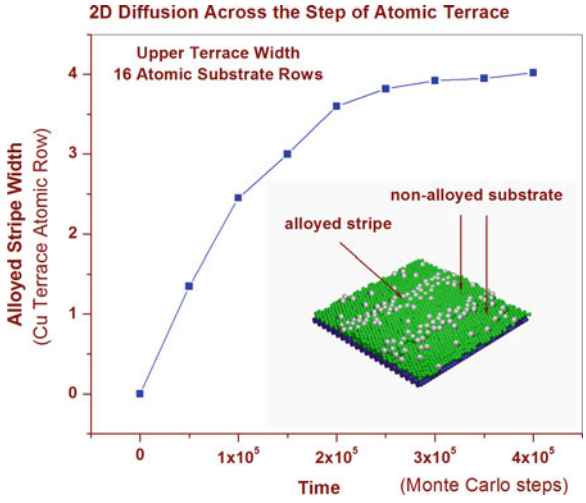

Fig. 6.10 Time evolution of Pb adatoms diffusion across atomic steps inside the Cu(111) terrace. After penetration in depth of three- to four-atomic Cu rows of both sides of the terrace, the Pb atoms migration is completely blocked. Surface alloying is avoided on a flat, step-free surface area (from Michailov [4], Copyright © 2009 The American Physical Society)

Time evolution analysis of the stripe width, Fig. 6.10, suggests a gradual increase of diffusion energy barriers in the direction toward the terrace center. The simulation results reveal diffusion coefficient (for migration across the step) dependent on the position of the terrace atomic row in direction to the center, Fig. 6.8. Following the general expression for diffusion coefficient D_i:

$$D_i \propto \exp\left(-\frac{E_i^{\mathrm{DB}}}{kT}\right) \tag{6.7}$$

in which k is the Boltzmann constant, the spreading of alloyed stripe depends on a series of increasing diffusion barriers E_i^{DB} for entering in the first, second, third, ith atomic rows. The evaluation of E_i^{DB} is a complex problem that should account for simultaneously acting physical effects such as elastic strain, non-symmetric terrace relaxation, step anisotropy, adlayer–substrate atomic interactions. The atomic relaxation is favorable exclusively in the direction out of the step, whereas inside the terrace the elastic strain increases and resists the penetration of foreign atoms. Therefore, the finite width of the stripe is a result of non-symmetric elastic strain field (physical boundaries) of alloyed domains at step edges.

6.5.2 Step Anisotropy Contribution to Step Diffusion Barriers

An important detail of step diffusion barriers relates to the crystallographic anisotropy of terraces. A very telling example of low-indexed <111> orientations of epitaxial interface is presented in Fig. 6.11. The symmetry and the resulting atomic arrangement on fcc(111) surface generate atomic terraces with two kinds of steps, A and B, Fig. 6.11 (inset down right), each of them having different step free energy and relaxation ability [7, 41].

Simple analysis of the geometrical atomic configuration presented on the inset down right in Fig. 6.11 shows that the atomic shift toward the nearest-neighbor threefold symmetry hollow site for Cu atom of the B-step (left step direction) costs less energy compared to that for identical peripheral Cu atom of the A-step (right step direction) on the terrace. The elastic strain generated by foreign atoms diffused into the terrace matrix is reduced preferably in the B-step direction. The favored terrace relaxation in direction B is consistent with the larger stripe width $L_{\mathrm{S}}^{\mathrm{B}}$ at the terrace step B, compared to the stripe width $L_{\mathrm{S}}^{\mathrm{A}}$ at the terrace step A, Fig. 6.8. Simulation snapshot analysis for equilibrium atomic configurations at constant $T = 300\,\mathrm{K}$ reveals $L_{\mathrm{S}}^{\mathrm{B}} \approx 1.4 L_{\mathrm{S}}^{\mathrm{A}}$. Therefore, the stripe width is affected by the step anisotropy resulting in different relaxation of the elastic strain in the system generated by "larger" foreign Pb atoms in the terrace [4, 42].

The presented diffusion scenario is rather promising for manipulation of high-indexed epitaxial interface. If the initial atomic configuration of the system is consisted of equidistant terraces on vicinal surface then the formation of alloyed stripes is restricted exclusively to the single step of the terrace, Fig. 6.12.

The interface forms staircase-up or staircase-down configuration of 2D regular stripes. In the energy gap $T_{\mathrm{L}} \le T \le T_{\mathrm{H}}$ the stripe width depends on T through the relaxation ability of the vicinal terrace. The critical terrace width was found to be three times the spreading width of stripe. Below this value the terrace is completely alloyed. Therefore, even at $T_{\mathrm{L}} \le T \le T_{\mathrm{H}}$, the vicinal epitaxial interface having

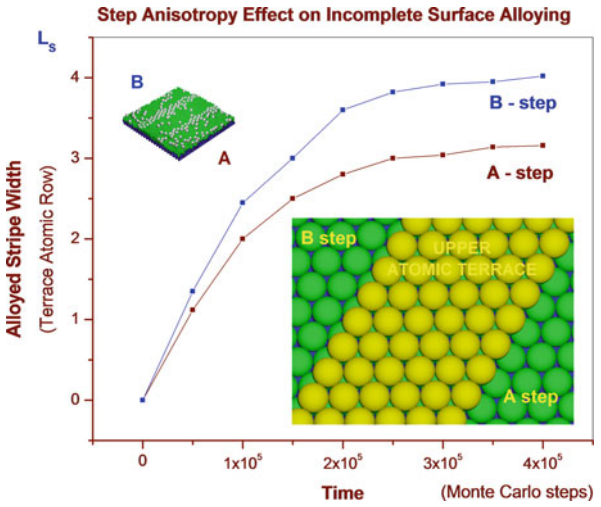

Fig. 6.11 Step anisotropy effect at incomplete surface alloying. Snapshot of a random MC atomic configuration of 0.1 ML Pb/Cu(111) at 300 K and initial substrate terrace width of 16 atomic rows. The larger alloyed stripe width at step B is a result of the eased atomic relaxation of the terrace in that direction. The *inset* (*down right*) shows atomic arrangement of A and B steps with feasible directions for relaxation toward threefold symmetry hollow sites on the substrate level. *Light gray balls* indicate upper Cu terrace atoms (from Michailov [4], Copyright © 2009 The American Physical Society)

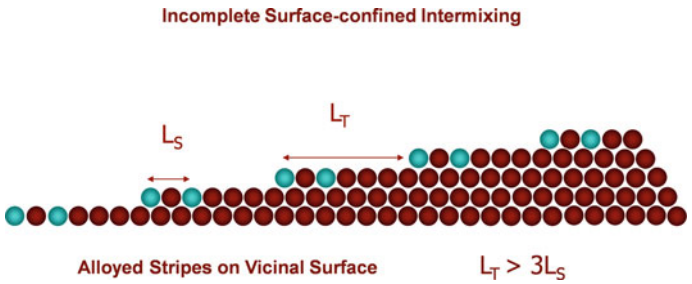

Fig. 6.12 Nanoscale staircase surface pattern formation on vicinal fcc(111) interface. Stable alloyed stripes followed by pure terrace domains are formed at $L_T > 3L_S$ and $T_L \leq T \leq T_H$. If the surface intermixing is realized across the single steps of the vicinal terraces, for $L_T < L_C$ (vicinal surface with narrow terraces) the formation of 2D surface alloy is spread over the entire interface although $E_{ATOM}^{D} < E_{DIRECT}^{DB}$

mean terrace width distribution $L_T \leq L_C$ could be completely alloyed despite that the system is outside the energy gap for complete alloying, (6.3).

6.5.3 Vacancy-Mediated Diffusion Inside Atomic Terraces

The diffusion slowing down inside the terrace argues for dramatic change in the elastic strain field toward the terrace center. The equilibrium state of the system

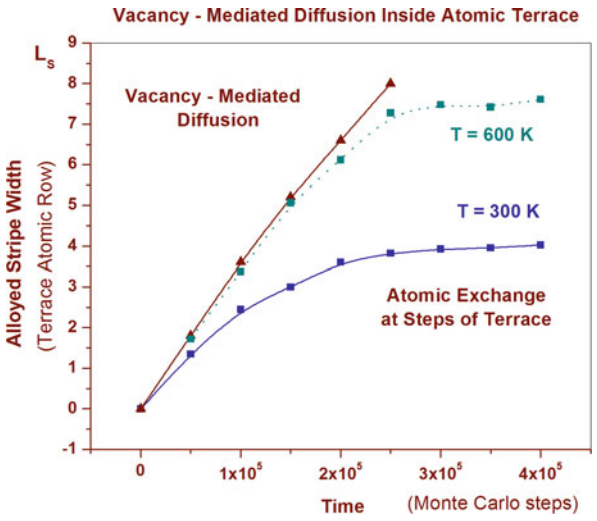

Fig. 6.13 Time evolution of Pb diffusion across atomic steps on Cu(111) surface. Pb migration inside the terrace is tightly suppressed for dense, vacancy-less substrate (lower curve), $T = 300\,\mathrm{K}$. At same $T = 300\,\mathrm{K}$ the diffusion slowing down is prevented on 5% vacancy-populated interface due to easier terrace relaxation (*upper solid curve*). Pb diffusion at $T = 600\,\mathrm{K}$ *(middle dashed curve*) after spontaneous generation of vacancies (from Michailov [43], Copyright © (2010) Trans Tech Publications, Switzerland)

shows completely blocked diffusion after third atomic row, resulting in final width of alloyed stripe. Since the atomic relaxation of the terrace is a temperature function, the stripe width is expected to increase at high temperatures. The simulations at $T = 600\,\mathrm{K}$, compared to that of $T = 300\,\mathrm{K}$, demonstrate clear enlargement of the stripe, as seen in Fig. 6.13 (middle dashed curve). The facilitated substrate matrix relaxation assists the diffusion of adatoms inside the terrace. Snapshot and PDF analysis show that the atomic relaxation in that case is a result of spontaneous generation of vacancies [43]. Let us remind that the density of vacancies increases exponentially with T. These results reveal largely vacancy-assisted diffusion of adatoms inside the terraces, far from terrace edges and steps. In real systems, this diffusion scenario will take place at high T, near the upper temperature limit of the region of incomplete alloying $T_\mathrm{L} \leq T \leq T_\mathrm{H}$ where the density of atomic vacancies is expected to be large.

We have also confirmed the mechanism of vacancy-mediated diffusion at reduced T. Since the process of spontaneous formation of vacancies is not favorable at low T, the epitaxial interface is nearly vacancy free. That is why, at $T = 300\,\mathrm{K}$ in the initial configuration, 5% atomic vacancies into the terrace have been randomly generated. The result, shown by the upper curve (solid line) in Fig. 6.13 demonstrates complete 2D alloying in the terrace. Even at low T the native presence of vacancies destroys the stripes due to the easier relaxation of the entire terrace [43]. Approaching the final equilibrium state, the system forms completely alloyed Pb/Cu 2D islands, on top of the pure, non-alloyed surface, similar to Fig. 6.14b.

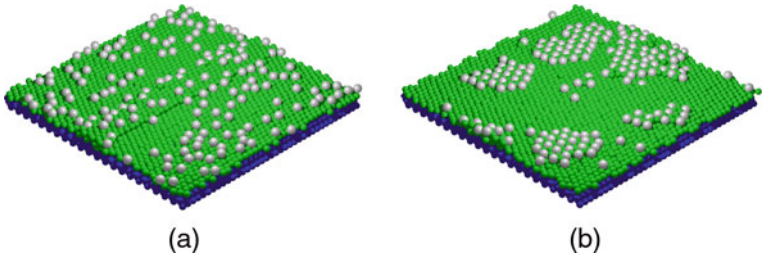

Fig. 6.14 Time evolution of the interface atomic configuration for initial terrace of 6 atomic rows. (**a**) Non-equilibrium configuration with terrace width comparable with the size of alloyed stripe. (**b**) Close to equilibrium configuration resulting from (**a**). Completely alloyed Pb-Cu islands are formed. (see also Fig. 6.9 curve II)

6.5.4 Terrace Stability

The problem of terrace stability directly relates to the surface pattern formation at different atomic levels at epitaxial interface. The decrease of terrace width below a given critical value causes overlapping of elastic strain fields generated by the left and right alloyed stripes, Fig. 6.14a. The smooth, non-alloyed area inside the terrace disappears. As a result, the terrace entirely releases the elastic strain and forms 2D homogeneously alloyed islands on top of pure, non-alloyed substrate, Fig. 6.14b. By variation of the initial terrace width, we found that the stripe width L_S does not depend on the terrace width L_T at $L_T > 3L_S$. The decrease of L_T more than three times L_S makes the terrace unstable and completely transparent for Pb atoms [4, 43]. On Cu substrate with initial terrace width L_T of six atomic rows we observed totally alloyed Pb–Cu domains. Therefore, at constant T, the variation of L_T gives the opportunity to form various surface patterns: (i) one-level patterns at $L_T > 3L_S$, i.e., alloyed stripes followed by smooth, pure terrace areas Fig. 6.8; (ii) two-level patterns at $L_T < 3L_S$, i.e., totally alloyed terraces (islands) and pure non-alloyed substrate domains, Fig. 6.14b.

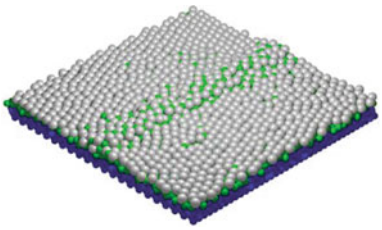

Fig. 6.15 The atomic configuration of epitaxial interface at high coverage (0.7 ML) at complete wetting of the substrate by adsorbed layer. Even being entirely alloyed, the terrace retains its linear shape and dimension. This is in contrast to the low-coverage case where the terrace destroys and forms 2D-alloyed islands, Fig. 6.14b

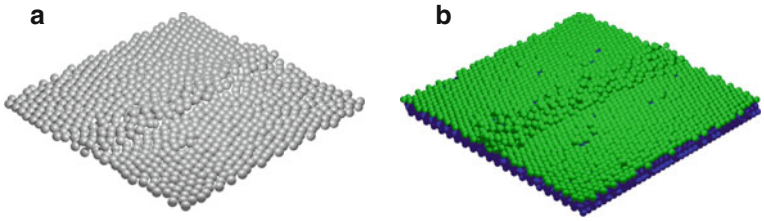

Fig. 6.16 (**a**) Atomic structure of the wetting layer as a replica of the substrate. Pure ordered and mixed disordered patterns are results of different energy barriers for diffusion inside smooth and stepped surface domains. (**b**) Atomic structure of the substrate below the wetting layer. Disordered and alloyed striped terrace on top of well-ordered, non-alloyed surface layer is formed. The specific atomic arrangement is a result of incomplete surface intermixing caused by diffusion across the steps of atomic terrace

The terrace stability at high coverage is rather different. The atomic configuration presented in Fig. 6.15 reflects the case of complete wetting of the substrate by adsorbed layer.

Snapshot analysis reveals similar critical width L_C (three to four atomic rows) for overlapping of alloyed stripes. The essential difference here relates to the stability of the terrace. Even being entirely alloyed, the terrace retains its shape, keeping the linear contours and dimensionality. The wetting layer, covering completely non-alloyed domains of the interface, confines the fluctuations of capillary waves causing the break of stripe. Hence, interface could be designed as a complete pure adsorbed layer followed by alloyed ordered or disordered stripes, Fig. 6.16.

6.6 Complete Surface Intermixing

The high-temperature region is characterized by adatom energy exceeding all diffusion barriers imposed by the surface morphology, (6.3). In this energy gap at low concentration of adatoms, the interface has completely alloyed structure confined to the outermost surface layer. The ensemble of experimental results of Pb submonolayers on (110), (100), and (111) Cu substrates reveals rather exotic behavior regarding the structure, alloying, and disalloying transitions in these systems [10, 13, 18–25]. The most impressive example has been reported for submonolayer Pb adsorption on Cu(110). On this substrate, close to complete 0.8 monolayer, in an extremely narrow coverage range of 0.05 monolayer, a sequence of 11 quasi-1D p(Nx1) phases (all alloyed) have been observed. At reduced coverage, 0.3–0.5 ML, the reverse process of alloying–disalloying has been found for the lattice gas to c(2×2) superstructure transition [18, 22, 23]. Well-ordered 2D-alloyed phases have been found on fcc(100) and fcc(111) surfaces, too [2]. In general, for one of the most studied metal/metal epitaxial interface Pb/Cu, the variety of 2D-alloyed phases and the respective phase transitions could be classified into two groups. The first group covers first-order phase transitions taking place in different atomic levels, while the second group relates to continuous order phase transitions taking place in one

and the same atomic level. To the first group of alloying–disalloying transitions the following could be assigned: Pb/Cu(110) – disordered alloy – pure c(2×2) phase – alloyed p(4×1) phase; Pb/Cu(100) – alloyed c(4×4) phase – pure on top c(2×2) phase; Pb/Cu(111) – disordered alloy – pure incommensurate compact layer, all being of first-order transitions. To the second group belongs the continuous transitions: Pb/Cu(100) – disordered alloy – alloyed c(4×4); Pb/Cu(110) – p(4×1) – p(13×1) – p(9×1) – p(14×1) – p(5×1) phases all being alloyed [25]. The fine competition between the energy of mixing and the substrate strain energy is the physical background for generation of this variety of ordered and disordered surface phases.

6.7 Classification Order of Surface-Confined Intermixing

The presented computation model reveals staircase behavior of diffusion energy barriers from atomically smooth to completely rough interface and identifies specific hierarchy of surface-confined intermixing. The temperature evolution of epitaxial interface from smooth toward rough interface consisting of terraces with kink-free line steps, terraces having kinked steps, terraces with complete step roughening, and finally terraces with large vacancy concentration suggests classification order of surface-confined intermixing shown in Fig. 6.17. On that background, depending on the adatom energy (system temperature) and the respective energy barriers (atomic-scale surface morphology) the surface alloying could be classified as follows [4]:

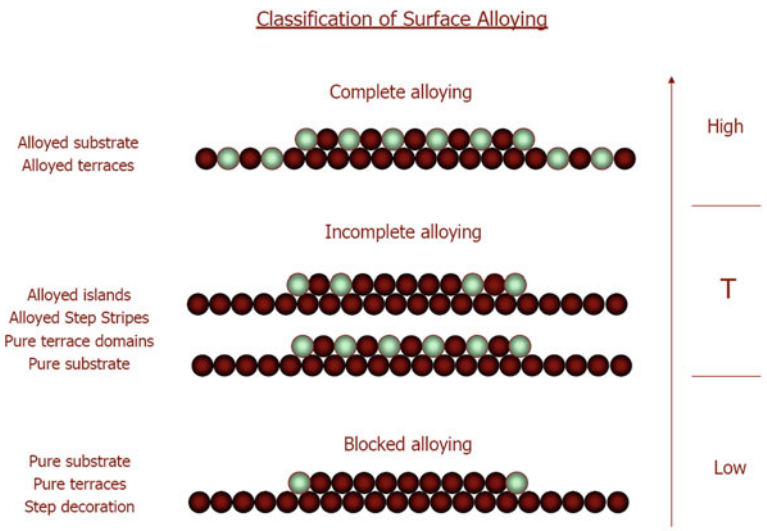

Fig. 6.17 Classification order of surface-confined intermixing. Light gray balls – adsorbed atoms, dark balls – substrate atoms (from Michailov [4], Copyright © 2009 The American Physical Society)

(i) complete alloying ($E^{\mathrm{D}}_{\mathrm{ATOM}} > E^{\mathrm{DB}}_{\mathrm{STEP}} \geq E^{\mathrm{DB}}_{\mathrm{DIRECT}}$),

(ii) incomplete alloying ($E^{\mathrm{DB}}_{\mathrm{STEP}} \leq E^{\mathrm{D}}_{\mathrm{ATOM}} < E^{\mathrm{DB}}_{\mathrm{DIRECT}}$),

(iii) blocked alloying ($E^{\mathrm{D}}_{\mathrm{ATOM}} < E^{\mathrm{DB}}_{\mathrm{STEP}} < E^{\mathrm{DB}}_{\mathrm{DIRECT}}$).

The suggested classification scheme opens up a way for fine-tuning surface design and pattern formation. As a result, in bulk-immiscible systems the adsorbed foreign adatoms pattern smooth, stepped, or vicinal surfaces in a diversity of modes:

(i) Pure substrate layer and pure terraces decorated at steps by 1D foreign atom lines (blocked alloying), Fig. 6.7.
(ii) Pure substrate layer and stripe-alloyed 2D terraces or islands (incomplete alloying with atomic exchange at steps), Fig. 6.8.
(iii) Pure substrate layer and completely alloyed 2D islands (incomplete alloying with vacancy-mediated atomic exchange into the terrace), Fig. 6.14b.
(iv) Pure adsorbed layer and completely alloyed stripes (incomplete alloying at high coverage with atomic exchange at steps for terraces having width below the critical), Fig. 6.15.
(v) Complete alloying (full intermixing at the epitaxial interface).

At incomplete alloying $E^{\mathrm{DB}}_{\mathrm{STEP}} \leq E^{\mathrm{D}}_{\mathrm{ATOM}} < E^{\mathrm{DB}}_{\mathrm{DIRECT}}$, this series of surface design modes could be extended to a multi-level pattern formation, too. At constant T and low concentration of adsorbed atoms, the alteration of initial terrace width L_{T} (e.g., by using equidistant terraces of different high-index vicinal surfaces) can create surface patterns on the epitaxial interface at different atomic levels:

(i) One-level patterns: pure non-alloyed terrace domains followed by alloyed stripes, Fig. 6.8.
(ii) Two-level patterns: totally alloyed terraces or islands and pure, non-alloyed substrate domains, Fig. 6.14b.

An essential advantage of the model is the ability to generate all atomic configurations of epitaxial interface shown here simply by temperature or coverage variation.

6.8 Conclusion

This review is focused on important details of the diffusion behavior of adsorbed atoms and clusters on the epitaxial interface. Accounting for the energy barriers imposed by the surface morphology (smooth domains, terraces, steps, kinks, etc.), the computational model reveals variety of diffusion scenarios that control in fine details the interface atomic structure.

On smooth interface, we found that the diffusion of atomic clusters (islands) is influenced by the cluster/substrate commensurability. Since the commensurability

implies stronger bonding of the island with the substrate, a relative "locking" of the clusters to the substrate potential is realized. In contrast, the incommensurate clusters exhibit floating solid behavior and migrate faster on the substrate. The value of the lattice misfit is dependent on the number of atoms in the cluster for $1 < N < 10$. This size-dependent misfit leads to oscillations that modulate the scaling dependence $D \propto N^{-\alpha}$ of diffusion coefficient or the oscillations being already caused by the cluster shape variation. The ensemble of results is in fairly good agreement with recent theoretical and experimental findings.

On epitaxial interface with atomic terraces, steps, and kinks, this study reveals diffusion mechanism of formation of 2D-alloyed stripes or 2D-alloyed islands.

The stripes formed at the terrace edges are followed by smooth, non-alloyed areas thus creating regular patterns on the surface. Atomic terraces having a critical width $L_T \leq 3L_S$ are unstable and completely transparent for the adsorbed atoms. The width of stripe is step anisotropy dependent and correlates with the relaxation ability of terraces in specific direction. The observed effect is a result of subtle interplay between layer strain energy and energy gained by mixing. Accounting for the energy barriers at specific atomic sites as smooth domains, terraces, and steps, the present model reveals a classification order of surface alloying: blocked, incomplete, and complete. Being in agreement with the experimental findings, the simulation results illuminate the crucial role of the competing atomic interactions that control the interface structure. The phenomenon of stripe alloy formation discussed here could be applied to nanoscale surface design of atomically smooth and vicinal surfaces in volume-immiscible systems.

References

1. D.P. Woodruff, E. Vilieg, in *Surface Alloy and Alloyed Surfaces*, ed. by D.P. Woodruff (Elsevier, Amsterdam, 2002), p. 277, and references therein
2. G. Kellogg, in *Surface Alloy and Alloyed Surfaces*, ed. by D.P. Woodruff (Elsevier, Amsterdam, 2002), p. 152, and references therein
3. R. van Gastel, R. Plass, N. Bartelt, G. Kellogg, Vacancy-mediated and exchange diffusion in a Pb/Cu(111) surface alloy: concurrent diffusion on two length scales. PRL **91**, 5 (2003)
4. M. Michailov, Computational study of stripe alloy formation on stepped surfaces. Phys. Rev. B **80**, 035425 (2009)
5. J. Terssoff, Surface-confined alloy formation in immiscible systems. Phys. Rev. Lett. **74**, 3 (1995)
6. H. Brune, Microscopic view of epitaxial metal growth: nucleation and aggregation. Surf. Sci. Rep. **31**, 121 (1998)
7. M. Giesen, Step and islands dynamics at solid/vacuum and solid/liquid interfaces. Prog. Surf. Sci. **68**, 1 (2001)
8. T.T. Tsong, Mechanisms and energetic of atomic processes in surface diffusion. Physica A, **357**, (2005)
9. D.P. Landau, K. Binder, *A Guide to Monte Carlo Simulations in Statistical Physics* (Cambridge University Press, Cambridge, 2000)
10. M. Michailov in *Computer Simulations Studies in Condensed Matter Physics XVI*, *Springer Series Proc. in Physics*, eds. by D.P. Landau, S.P. Lewis, H.B. Schettler vol. 95 (Springer, Heidelberg, 2004), p. 226, and references therein

11. F. Cleri, V. Rosato, Tight-binding potentials for transition metals and alloys. Phys. Rev. B **48**, 22 (1993)
12. V. Rosato, M. Guillopé, B. Legrand, Thermodynamical and structural properties of f.c.c. transition metals using a simple tight-binding model. Phil. Mag. **59**, 321 (1989)
13. N. Georgiev, M. Michailov, Order-disorder transition of the c(2x2) phase in the Pb/Cu(110) system: significance of surface defects. Phys. Rev. B **58**, 13895 (1998)
14. L. Gómez, H.T. Dieb, Structure and melting of lead monolayer adsorbed on a copper substrate. Phys. Rev. Lett. **74**, 1807 (1995)
15. M. Michailov, N. Georgiev, Monte carlo simulations of the interface layer in Pb/Cu(110); a tight binding model calculation. J. Phys. C **11**, 9889 (1999)
16. G. Meyer, M. Michailov, M. Henzler, LEED studies of the epitaxy of Pb on Cu(111). Surf. Sci. **202**, 125 (1988)
17. M.L. Anderson, M.J.D'Amato, P.J. Feibelman, B.S. Swartzentruber, Vacancy-mediated and exchange diffusion in a Pb/Cu(111) surface alloy: concurrent diffusion on two length scales. Phys. Rev. Lett. **90**, 126102 (2003)
18. C. Nagl, O. Haller, E. Platzgummer, M. Schmid, P. Varga, Submonolayer growth of Pb on Cu(111): surface alloying and de-alloying. Surf. Sci. **321**, 237 (1994)
19. C. Nagl, M. Pinczolits, M. Schmid, P. Varga, I. Robinson, $p(n\times1)$ superstructures of Pb on Cu(110). Phys. Rev. B **52**, 16796 (1995)
20. C. Nagl, M. Schmid, P. Varga, Inverse corrugation and corrugation enhancement of Pb superstructures on Cu(111) and (110). Surf. Sci. **369**, 159 (1996)
21. A. Sanchez, S. Ferrer, Structure and melting of lead overlayers on Cu(100) studied with thermal energy atom scattering. Phys. Rev. B **39**, 5778 (1989)
22. C. Beauvais de, D. Rouxel, M. Michailov, B. Mutaftschiev, Two-Dimensional overgrowth in the low submonolayer range: the case of c(2x2) – Pb/Cu(111). Surf. Sci. **324**, 1 (1995)
23. M. Michailov, C. de Beauvais, D. Rouxel, B. Mutaftschiev, Thermal behavior of c(2x2) layers in the Pb/Cu.(110) system and the influence of surface defects on the order-disorder transition. Phys. Rev. B **61**, 5987 (2000)
24. R. Plass, J. Last, N. Bartelt, G. Kellogg, Nanostructures – self-assembled domain patterns. Nature (London) **412**, 875 (2001)
25. B. Mutaftschiev, in *Proceedings of the Second East West Surface Science Workshop*, Bulgaria, ed. by M. Michailov (Coral Press, Sofia, 1996), p. 13
26. W. Pai, A. Swan, Zh. Zhang, J.F. Wendelken, Island diffusion and coarsening on metal (100) surfaces. Phys. Rev. Lett. **79**, 3210 (1997)
27. S.W. Khare, N.C. Bartelt, T.L. Einstein, Diffusion of monolayer adatom and vacancy clusters: Langevin analysis and Monte Carlo simulations of their Brownian motion. Phys. Rev. Lett. **75**, 2148 (1995)
28. S. Pal, K. Fichthorn, Size dependence of the diffusion coefficient for large adsorbed clusters. Phys. Rev. B **60**, 7804 (1999)
29. G.L. Kellogg, Oscillatory behavior in the size dependence of cluster mobility on metal surfaces: Rh on Rh(100). Rev. Lett. **73**, 1833–1836 (1994)
30. P. Salo, J. Hirvonen, I.T. Koponen, O.S. Trushin, J. Heinonen, T. Ala-Nissila, Role of concerted atomic movements on the diffusion of small islands on fcc(100) metal surfaces. Phys. Rev. B **64**, 161405 (2001)
31. P. Shi, Zh. Zhang, A. Swan, J.F. Wendelken, Dimer shearing as a novel mechanism for cluster diffusion and dissociation on metal (100) Surfaces. Phys. Rev. Lett. **76**, 4927 (1996)
32. M. Michailov, M. Vladkov, Surface diffusion of Pb clusters on Cu(111) influenced by size dependent cluster-substrate misfit: Monte Carlo tight binding simulation model. Surf. Sci. **601**, 3912 (2007)
33. J.C. Hamilton, M.S. Daw, S.M. Foiles, Dislocation mechanism for island diffusion on fcc (111) surfaces. Phys. Rev. Lett. **74**, 2760 (1995)
34. J.C. Hamilton, Magic size effects for heteroepitaxial island diffusion. Phys. Rev. Lett. **77**, 885 (1996)

35. S. Aubry, P.Y. Le Daeron, The discrete Frenkel-Kontorova model and its extensions. Physica (Amsterdam) D **8**, 381 (1983)
36. I. Shyjumon, M. Gopindahan, O. Ivanova, M. Quass, H. Wulff, C. Helm, R. Hipper, Structural deformation, melting point and lattice parameter studies of size selected silver clusters. Eur. Phys. J. D **37**, 409–415 (2006)
37. W.H. Qi, M.P. Wang, Size and shape dependent lattice parameters of metallic nanoparticles. J. Nanopart. Res. **7**, 51–57 (2005)
38. E. Vamvakopoulos, D. Papageorgiou, G. Evangelakis, Solidification of Pb overlayer on Cu(111) surface by molecular dynamics simulation. Thin Solid Films **485**, 290 (2005)
39. A. Karim, APS March Meeting 2005. http://meetings.aps.org/Meeting/MAR05/Event/22628
40. T. Raecker, A. DePristo, Alloy formation energetics and dynamics in the Ni/Cu(100) and Ni/Cu(111) systems. J. Vac. Sci. Technol. **A 10**, 4 (1992)
41. M. Giesen, H. Ibach, Step edge barrier controlled decay of multilayer islands on Cu(111). Surf. Sci. **431**, 109(1999)
42. M. Michailov, in *Nanoscale Phenomena and Surfaces* ed. by D. Kaschiev (Prof. M. Drinov Academic House, Sofia, 2008), p. 73
43. M. Michailov, Vacancy-mediated diffusion at surface-confined atomic intermixing. Solid State Phenomena, **159**, 121 (2010)

Chapter 7
Biologically Inspired Surface Physics: The HP Protein Model

Y.W. Li, T. Wüst, and D.P. Landau

Abstract The nature of proteins in contact with surfaces is a topic of great practical importance as well as of intellectual interest. We describe the use of a minimalistic model, the HP model of protein folding, to examine the general characteristics of proteins. We also review attempts to understand how the presence of a surface will modify their behavior.

7.1 Introduction

Protein folding is one of the great frontiers of early 21st century science and methods of statistical physics are finding their way in investigation of these systems. Proteins are long, linear polymers of amino acids connected by peptide bonds along the backbone, and rather complicated interactions that result in rough free energy landscapes [1, 2]. ("Peptide" is merely the term applied to short proteins.) At high temperatures proteins are distended, but below some characteristic temperature they fold into a "native state" of low free energy [3]. Proteins are sufficiently complicated that attempts to study them numerically rely upon simplifying the problem to one of manageable proportions yet retaining the fundamental features of the protein. An additional level of complexity enters when a surface is introduced and parts of the protein are either attracted or repelled by the surface. Immobilization of proteins on a solid substrate is important for the study of protein functions [4] and the synthesis of materials [5, 6]. Drug delivery [7] is one of the potential medical applications of these artificial materials, yet only a limited amount of information is available.

In this presentation we shall describe a very simplified, HP (hydrophobic-polar) lattice protein model that was introduced by biochemists over 20 years ago. In spite of its simplicity the model is quite challenging to study, particularly as it attempts

Y.W. Li (✉)
Center for Simulational Physics, The University of Georgia, Athens, GA 30602, USA
e-mail: ywli@hal.physast.uga.edu

M. Michailov (ed.), *Nanophenomena at Surfaces,* Springer Series in Surface Sciences 47,
DOI 10.1007/978-3-642-16510-8_7,

to fold into the native state. It has been shown that searching for the ground states for an HP sequence is an NP-complete problem [8, 9].

The lattice proteins with which we shall deal are of nanoscale dimensions and hence are at the interface between biology and surface nanoscience. In this chapter we shall review numerical studies of lattice proteins with different sequences and also describe our large-scale Monte Carlo studies of several different HP proteins, both in free space and in contact with an attractive surface.

7.2 Background

7.2.1 The HP Model

In proteins, 20 amino acids are commonly found and they serve as the basic "building blocks" [10]. Each amino acid contains an amino group ($-NH_2$) and a carboxylic acid group ($-COOH$), both are bonded to the same α-carbon atom. Amino acids are covalently bonded together by a peptide bond between the amino group of one amino acid and the carboxyl group of another. This forms the linear, rigid backbone of the protein. The only difference that distinguishes the amino acids is the side chain to which the α-carbon is attached. Side chains can be acidic, basic, uncharged polar, or non-polar. The first three types are basically hydrophilic, and the non-polar type is hydrophobic. Hence, the amino acids are classified according to the types of their side chains.

Amino acids interact with one another or with the environment through non-covalent bonds: ionic bonds, hydrogen bonds, and van der Waals forces. In an aqueous environment, hydrophobic amino acids are forced to group together in order to minimize the disturbance on the hydrogen-bonded networks of water [11]. Hydrophobic residues held together in this manner have been regarded as being "pulled" by their own attraction, the so-called hydrophobic bonds, although it originates from the repulsive force by the water molecules. Such a hydrophobic interaction is believed to be the most significant factor that governs the structure of proteins [12, 13].

The hydrophobic-polar (HP) lattice model [14] was proposed to capture the hydrophobic effect in protein folding. In this model, the protein is represented as a self-avoiding chain of beads (i.e., coarse-grained representations of the amino acid residues) on a rigid lattice. Amino acids are classified into two types: hydrophobic (H) and polar (P), and an attractive interaction ϵ acts only between non-bonded neighboring H residues (i.e., $\epsilon_{HH} = -1, \epsilon_{HP} = \epsilon_{PP} = 0$). Different sequences of H and P monomers are used to "match" different proteins, and several sequences which have been deemed "benchmarks" have been studied extensively by a variety of methods with varying success. Some benchmark sequences are listed in Table 7.1. If a surface is added additional couplings between monomers and the surface must be included. In the case of a hydrophobic surface, an additional energy ϵ_{HS} is won if an H is adjacent to the surface.

Table 7.1 Benchmark HP sequences used in this text

Seq. code	Reference	Sequence
2D50	[15]	HHPHPHPHPHHHHPHPPPHPPPHPPPPHPPPHPPPHPH HHHPHPHPHPHH
2D60	[15]	PPHHHPHHHHHHHHPPPHHHHHHHHHHPHPPPHHHHH HHHHHHHPPPPHHHHHHPHPHP
2D64	[15]	HHHHHHHHHHHHPHPHPPHHPPHPPHPPHPPHPPHPP HPPHHPPHHPPHPHPHHHHHHHHHHHH
2D85	[16]	HHHHPPPPHHHHHHHHHHHHPPPPPPHHHHHHHHHHHH HPPPHHHHHHHHHHHHPPPHHHHHHHHHHHHPPPHPP HHPPHHPPHPH
2D100a	[17]	PPPPPPHPHHPPPPPHHHPHHHHHPHHPPPPHHPPHH PHHHHHPHHHHHHHHHHPHHPHHHHHHHPPPPPPPPP PPHHHHHHHHPPHPHHHPPPPPPHPHH
2D100b	[17]	PPPHHPPHHHHPPHHHPHHPHHPHHHHPPPPPPPPHH HHHHPPHHHHHHPPPPPPPPPHPHHPHHHHHHHHHHHH PPHHHPHHPHPPHPHHHPPPPPPHHH
3D42	[18]	PHHPHPHHPHPHPPHHHPHPHHPHPHHHPPHPHPHHP HPHHP
3D48	[19]	PHPHPPPPHPHPHPPHPHHHHHHPPHHHPHPPHPHHP PHPHHHPPPPH
3D67	[18]	PHPHHPHHPHPPHHHPPPHPHHPHHPHPPHHHPPPHP HHPHHPHPPHHHPPPPHPHHPHHPHPPHHHP
3D88	[20]	PHPHHPHHPHPPHHPPHPPHPPHPPHPPHPPHHPPHHH PPHHHPPHHHPPHHHPPHPHHPHHPHPPHPPHPPHHP
3D103	[21]	PPHHPPPPPPHHPPHHPHPPHPPPPPPPHPPPHHPHHP PPPPPHPPHPHPPHPPPPPPHHHPPPPPHHPHPPPPPH HPPPPHHHHHPHPPPPPPPPHHHHHPPHPP
3D124	[21]	PPPHHHPHPPPPHPPPPPHHPPPPHHPPHHPPPPPHPP PPHPPHPPHHPPPHHPHPHHHPPPPHHHPPPPPPHHP PHPPHPHPPHPPPPPPPHPPHHHPPPPHPPPHHHHHP PPPHHPHPHPHPH
3D136	[21]	HPPPPPHPPPPHPHHPHHPPPPHPHHHPPPPHPHPHH HHPPPPPPPPPPPHPPHPPPHPHHPPPHHPPHPPHPH PHPPPPPPPPHPPPHHHHHHPPPHHPPHHHPPPHHPH HHHHPPPPPPPPPPHPPPPHPHPPPP

7.2.2 Numerical Methods

Previous work showed that the knowledge of the free energy landscape and the thermodynamics of a protein system is essential to completely understand the folding process [2, 22, 23], and thus Monte Carlo (MC) methods are indispensable tools for this purpose [24]. The configurations of a polymer may be studied using the traditional Metropolis method [25], but the complexity of the resultant free energy surface at low temperature renders the method extremely inefficient [26]. Two approaches have been taken to resolve the problem. One is to search only for the ground state configuration with the lowest energy, e.g., MC with minimization [27], simulated annealing [28], genetic algorithms [15], pruned–enriched Rosenbluth method (PERM) [29] and its variants [30, 31], tabu search [32], evolution-

ary Monte Carlo (EMC) [33], fragment regrowth Monte Carlo via energy-guided sequential sampling (FRESS) [34]. Detailed reviews can be found in [24, 35]. Apart from Monte Carlo methods, ground state conformation searches for HP sequences can also be performed by specific methods like hydrophobic core construction [18, 19, 36, 37].

Another approach allows one to estimate the density of states as a function of energy, $g(E)$, from which the thermodynamic properties of the system can be obtained. Examples include the multi-self-overlap-ensemble simulation (MSOE) [38], multicanonical chain growth (MCCG) [39, 40], equi-energy sampling (EES) [41], and Wang–Landau (WL) sampling [42–44]. As the HP model is a preliminary step toward the real protein folding problem, all these algorithms have used it as a common testing ground for their capacities.

Wang–Landau (WL) sampling is a very flexible and highly efficient and *robust* Monte Carlo algorithm for the determination of $g(E)$ of quite diverse statistical physical systems [42, 43, 45]. Instead of using the Boltzmann factor to determine if a trial move is accepted, as in the case of Metropolis sampling, WL sampling uses $g(E)$, and improves it iteratively as the simulation progresses. This tactic makes WL sampling advantageous over other simulation methods when dealing with systems having rough free energy landscapes, as it is not trapped in local minima. As an illustration we show the canonical probabilities of states for the Edwards-Anderson spin glass in 3D as a function of the order parameter q at low temperature in Fig. 7.1. The dramatic variations in the canonical probabilities make the simulation of such system very challenging for traditional Metropolis methods, but WL sampling is capable of obtaining it from a single simulation without difficulty. Thus, we believe that WL sampling is potentially effective for protein folding problems where the free energy landscape is known to be rather rough.

In our WL sampling with HP sequences we have determined that traditional trial moves, e.g., end-flips, kink-flips, crankshaft, and pivots, are inadequate in the collapsed state, so we have implemented new sets of trial moves introduced in [32, 46] that turn out to be very efficient [44]. Our approach has been to implement WL

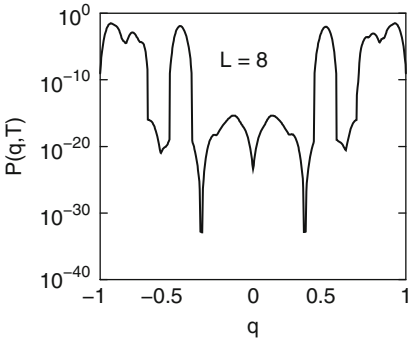

Fig. 7.1 Low-temperature canonical probability for the Edwards-Anderson spin glass in 3D as determined from a single simulation. The order parameter is q (from Wang and Landau [42])

sampling together with these new types of trial moves to determine $g(E)$ over the entire range of energies in a single run. In addition to allowing us to find the ground state (or "native state" in biological language) we can determine thermodynamic properties as a function of temperature.

The accuracies of the estimates for $g(E)$ are controlled by the final modification factor f_{final} and the flatness criterion p. Whereas WL studies of other polymeric systems reported that $\ln(f_{\text{final}}) \simeq 10^{-6}$ is sufficient, we have found that reliable estimates for $g(E)$ over the entire energy range (including the lowest energies) required $\ln(f_{\text{final}}) \leq 10^{-7}$. We, thus, used a very stringent parameter set for all our simulations: $\ln(f_{\text{final}}) = 10^{-8}$ and $p = 0.8$.

7.3 What Have We Already Learned?

7.3.1 The HP Model in the Absence of a Surface

We first examine the behavior of a few characteristic lattice proteins without a surface.

The knowledge of the full energy range is essential in the WL algorithm for the examination of the flatness of the histogram, but the energy boundaries are a priori unknown. (For this reason, there has been substantial use of ground state search algorithms, e.g., for the HP model.) To overcome this difficulty, the following procedure was used: Each time a new energy level E_{new} was found, it was marked as "visited" and $g(E_{\text{new}})$ was set to $g_{\min}$, i.e., the minimum of g among all previously visited energy levels. The flatness of the histogram is checked only for those energy levels that have been visited. With this self-adaptive procedure, new regions of conformational space can be explored simultaneously as the current estimate of $g(E)$ is further refined. First, we applied our procedure to various HP benchmark sequences as shown in Table 7.1. The ground states of sequence 2D100b are believed to have an energy $E = -50$ [38], and various methods have confirmed this result [30–32, 34]. However, previous attempts to obtain $g(E)$ over the entire energy range $[-50, 0]$ within a single simulation have failed [38, 41]. In contrast, with our approach we were able to achieve this with high accuracy and Fig. 7.2 shows the resulting specific heat $C_V(T)/N$, depicting a peak at $T \approx 0.48$ (coil–globule transition) and a very weak shoulder at $T \approx 0.23$ (folding transition). Such two-step acquisition of the ground (native) state has been observed in studies of realistic protein models, e.g., glycophorin A [47], and is not restricted to lattice models!

For sequence 3D103, the lowest energy found by fragment regrowth Monte Carlo via energy-guided sequential sampling (FRESS) [34] was $E = -57$, but with our approach, we discovered an even lower state with energy -58. It was also possible to determine $g(E)$ in the energy range $[-57, 0]$ from a single simulation, and with very high accuracy, although it was not possible to determine the relative magnitudes of the ground state and first excited state $g(E)$ with high precision. Figure 7.3 displays the specific heat for 3D103, manifesting a peak at $T \approx 0.51$ and a shoulder at

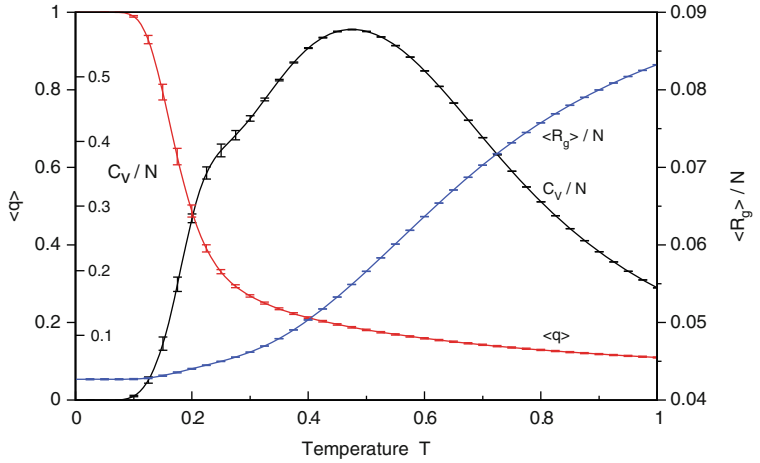

Fig. 7.2 Specific heat C_V/N, mean radius of gyration $\langle R_g\rangle/N$ (N, chain length) as a function of temperature T for the 2D HP sequence 2D100b. Statistical errors were calculated by a Jackknife analysis from 15 independent Wang–Landau (C_V) and multicanonical production runs ($\langle R_g\rangle$ and $\langle q\rangle$) for each sequence (from Wüst and Landau [44])

$T \approx 0.27$, but we observed no additional peak in C_V at low temperatures as in [39]. The C_V curves indicate that the folding transitions from unstructured globular conformations to the ground states are rather weak for both sequences.

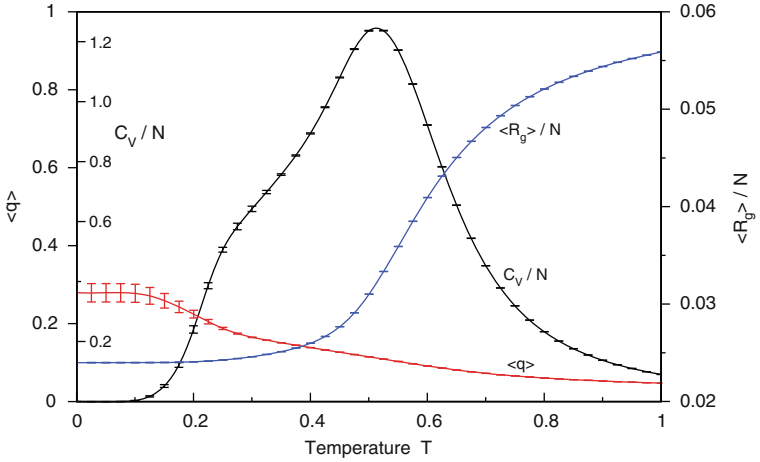

Fig. 7.3 Specific heat C_V/N, mean radius of gyration $\langle R_g\rangle/N$ (N, chain length) as a function of temperature T for the 3D HP sequence 3D103. Statistical errors were calculated by a Jackknife analysis from 15 independent Wang–Landau (C_V) and multicanonical production runs ($\langle R_g\rangle$ and $\langle q\rangle$) for each sequence (from Wüst and Landau [44])

By means of multicanonical sampling [48] given our estimates for $g(E)$, we obtained the radius of gyration R_g [49] and the Jaccard index q [50], here measuring the similarity between any conformation and the ground states of an HP sequence, i.e.,

$$q = \max \left\{ \left. \frac{C_{s,g}}{C_{s,g} + C_s + C_g} \right|_{E_g = E_{min}} \right\} \tag{7.1}$$

$C_{s,g}$ denotes the number of common (native) H–H contacts between a conformation s and the ground state g, and C_s, C_g are the numbers of H–H contacts found only in s and g, respectively (the maximum stems from the degeneracy of ground states). Figures 7.2 and 7.3 also show the temperature averages $\langle R_g \rangle$ and $\langle q \rangle$ for sequences 2D100b and 3D103 and illustrates the complementary information of these two quantities. While $\langle R_g \rangle$ indicates the coil-to-globule collapse, $\langle q \rangle$ identifies the folding transition to the native state and thus may serve as a suitable structural order parameter for these kinds of systems. In case of sequence 3D103, the ground state ($E = -58$) was excluded from the sampling (due to the difficulty of finding this state) which results in only rather small Jaccard indices for $T \to 0$. This shows that there are still large structural differences between conformations with $E = -57$ and the ground state with $E = -58$.

Table 7.2 compares results obtained using various methods, and, if available, the density of states $g(E)$ for common benchmark HP sequences. We also include results from methods which were focused on the low-temperature range only, i.e., FRESS [34] and the variants of PERM (pruned–enriched Rosenbluth method) [30, 31] and do not provide the entire density of states. Except for the longest sequence (3D136), we could confirm all minimum energy states found previously.

Table 7.2 Energy minima (E_{min}) found by several methods for benchmark HP sequences in 2D and 3D. The first column names the sequence (dimension and length); see Table 7.1. Dashes mean no data available. For abbreviations, see text

Seq.	WLS	EES	MCCG	MSOE	FRESS[a]	PERM[a]
2D50	−21	−21	–	–	−21	–
2D60	−36	−36	–	–	−36	−36
2D64	−42	−42	–	−42	−42	−42
2D85	−53	−53	–	–	−53	−53
2D100a	−48	−48	–	−47	−48	−48
2D100b	−50	−49	–	−50[b]	−50	−50
3D42	−34	–	−34	−34	–	–
3D48	−34	–	−34	–	−34	–
3D67	−56	–	–	–	−56	−56
3D88	−72	–	–	–	−72	−69
3D103	−58	–	−56	–	−57	−55
3D124	−75	–	–	–	−75	−71
3D136	−82	–	–	–	−83	−80

[a]Ground state search only
[b]$g(E)$ not attained

7.3.2 The HP Model with an Attractive Surface

We have also examined the behavior of several HP sequences when a surface is introduced. As an example we have performed Wang–Landau simulations for a rather short sequence, a 48mer, in a 3D space both with and without a surface field. In our simulations, one of the 48mers proposed in [19] was used (also see Table 7.1). It is merely an artificial sequence originally designed to test folding algorithms and so it might not have direct correspondence to real proteins. We have compared the results obtained from it with those from other HP sequences and found that this 48mer has already captured general behaviors. Nevertheless, it should be noted that the details of the properties still vary from sequence to sequence.

Common inorganic substrates include metals (Ag, Au, Pd, Pt), oxides ($CaCO_3$, Cr_2O_3, Fe_2O_3, SiO_2, ZnO) or semiconductors (GaAs, ZnS). Their adsorption properties are so well studied that polypeptide sequences can even be tailor-made to bind with a particular material [51]. Substrates made with different materials have various surface properties. When a protein interacts with a substrate, its surface can be attractive, neutral, or repulsive to different amino acids due to, for examples, the presence of charges, acidity (or basicity), and hydrophobicity. Handling charges or acidity is beyond the scope of the HP model, but we can still take the hydrophobicity of the surface into account and identify three types of attractive surface fields for the HP model. The first surface attracts both hydrophobic (H) and polar (P) monomers with the same magnitude. The second one is hydrophobic, i.e., it only attracts H monomers. The third one is polar, i.e., it only attracts P monomers. Here, we only consider the first type of surface for illustrative purpose.

In the absence of a surface field the 48mer folds into a compact globule as shown in Fig. 7.4. With the peripheral polar monomers surrounding a hydrophobic core, this structure maximizes the number of H–H bond pairs so as to attain the minimum energy $E_{\min} = -34$. Equivalently, 34 H–H bond pairs are formed. The simulation found the lowest energy and its corresponding states without difficulties, and the density of states was determined in the energy range $[-34, 0]$.

In the limiting case where the surface attraction is infinite, on the other hand, the HP polymer is completely attached to the surface and forms a 2D structure that is very different from the 3D native state. Figures 7.5 and 7.6 show two typical ground state structures of energy $E_{\min} = -21$ (i.e., there are 21 H–H bonds). The density of states was also determined with energies ranging from zero down to this ground state energy. A hydrophobic "core" is still observed in this case, but it does not remain as intact as in the case of the 3D free space. Figure 7.5 represents some configurations that still retain marginally the single hydrophobic core, although it has to be forced into a 2D structure. Some configurations might have the hydrophobic core broken into pieces as seen in Fig. 7.6. This suggests that with the presence of a strong attractive surface field, a protein would be deformed into a shape that is very different from its native one. Whether the protein in an adsorbed condition would still retain its function is not guaranteed.

After obtaining the density of states, the specific heat is then calculated. In Fig. 7.7, the two-step acquisition of the ground state is again observed as for the

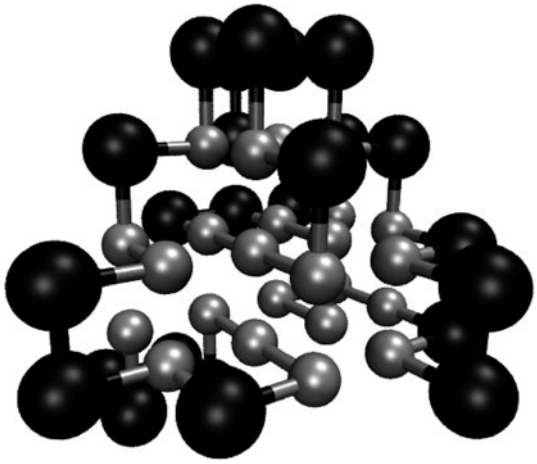

Fig. 7.4 A typical ground state configuration with energy of −34 of the 48mer in a 3D free space. A hydrophobic central core is formed to maximize the number of H–H contacts. The *black and gray beads* represent the polar and the hydrophobic residues, respectively, and the size of the beads is merely for visualization purpose without correspondence to the real size of the residues. Graphic is created by VMD [52]

103mer in 3D free space. A peak appears at $T \approx 0.50$ which signifies the transition from an extended coil to a rather compact globular structure. A weak shoulder is found at $T \approx 0.25$ representing the rearrangements of bonds to bring the globule to a even more compact state with a lower energy. As the magnitude of the surface field increases, the folding process first becomes more complex, but when the surface field is infinitely attractive so that the protein must lie entirely on the surface, only a single specific heat peak is seen at $T \approx 0.38$. This suggests that the transition behavior is somewhat "simplified" into a single step process, where the adsorbed, extended coil transforms into an absorbed, compact globular conformation.

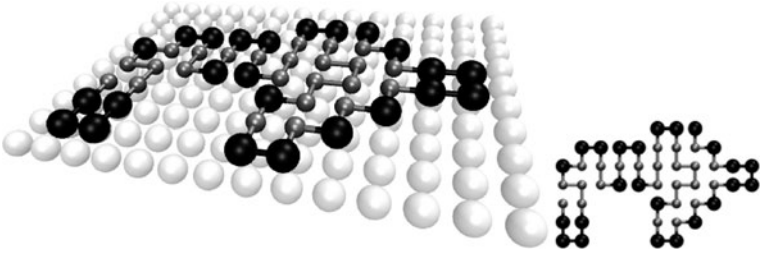

Fig. 7.5 Typical ground state configurations with energy of −21 of the 48mer attached to a surface of infinite strength. This configuration has an intact hydrophobic core. The *black and gray beads* represent the polar and the hydrophobic residues, respectively, the *white beads* represent the surface. The size of the beads is merely for visualization purpose without correspondence to the real size of the residues. Graphic is created by VMD [52]

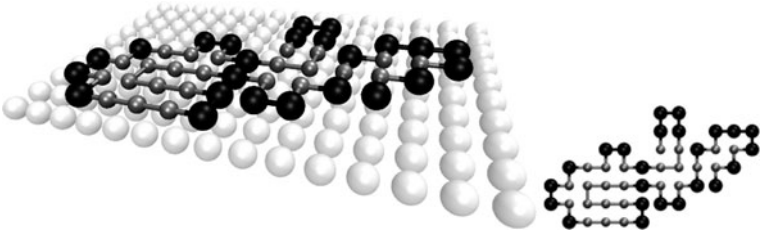

Fig. 7.6 Typical ground state configurations with energy of −21 of the 48mer attached to a surface of infinite strength. The hydrophobic core is broken into two pieces in this case. The *black and gray beads* represent the polar and the hydrophobic residues, respectively, the *white beads* represent the surface. The size of the beads is merely for visualization purpose without correspondence to the real size of the residues. Graphic is created by VMD [52]

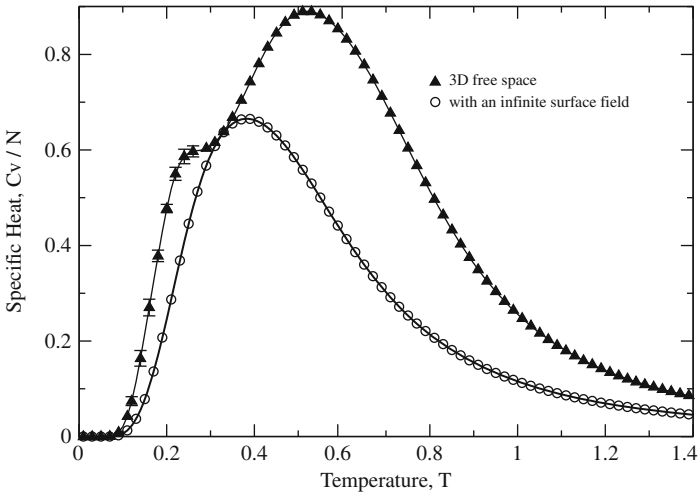

Fig. 7.7 Specific heat, C_V/N, of the 48mer with (i) no surface fields (*circles*), and (ii) a surface field with an infinite strength (*triangles*). Statistical errors were calculated from 10 independent runs. Error bars are shown only if the errors are larger than the size of the points. Without a surface, the sequence acquires the ground state in a two-step process as indicated by the peak and the weak shoulder in the specific heat. With a surface of infinite strength, the sequence undergoes transition in a one-step process in which a single peak is shown in the specific heat

The specific heat is a crucial key to reveal the phase transition behaviors. Pioneering work by Bachmann et al. studied the interactions of the 3D103 sequence with the three different surfaces of finite strength using the MCCG algorithm [53]. They have identified five conformational pseudophases which are separated by the peaks in the specific heat at a given value of ϵ_{HH}. (The term "solubility" s is used in [53] for the same quantity.) As ϵ_{HH} varies, peaks in the specific heat join together to form "ridges," which give the pseudophase transition lines. Depending on the structures and the degree of adhesion to the substrate, the pseudophases are classified into the

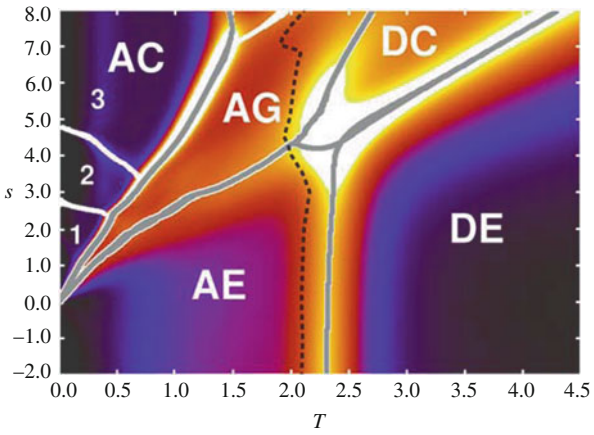

Fig. 7.8 A pseudophase diagram for the 103mer interacting with a surface that is attractive to both H and P monomers. See the text for a description of the pseudophases. (From Bachmann and Janke [53])

adsorbed compact (AC), adsorbed expanded (AE), adsorbed globule (AG), desorbed compact (DC), and desorbed expanded (DE) phases (Fig. 7.8).

7.4 What Do We Still Want to Learn?

In order to understand how a protein reacts toward various materials in a coarse-grained perspective, simulations of HP sequences interacting with hydrophobic surfaces or polar surfaces will be necessary, in addition to surfaces attracting all kinds of residues regardless of their hydrophobicity. One step further, surfaces of finite attraction strength should be considered in order to simulate systems closer to realistic experimental scenarios.

We have carried out simulations on the same 103mer and physical settings as in [53] using Wang–Landau sampling. In principle our preliminary results agree with previous studies, but we got slightly different observations in the specific heat which might lead to different transition behaviors (Li et al., unpublished). Further investigations are definitely required before drawing any conclusion.

In fact, there are growing attention and developments in treating the problem of protein–substrate interactions using coarse-grained models. For example, a refined HP model is used to study the adsorption of peptides on gold and palladium surfaces in [54]. Apart from the hydrophobic and polar effects among amino acid residues, interactions due to electrostatic forces, the presence of solvents, and more detailed substrate–amino acid interaction potentials (obtained from all-atomistic point of view instead of just classifying the surface briefly into hydrophobic or polar) are considered. The relative field strengths can also be adjusted by defining an interaction matrix so as to introduce diversities to the interactions.

With the effectiveness and accuracy, Wang–Landau sampling is believed to be one of the feasible methods for such systems, and its performance has been proven using the HP sequences. Recently, Swetnam et al. have proposed ways to improve the efficiency of simulating lattice peptides adsorption (including homopolymers and HP sequences) using Wang–Landau sampling [55]. The improvement scheme is in two aspects: the first one is to reduce the time used during the process of selecting a valid pull move that brings the polymer from one conformation to another. It is made possible by not counting all available moves given a conformation. The second proposed improvement is to shift the surface accordingly so that it is always touching the polymer. In this way, every state generated would be a state absorbed to the surface, and time would not be wasted in simulating desorbed conformations. These reduce the computation time to a certain extent and will allow simulations of larger systems.

7.5 Conclusion

In this work, we have reviewed a minimalistic lattice model for proteins, the HP model, and some numerical methods to study HP benchmark sequences. We have also illustrated how the HP model can be used to study the effects of protein–surface interactions via a coarse-grained approach. In spite of the simplicity of the model, it successfully recovers major features found in real proteins and shows how the presence of a surface affects the conformations of proteins. Nevertheless, the use of coarse-grained models to study peptide–substrate activities is still in its initial stage, and the richness and complexities in thermodynamics properties are yet to understand thoroughly. Further developments and advancements are certainly essential in this emerging area.

Acknowledgments This research was supported by NSF Grant DMR-0810223 and NIH Grant 1R01GM075331.

References

1. J.D. Bryngelson, J.N. Onuchic, N.D. Socci, P.G. Wolynes, Funnels, pathways and the energy landscape of protein folding: a synthesis. Prot. Struct. Funct. Genet. **21**, 167 (1995)
2. J.N. Onuchic, Z. Luthey-Schulten, P.G. Wolynes, Theory of protein folding: the energy landscape perspective. Ann. Rev. Phys. Chem. **48**, 545 (1997)
3. C.B. Anfinsen, Principles that govern the folding of protein chains. Science **181**, 223 (1973)
4. G. MacBeath, S.L. Schreiber, Printing proteins as microarrays for high-throughput function determination. Science **289**, 1760 (2000)
5. R. Fernandez-Lafuente et al., Immobilization of lipases by selective adsorption on hydrophobic supports. Chem. Phys. Lipids **93**, 185 (1998)
6. R.S. Kane, A.D. Stroock, Nanobiotechnology: protein-nanomaterial interactions. Biotechnol. Prog. **23**, 316 (2007)

7. S.S. Davis, L. Illum, Polymeric microspheres as drug carriers. Biomaterials **9**, 111 (1988)
8. B. Berger, T. Leighton, Protein folding in the hydrophobic-hydrophilic (HP) model is NP-complete. J. Comp. Biol. **5**, 27 (1998)
9. P. Crescenzi et al., On the complexity of protein folding. J. Comp. Biol. **5**, 409 (1998)
10. C. Branden, J. Tooze, *Introduction to Protein Structure* (Garland, New York, NY, 1991)
11. B. Alberts, D. Bray, J. Lewis, M. Raff, K. Roberts, J.D. Watson, *Molecular Biology of the Cell*, 3rd edn. (Garland, New York, NY, 1994), pp. 90–93
12. W. Kauzmann, Some factors in the interpretation of protein denaturation. Adv. Protein Chem. **14**, 1 (1959)
13. K.A. Dill, The meaning of hydrophobicity. Science **250**, 297 (1990)
14. K.A. Dill, Theory for the folding and stability of globular proteins, Biochemistry **24**, 1501 (1985); K.F. Lau, K.A. Dill, A lattice statistical mechanics model of the conformational and sequence spaces of protein. Macromolecules **22**, 3986 (1989)
15. R. Unger, J. Moult, Genetic algorithms for protein folding simulations, J. Mol. Biol. **231**, 75 (1993); J.T. Pedersen, J. Moult, Genetic algorithms for protein structure prediction. Curr. Opin. Struct. Biol. **6**, 227 (1996)
16. R. König, T. Dandekar, Improving genetic algorithms for protein folding simulations by systematic crossover. Biosystems **50**, 17 (1999)
17. R. Ramakrishnan, B. Ramachandran, J.F. Pekny, A dynamic Monte Carlo algorithm for exploration of dense conformational spaces in heteropolymers. J. Chem. Phys. **106**, 2418 (1997)
18. K. Yue, K.A. Dill, Forces of tertiary structural organization in globular proteins. Proc. Natl. Acad. Sci. USA **92**, 146 (1995)
19. K. Yue, K.M. Fiebig, P.D. Thomas, H.S. Chan, E.I. Shakhnovich, K.A. Dill, A test of lattice protein folding algorithms, Proc. Natl. Acad. Sci. USA **92**, 325 (1995)
20. T.C. Beutler, K.A. Dill, A fast conformational search strategy for finding low energy structures of model proteins. Protein Sci. **5**, 2037 (1996)
21. E.E. Lattman, K.M. Fiebig, K.A. Dill, Modeling compact denatured states of proteins. Biochemistry **33**, 6158 (1994)
22. K.A. Dill et al., Principles of protein folding – A perspective from simple exact models, Protein Sci. **4**, 561 (1995); K.A. Dill, Polymer principles and protein folding. Protein Sci. **8**, 1166 (1999)
23. A. Sali, E. Shakhnovich, M. Karplus, How does a protein fold?, Nature **369**, 248 (1994); Kinetics of protein folding. A lattice model study of the requirements for folding to the native state. J. Mol. Biol. **235**, 1614 (1994)
24. U.H.E. Hansmann, Y. Okamoto, New Monte Carlo algorithms for protein folding. Curr. Opin. Struct. Biol. **9**, 177 (1999)
25. N. Metropolis et al., Equation of state calculations by fast computing machines. J. Chem. Phys. **21**, 1087(1953)
26. G.H. Paine, H.A. Scheraga, Prediction of the native conformation of a polypeptide by a statistical mechanical procedure. I. Backbone structure of enkephalin. Biopolymers **24**, 1391 (1985)
27. Z.Q. Li, H.A. Scheraga, Monte-Carlo-minimization approach to the multiple-minima problem in protein folding. Proc. Natl. Acad. Sci. USA **84**, 6611 (1987)
28. S. Kirkpatrick, C.D. Gelatt, M.P. Vecchi, Optimization by simulated annealing. Science **220**, 671 (1983)
29. P. Grassberger, Pruned-enriched Rosenbluth method: Simulations of ϑ polymers of chain length up to 1 000 000. Phys. Rev. E **56**, 3682 (1997)
30. H. Frauenkron et al., New Monte Carlo algorithm for protein folding. Phys. Rev. Lett. **80**, 3149 (1998); U. Bastolla et al., Testing a new Monte Carlo algorithm for protein folding. Proteins **32**, 52 (1998)
31. H.-P. Hsu et al., Growth algorithms for lattice heteropolymers at low temperatures. J. Chem. Phys. **118**, 444 (2003); H.-P. Hsu et al., Growth-based optimization algorithm for lattice heteropolymers. Phys. Rev. E **68**, 021113 (2003)

32. N. Lesh, M. Mitzenmacher, S. Whitesides, A complete and effective move set for simplified protein folding. Proceedings of the 7th annual int'l conference on research in computational molecular biology (RECOMB) (2003), p. 188
33. F. Liang, W.H. Wong, Evolutionary Monte Carlo for protein folding simulations. J. Chem. Phys. **115**, 3374 (2001)
34. J. Zhang, S.C. Kou, J.S. Liu, Biopolymer structure simulation and optimization via fragment regrowth Monte Carlo. J. Chem. Phys. **126**, 225101 (2007)
35. X. Zhao, Advances on protein folding simulations based on the lattice HP models with natural computing. Applied Soft Computing **8**, 1029 (2008)
36. K. Yue, K.A. Dill, Sequence-structure relationships in proteins and copolymers. Phys. Rev. E **48**, 2267 (1993)
37. R. Backofen, S. Will, A constraint-based approach to fast and exact structure prediction in three dimensional protein models. Constraints **11**, 5 (2006)
38. Y. Iba, G. Chikenji, M. Kikuchi, Simulation of lattice polymers with multi-self-overlap ensemble. J. Phys. Soc. Jpn. **67**, 3327 (1998); Multi-self-overlap ensemble for protein folding: ground state search and thermodynamics. Phys. Rev. Lett. **83**, 1886 (1999)
39. M. Bachmann, W. Janke, Multicanonical chain-growth algorithm. Phys. Rev. Lett. **91**, 208105 (2003); Thermodynamics of lattice heteropolymers. J. Chem. Phys. **120**, 6779 (2004)
40. T. Prellberg, J. Krawczyk, Flat histogram version of the pruned and enriched Rosenbluth method. Phys. Rev. Lett. **92**, 120602(2004); T. Prellberg, J. Krawczyk, A. Rechnitzer, Polymer simulations with a flat histogram stochastic growth algorithm. In *Computer Simulation Studies in Condensed-Matter Physics XVII*, ed. by D.P. Landau, S.P. Lewis, H.-B. Schüttler. Proceedings of the 17th Workshop on Recent Developments in Computer Simulation Studies in Condensed Matter Physics (Springer, Berlin Heidelberg New York, NY, 2006), pp. 122–135; cond-mat/0402549
41. S.C. Kou, J.Oh, W.H. Wong, A study of density of states and ground states in hydrophobic-hydrophilic protein folding models by equi-energy sampling. J. Chem. Phys. **124**, 244903 (2006)
42. F. Wang, D.P. Landau, Efficient, multiple-range random walk algorithm to calculate the density of states. Phys. Rev. Lett. **86**, 2050 (2001); Determining the density of states for classical statistical models: a random walk algorithm to produce a flat histogram. Phys. Rev. E **64**, 056101 (2001); Determining the density of states for classical statistical models by a flat-histogram random walk. Comput. Phys. Commun. **147**, 674 (2002)
43. T. Wüst, D.P. Landau, The HP model of protein folding: a challenging testing ground for Wang-Landau sampling. Comput. Phys. Commun. **179**, 124 (2008)
44. T. Wüst, D.P. Landau, Versatile approach to access the low temperature thermodynamics of lattice polymers and proteins. Phys. Rev. Lett. **102**, 178101 (2009)
45. D.P. Landau, K. Binder, *A Guide to Monte Carlo Simulations in Statistical Physics*, 2nd edn. (Cambridge University Press, Cambridge, MA, 2005)
46. J.M. Deutsch, Long range moves for high density polymer simulations. J. Chem. Phys. **106**, 8849 (1997)
47. C. Gervais, T. Wüst, D.P. Landau, Y. Xu, Application of the Wang-Landau algorithm to the dimerization of glycophorin A. J. Chem. Phys. **130**, 215106 (2009)
48. B. Berg, T. Neuhaus, Multicanonical algorithms for first order phase transitions. Phys. Lett. B **267**, 249 (1991); Multicanonical ensemble: a new approach to simulate first-order phase transitions, Phys. Rev. Lett. **68**, 9 (1992)
49. A.D. Sokal in *Monte Carlo and Molecular Dynamics Simulations in Polymer Science*, ed. by K. Binder (Oxford University Press, Oxford, 1995), p. 47
50. R. Fraser, J.I. Glasgow, A demonstration of clustering in protein contact maps for Alpha Helix Pairs. In *ICANNGA*, vol. 1, (2007), p. 758
51. M. Sarikaya, C. Tamerler, A.K.Y. Jen, K. Schulten, F. Baneyx, Molecular biomimetics: nanotechnology through biology. Nature Materials **2**, 577 (2003)

52. W. Humphrey, A. Dalke, K. Schulten, VMD – visual molecular dynamics. J. Mol. Graphics **14**, 33 (1996)
53. M. Bachmann, W. Janke, Substrate adhesion of a nongrafted flexible polymer in a cavity. Phys. Rev. E **73**, 020901(R) (2006); Minimalistic hybrid models for the adsorption of polymers and peptides to solid substrates. Phys. Particles Nuclei Lett. **5**, 243 (2008)
54. R.B. Pandey et al., Adsorption of peptides (A3, Flg, Pd2, Pd4) on gold and palladium surfaces by a coarse-grained Monte Carlo simulation. Phys. Chem. Chem. Phys. **11**, 1989 (2009)
55. A.D. Swetnam, M.P. Allen, Improved simulations of lattice peptide adsorption. Phys. Chem. Chem. Phys. **11**, 2046 (2009)

Chapter 8
Polymer Chain Adsorption on a Solid Surface: Scaling Arguments and Computer Simulations

A. Milchev, V. Rostiashvili, S. Bhattacharya, and T. Vilgis

Abstract We examine the phase transition of polymer adsorption as well as the underlying kinetics of polymer binding from dilute solutions on a structureless solid surface. The emphasis is put on the properties of regular multiblock copolymers, characterized by block size M and total length N as well as on random copolymers with quenched composition p of sticky and neutral segments. The macromolecules are modeled as coarse-grained bead-spring chains subject to a short-ranged surface adhesive potential. Phase diagrams, showing the variation of the critical threshold for single chain adsorption in terms of M and p, are derived from scaling considerations in agreement with results from computer experiment. Using both scaling analysis and numerical data from solving a system of coupled master equations, we demonstrate that the phase behavior at criticality and the adsorption kinetics may be adequately predicted and understood, in agreement with the results of extensive Monte Carlo simulations. Derived analytic expressions for the mean fraction of adsorbed segments as well as for probability distribution functions of the various structural building blocks (i.e., trains, loops, tails) at time t during the chain attachment process are in good agreement with our numeric experiments and provide insight into the mechanism of polymer adsorption.

8.1 Introduction

The adsorption of polymers on solid surfaces is a long-standing problem which plays an important role in a number of applications in technology (protective coatings, adhesives, lubricants, stabilization of colloids, flocculation, etc.) and biology (adsorption of biopolymers, etc.). As a phenomenon it poses a number of challenging scientific problems [1–4] too. Important theoretical contributions have been made by Birshtein [5], de Gennes [6], and Eisenriegler et al. [7]. Later studies have covered adsorption of polyelectrolytes [8], dynamics of adsorbed chains [9], and adsorption on chemically heterogeneous surfaces [10]. The close relationship

A. Milchev (✉)
Institute of Physical Chemistry, Bulgarian Academy of Sciences, 1113 Sofia, Bulgaria
e-mail: milchev@ipc.bas.bg

M. Michailov (ed.), *Nanophenomena at Surfaces,* Springer Series in Surface Sciences 47,
DOI 10.1007/978-3-642-16510-8_8,

between analytic theory and computer experiments in this field [10–14] has proved especially fruitful and instructive.

While the investigations mentioned above have been devoted exclusively to homopolymers, the adsorption of copolymers (e.g., random or multiblock copolymers) still poses open questions. Thus, for instance, the critical adsorption potential (CAP) dependence on block size M at fixed concentration of the sticking A-monomers is still unknown as are the scaling properties of *regular multiblock copolymers* in the vicinity of the CAP. From the theoretical perspective, the case of diblock copolymers has been studied by means of the grand canonical ensemble (GCE) approach [15, 16], within the self-consistent field (SCF) approach [17, 18], or by Monte Carlo computer simulations [19, 20]. The case of *random copolymers* adsorption has gained comparatively more attention by researcher so far. It has been investigated by Whittington et al. [21, 22] using both the annealed and quenched models of randomness. The influence of sequence correlations on the adsorption of random copolymers has been treated by means of the variational and replica method approach [23]. Sumithra and Baumgaertner [24] examined the question of how the critical behavior of random copolymers differs from that of homopolymers. Thus, among a number of important conclusions, the results of Monte Carlo simulations demonstrated that the so-called adsorption (or, crossover) exponent ϕ (see below) is independent of the fraction of attractive monomers n.

The adsorption kinetics of polymers has been intensively studied both experimentally [25, 26] and theoretically [27–33] since more than two decades now. A key parameter thereby is the height of the free energy adsorption barrier that the polymer chain has to overcome so as to bind to the surface. High barriers are usually referred to as cases of *chemisorption* as opposed to those of *physisorption* which are characterized by low barriers for adsorption. Depending on the strength of the binding interaction ϵ, one distinguishes then between weak physisorption when ϵ is of the order of the thermal energy $k_{\mathrm{B}}T$ (with k_{B} being the Boltzmann constant), and strong physisorption when $\epsilon \geq 2k_{\mathrm{B}}T$. One of the important questions concerns the scaling of the adsorption time τ_{ads} with the length of the polymer chain N in dilute solutions. For homopolymers in the regime of strong physisorption (that is, for sticking energy considerably above the CAP) computer experiments [28, 31, 32] suggest $\tau_{\mathrm{ads}} \propto N^{\alpha}$ where α is related to the Flory exponent ν as $\alpha = 1 + \nu \approx 1.59$. This result follows from the assumed *zipping* mechanism in the absence of a significant barrier whereby the chain adsorbs predominantly by means of sequential, consecutive attachment of monomers, a process that quickly erases existing loops on the substrate. For the case of *weak* adsorption, one should mention a recent study [33], where one finds in contrast $\alpha = (1 + 2\nu)/(1 + \nu) \approx 1.37$ which suggests shorter timescale for surface attachment. In chemisorption, the high barrier which attaching monomers encounter slows down the binding to the surface, the chain gains more time to attain equilibrium conformation, and the adsorption process is believed to involve large loop formation giving rise to *accelerated zipping* mechanism [29, 30]. The predicted value of α in agreement with MC results is $\alpha \approx 0.8 \pm 0.02$ [32]. A comprehensive overview of experimental work and theoretic considerations may be found in the recent review of O'Shaughnessy and Vavylonis [30].

In the present contribution we focus on copolymer physisorption, extending thus the aforementioned studies of homopolymers statics and kinetics. We show how scaling analysis as well as different MC simulation methods help understand the critical behavior of multiblock and random copolymers. It turns out that the critical behavior of these two types of copolymers can be reduced to the behavior of an effective homopolymer chain with "renormalized" segments. For multiblock copolymers one can thus explain how the adsorption threshold depends on the block length M and even derive an adsorption phase diagram in terms of CAP against M. In the case of random copolymers, the sequence of sticky and neutral (as regards the solid substrate) monomers within a particular chain is usually fixed which exemplifies a system with *quenched randomness*. Nevertheless, close to criticality the chain is still rather mobile, so that the sequence dependence is effectively averaged over the time of the experiment and the problem can be reduced to the easier case of *annealed randomness*. We show that the MC findings close to criticality could be perfectly described within the annealed randomness model.

For both regular multiblock and random copolymers, we compare the predicted kinetics of adsorption in the regime of strong physisorption, to consistent numeric data derived from simulations and coupled master equations. We demonstrate that the observed adsorption kinetics is close to that of homopolymers and suggest interpretation of typical deviations. Eventually, we should like to stress that the complex polymer hydrodynamics near an interface has remained beyond the scope of this chapter.

8.2 Simulation Methods

Apart from the frequently used bond fluctuation method (BFM) [28, 32], two coarse-grained models, a bead-spring off-lattice model [9] and a cubic lattice model implementing the so-called pruned–enriched Rosenbluth method (PERM) [14], are used to test theoretical predictions.

8.2.1 Off-Lattice Bead-Spring Model

In our computer simulations we use a coarse-grained off-lattice bead-spring model [11] to describe polymer chains. The system consists of a single chain tethered at one end to a flat structureless surface so as to avoid problems with translational entropy depending on the box size. There are two kinds of monomers: "A" and "B," of which only the "A" type feels an attraction to the surface. The surface interaction of the "A"-type monomers is described by a short-range square well potential $U_{\mathrm{w}}(z) = \epsilon$ for $z < \delta$ and $U_{\mathrm{w}}(z) = 0$ otherwise, whereby the range $\delta = 0.125$ (in units of the maximal bond length extension $l_{\max}$ between adjacent beads). The effective bonded interaction is described by the FENE (finitely extensible nonlinear elastic) potential:

$$U_{\mathrm{FENE}} = -K(1-l_0)^2 \ln\left[1-\left(\frac{l-l_0}{l_{\max}-l_0}\right)^2\right] \tag{8.1}$$

with $K = 20, l_{\max} = 1, l_0 = 0.7, l_{\min} = 0.4$.

The nonbonded interactions are described by the Morse potential:

$$\frac{U_{\mathrm{M}}(r)}{\epsilon_{\mathrm{M}}} = \exp(-2\alpha(r-r_{\min})) - 2\exp(-\alpha(r-r_{\min})) \tag{8.2}$$

with $\alpha = 24$, $r_{\min} = 0.8$, $\epsilon_{\mathrm{M}}/k_{\mathrm{B}}T = 1$.

We use periodic boundary conditions in the $x-y$-directions and impenetrable walls in the z-direction. We study homopolymer chains, regular multiblock copolymers, and random copolymers (with a fraction of attractive monomers, $p = 0.25, 0.5, 0.75$) of length 32, 64, 128, 256, and 512. The size of the box is $64 \times 64 \times 64$ in all cases except for the 512 chains where we use a larger box size of $128 \times 128 \times 128$. The standard Metropolis algorithm is employed to govern the moves with self-avoidance automatically incorporated in the potentials. In each Monte Carlo update, a monomer is chosen at random and a random displacement attempted with Δx, Δy, Δz chosen uniformly from the interval $-0.5 \leq \Delta x, \Delta y, \Delta z \leq 0.5$. The transition probability for the attempted move is calculated from the change ΔU of the potential energies before and after the move as $W = \exp(-\Delta U/k_{\mathrm{B}}T)$. As for a standard Metropolis algorithm, the attempted move is accepted if W exceeds a random number uniformly distributed in the interval (0, 1).

Typically, the polymer chains are originally equilibrated in the MC method for a period of about 10^6 MCS (depending on degree of adsorption ϵ and chain length N this period is varied) whereupon one performs 200 measurement runs, each of length 8×10^6 MCS. In the case of random copolymers, for a given composition, i.e., percentage p of the A-monomers, we create a new polymer chain in the beginning of the simulation run by means of a randomly chosen sequence of segments. This chain is then sampled during the course of the run and replaced by a new sequence in the beginning of the next run.

8.2.2 Coarse-Grained Lattice Model with PERM

The adsorption of a diblock AB copolymer with one end (monomer A) grafted to a flat impenetrable surface and with only the A-monomers attractive to the surface is described by self-avoiding walks (SAW) of $N-1$ steps on a simple cubic lattice with restriction $z \geq 0$. The partition sum may be written as

$$Z_N^{(1)}(q) = \sum_{N_{\mathrm{s}}} A_N(N_{\mathrm{s}}) q^{N_{\mathrm{s}}} \tag{8.3}$$

where $A_N(N_{\mathrm{s}})$ is the number of configurations of SAWs with N steps having N_{s} sites on the wall, and $q = e^{\epsilon/k_{\mathrm{B}}T}$ is the Boltzmann factor ($\epsilon > 0$ is the attractive

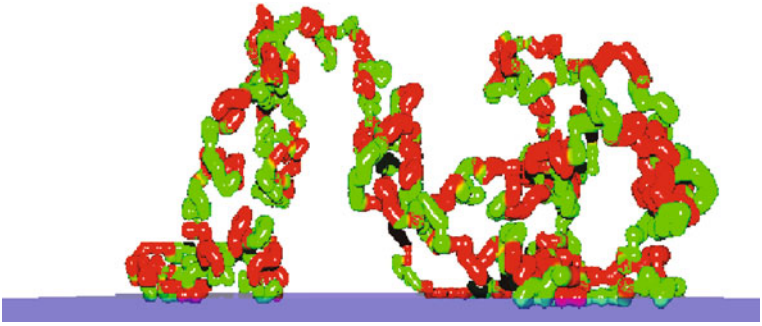

Fig. 8.1 Schematic representation of a grafted chain close to criticality. Snapshot of a regular multiblock copolymer with length $N = 2048$ and block size $M = 8$ from the PERM simulation

energy between the monomer A and the wall). Clearly, any copolymer will collapse onto the wall, if q becomes sufficiently large. Therefore one expects a phase transition from a grafted but otherwise detached phase into an adsorbed phase, similar to the transition observed for homopolymers.

The pruned–enriched Rosenbluth method (PERM) [14], also used in our simulations, is a *biased* chain growth algorithm with resampling ("population control") and depth-first implementation. Polymer chains are built like random walks by adding one monomer at each step. Thus the total weight of a configuration for a polymer consisting of N monomers is a product of those weight gains at each step, i.e., $W_N = \Pi_{i=0}^{N-1} w_i$. As in any such algorithm, there is a wide range of possible distributions of sampling so we have the freedom to give a bias at each step while the chain grows, and the bias is corrected by means of giving a weight to each sample configuration, namely, $w_i \to w_i/p_i$ where p_i is the probability for putting the monomer at step i. In order to suppress the fluctuations of weights as the chain is growing, the population control is done by "pruning" configurations with too low weight and "enriching" the sample with copies of high-weight configurations. Therefore, two thresholds are introduced here, $W_n^+ = c^+ Z_n$ and $W_n^- = c^- Z_n$, where $Z_n = \frac{1}{M_n} \sum_{\text{config.}} W_n$ from the M_n trail configuration is the current estimate of partition sum at the $n-1$ step, c^+ and c^- are constants of order unity and $c^+/c^- \approx 10$. In order to compare with the results obtained by the first MC method, we simulate homopolymers of length $N = 2048$ and multiblock copolymers with block size $M = 2^k$, $k = 0, 1, 2, \ldots, 9$ (see Fig. 8.1). The number of monomers is increased to $N = 8192$ as the block size increases. There are 10^5–10^6 independent configurations for each measurement. We also simulate random copolymers of $N = 2048$ monomers with composition $p = 0.125$, 0.25, 0.50, and 0.75.

8.3 Scaling Behavior at Criticality

8.3.1 A Homopolymer Chain

It is well known [7, 12, 13] that a single polymer chain undergoes a transition from a non-bound into an adsorbed state when the adsorption energy ϵ per monomer

increases beyond a critical value $\epsilon_c \approx k_B T$ (where T stands for the temperature of the system). The adsorption transition can be interpreted as a second-order phase transition at the critical point (CAP) of adsorption $\epsilon = \epsilon_c$ in the thermodynamical limit, i.e., $N \to \infty$. Close to the CAP the number of surface contacts N_s scales as $N_s(\epsilon = \epsilon_c) \sim N^{\phi}$. The numerical value of ϕ is somewhat controversial and lies in a range between $\phi = 0.59$ [7] and $\phi = 0.484$ [14]; we adopt, however, the value $\phi = 0.50 \pm 0.02$ which has been suggested as the most satisfactory [13] by comparison with comprehensive simulation results.

How does polymer structure vary with adsorption strength? Consider a chain tethered to the surface at the one end. The fraction of monomers on the surface $n = N_s/N$ may be viewed as an order parameter measuring the degree of adsorption. In the thermodynamic limit $N \to \infty$, the fraction n goes to zero ($\approx \mathcal{O}(1/N)$) for $\epsilon \ll \epsilon_c$, then near ϵ_c, $n \sim N^{\phi-1}$ whereas for $\epsilon \gg \epsilon_c$ (in the strong coupling limit) n is independent of N. Let us measure the distance from the CAP by the dimensionless quantity $\kappa = (\epsilon - \epsilon_c)/\epsilon_c$ and also introduce the scaling variable $\eta \equiv \kappa N^{\phi}$. The corresponding scaling ansatz [34] is then $n(\eta) = N^{\phi-1} G(\eta)$ with the scaling function

$$G(\eta) = \begin{cases} \text{const} & \text{for} \quad \eta \to 0 \\ \eta^{(1-\phi)/\phi} & \text{for} \quad \eta \gg 1 \end{cases} \tag{8.4}$$

The resulting scaling behavior of n follows as,

$$n \propto \begin{cases} 1/N & \text{for} \quad \kappa \ll 0 \\ N^{\phi-1} & \text{for} \quad \kappa \to 0 \\ \kappa^{(1-\phi)/\phi} & \text{for} \quad \kappa \gg 1 \end{cases} \tag{8.5}$$

The gyration radius in direction perpendicular to the surface, $R_{g\perp}(\eta)$, has the form $R_{g\perp}(\eta) = aN^{\nu}\mathcal{G}_{g\perp}(\eta)$. One may determine the form of the scaling function $\mathcal{G}_{g\perp}(\eta)$ from the fact that for $\kappa < 0$ one has $R_{g\perp} \sim aN^{\nu}$ so that $\mathcal{G}_{g\perp} = \text{const}$. In the opposite limit, $\eta \gg 0$ the N-dependence drops out and $\mathcal{G}_{g\perp}(\eta) \sim \eta^{-\nu/\phi}$. In result

$$R_{g\perp}(\eta) \propto \begin{cases} aN^{\nu} & \text{for} \quad \eta \le 0 \\ \kappa^{-\nu/\phi} & \text{for} \quad \eta \gg 0 \end{cases} \tag{8.6}$$

The gyration radius in direction parallel to the surface has similar scaling representation, $R_{g\parallel}(\eta) = aN^{\nu}\mathcal{G}_{g\parallel}(\eta)$. Again at $\kappa < 0$ the gyration radius $R_{g\parallel} \sim aN^{\nu}$ and $\mathcal{G}_{g\parallel} = \text{const}$. At $\eta \gg 0$ the chain behaves as a two-dimensional self-avoiding walk (SAW), i.e., $R_{g\parallel} \sim aN^{\nu_2}$, where $\nu_2 = 3/4$ denotes the Flory exponent in two dimensions. In result, the scaling function behaves as $\mathcal{G}_{g\parallel}(\eta) = \eta^{(\nu_2-\nu)/\phi}, \quad \text{at} \quad \eta \gg 0$. Thus

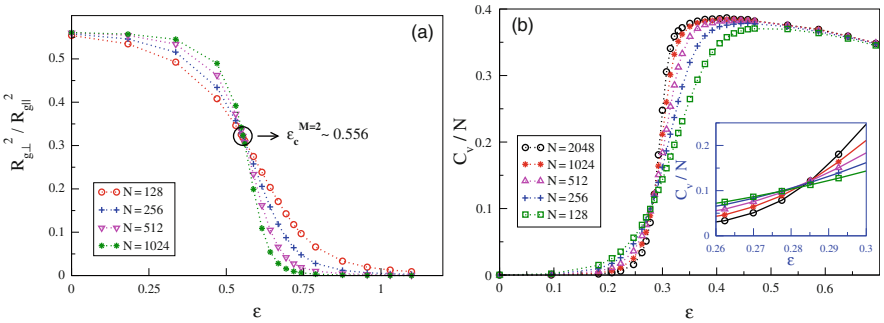

Fig. 8.2 Variation of the ratio $R_{g\perp}^2/R_{g\parallel}^2$ for a copolymer of block size $M = 2$ (**a**) and of the specific heat per monomer, $C_v(\epsilon)/N$, for a homopolymer (**b**) with surface energy ϵ for different chain length N. One gets $\epsilon_c^{M=2} \approx 0.556$ and $\epsilon_c^{h} \approx 0.284$ (PERM)

$$R_{g\parallel}(\eta) \propto \begin{cases} aN^{\nu} & \text{at} \quad \eta \leq 0 \\ \kappa^{(\nu_2-\nu)/\phi} N^{\nu_2} & \text{at} \quad \eta \gg 0 \end{cases} \tag{8.7}$$

The study of the ratio $r(\eta) \equiv R_{g\perp}/R_{g\parallel}$ of gyration radius components is a convenient way to find the value of ϵ_c [9, 12, 13]. In fact, from the previous scaling equations $r(\eta) = \mathcal{G}_{g\perp}(\eta)/\mathcal{G}_{g\parallel}(\eta)$. Hence at the CAP, i.e., at $\eta \to 0$ the ratio $r(0) = \text{const.}$ is *independent* of N. Thus, by plotting r vs ϵ for different N all such curves should intersect at a single point which gives ϵ_c; cf. Fig. 8.2a.

If the well-known picture of blobs [6] is invoked, then in the limit $\kappa N^{\phi} \gg 1$ the adsorbed chain can be visualized as a string of *adsorption blobs* which forms a pancake-like quasi-two-dimensional layer on the surface. The blobs are defined to contain as many monomers g as necessary to be on the verge of being adsorbed and therefore carry an adsorption energy of the order of $k_B T$ each. The thickness of the pancake $R_{g\perp}$ corresponds to the size of the blob while the chain conformation within a blob stays unperturbed (i.e., it is simply a SAW); therefore, $g \sim \left(R_{g\perp}/a\right)^{1/\nu} = \kappa^{-1/\phi}$ where we have used (8.6). The gyration radius can be represented thus as

$$R_{g\parallel} = R_{g\perp}\left(\frac{N}{g}\right)^{\nu_2} \propto \kappa^{(\nu_2-\nu)/\phi} N^{\nu_2} \tag{8.8}$$

and one goes back to (8.7) which proves the consistency of the adsorption blob picture. Generally speaking, the number of blobs, $N/g \sim \kappa^{1/\phi} N$, is essential for the main scaling argument in the above-mentioned scaling functions. The adsorption on a plane at $\kappa > 0$ is due to free energy gain which is then proportional to the number of blobs, i.e., $F - F_{\text{bulk}} \propto -N/g \sim -\kappa^{1/\phi} N$. The expression for the specific heat per monomer may be then obtained as

$$C_V = -\frac{\partial^2 (F - F_{\text{bulk}})}{\partial^2 \kappa} \propto \kappa^{-\alpha} \tag{8.9}$$

where $\alpha = 2 - \phi^{-1}$. If $\phi = 0.5$ then $\alpha = 0$ and the specific heat does not diverge but rather undergoes a jump at the CAP; cf. Fig. 8.2b.

8.3.2 Multiblock Copolymer Adsorption

One may now consider the adsorption of a regular multiblock copolymer comprising monomers A which attract (stick) to the substrate and monomers B which are neutral to the substrate. In order to treat the adsorption of a regular multiblock AB copolymer it may be reduced to that of a homopolymer which has been considered above. Thus a regular multiblock copolymer can be treated as a "homopolymer" where a single AB-diblock plays the role of an *effective monomer* [35]. Let each individual diblock consist of an attractive A-block of length M and a neutral B-block of the same length. Upon adsorption, the A-block would form a string of blobs whereas the B-part forms a non-adsorbed loop or a tail. The free energy gain of the attractive block may be written then (in units of $k_B T$) as $F_{\rm attr} = -\kappa^{1/\phi} M$ where $\kappa \equiv (\epsilon - \epsilon_c^h)/\epsilon_c^h$ now measures the normalized distance from the CAP ϵ_c^h of a homopolymer. The neutral B-part which is most frequently a loop connecting adjacent A-blocks, but could also be a tail with the one end free, contributes only to the entropy loss $F_{\rm rep} = (\gamma - \gamma_{11}) \ln M$ where the universal exponents γ and γ_{11} are well known [36] (e.g., in three-dimensional space $\gamma = 1.159$, $\gamma_{11} = -0.390$). If a tail is involved, one should also use the exponent $\gamma_1 = 0.679$ albeit this does not change qualitatively the expression for $F_{\rm rep}$. These expressions reflect the standard partition functions for a free chain, a chain with both ends fixed at two points, and for a chain, tethered by the one end [36]. In result the effective adsorption energy of a diblock is [34]

$$E(M) = \kappa^{1/\phi} M - (\gamma - \gamma_{11}) \ln M \tag{8.10}$$

One can tackle the problem of regular copolymer adsorption by mapping it on that of a "homopolymer," consisting of $\mathcal{N} = N/2M$ such effective units by using $a \longrightarrow aM^{\nu}, \kappa \longrightarrow \Delta = \frac{E - E_c^h}{E_c^h}, N \longrightarrow \mathcal{N}$ where a denotes the monomer size, and E_c^h is the critical adsorption energy of the renormalized homopolymer. Generally, one would expect E_c^h to be of the order of ϵ_c^h, reflecting the model dependence of the latter. At the CAP of the multiblock chain one has $\Delta = 0$, thus one can estimate the deviation κ_c^M, of the corresponding critical energy of adsorption, ϵ_c^M, from that of a homopolymer, namely,

$$\kappa_c^M \equiv \frac{\epsilon_c^M - \epsilon_c^h}{\epsilon_c^h} = \left(\frac{(\gamma - \gamma_{11}) \ln M + E_c^h}{M} \right)^{\phi} \tag{8.11}$$

where we have used (8.10). It is seen from the phase diagram, Fig. 8.3a, that the deviation κ_c^M, (8.11) with $\phi = 0.5$, steadily grows with decreasing block length M, in agreement with the computer experiment. The fraction of effective units

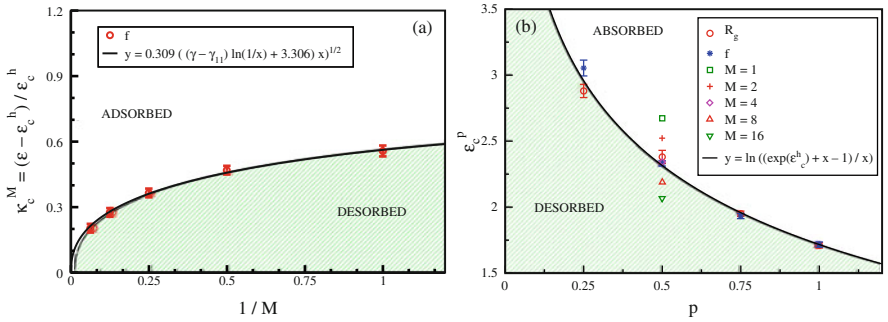

Fig. 8.3 (**a**) Phase diagram showing $\kappa_c^M = (\epsilon_c^M - \epsilon_c^h)/\epsilon_c^h$ plotted vs $1/M$ for multiblock copolymers with various values of M and $\epsilon_c^h = 1.716$. The *curve* gives the best fit of (8.11). (**b**) The CAP, ϵ_c^p, plotted vs the composition p for random copolymers. *Symbols* denote the CAP for multiblock copolymers with block size M. The *curve* corresponds to the best fit of (8.16). Data obtained employing the off-lattice bead-spring model

on the surface obeys the same scaling law as given by (8.5), i.e., $n \equiv \frac{\mathcal{N}_s}{\mathcal{N}} = \mathcal{N}^{\phi-1} G\left(\Delta \mathcal{N}^{\phi}\right)$ which becomes accurate, provided (i) $\kappa \ll 1$ but $M \gg 1$ such that $\ln M \gg 1$ and $\kappa^{1/\phi} M \gg 1$ and (ii) $\mathcal{N} \gg 1$. Thus, within each effective unit of the A-monomers only M_s will be adsorbed at criticality whereby M_s scales as $M_s = M^{\phi} G\left(\kappa M^{\phi}\right)$ so that the total number of adsorbed monomer $N_s = \mathcal{N}_s M_s = \mathcal{N}_s M^{\phi} G\left(\kappa M^{\phi}\right)$. The adsorbed fraction of monomers then is expected to scale with both N and M as

$$n \propto N^{\phi-1}\, G\left(\kappa M^{\phi}\right)\, G\left(\Delta \left(\frac{N}{M}\right)^{\phi}\right) \tag{8.12}$$

For sufficiently strong adsorption, $\kappa\sqrt{M} \gg 1$ and $\Delta\sqrt{N/M} \gg 1$, one gets thus $n \propto \kappa\Delta$.

The gyration radius component in direction perpendicular to the surface $\mathcal{R}_{g\perp} = a N^{\nu}\, \mathcal{G}_{g\perp}\left(\Delta\,(N/M)^{\phi}\right)$ becomes $\mathcal{R}_{\perp} \sim a \Delta^{-\nu/\phi} M^{\nu}$, which yields

$$\mathcal{R}_{\perp} \simeq \frac{a M^{\nu} E_c^{h\,2\nu}}{\left[\kappa^2 M - (\gamma - \gamma_{11}) \ln M - E_c^h\right]^{2\nu}} \tag{8.13}$$

In a similar manner, the gyration radius component parallel to the surface has the form $\mathcal{R}_{g\parallel} = a N^{\nu}\, \mathcal{G}_{g\parallel}\left(\Delta \left(\frac{N}{M}\right)^{\phi}\right)$ which in the limit $\Delta\sqrt{N/M} \gg 1$ results in $\mathcal{R}_{g\parallel} \simeq a \left(\frac{\Delta^{1/\phi}}{M}\right)^{\nu_2 - \nu} N^{\nu_2}$, i.e.,

$$\mathcal{R}_{g\parallel} \simeq \frac{a \left[\kappa^2 M - (\gamma - \gamma_{11}) \ln M - E_c^h\right]^{2(\nu_2-\nu)}}{M^{\nu_2-\nu}}\, N^{\nu_2} \tag{8.14}$$

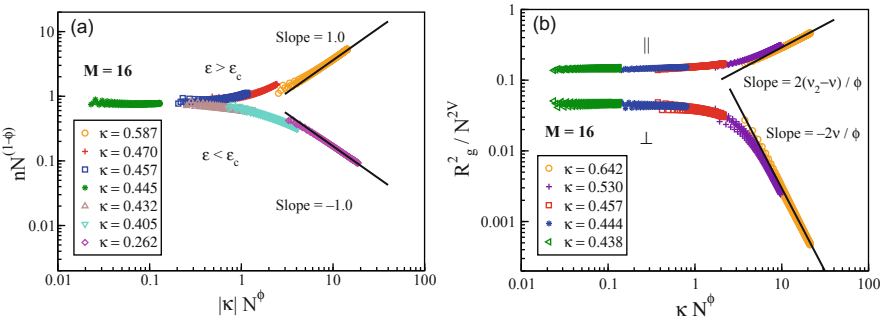

Fig. 8.4 Log–log plots of the order parameter n (**a**), and $R^2_{g\parallel}/N^{2\nu}$ and $Rg^2_{g\perp}/N^{2\nu}$ vs κN^{ϕ} (**b**) with $\nu = 0.588$ and $\nu_2 = 3/4$. The *straight lines* indicate the asymptotic behavior of the scaling functions given by (8.12), (8.13), and (8.14) for regular multiblock copolymers with block size $M = 16$ (PERM)

As shown in Fig. 8.4, one finds indeed the expected scaling behavior which is demonstrated by the collapse of the simulation data on few "master curves," absorbing cases of different strengths of adsorption κ. Like in the homopolymer case, one can define a blob length $\mathcal{G} \sim (\mathcal{R}_\perp/a)^{1/\nu} \sim \Delta^{-1/\phi}\, M$ which in the strong adsorption limit, $\Delta \geq 1$, approaches the block length, $\mathcal{G} \simeq M$, as it should be.

8.3.3 Random Copolymer Adsorption

The adsorption of a random copolymer on a homogeneous surface has been studied by Whittington et al. [21, 22] within the framework of the annealed disorder approximation. Physically this means that during the measurements the chain touches the substrate at random in such a way that one samples all possible monomer sequences along the backbone of the macromolecule. Following this assumption [21], let $c_N(n)$ be the number of polymer configurations such that n units have contact with the surface simultaneously. The percentage of A-monomers (composition) is denoted by p. In the annealed approximation one then averages the partition function over the disorder distribution, i.e.,

$$
\begin{aligned}
Z(\epsilon) &= \sum_{n=1}^{N} \sum_{n_p=0}^{n} c_N(n) \binom{n}{n_p} p^{n_p} (1-p)^{n-n_p}\, \mathrm{e}^{\epsilon n_p} \\
&= \sum_{n=1}^{N} c_N(n) \left[p\mathrm{e}^{\epsilon} + 1 - p \right]^n = \sum_{n=1}^{N} c_N(n)\, \mathrm{e}^{n\, \epsilon^{\mathrm{h}}_{\mathrm{eff}}}
\end{aligned}
\tag{8.15}
$$

where $\epsilon^{\mathrm{h}}_{\mathrm{eff}}$ is the attraction energy of an effective homopolymer. From (8.15) one can see that the annealed problem is reduced to that of a homopolymer where the effective attractive energy is defined as $\epsilon^{\mathrm{h}}_{\mathrm{eff}} = \ln\left[p\mathrm{e}^{\epsilon} + 1 - p \right]$. Since the homopolymer

attraction energy at the CAP is $\epsilon_{\mathrm{eff}}^{\mathrm{h}} = \epsilon_{\mathrm{c}}^{\mathrm{h}}$, the critical attraction energy $\epsilon = \epsilon_{\mathrm{c}}^{p}$ of a random copolymer will be

$$\epsilon_{\mathrm{c}}^{p} = \ln\left[\frac{\exp\epsilon_{\mathrm{c}}^{\mathrm{h}} + p - 1}{p}\right] \geq \epsilon_{\mathrm{c}}^{\mathrm{h}} \tag{8.16}$$

where the composition $0 \leq p \leq 1$. At $p \to 0$ $\epsilon_{\mathrm{c}}^{p} \to \infty$ whereas at $p = 1$ $\epsilon_{\mathrm{c}}^{p} = \epsilon_{\mathrm{c}}^{\mathrm{h}}$. This prediction which has been recently confirmed by Monte Carlo simulations [37] is plotted in Fig. 8.3b. It shows that close to criticality the chain is still rather mobile, so that the sequence dependence is effectively averaged over the time of the experiment and that of quenched disorder can be reduced to that of annealed randomness.

8.4 Adsorption Kinetics

8.4.1 Variation of the Adsorbed Fraction with Elapsed Time – Theory

We illustrate here how one can use the "stem–flower" notion of adsorbing linear macromolecule, suggested by Descas et al. [31], to describe the observed "zipping" dynamics [32] of adsorption not only in terms of the average fraction of adsorbed segments but to include also time-dependent train and tail distribution functions as main constituents of the dynamic adsorption theory. The simple "zipping" mechanism along with the underlying stem–flower model are illustrated in Fig. 8.5a,b. The number of the adsorbed monomers at time t is denoted by $n(t)$. The non-adsorbed fraction of the chain is subdivided into two parts: a stretched part ("stem") of length $m(t)$ and a remaining part ("flower") which is yet not affected by the tensile force of the substrate. The tensile force propagation front is at distance $R(t)$ from the surface. The rate of adsorption is denoted as $v(t) = a\frac{\mathrm{d}n(t)}{\mathrm{d}t}$, where a is the chain segment length.

A single adsorption event occurs with energy gain ϵ and entropy loss $\ln(\mu_3/\mu_2)$, where μ_3 and μ_2 are the connectivity constants in three and two dimensions, respectively [36], so that the driving free energy $F_{\mathrm{dr}} = \epsilon - k_{\mathrm{B}}T\ln(\mu_3/\mu_2)$ whereas the driving force $f_{\mathrm{dr}} = F_{\mathrm{dr}}/a$. The friction force is related to the pulling of the stem at rate $v(t)$, i.e., $f_{\mathrm{fr}} = \zeta_0\, a\, m(t)\frac{\mathrm{d}n(t)}{\mathrm{d}t}$ where ζ_0 is the Stokes friction coefficient of a single bead. The equation of motion, following from the balance of driving, and drag force, is then $f_{\mathrm{dr}} = f_{\mathrm{fr}}$. Inspection of Fig. 8.5a suggests that the distance $R(t)$ between the flower and the plane changes during the adsorption process until the flower is eventually "consumed." In so doing $R(t)$ obeys two relationships: $R(t) \approx a[n(t) + m(t)]^{\nu}$ (because it is actually the size which the chain portion $n(t) + m(t)$ occupied before the adsorption has started) and $R(t) \approx m(t)$ (up to a geometric factor of order unity). Thus $n(t) \approx m(t)^{1/\nu} - m(t)$ which yields $m(t) \approx n(t)^{\nu}$ for the typically long stems $m(t) \gg 1$. From the resulting equation

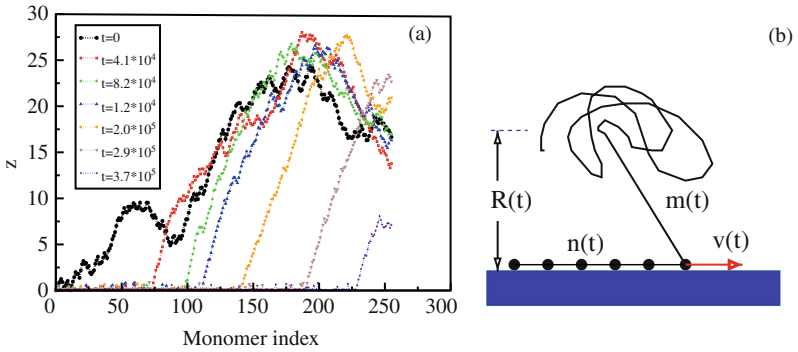

Fig. 8.5 (**a**) Chain conformation at successive time moments during the adsorption process for a polymer with $N = 256$. The z-coordinate of the ith monomer is plotted against monomer index i. (**b**) Stem–flower picture of the adsorption dynamics. The total number of adsorbed monomers at time t is denoted by $n(t)$. The tail which, contains all non-adsorbed monomers, consists of a stretched part, a "stem," of length $m(t)$, and of a nonperturbed part – a "flower." The rate of adsorption is $v(t)$. The distance between the surface and the front of the tension propagation is $R(t)$

$\zeta_0\, n(t)^{\nu} \mathrm{d}n(t)/\mathrm{d}t = f_{\mathrm{dr}}/a^2$ then follows $n(t) \propto t^{1/(1+\nu)} \approx t^{0.62}$ which is in good agreement with simulation results [28, 31, 32].

8.4.2 Time Evolution of the Distribution Functions – Theory

Consider the instantaneous number of adsorbed monomers n at time t (i.e., the total train length) distribution function $P(n, t)$. Using the "master equation" method [38], one may derive a system of coupled kinetic equations for $P(n, t)$ by treating the zipping dynamics as a *one-step* adsorption/desorption process within an elementary time interval. Assuming that the corresponding rate constants $w^+(n)$, $w^-(n)$ of monomer attachment/detachment are related by the detailed balance condition [38] (which is an approximation for a non-equilibrium process), one can fix their ratio $w^+(n-1)/w^-(n) = \exp(F_{\mathrm{dr}}/k_{\mathrm{B}}T)$, and even fully specify them by introducing a friction-dependent *transmission* coefficient $q(m) = k_{\mathrm{B}}T/(a^2\zeta) = k_{\mathrm{B}}T/(a^2\zeta_0 m)$ (whereby the stem length m depends on the total train length n, according to $n \approx m^{1/\nu} - m$). Then the one-step master equation reads [38]

$$\frac{\mathrm{d}}{\mathrm{d}t} P(n,t) = w^-(n+1)\, P(n+1,t) + w^+(n-1)\, P(n-1,t) - w^+(n)\, P(n,t) - w^-(n)\, P(n,t) \tag{8.17}$$

which along with the boundary conditions

$$\frac{\mathrm{d}}{\mathrm{d}t}P(1,t) = w^{-}(2)P(2,t) - w^{+}(1)P(1,t) \quad \text{for } n = 1 \tag{8.18}$$
$$\frac{\mathrm{d}}{\mathrm{d}t}P(N,t) = w^{+}(N-1)P(N-1,t) - w^{-}(N)P(N,t) \quad \text{for } n = N$$

and $P(n, t = 0) = \delta(n - 1)$ fully describe the single chain adsorption kinetics.

The equation of motion for the mean number of adsorbed segments $\langle n\rangle = \sum_{n=1}^{\infty} nP(n,t)$ can be obtained from (8.17), assuming for simplicity $P(N,t) = P(0,t) = 0$:

$$\frac{\mathrm{d}}{\mathrm{d}t}\,\langle n\rangle = -\left\langle w^{-}(n)\right\rangle + \left\langle w^{+}(n)\right\rangle \tag{8.19}$$

With the relations for the rate constants, $w^{+}(n)$, $w^{-}(n)$, this equation of motion becomes

$$\zeta_0\, m(t)\,\frac{\mathrm{d}}{\mathrm{d}t}\,n(t) = \frac{k_{\mathrm{B}}T}{a^2}\left[1 - \mathrm{e}^{-F_{\mathrm{dr}}/k_{\mathrm{B}}T}\right] \tag{8.20}$$

where for brevity we use the notations $n(t) = \langle n\rangle$ and $m(t) = \langle m\rangle$. Note that (8.20) reduces to the kinetic equation [31], derived at the end of Sect. 8.4.1 for weak driving force, $F_{\mathrm{dr}} \ll k_{\mathrm{B}}T$, by neglecting fluctuations in the zipping mechanism. Evidently, by taking fluctuations into account, F_{dr}/a is replaced by a kind of effective *second virial* coefficient $(k_{\mathrm{B}}T/a)[1 - \exp(-F_{\mathrm{dr}}/k_{\mathrm{B}}T)]$. Thus, the zipping as a strongly non-equilibrium process cannot be treated quasistatically by making use of a simple "force balance."

8.4.3 Order Parameter Adsorption Kinetics – MC Results

The time variation of the order parameter $n(t)/N$ (the fraction of adsorbed segments) for homopolymer chains of different length N and strong adhesion $\epsilon/k_{\mathrm{B}}T = 4.0$ is shown in Fig. 8.6a, b whereby the observed straight lines in double-log coordinates suggest that the time evolution of the adsorption process is governed by a power law. As the chain length N is increased, the slope of the curves grows steadily, and for length $N = 256$ it is equal to ≈0.56. This value is close to the theoretically expected slope of $(1 + \nu)^{-1} \approx 0.62$. The total time τ it takes a polymer chain to be fully adsorbed is found to scale with chain length as $\tau \propto N^{\alpha}$ whereby the observed power $\alpha \approx 1.51$ is again somewhat smaller than the expected one $1 + \nu \approx 1.59$, most probably due to finite-size effects. One may also verify from Fig. 8.6b that for a given length N the final (equilibrium) values of the transients at late times $t \to \infty$ grow while the curves are horizontally shifted to shorter times as the surface potential gets stronger. Nonetheless, the slope of the $n(t)$ curves remains unchanged when $\epsilon/k_{\mathrm{B}}T$ is varied, suggesting that the kinetics of the process is well described by the assumed zipping mechanism. The changing plateau height may readily be understood as reflecting the correction in the equilibrium fraction of adsorbed monomers

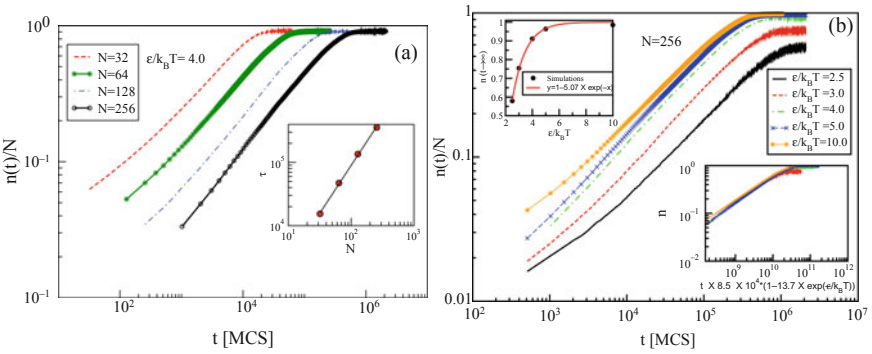

Fig. 8.6 (**a**) Time evolution of the order parameter (fraction of adsorbed segments) for four different chain lengths $N = 32$, 64, 128, and 256 at surface potential $\epsilon/k_BT = 4.0$. The slope of the $N = 256$ curve is 0.56. The *inset* shows the scaling of the adsorption time with chain length, $\tau \propto N^{1.51}$. The time τ is determined from the intersection point of the late time plateau with the tangent $t^{0.56}$ to the respective $n(t)$ curve. (**b**) Adsorption kinetics for different strengths ϵ of the surface potential. The variation of the plateau height (i.e., the fraction of adsorbed monomers at equilibrium) with ϵ is depicted in the *upper inset* where the *solid line* $n_{t\to\infty} = 1-5\exp(-\epsilon/k_BT)$ describes the equilibrium number of defects (vacancies). The *lower inset* shows a collapse of the adsorption transients on a single "master curve," if the time axis is rescaled appropriately

due to the presence of defects (vacancies) for any given value of ϵ/k_BT. For the transients which collapse on a master curve, cf. the second inset in Fig. 8.6b, one may view the rescaling of the time axis by the expression $t \to t[1 - 13.7\exp\frac{-\epsilon}{k_BT}]$ as a direct confirmation of (8.20) where the time variable t may be rescaled with the driving force of the process (i.e., with the expression in square brackets). The factor ≈ 13.7 gives then the ratio μ_3/μ_2 of the effective coordination numbers in three and two dimensions of a polymer chain with excluded volume interactions. μ_3 and μ_2 are model dependent and characterize, therefore, our off-lattice model.

The more complex adsorption kinetics, shown in Fig. 8.7a for regular multiblock copolymers of block size M and in Fig. 8.7b for random copolymers, suggests, however, that the power-law character of the order parameter variation with time is retained except for a characteristic "shoulder" in the adsorption transients. Indeed, one should bear in mind that the zipping mechanism, assumed in our theoretical treatment, is by no means self-evident when the file of sticking A-monomers is interrupted by neutral B segments. The characteristic shoulder in the adsorption transients of regular multiblock copolymers manifests itself in the early stage of adsorption and lasts progressively longer when M grows. The temporal length of this shoulder reflects the time it takes for a segment from the *second* adsorptive A-block in the polymer chain to be captured by the attractive surface, once the first A-block has been entirely adsorbed. For sufficiently large blocks one would therefore expect that this time interval, τ_1, associated with the capture event, will scale as the Rouse time, $M^{1+2\nu}$, of a non-adsorbing tethered chain of length M. The observed τ_1 vs M relationship has been shown in the upper left inset in Fig. 8.7a. The slope of ≈ 1.49 is less than the Rouse time scaling exponent, 2.18, which one

may attribute to the rather small values of the block length M that were accessible in our simulation. One should also allow for scatter in the end time of the shoulder due to the mismatch in the capture times of all the successive A-blocks in the course of our statistical averaging over many chains during the computer experiment.

Somewhat surprisingly, α which describes the scaling of the total adsorption time with polymer size, $\tau \propto N^{\alpha}$, is observed to *decline* as the block size M is increased – in contrast to the general trend of regular multiblock copolymers which resemble more and more homopolymers (where $\alpha = 1 + \nu$), as the block size $M \to \infty$. Evidently, the frequent disruption of the zipping process for smaller blocks M slows down the overall adsorption.

In the case of random copolymers, Fig. 8.7b, the transients resemble largely those of a homopolymer chain with the same number of beads again, apart from the expected difference in the plateau height which is determined by the equilibrium number of adsorbed monomers. A rescaling of the vertical axis with the fraction of sticking monomers, p, however, does not lead to coinciding plateau heights – evidently the loops, whose size also depends on p, affect the equilibrium number of adsorbed monomers. The variation of the observed scaling exponent α with composition p is shown in the inset to Fig. 8.7b wherefrom one gets $\alpha \approx 1.6$ with α being largely independent of p. Note that this value is considerably lower than the power of 2.24 which has been observed earlier [28], however, for very short chains with only 10 sticking beads. One may conclude that even for random copolymer adsorption the typical time of the process scales as $\tau \propto N^{\alpha}$, as observed for homopolymers and regular block copolymers. It is conceivable, therefore, that an *effective* zipping mechanism in terms of renormalized segments, that is, segments consisting of an A and B diblock unit of length $2M$ for regular multiblock copolymers, provides an adequate notion of the way the adsorption kinetics may be treated even in such

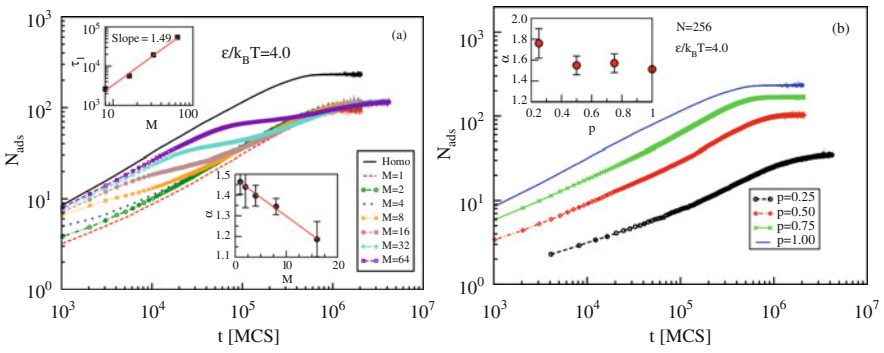

Fig. 8.7 (**a**) Number of adsorbed segments, $N_{\rm ads}(t)$), vs time t for regular AB-copolymers with block size $M = 1$–64 and length $N = 256$. For comparison, the transient of a homopolymer is shown by a *solid line* too. The time interval, taken by the initial "shoulder," is shown in the *upper left inset*. The *lower inset* displays the variation of the scaling exponent, α, for the time of adsorption $\tau \propto N^{\alpha}$ vs block length relationship. (**b**) The same as in (**a**) but for random copolymers of length $N = 256$ and different composition $p = 0.25,\ 0.5,\ 0.75$. For $p = 1$ one has the case of a homopolymer. The *inset* shows the variation of α with p

more complicated cases. For random copolymers the role of the block length M would then be played by the typical correlation length.

8.4.4 Time Evolution of the Distribution Functions – MC Data

One gains most comprehensive information regarding the adsorption process from the time evolution of the different building blocks (trains, loops, and tails) probability distribution functions (PDF) [39]. From the MC simulation data, displayed in Fig. 8.8a, for example, one may verify that the resulting distribution $D(h, t)$ of different train lengths is found to be exponential, in close agreement with the theoretically expected shape [39], predicted under the assumption that local equilibrium of loops of unit length is established much faster than the characteristic time of adsorption itself. When scaled with the mean train length $h_{\rm av}(t) = \langle h(t)\rangle$, at time t, in both cases for $\epsilon/k_{\rm B}T = 3.0$ and 5.0 one finds an almost perfect straight line in semi-log coordinates. One may thus conclude that $D(h, t)$ preserves its exponential form during the course of the adsorption process, validating thus the conjecture of rapid local equilibrium. The latter, however, is somewhat violated for the case of very strong adsorption, $\epsilon/k_{\rm B}T = 5.0$, where the rather scattered data suggest that the process of loop equilibration is slowed down and the aforementioned time separation is deteriorated.

The PDF of loops $W(k, t)$ at different times after the onset of adsorption is shown in Fig. 8.8b. Evidently, the distribution is sharply peaked at size 1 whereas less than the remaining 20% of the loops are of size 2. Thus the loops can be viewed as single thermally activated defects (vacancies) comprising a desorbed single bead with both of its nearest neighbors still attached to the adsorption plane. As the inset

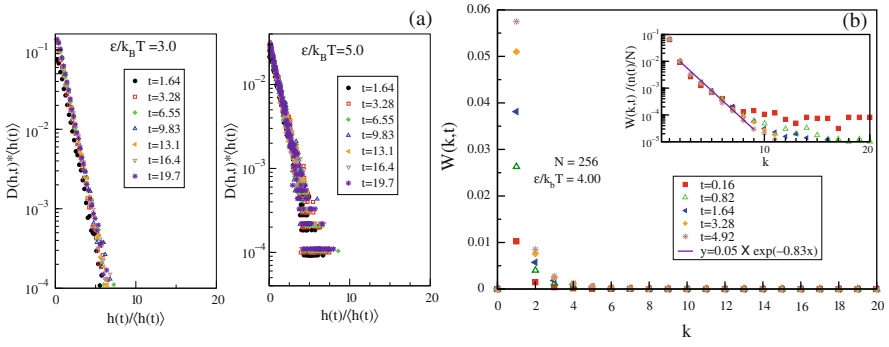

Fig. 8.8 (**a**) Distribution of train lengths during the adsorption process of a homopolymer chain with $N = 256$ at two strengths of the adsorption potential ϵ, shown in semi-log coordinates. PDFs for different times (in units of 10^5 MCS) collapse on master curves when rescaled by the mean train length $h_{\rm av}(t)$. (**b**) Distribution of loop lengths $W(k, t)$ for $N = 256$ and $\epsilon/k_{\rm B}T = 4.0$ during ongoing polymer adsorption. In the *inset* the PDF is normalized by $n(t)$ and shown to be a *straight line* in log–log coordinates

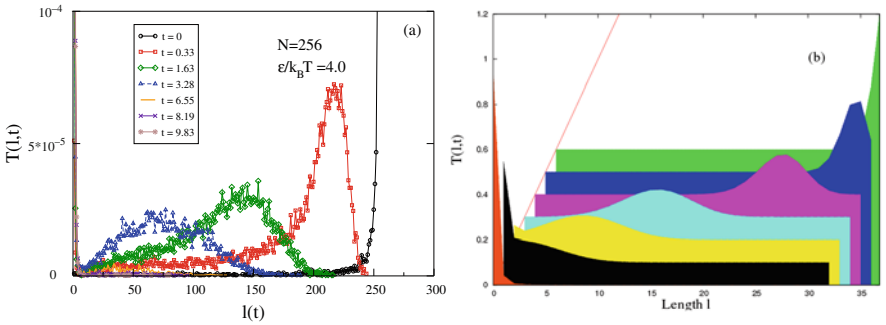

Fig. 8.9 (**a**) Distribution of tail size for different times (in units of 10^5 MCS) during the polymer chain adsorption for a chain with $N = 256$ at $\epsilon/k_BT = 4.0$. (**b**) The same as in (**a**) as derived from the solution of the ME for chain length $N = 32$. For better visibility the time slices for $t = 1, 5, 30\,100, 150, 200$, and 300 are shifted along the time axis and arranged such that the initial distribution for $t = 1$ is represented by the most distant slice

in Fig. 8.8b indicates, the PDF of loops is also described by an exponential function. The PDFs for loops at different time collapse on a master curve, if scaled appropriately with the instantaneous order parameter $n(t)/N$. Eventually, in Fig. 8.9a we present the observed PDF $T(l, t)$ of tails for different times t after the start of adsorption and compare the simulation results with those from the numeric solution of (8.17), taking into account that $T(l, t) = P(N - l, t)$. One may readily verify from Fig. 8.9 that the similarity between simulational and theoretic results is really strong. In both cases one starts at $t = 1$ with a sharply peaked PDF at the full tail length $l(t = 1) = N$. As time proceeds, the distribution becomes broader and its maximum shifts to smaller values. At late times the moving peak shrinks again and the tail either vanishes or reduces to a size of single segment which is expressed by the sharp peak at the origin of the abscissa.

8.5 Summary

The main focus of this contribution has been aimed at the adsorption transition of random and regular multiblock copolymers on a flat structureless substrate whereby by different means – scaling considerations and computer simulations – a consistent picture of the macromolecule behavior at criticality is derived.

As a central result one should point out the phase diagram of regular multiblock adsorption which gives the increase of the critical adsorption potential ϵ_c^M with decreasing length M of the adsorbing blocks. For very large block length, $M^{-1} \to 0$, one finds that the CAP approaches systematically that of a homogeneous polymer.

The phase diagram for random copolymers with quenched disorder which gives the change in the critical adsorption potential, ϵ_c^p, with changing percentage of the sticking A-monomers, p, is observed to be in perfect agreement with the theoreti-

cally predicted result which has been derived by treating the adsorption transition in terms of the "annealed disorder" approximation.

Evidently, a consistent picture of how some basic polymer chain properties of interest such as the gyration radius components perpendicular and parallel to the substrate, or the fraction of adsorbed monomers at criticality, scale when a chain undergoes an adsorption transition emerges regardless of the particular simulation approach. An important conclusion thereby concerns the value of the universal crossover exponent $\phi = 0.5$ which is found to remain unchanged, regardless of whether homopolymers, regular multiblock polymers, or random polymers are concerned. Thus the universality class of the adsorption transition of a heteropolymer is the same as that of a homopolymer.

Concerning the adsorption kinetics of a single polymer chain on a flat surface, it is shown that within the "stem–flower" model and the assumption that the segment attachment process follows a "zipping" mechanism, one may adequately describe the time evolution of the adsorbed fraction of monomers and of the probability distribution functions of the various structural building units (trains, loops, tails) during the adsorption process. For regular multiblock and random copolymers it is found that the adsorption kinetics strongly resembles that of homopolymers. The observed deviations from the latter suggest plausible interpretations in terms of polymer dynamics; however, it is clear that additional investigations will be warranted before a complete picture of the adsorption kinetics in this case is established too.

References

1. S. Wu, *Polymer Interfaces and Adhesion* (Mercel Dekker, New York, NY, 1982)
2. E. Eisenriegler, *Polymers Near Surfaces* (World Scientific, Singapore, 1993)
3. I.C. Sanchez, in *Physics of Polymer Surfaces and Interfaces*, ed. by I.C. Sanchez (Butterworth-Heinemann, Boston MA, 1992), p. 97
4. R.R. Netz, D. Andelman, Neutral and charged polymers at interfaces. Phys. Rep. **380**, 1(2003)
5. T.M. Birshtein, Theory of adsorption of macromolecules. 1. Desorption-adsorption transition point. Macromolecules **12**, 715(1979); Theory of adsorption of macromolecules. 2. Phase transitions in adsorption: general approach. Macromolecules **16**, 45(1983)
6. P.-G. de Gennes, Conformations of polymers attached to an Interface. Macromolecules **13**, 1069(1980)
7. E. Eisenriegler, K. Kremer, K. Binder, Adsorption of polymer chains at surfaces: scaling and Monte Carlo analyses. J. Chem. Phys. **77**, 6296(1982)
8. V. Yamakov, A. Milchev, O. Borisov, B. Dünweg, Adsorption of a polyelectrolyte chain on a charged surface: a Monte Carlo simulation of scaling behavior. J. Phys. Condens. Matt. **11**, 9907(1999)
9. A. Milchev, K. Binder, Static and dynamic properties of adsorbed chains at surfaces: Monte Carlo simulation of a bead-spring model. Macromolecules **29**, 343(1996)
10. A. Balasz, M.C. Gempe, Z. Zhou, Polymer adsorption on chemically heterogeneous substrates. Macromolecules **24**, 4918(1991)
11. A. Milchev, in *Computational Methods in Surface Science*, vol. 89, ed. by M. Borowko (Marcel Dekker, New York, NY, 2000), p. 569

12. R. Descas, J.U. Sommer, A. Blumen, Static and dynamic properties of tethered chains at adsorbing surfaces: a Monte Carlo study. J. Chem. Phys. **120**, 8831(2004)
13. S. Metzger, M. Müller, K. Binder, J. Baschnagel, Adsorption transition of a polymer chain at a weakly attractive surface: Monte Carlo simulation of off-lattice models. Macromol. Theory Simul. **11**, 985(2002)
14. P. Grassberger, Simulations of grafted polymers in a good solvent. J. Phys. A **38**, 323(2005)
15. E. Zhulina, A.M. Skvortsov, T.M. Birshtein, Adsorption of dyblock copolymers: method of the grand canonical ensemble. Vysokomol. Soed. Ser. A **23**, 304(1981)
16. E.A. Di Marzio, C.M. Guttman, A. Mah, Effect of heterogeneous energies on adsorption properties: adsorption of copolymers, comb Polymers, and stars onto a surface. Macromolecules **28**, 2930(1995)
17. O.A. Evers, J.M.H.M. Scheutjens, G.J. Fleer, Statistical thermodynamics of block copolymer adsorption. 1. Formulation of the model and results for the adsorbed layer structure. Macromolecules **23**, 5221(1990)
18. G.J. Fleer, J.M.H.M. Scheutjens, T.C.M.A. Cohen-Stuart, B. Vincent, *Polymers at Interface* (Chapman and Hall, London, 1993)
19. A. Balasz, M.C. Gempe, C.W. Lantman, Effect of molecular architecture on the adsorption of copolymers. Macromolecules **24**, 168(1991)
20. E.A. Zheligovskaya, P.G. Khalatur, A.R. Khokhlov, Properties of AB copolymers with a special adsorption-tuned primary structure. Phys. Rev. E **59**, 3071(1999)
21. C.E. Soteros, S.G. Whittington, The statistical mechanics of random copolymers. J. Phys. A **37**, R279(2004)
22. M. Sabaye, S.G. Whittington, A Monte Carlo study of polymer adsorption: random copolymers and random surfaces. J. Phys. A **35**, 33(2002)
23. A. Polotsky, F. Schmidt, A. Degenhard, Polymer adsorption onto random planar surfaces: interplay of polymer and surface correlation. J. Chem. Phys. **121**, 4853(2004)
24. K. Sumithra, A. Baumgaertner, Adsorption of random copolymers: a scaling analysis. J. Chem. Phys. **110**, 2727(1999)
25. M.A. Cohen-Stuart, T. Cosgrove, B. Vincent, Experimental aspects of polymer adsorption at solid/solution interfaces. Adv. Colloid Interface Sci. **24**, 143(1986)
26. M. Kamaguchi, A. Takahashi, Polymer adsorption at solid-liquid interfaces. Adv. Colloid Interface Sci. **37**, 219(1992)
27. K. Konstadinidis, S. Prager, M. Tirrell, Monte Carlo simulation of irreversible polymer adsorption: single chains. J. Chem. Phys. **97**, 7777(1992)
28. J.S. Shaffer, Computer simulation of homopolymer and copolymer adsorption dynamics. Macromolecules **27**, 2987(1994)
29. B. O'Shaughnessy, D. Vavilonis, Irreversible adsorption from dilute polymer solution. Eur. Phys. J. E **11**, 213(2003)
30. B. O'Shaughnessy, D. Vavilonis, Non-equilibrium in adsorbed polymer layers. J. Phys.: Condens. Matter **17**, R63(2003)
31. R. Descas, J.-U. Sommer, A. Blumen, Irreversible adsorption of tethered chains at substrates: Monte Carlo study. J. Chem. Phys. **124**, 094701(2006)
32. A.L. Ponomarev, T.D. Sewell, C.J. Durning, Adsorption of isolated, flexible polymers onto a strongly attracting surface. Macromolecules **33**, 2662(2000)
33. D. Panja, G.T. Barkema, A. Kolomeisky, Non-equilibrium dynamics of single polymer adsorption to solid surfaces. J. Phys. Condens. Matt. **21**, 242101(2009)
34. S. Bhattacharya, H.-P. Hsu, A. Milchev, V.G. Rostiashvili, T.A. Vilgis, Adsorption of multiblock and random copolymer on a solid surface: critical behavior and phase diagram. Macromolecules **41**, 2920(2008)
35. A. Corsi, A. Milchev, V.G. Rostiashvili, T.A. Vilgis, Localization of a multiblock copolymer at a selective interface: scaling predictions and Monte Carlo verification. J. Chem. Phys. **122**, 094907(2005)
36. C. Vanderzande, *Lattice Models of Polymers* (Cambridge University Press, Cambridge, 1998)

37. J.D. Ziebarth, Y. Wang, A. Polotsky, M. Luo, Dependence of the critical adsorption point on surface and sequence: disorders for self-avoiding walks interacting with a planar surface. Macromolecules **40**, 3498(2007)
38. N.G. van Kampen, *Stochastic Processes in Physics and Chemistry* (North – Holland, Amsterdam, 1992)
39. S. Bhattacharya, A. Milchev, V.G. Rostiashvili, A.Y. Grosberg, T.A. Vilgis, Adsorption kinetics of a single polymer on a solid plane. Phys. Rev. E **77**, 061603(2008)

Chapter 9
Metallic Nanowires on the Atomic Scale: Correlation Between Structure, Electronic Properties, and Electronic Transport

H. Pfnür

Abstract One-dimensional (1D) properties with strong electron correlation and various instabilities have been found recently in metallic chains or ribbons generated by metal adsorption of sub-monolayers on insulating substrates like Si(111) or Si(557). The unavoidable coupling to 2D and 3D for all these cases results in a wealth of new phenomena. Here we concentrate on the Pb/Si(557) system, where these couplings in 2D and 3D become very obvious, and discuss structural self-stabilization as the origin of 1D electronic transport. Finally, a new 1D state generated by step decoration is described and its properties are discussed.

9.1 Introduction

One-dimensional electronic systems have attracted great interest recently because of their exotic electronic properties. These comprise quantization of conductance, charge density waves (CDW), spin-density waves (SDW) [1] triplet superconductivity, and Luttinger-liquid behavior [2]. Properties of electrons related to charge and spin may be separated in a quasiparticle picture [3]. As a consequence, low-dimensional systems, and in particular 1D chains, exhibit a variety of instabilities with a wealth of associated phase transitions. Especially 1D metallic chains should undergo a Peierls instability accompanied by a significant change of the conductivity due to a metal–insulator transition. In the classical picture, electron–phonon interaction drives CDW formation (Peierls instability) and the opening of a band gap at the Fermi surface [4]. Apart from interesting physical properties, new perspectives of potential applications of metallic quantum wires in context with molecular electronics and nanoscale interconnects [5], nanoscale devices, or optical waveguides [6] are expected.

Metallic wires exceeding the length of a few atoms cannot be suspended freely, i.e., they have to be embedded into a 2D or 3D environment causing inevitably 2D or

H. Pfnür (✉)
Institut für Festkörperphysik, Abteilung ATMOS, Leibniz Universität Hannover,
Appelstr. 2, D-30167 Hannover, Germany
e-mail: pfnuer@fkp.uni-hannover.de

M. Michailov (ed.), *Nanophenomena at Surfaces,* Springer Series in Surface Sciences 47,
DOI 10.1007/978-3-642-16510-8_9,

3D interactions of the 1D system with its surroundings. These interactions modify the properties of a 1D system and need to be controlled precisely, therefore. On the other hand, control of these interactions may allow tuning of certain physical properties, e.g., suppression of the metal–insulator transition.

An obvious strategy of making 1D conductors is the use of nano-assemblies on semiconducting or insulating solid surfaces as well as highly anisotropic (and possibly modified) surface superstructures, which provide excellent model systems to study electron transport and its modification on the atomic scale accurately and under well-defined conditions [7–9]. Examples are chain structures on uniaxial surfaces generated by adsorption of submonolayer amounts of metals and subsequent self-organization and/or reaction with a strongly anisotropic (vicinal) single crystalline surface. These structures have several advantages: The geometry can be controlled on the atomic scale and the electronic properties can be changed gradually by adsorbate concentrations, by adatom mixing, and by varying the degree of localization, e.g., by changing terrace widths.

Very few studies on such systems have been performed so far, e.g., for Au nanowires on highly stepped Si(111) [10] and the system (4×1)-In/Si(111) [11]. In both cases, the metallic nanowires exhibit a CDW instability. Notably the properties of chains on stepped substrates can be varied to some extent by changing the terrace width defined by the miscut, e.g., using Si(553) surfaces as compared to Si(557). This leads to changes in both band filling and the CDW transition temperature [12]. It is important to note that these realizations of 1D reconstructions contain multiple bands derived from the various constituent atoms. Therefore, while one band may undergo a Peierls distortion, other bands may remain metallic. This reflects that real-world systems are much more complex than a simple one-band scenario. While dc transport measurements form the basis for a deeper understanding also of related properties, such as optical or plasmonic excitations [13], they turn out to be extremely demanding [14] and are still extremely scarce for metallic wires [9, 15]. Furthermore, no information exists so far about the magnetotransport properties in these systems. An important prerequisite for such measurements is the formation of reliable contacts on the atomic or at least on the nanoscale. While the existence of such contacts, e.g., in break junctions [16], is well established, the control on the atomic scale is still at its beginning [17].

Here we want to present a short overview of Pb nanowires on Si(557) close to the concentration of a physical monolayer, which represent a completely different physical scenario than all of those mentioned above. Because of the high concentration of Pb, coupling between the wires cannot be neglected. This leads to an interesting interplay between 1D and 2D properties, as seen, e.g., by the close dependence of electronic transport behavior on the geometric structure.

9.2 Experimental

All experiments were carried out in UHV at base pressures of 3–5 $\times$ 10^{-11} mbar. For the LEED experiments we used an instrument that allows high-resolution profile analysis (SPALEED). STM data were taken in a different chamber with a

Besocke-type variable temperature STM manufactured by RHK. It allows temperatures down to 35 K with LHE cooling. Conductance measurements were carried out in situ after evaporating ex situ Ti onto the samples ($15 \times 15\,mm^2$) using a mask technique. Contacts were formed by heating the sample to 600°C. At this temperature Ti reacts with the Si to form $TiSi_2$.

The samples were very low-doped p-type Si samples (specific resistance at room temperature 5–10 kΩ cm). Four laser cut slits prevented cross talk between the eight contacts, which allowed four-point measurements with a precise adjustment of the current parallel and perpendicular to the steps. The distance between the contacts was 10 mm. Pb was evaporated thermally and monitored with a quartz microbalance. Coverage was calibrated using several LEED structures. Thus a reproducibility of Pb concentrations of 0.3% was obtained.

9.3 Results and Discussion

9.3.1 Pb-Stabilized Facets on Si(557)

While for most systems mentioned above the surface orientation remains unchanged upon chain formation by adsorbed adatoms, we found for the Pb/Si(557) system in the coverage range close to one physical monolayer (1.2–1.5 ML with respect to the Si surface concentration) that the microscopic surface orientation is unstable in the presence of these concentrations of Pb, and new periodic mini-facets appear, depending on Pb concentration. This is not only an indication for 2D, though anisotropic, interactions, but at the same time it illustrates the intriguing interplay of interactions in dimensions higher than 1, which nevertheless can result in 1D properties, as described in detail below.

Pb-induced changes in surface morphology become most obvious in systematic LEED investigations carried out in our group recently [19–21]: In Fig. 9.1a the

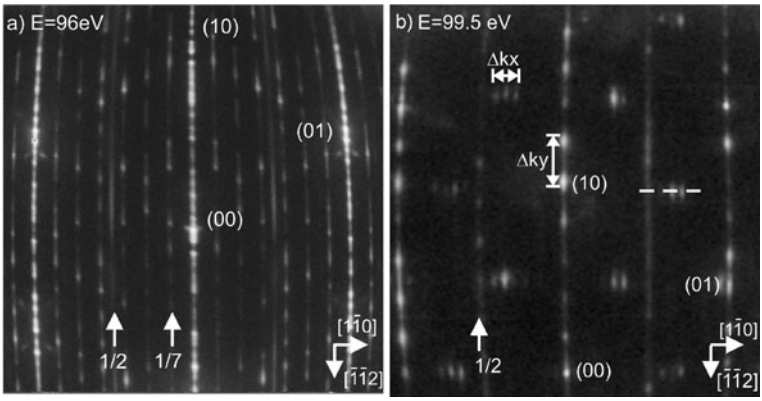

Fig. 9.1 (**a**) LEED pattern of the clean Si(557) surface. (**b**) Adsorption of 1.31ML of Pb leads to periodic refacetting after annealing to 640 K

LEED pattern of the clean (557) surface is seen. It consists of a regular sequence of small (111) and (112) terraces [15]. Marked are the integer order spots of the small (111) terraces. The multiple spots in-between correspond to a regular array of steps with a periodicity of 5.7 nm. Also visible are streaky (7 × 7) spots, which are due to the small (111) oriented terraces, and streaks at half-order positions. These indicate a period doubling at the step edges.

This step morphology changes dramatically, when Pb is adsorbed at concentrations between 1.2 and 1.4 monolayers (ML, referenced to the Si density of surface atoms) onto this surface once the Si(7×7) reconstruction on the terraces is destroyed by an annealing step to 640 K in presence of (at least) 1 ML of Pb. Subsequent coverage increments lead to further refacetting at temperatures as low as 180 K. The result at a coverage of 1.3 ML is shown in Fig. 9.1b. As seen there, the average step separation has changed dramatically. From the distance of the spots between those marked (00) and (01) we deduce an average Pb-induced step separation of 4.67 Si lattice constants. This corresponds to the formation of a (223) oriented facet, which has a higher step density than the original (557) surface. Occasional formation of steps in the opposite direction can compensate for the higher step density in order to maintain the macroscopic surface orientation. These, however, are not periodic and are therefore not visible in LEED. This Pb-induced step array is not a minority species on the surface. Otherwise the surface conductance properties described below would not be possible. As explicitly tested with LEED, larger (111) terraces are only a small minority, which do not influence the main conclusions drawn here.

Measurements as shown exemplarily for the Pb concentration of 1.30 ML were carried out systematically in the coverage range between 1.20 and 1.50 ML. After carrying out the high-temperature annealing step once, tuning of the facet orientation and thus of the step density is possible just by increasing the Pb concentration in small increments. Starting with the (112) orientation at 1.2 ML the (335) orientation follows at 1.24 ML. At 1.27 ML the (223) facet appears, which turned out to be the most stable. It exists at Pb concentrations above 1.27 ML up to saturation of the physical monolayer close to 1.5 ML. The homogeneously stepped (557) surface turned out to be stable only for annealing temperatures up to 80 K at a Pb concentration close to 1.35 ML. At higher annealing temperatures it irreversibly transforms into (223) facets.

In Fig. 9.2 we summarize our main results in a phase diagram of the Pb-induced facetting transformations. The phase diagram includes, apart from the facet orientation, also the periodic structures seen in LEED parallel to the step edges, as judged from the spots of the superstructures seen in between the integer order spots. At 1.2 ML the structure on the remaining (111) terraces is given. In all LEED images the ×2 reconstruction of step edges of the clean Si(111) surface remains, indicating that the step edges are not covered by Pb up to 1.31 ML when the LEED pattern starts to change. This leads to new phenomena also in conductance and will be discussed in a separate section below.

Going back to Pb concentrations close to 1.2 ML, it seems that the smaller size of Pb compared to Si leads to an increasing tensile stress at the surface with increasing Pb concentration, favoring not only formation of a homogeneously stepped

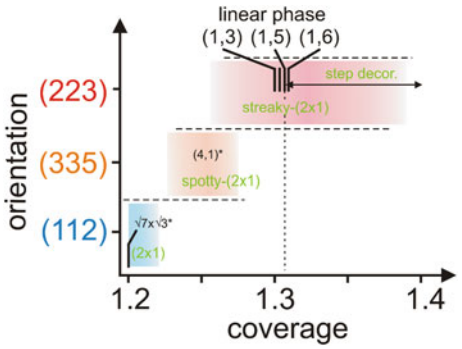

Fig. 9.2 Phase diagram of the Pb-induced facet orientations after high-temperature annealing of the Si(557) surface

(557) surface, but formation of facets with higher step densities. On the other hand, adsorption directly on the step edges seems to be energetically unfavorable. Indeed, the observed reduction of step density as a function of concentration for $\Theta \geq 1.2$ ML can be quantitatively modeled assuming that it is energetically less expensive (in presence of Pb) to annihilate steps and increase the size of the terraces than to occupy step sites [19]. All structures observed are periodic over many terrace lengths. Even the $\times 2$ reconstruction develops into a "spotty" phase at concentrations close to 1.27 ML, which indicates strong correlation even within this $\times 2$ structure between individual terraces, and shows the same periodicity as the terrace structure itself at this Pb concentration.

Finally, we mention the structures parallel to the terraces. They consist mostly of domain wall structures with periodically alternating $\sqrt{3} \times \sqrt{3}$ and $\sqrt{7} \times \sqrt{3}$ units, which form a devil's staircase on the isotropic Si(111) surface [22]. Here only parts of this devil's staircase structure are seen and indicated by the (m, n) notation, where m indicates the number of $\sqrt{3} \times \sqrt{3}$ units and n the $\sqrt{7} \times \sqrt{3}$ units. These structures were used in our case for fine-tuning of concentrations to less than 1% of a monolayer. A schematic of the step structures found is given in Fig. 9.3. As we will see later, these facet transformations are, at least in part, triggered by electronic properties of the system, i.e., they are electronically stabilized, as explicitly demonstrated for the (223) facets below.

9.3.2 1D Conductance

Formation of (223) facets results close to a Pb concentration of 1.30 ML in 1D dc conductance below 78 K [18], as shown in Fig. 9.4. For this measurement, we used a macrosopic modified four-point technique with eight contacts that were separated by slits machined into the sample in order to avoid cross talk, as described above.

As seen in Fig. 9.4, there is an abrupt, but reversible change in conductance at 78 K. Above 78 K there is activated conductance in both directions parallel ($\sigma_{\parallel}$) and

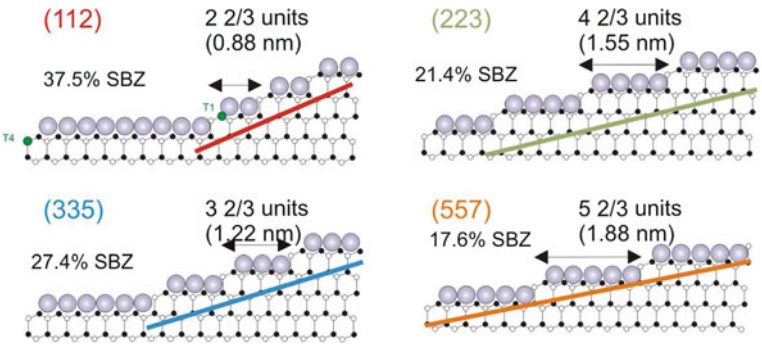

Fig. 9.3 Observed Pb-induced step densities on Si(557) after annealing to 600 K at Pb concentrations between 1.20 ML (*top left*, (112) facet), 1.24 ML (*bottom left*, (335) facet), 1.30 ML (*top right*, (223) facet), and 1.35 ML ((557) facet)

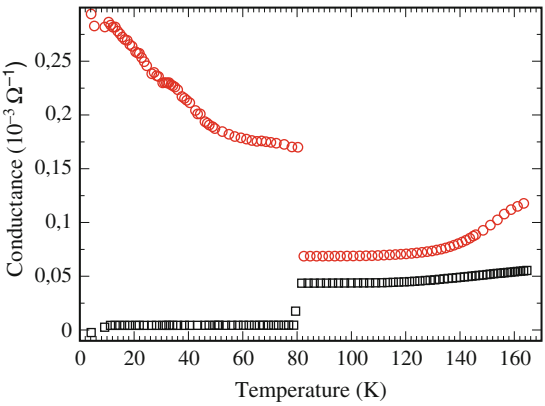

Fig. 9.4 Measured conductance after adsorption of 1.31 ML (i.e., one physical monolayer) of Pb on Si(557) and annealing to 640 K. For the data points marked by *circles*, the current direction was parallel, for those marked by *squares* perpendicular to the steps

perpendicular ($\sigma_\perp$) to the steps with weak anisotropy of a factor of 2 at most. Strong anisotropy is seen at lower temperature, and essentially insulating behavior perpendicular to the steps of the surface. Surprisingly, and in contrast to all other examples of 1D conductance discussed so far in the literature, this system is metallic at low temperatures in the direction parallel to the step edges, and there is no indication for any kind of instability as a function of temperature in the measured conductance down to 4 K.

9.3.3 Electronic Origin of 1D Conductance

The high Pb concentration of close to one physical monolayer and the Pb-induced changes of morphology suggest that the Pb nanowires are strongly coupled. There-

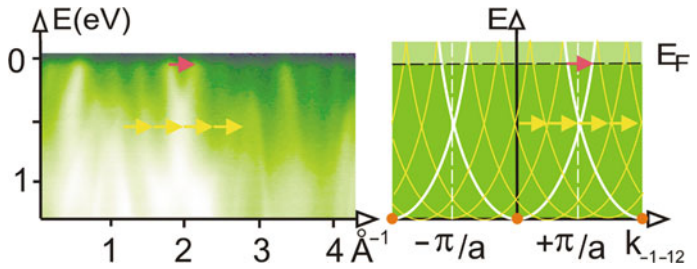

Fig. 9.5 *Left*: Angular-resolved photoemission data in the direction normal to the steps after adsorption of 1.3 ML of Pb on Si(557). *Right*: Schematic of the Umklapp process leading to insulating behavior in this direction (for details, see text)

fore, 1D conductance cannot be due to 1D bandstructures close to E_F, but must be caused by special properties of the 2D band structure. This is indeed found in angular-resolved photoemission (ARPES) measurements [23]. Pronounced dispersion is seen in both directions, in particular in the direction normal to the steps. An example of the photoemission intensity close to the Fermi energy as a function $k_\perp$ at $k_\parallel = 0.24$ Å is shown in the left part of Fig. 9.5. A detailed analysis reveals that only bands associated with (Pb-modified) surface states have intensity close to the Fermi level (E_F), whereas valence band states of Si reach their maximum close to $E_F - 0.3$ eV. A characteristic repetition of bands can be also seen, which is due to the periodicity introduced by the steps. The connecting vector is marked by yellow arrows. Its length $2\pi/d$ with the characteristic terrace length d corresponds exactly to $d = 4\frac{2}{3}a_0$, in agreement with our findings above (see also schematic in the right part of Fig. 9.5).

Further inspection of the ARPES data reveals that for exactly this step separation the condition $2k_F = 2\pi/d$ is fulfilled in the direction normal to the steps (red arrow in Fig. 9.5). Thus the topmost band is completely filled in this direction leading to strong Umklapp scattering, to Fermi nesting and to gap opening of a gap of ≈ 20 meV. Along the step direction we found two split bands [23]. This splitting may be caused by the Rashba effect. Only one of them can carry current. The other falls again on the edge of the small Brillouin zone due to the 10-fold periodicity parallel to the mini-terraces, which is formed at this Pb concentration. Thus only electronic states with very long wavelengths cross the Fermi level and lead to the 1D conductance observed at temperatures below 78 K.

We note here that this 1D band filling is directly related to the Pb-induced formation of (223) facets and must be a result of electronic stabilization of the associated terrace length, therefore. It thus corresponds to a modified Peierls mechanism, where step formation energies take over the role of lattice deformations in the direction perpendicular to the steps. Indeed the transition to an insulating state in this direction can be considered as formation of a 1D charge density wave. Because of the very different nature of step interactions and Pb-modified step formation energies, no period doubling, etc., should be expected.

9.3.4 Temperature-Driven Phase Transitions

Nevertheless, Fermi nesting is removed above 78 K by a structural phase transition, as we will show now. In fact it turns out that this phase transition is an order–order transition with a relatively small change in average step separation. We again used LEED for the quantitative determination of changes in the step density and measured 1D profiles in the direction normal to the steps, e.g., along a vertical line in the center of Fig. 9.1b.

Contrary to earlier assumptions of an order–disorder phase transition at 78 K, the LEED profiles in the top part of Fig.9.6 demonstrate that in fact a temperature-driven order–order transition occurs at 1.31 ML Pb concentration. The original spot

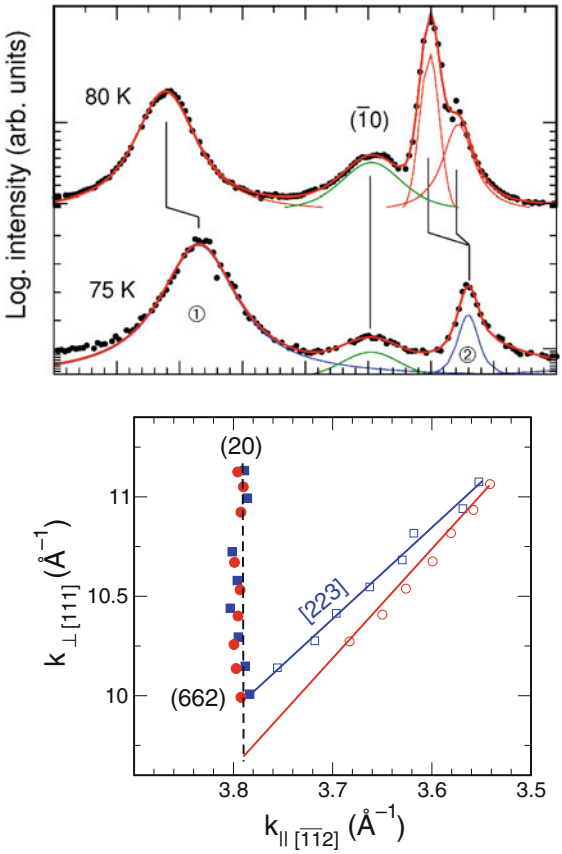

Fig. 9.6 *Top*: Line scans through LEED spots perpendicular to step directions (see Fig. 9.1) below ($T = 75$ K) and above the phase transition ($T = 80$ K) seen in conductance showing peak shifts and splittings. *Bottom*: Section of an Ewald construction close to the (662) 3D Bragg point. *Squares* are measured below, *circles* above the phase transition. The *lines* interpolate the data points and correspond to (111) [*vertical line*], (223), and (17 17 25) orientations, respectively (see also text)

separation corresponding to the (223) facet orientation changes, the peaks shift, and in part even split. A detailed analysis of this behavior at many different incident electron energies reveals [20], taking the $(\bar{1}0)$ or (20) spots of a minority species of larger (111) terraces as reference (see Fig. 9.6), that this behavior is to be expected for a transition to a high-index surface plane, which is close to a (17 17 25) orientation. Thus the average angle of inclination changes by 4%, as seen in the bottom part of Fig. 9.6. This corresponds to adding one row of Si atoms every three terraces on average. It is worth to be pointed out, however, that no local expansions of lattice constant are involved in this phase transition and all atoms remain on their crystalline sites. It is thus a new type of order–order phase transition, in which only the average inclination of the facets on the surface changes at T_c. We call this a refacetting surface phase transition. From the small background intensity and the absence of clear fluctuation-induced contributions to the diffraction profiles we conclude that this phase transition is of first order. This fits to the abrupt change of the average terrace length.

From the ARPES data above a gap around 20 meV were deduced for the majority of electrons. Excitation of electrons across this gap is obviously coupled with a destabilization of the (223) facet in favor of the (17 17 25) facet with a lower step density. While this small change of periodicity leads to a breakdown of the Fermi nesting condition and to a transformation of 1D to 2D conductance, it directly demonstrates the strong coupling between electronic and lattice degrees of freedom. In that sense a modified Peierls mechanism seems to be still relevant in the direction normal to the steps, and the transition to an insulating state at low temperature in this direction can be regarded as a charge density wave transition.

Small changes in periodicity along the wires were also observed at 78 K [20]. Associated with this change is a different size of the Brillouin zone at higher temperature and an effectively shorter Fermi wavelength. Thus there is an enhanced scattering probability at defects within the chains, which leads to a significant drop in $\sigma_{\|}$ and an overall activated behavior as a function of temperature above 78 K.

9.3.5 Stability of the Charge Density Wave Mechanism Normal to the Step Direction

Step decoration cannot be avoided anymore at Pb concentrations above 1.31 ML, as concluded from the fact that the dimerization at step sites with the characteristic streaky $(\times 2)$ reconstruction is now reduced continuously in intensity as a function of Pb concentration. It vanishes completely as the excess concentration, $\delta\Theta$, reaches 0.22 ML. This excess concentration corresponds exactly to the concentration that allows to cover all Si atoms at the (223) steps by one Pb atom.

When excess coverage relative to 1.31 ML is deposited, satellite peaks appear immediately at positions Δk_{deco}, which correspond to periodicities described by integer multiples of the (223) terrace width. Furthermore, their positions as a function of $\delta\Theta$ indicate unambiguously that the additional ordering is induced by the

excess coverage. On the other hand, the spot positions due to the (223) facet structure remain fixed, i.e., the additional coverage and the associated additional electron density do not change the terrace structure of the (223) surface orientation. An example is shown in the top part of Fig. 9.7. Here the splitting is 5.3% SBZ for 1.35

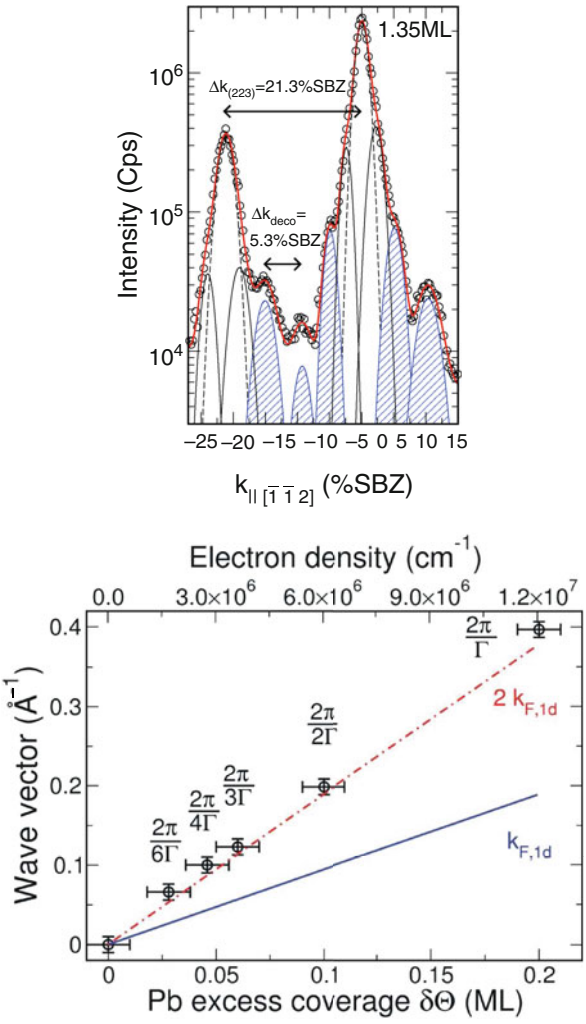

Fig. 9.7 *Top*: Exemplary line scan in LEED taken along the $[\bar{1}\bar{1}2]$ direction for a Pb coverage of 1.35 ML together with fits of new satellite peaks (see text). Pb layers were adsorbed at 75 K substrate temperature. *Bottom*: Plot of reciprocal lattice vectors of the satellite peaks versus the Pb excess coverage $\delta\Theta$ (relative to 1.31 ML). The solid (*blue*) curves represent the Fermi wave vector $k_{F,1D}$ of a 1D electron gas induced by the Pb excess coverage assuming a valence state of 2. The coincidence of $2k_F$ (*dashed-dotted (red) line*) with the lattice vectors of the superlattice results in nesting

ML Pb coverage, i.e., the lattice factor is modulated by four (223) terrace lengths, Γ_{223}. All spot profiles have been evaluated as shown by the fitting curves in this figure. Quantitative agreement was obtained using Gaussian functions (shaded peaks) in addition to the peaks representing the (223) facet structure (dashed). However, two further functions (solid lines) were needed in order to stabilize the fit. Their peak positions are in-between the (00)-peak and the first-order peaks of the $4 \times \Gamma_{223}$ periodicity and, thus, parts of the surface with decoration of only every eighth step may exist, because the coverage of 0.04 ML is somewhat too low to decorate all step sites within the $4 \times \Gamma_{223}$. Because of this remaining uncertainty with respect to the absolute coverage, the comparably broad peak structure of the nominally perfect (223) facet structure may contain also satellite peaks of even extraordinarily long-range ordered phases ($>10 \times \Gamma_{223}$).

The satellite spacings at various excess Pb concentrations have been analyzed systematically and are plotted versus the Pb excess coverage in the bottom part of Fig. 9.7. Spacings do not vary continuously. They always correspond to integer multiples of the inverse terrace length over the full range of excess concentrations up to 1.52 ML with a linear relation between Δk_{deco} and the excess concentration. It should be emphasized that an excess coverage of 1% leads already to the formation of long-range ordered structures.

Ordering with such long periodicities requires long-range interactions, which must again have an electronic origin. Since correlations seem to exist only in 1D in this case, we determined the Fermi wave vector k_{F} for a spin-degenerate 1D electron gas ($k_{\mathrm{F,1D}} = \frac{1}{2}\pi n$) (solid line in the lower part of Fig. 9.7) with an electron density n proportional to the Pb excess coverage assuming two electrons per Pb atom contributing to the split-off bands. The $(m \times 1)$ periodicity observed suggests that the Pb density within the chains is that of the underlying Si substrate at the step edges. With this assumption, as obvious from the figure, twice the Fermi vectors as a function of Pb concentration (dashed-dotted line) coincide perfectly with the reciprocal lattice vectors associated with the periodicities observed at the various excess Pb concentrations. This condition ($g = 2k_{\mathrm{F}}$) is exactly the same as that for 1D conductance on the pure (223) facet structure (see above).

Therefore, we suggest that the long-range ordering is again the result of an electron–electron interaction, band filling and gap opening. As in the case of the Pb coverage of 1.31 ML, the electronic stabilization means that parts of the gain of electronic energy is by filling a (sub)band completely and opening of a band gap. If this is correct, the structure should be electrically insulating at low temperature in the $[\bar{1}\bar{1}2]$ direction. This is indeed seen in surface conductivity measurements, as shown below. It means that the formation of the long-range ordered chain structure is energetically driven by the formation of split-off and fully occupied subbands, which must be located in the original band gap along $k_{\perp}$ found at $\Theta_{\mathrm{Pb}} = 1.31$ ML. In this sense the superlattice can be treated as charge density waves, i.e., the topmost electrons are still strongly correlated.

The existence of an insulating state in the direction normal to the steps is demonstrated in Fig. 9.8. Here we plotted $\sigma_{\perp}$ as a function of inverse temperature in

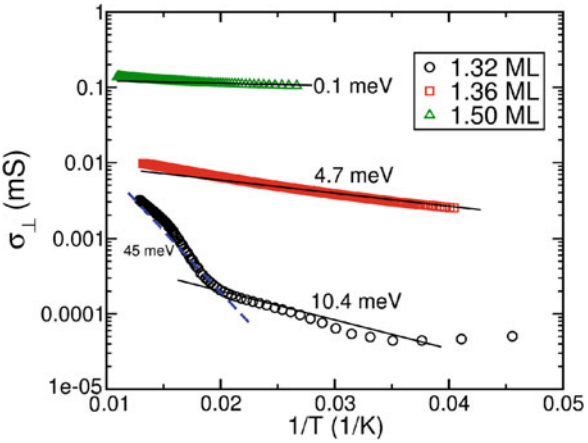

Fig. 9.8 Semi-log plots of $\sigma_\perp$ for Pb concentrations between 1.32 and 1.50 ML versus $1/T$ in the temperature range below 100 K. Temperature-activated behavior is found, and the activation energies are given at each curve

the temperature range below 100 K. At all excess concentrations $\delta\Theta$ up to a total concentration of 1.50 ML we see temperature-activated behavior, i.e., the system remains in an insulating state in the limit $T \rightarrow 0$, as expected for a charge density wave behavior. The effective band gaps, as determined from plots of Fig. 9.8, gradually shrink up to a total Pb concentration of 1.50 ML. At this concentration the measured activation energy is so small that we expect a transition to metallic behavior slightly above this concentration. Here the step decoration is completed, and adsorption of the second physical monolayer starts, which is most likely metallic.

At the concentration of 1.31 ML (not shown in Fig. 9.8) the band gap was estimated to be larger than 20 meV, as mentioned above, so that no conductance exceeding the conductance of the substrate can be measured below 80 K and a step-wise increase was found due to the phase transition at 78 K (see Fig. 9.4) from the insulating to a conducting state. This phase transition quickly disappears as a function of increasing Pb coverage both in conductance and in LEED. Even at an excess concentration as low as 0.01 ML (total Pb concentration 1.32 ML), the transition in conductance is strongly broadened resulting in an apparent activation of 45 meV close to the transition, which is not seen anymore at higher concentrations.

Indeed no structural phase transition was found at all for the superlattice structure of Fig. 9.7. The peak intensity of the satellite peaks shows only an attenuation according to the Debye–Waller effect up to 220 K. In view of a "classical" Peierls transition, which is the result of a balance between electric energy gain at the expense of lattice distortion energy, this result seems to be surprising. However, for the occupation of step edges no lattice distortion is necessary in the periodic arrangement of these chains so that only the electronic energy gain remains. This explains the missing phase transition (apart from final disorder at high temperatures) and the comparatively high stability.

9.4 Conclusions

The Pb/Si(557) system is an example of a system that is strongly coupled in 2D. Contrary to the standard impression gained from literature, this must be also true for systems that exhibit a 1D band structure close to the Fermi level like In/Si(111) [10, 11], as obvious from their well-ordered arrays of metallic chains. The difference between the Pb system and those examples is that not only electronic levels far below the Fermi level are responsible for 2D ordering but also the electrons close to the Fermi level take part in the 2D interaction. As we have shown, this fact does not prevent occurrence of 1D conductance, but gives rise to a number of phenomena not seen in systems with a purely 1D Fermi surface.

The most prominent one is the occurrence of Pb-induced self-stabilized reordering of the step structure at the surface. It is this self-organized generation of new average terrace widths that does not exist without the Pb coverage and leads to a Pb concentration of 1.31 ML to complete 1D band filling and to 1D conductance. In the direction normal to the steps the switching-off of conductance is equivalent to CDW formation. The associated Fermi nesting can be destroyed by temperature. Although there is still a structural phase transition, the step structure does not undergo a "normal" Peierls transition, because of the different nature of step–step and step–surface interactions. Only a small distortion of the regular (223) facet orientation is seen.

CDW formation because of periodic step decoration and the split-off electronic states associated with chains at step edges is another phenomenon that was not seen previously. Here the structural phase transition is completely missing. This means that the 1D ordering of Pb chains at the step edges is a purely electronic effect with weak coupling to the lattice and to the step structure. Therefore, no structural phase transition can be driven by the interplay between these interactions.

These results show that our understanding of these phenomena is still far from being complete and still require more effort both from the experimental side and from the theoretical side in order to elucidate the wealth of phenomena generated by this intriguing interplay of interactions in various dimensions.

Acknowledgments It is a pleasure to acknowledge the very fruitful and continuing collaboration with my coworkers, in particular with C. Tegenkamp, M. Czubanowski, M. Gauch, and D. Lükermann. This work was supported by the Deutsche Forschungsgemeinschaft.

References

1. G. Grüner, The dynamics of charge-density waves. Rev. Modern Phys. **60**, 1129 (1988)
2. J.M. Luttinger, An exactly soluble model of a Many-Fermion System. J. Math. Phys. (N.Y.) **4**, 1154 (1963)
3. M.G. Zacher, E. Arrigoni, W. Hanke, J.R. Schrieffer, Systematic numerical study of spin-charge separation in one dimension. Phys. Rev. B **57**, 6370 (1998)
4. G.Grüner, *Density Waves in Solids* (Addison-Wesley, New York, 1994)

5. G.S. Snider, R.S. Williams, Nano/CMOS architectures using a field-programmable nanowire interconnect. Nanotechnol. **18**, 035204 (2007)
6. D.E. Chang, A.S. Sørensen, P.R. Hemmer, M.D. Lukin, Quantum optics with surface plasmons. Phys. Rev. Lett. **97**, 053002 (2006)
7. N. Nilius, T. M. Wallis, W. Ho, Localized molecular constraint on electron delocalization in a metallic chain. Phys. Rev. Lett. **90**,186102 (2003)
8. T. Kanagawa, R. Hobara, I. Matsuda, T. Tanikawa, A. Natori, S. Hasegawa, Anisotropy in conductance of a quasi-one-dimensional metallic surface state measured by a square microfour-point probe method. Phys. Rev. Lett. **91**, 036805 (2003)
9. T. Tanikawa, I. Matsuda, T. Kanagawa, S. Hasegawa, Surface-state electrical conductivity at a metal-insulator transition on silicon. Phys. Rev. Lett. **93**, 016801 (2004)
10. J.N. Crain, A. Kirakosian, K.N. Altmann, C. Bromberger, S.C. Erwin, J.L. McChesney, J.L. Lin, F.J. Himpsel, Fractional band filling in an atomic chain structure. Phys. Rev. Lett. **90**, 176805 (2003)
11. H.W. Yeom, S. Takeda, E. Rotenberg, I. Matsuda, K. Horikoshi, J. Schäfer, C.M. Lee, S. D. Kevan, T. Ohta, T. Nagao, S. Hasegawa, Instability and charge density wave of metallic quantum chains on a silicon surface. Phys. Rev. Lett. **82**, 4898 (1999)
12. J.R. Ahn, P.G. Kang, K.D. Ryang, H.W. Yeom, Coexistence of two different peierls distortions within an atomic scale wire: Si(553)-Au. Phys. Rev. Lett. **95**, 196402 (2005)
13. E.P. Rugeramigabo, T. Nagao, H. Pfnür, Two-dimensional plasmons in a DySi$_2$ monolayer on Si(111). Phys. Rev. B **78**, 155402 (2008)
14. Ph. Hofmann, J.W. Wells, Surface-sensitive conductance measurements. J. Phys. Condens. Matter **21**, 013003 (2009)
15. C. Tegenkamp, H. Pfnür, Switchable nanometer contacts: Epitaxial Ag nanostructures on Si(100). Surf. Sci. **601**, 2641 (2007)
16. R.H.M. Smit, Y. Noat, C. Untiedt, N.D. Lang, M.C. van Hemert, J.M. van Ruitenbeek, Measurement of the conductance of a hydrogen molecule. Nat. Lond. **419**, 906 (2002)
17. G. Gardinowski, J. Schmeidel, H. Pfnür, C. Tegenkamp, Switchable nanometer contacts: Epitaxial Ag nanostructures on Si(100). Appl. Phys. Lett. **89**, 063120 (2006)
18. C. Tegenkamp, Z. Kallassy, H. Pfnür, H.-L. Günter, V. Zielasek, M. Henzler, Switching between one and two dimensions: conductivity of Pb-induced chain structures on Si(557). Phys. Rev. Lett. **95**, 176804 (2005); C. Tegenkamp, Z. Kallassy, H.-L.Günter, V. Zielasek, H. Pfnür, Anisotropic conductance of Pb-induced chain structures on Si(557) in the monolayer regime. Eur. Phys. J. B **43**, 557 (2005)
19. M. Czubanowski, A. Schuster, S. Akbari, H. Pfnür, C. Tegenkamp, Adsorbate induced refacetting: Pb chains on Si(557). New J. Phys. **9**, 338 (2007)
20. C. Czubanowski, C. Tegenkamp, H. Pfnür, Temperature-driven refacetting phase transition in Pb chains on Si(557). Phys. Rev. B **77**, 174108 (2008)
21. M. Czubanowski, H. Pfnür, C. Tegenkamp, Atomic chain ordering with ultra-long periods: Pb/Si(557). Surf. Sci. **603**, L121 (2009)
22. M. Yakes, V. Yeh, M. Hupalo, M.C. Tringides, Self-organization at finite temperatures of the devil's staircase in Pb/Si(111). Phys. Rev. B **69**, 224103 (2004)
23. C. Tegenkamp, T. Ohta, J.L. McChesney, H. Dil, E. Rothenberg, H. Pfnür, K. Horn, Coupled Pb-chains on Si(557): origin of one-dimensional conductance. Phys. Rev. Lett. **100**, 076802 (2008)

Chapter 10
Formation and Opto-electronic Properties of Nanostructures on Ultrathin SiO_2-Covered Si Surfaces

M. Ichikawa

Abstract We review a method to form semiconductor nanodots on Si substrates by using ultrathin Si oxide technology and the results on their opto-electronic properties. We can form ultrasmall semiconductor nanodots with the size of ~5 nm and ultrahigh density of $\sim 10^{12}\,cm^{-2}$ on Si surfaces covered with ultrathin SiO_2 films of ~0.3 nm thickness. We focus on the Ge, GeSn, and GaSb nanodots on Si substrates and those embedded in Si films. These structures exhibit quantum confinement effects and intense luminescence in the energy region of about 0.8 eV. We also report an application result to grow GaSb thin films on Si substrates covered with ultrathin SiO_2 films using GaSb nanodots as seeding crystals.

10.1 Introduction

Quantum confinement effects in semiconductor nanodots lead to the concentration of continuous electronic density of states into discrete one, the enhancement of oscillator strengths due to the increase of overlap between electron and hole wave functions, and the relaxation of carrier momentum conservation. Many studies have been done for compound and group IV semiconductors since the above effects contribute to the enhancement of luminescence efficiency from nanodots [1]. Especially, in group IV indirect transition semiconductors such as Si or Ge, the relaxation of momentum conservation is thought to much enhance the luminescence efficiency [2]. This leads to the development of CMOS-compatible integrated opto-electronic systems.

The Stranski–Krastanov (SK) growth on substrates is a well-known method to form nanoislands on substrates [3]. In this growth, nanoislands are grown on wetting

M. Ichikawa (✉)
Department of Applied Physics, Graduate School of Engineering, The University of Tokyo, 7-3-1 Hongo, Bunkyo-ku, Tokyo 113-8656 Japan,
e-mail: ichikawa@ap.t.u-tokyo.ac.jp

M. Michailov (ed.), *Nanophenomena at Surfaces,* Springer Series in Surface Sciences 47,
DOI 10.1007/978-3-642-16510-8_10,

layers to minimize the sum of surface, interface, and strain energies during heteroepitaxy. The size and areal density of nanoislands, however, are limited to several tens of nanometers and $\sim 10^{11}$ cm^{-2}, respectively, since they are determined by the surface diffusion on the wetting layers and growth rate of critical nuclei of deposited atoms. Many studies have been done to solve the problems so far [4]. We have developed a self-assembled method to form nanodots with $\sim$5 nm size and $\sim 10^{12}$ cm^{-2} density on Si substrates by depositing different materials on Si surfaces covered with ultrathin Si oxide films of $\sim$0.3 nm thickness [5, 6]. Several researchers have afterward developed similar nanodot formation methods on Si surfaces covered with thin oxide films of thickness thicker than 1 nm [7, 8].

In this chapter, we report a method to form ultrasmall and ultrahigh density nanodots on Si substrates and focus on electronic properties of the Ge, GeSn, and GaSb nanodots on Si substrates and optical properties of the nanodots embedded in Si films. We also report an application result to grow GaSb thin films on Si substrates covered with ultrathin SiO_2 films using GaSb nanodots as seeding crystals.

10.2 Experimental Procedure

We used solid source molecular beam epitaxy (MBE) apparatus to form Ge nanodots on Si substrates. After formation of thin Si oxides ($\sim$1 nm) by chemical treatment of Si wafers, the wafer surfaces were cleaned by decomposition of the Si oxides in the MBE chamber at 830°C under a weak Si flux from an electron beam evaporator. Next Si buffer layers of about 100 nm thickness were grown at 550°C. The ultrathin Si oxides were formed on Si surfaces at 500°C by introducing oxygen in the chamber at a pressure of 2×10^{-4} Pa for 10 min. The thickness of the ultrathin Si oxide was estimated to be about 0.3 nm and the oxide was mainly composed of silicon dioxide (SiO_2) [9]. For Ge nanodot formation, Ge with nominal thickness of several monolayers (ML) was deposited on the surface at the substrate temperature of about 500°C. This resulted in the formation of Ge nanodots with about 5 nm in size and the areal density of $\sim 10^{12}$ cm^{-2} [5]. The layer of Ge nanodots was covered with about 100 nm thick Si capping layer at 500°C. Some samples were annealed in a separate lamp furnace at temperatures in the range of 700–900°C for 30 min in dry oxygen atmosphere.

An ultrahigh vacuum scanning tunneling microscope (STM) was used to observe surface structures and electronic properties of nanodots. A transmission electron microscope (TEM) and a scanning transmission electron microscope (STEM) were used to observe cross-sectional structures of the nanostructures. Photoluminescence (PL) and electroluminescence (EL) spectra of the samples were obtained at temperatures in the range from 4 to $\sim$300 K using a standard lock-in technique in conjunction with an InGaAs photomultiplier detector, a grating monochromator, and a He–Cd laser with the 325 nm line. The laser beam had about 1 mm diameter and 8 mW power.

10.3 Formation and Properties of Nanostructures

10.3.1 Formation of Ge Nanodots

Figure 10.1 shows STM images of Ge nanodots on an ultrathin SiO_2-covered Si(001) surface with linear clean Si windows having about 20 nm width after 8 ML thick Ge was deposited on the surface at 400°C. This experiment was performed using a different apparatus where an ultrahigh vacuum scanning reflection electron microscope and STM were combined [10]. Linear clean Si windows were produced by irradiating a focused electron beam on ultrathin Si oxide-covered Si(001) at room temperature and by subsequently annealing the sample at 750°C for 30 s. Selective thermal decomposition of the Si oxide from the focused electron beam-irradiated areas produced clean Si windows on the surface [11].

Ge nanoislands with ∼20 nm size were grown on the linear Si windows due to the SK growth mode. Ge nanodots with less than 10 nm size and the density of $\sim 10^{12}\,\mathrm{cm}^{-2}$ were grown on ultrathin Si oxides. The growth mode on the SiO_2 areas was caused by the chemical reactions of Ge atoms with ultrathin SiO_2 films such as $Ge + SiO_2 \rightarrow GeO(gas) + SiO(gas)$ [5]. This chemical reaction formed heterogeneous nucleation sites for Ge nanodots on the SiO_2 surface region resulting in ultrahigh density. The Ge nanodot size could be controlled by the total Ge deposition amount.

Figure 10.2 shows reflection high-energy electron diffraction (RHEED) patterns ((b) and (d)) from the Ge nanodots and their STM images ((a) and (c)). In

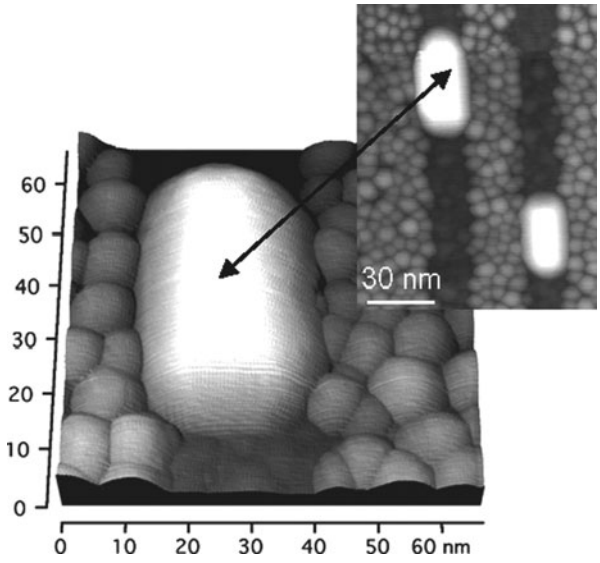

Fig. 10.1 Three-dimensional and conventional STM images of Ge nanodots grown on ultrathin Si oxides with linear Si(001) windows. Nanoislands indicated by *arrow* are the same ones

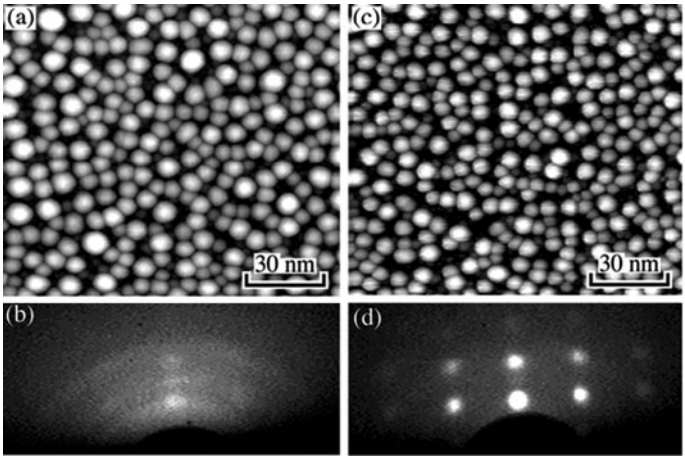

Fig. 10.2 STM images and RHEED patterns after two bilayer (BL) Ge deposition at 390°C (**a**) and (**b**), and at 500°C (**c**) and (**d**)

spite of the fact that the Ge was deposited on the amorphous SiO_2 films, the RHEED pattern (Fig. 10.2d) shows that Ge nanodots were epitaxially grown on the Si(111) substrate at higher deposition temperatures higher than 500°C. The Ge deposition can create areas of bare Si through the SiO_2 decomposition reaction. These Si bare areas provided conditions for the epitaxial growth of Ge nanodots. At lower deposition temperatures lower than 400°C shown in Fig. 10.2a, b, bare Si areas were not created, resulting in the growth of non-epitaxial Ge nanodots. The island density hardly depended on the deposition rate, indicating that the island density was mainly determined by the Ge chemical reactions with the ultrathin SiO_2 films. Stacked structures were made by repeating the process in which the epitaxial Ge nanodots were embedded in Si films by depositing Si and the Si film surface was oxidized to form ultrathin SiO_2 films and then Ge was deposited to grow new Ge nanodots [12].

The SiO_2 surfaces are chemically inert resulting in small adsorption energy for Ge atoms on the surfaces. The Si window and Ge nucleated areas are chemically active resulting in the large adsorption energy on the surfaces. The adsorption difference produces the potential barriers of about 3 eV between the SiO_2 and Si window and Ge nucleated areas [13]. The potential barriers interrupt the atom exchanges on the surfaces resulting in the selective growth of Ge nanoislands and nanodots as shown in Fig. 10.1, and also in uniform size distribution of the nanodots due to the suppression of the Ostwald ripening.

This formation technology could also be applied to form Si [14] and β-$FeSi_2$ [15] ultrasmall nanodots with ultrahigh densities on Si substrates. We could observe carrier quantum confinement effects in Ge [16] and β-$FeSi_2$ [17] nanodots, and Coulomb blockade effect in Ge nanodots [18] even at room temperature due to the ultrasmall sizes.

10.3.2 Structures and Optical Properties of Ge Nanodots in Si Films

Figure 10.3 shows scanning transmission electron microscope (STEM) dark-field images of cross sections of Ge nanodots embedded in Si films on Si(001) substrates, (a) as grown and (b) after annealing at 900°C for 30 min [19]. Ge nanodots have bright contrast against Si films due to larger atomic number of Ge than that of Si. Ge nanodots were formed in the Si(001) films for as-grown case, but decayed after the annealing, forming thin film-like structures (Fig. 10.3b).

Figure 10.4 shows annealing temperature dependence of photoluminescence (PL) intensities at 4 K after 30-min annealing. The PL intensities became higher in the energy region of ~0.8 eV (~1.5 μm wavelength) with the increase of the annealing temperatures. This PL energy region is of practical importance for optical fiber communication systems.

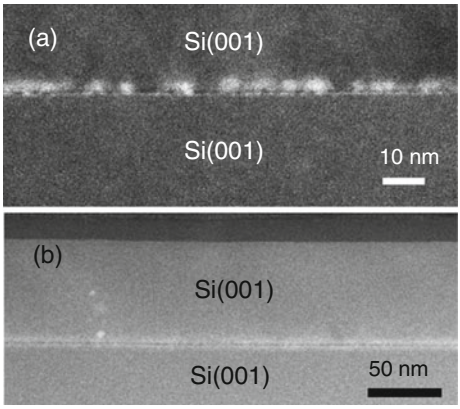

Fig. 10.3 STEM images of Ge nanodots embedded in Si films: (**a**) As grown and (**b**) after 900°C–30 min annealing

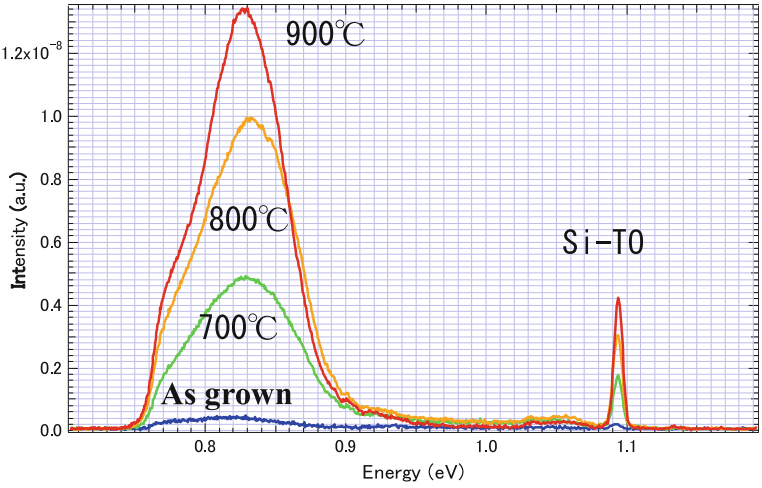

Fig. 10.4 Annealing temperature dependence of PL intensities at 4 K after 30-min annealing

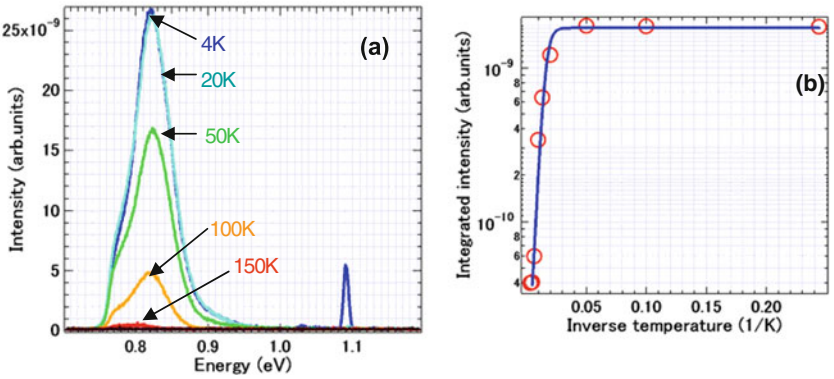

Fig. 10.5 Sample temperature dependence of PL intensities after annealing at 900°C for 30 min: (**a**) PL spectra and (**b**) integrated PL intensities

The PL intensities after high-temperature annealing cannot be attributed to the Ge nanodots since the Ge nanodots decayed after high-temperature annealing as shown in Fig. 10.3b. We have not observed any dot size dependence of the PL peak position of ~0.8 eV. They can originate from radiative defects such as Ge–Si–O or Si–O complexes in Si capping layers near the Ge nanodot layer [20–23]. The high-temperature annealing produced these complexes and decreased defects for non-radiative carrier recombination, which resulted in the enhancement of PL intensities.

Figure 10.5 shows sample temperature dependence of (a) PL spectra and (b) integrated PL intensities in 0.75–0.9 eV range after annealing at 900°C for 30 min. PL intensities decreased with the increase of the sample temperatures. The integrated intensity profile can be fitted by a formula of $a/\{1 + b\exp(-E_a/kT)\}$, where a and b are some constants, E_a is the activation energy for thermal quenching of PL intensity. We obtained about 30 meV for E_a. This indicates that carriers escape from the radiative defect sites having 30 meV barrier before radiative recombination and are non-radiatively recombined.

We made metal electrodes (Au and Al) on front and back sides of the annealed sample and performed electroluminescence (EL) measurement. Figure 10.6 shows sample temperature dependence of EL intensities at sample voltage of 6.8 V and sample current of 48 mA. We obtained similar EL spectra to the PL ones with high intensities in the energy region of ~0.8 eV. The integrated EL intensity profile was similar to the PL one (Fig. 10.5b) and the activation energy for thermal quenching of EL intensity was about 20 meV. This indicates that the EL was caused by the same mechanism as the PL one. EL intensity, however, became very low at room temperature.

We formed multilayer structures of Ge nanodots (five layers) by repeating Ge nanodot and Si film growths on p-type Si(001) substrates [24]. To fabricate light-emitting diodes (p–i–n), plasma etching was applied to form 0.6 μm high and 0.3 mm diameter mesa structures. The sample was thermally oxidized at 900°C to grow 300 nm thick SiO_2 films. Then SiO_2 etching, P^+ ion implantation and metal deposition were performed to make Au and Al electrodes (the inset in Fig. 10.7a).

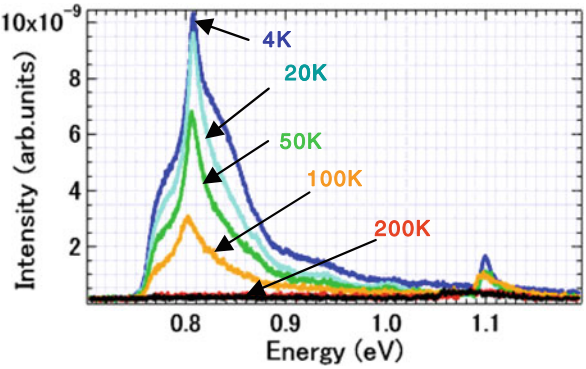

Fig. 10.6 Sample temperature dependence of EL intensities from the annealed sample

The P^+ ion implantation was carried out with the ion energy of 30 keV and a dose of 10^{14} cm^{-2} followed by annealing at 500°C to make n-type regions. The temperature dependence of the EL spectra at 6 mA injection current is shown in Fig. 10.7a. EL peaks with very broad distribution in 1.5–1.7 μm range are observed even at room temperature. This is considered due to the fact that the radiative recombination processes increase in the multilayer structures by the increase of the radiative Ge–Si–O complex areas.

Figure 10.7b shows injection current density J dependence of EL peak intensities I's centered at 1.55 μm at several measurement temperatures. The EL intensities are proportional to J^m. The exponent m's increase from 0.74 to 1.3 with the increase of the measurement temperatures. This suggests that the recombination processes are dominated by the process of Auger recombination at low temperature (7 K) and by the recombination process at non-radiative recombination sites at room temperature (300 K).

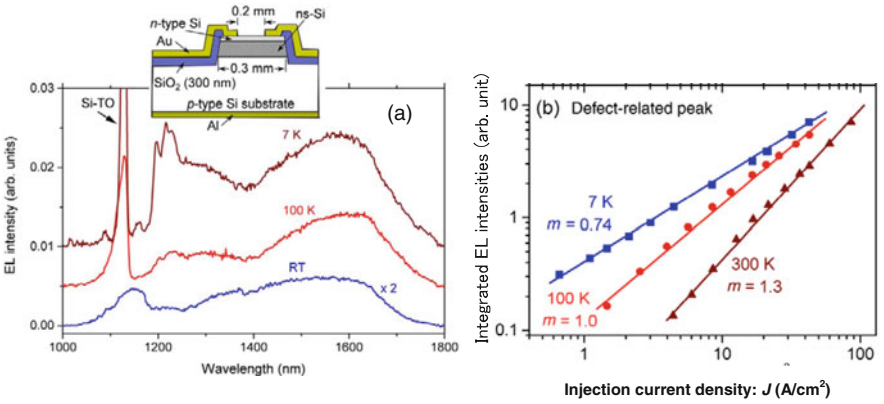

Fig. 10.7 EL intensities from Ge nanodot multilayer structures. (**a**) EL spectra at different sample temperatures and (**b**) injection current dependence of EL peak intensities at 1.55 μm region at different sample temperatures (7, 100, 300 K)

10.3.3 Formation of GeSn Nanodots

$Ge_{1-x}Sn_x$ alloys have been intensively studied as promising materials for use in light-emitting devices made of group IV semiconductors since some studies reported on direct transition semiconductor $Ge_{1-x}Sn_x$ alloys [25–28] with Sn composition, x larger than critical composition, x_c of ∼0.12 [27, 28]. The conduction band minimum at the Γ point preferentially decreases with the increase of x, suggesting the type I band alignment in Si films. Despite the limited mutual solid solubility of Ge and Sn < 1 %, supersaturated solid solutions of $Ge_{1-x}Sn_x$ alloys can be formed using nonequilibrium growth methods such as low-temperature molecular beam epitaxy, magnetron sputtering, chemical vapor deposition [27–32]. However, direct transition semiconductor $Ge_{1-x}Sn_x$ alloys with $x > x_c$ have an energy band gap, E_g, of less than 0.3–0.5 eV [27, 28], which is too small to apply to light-emitting devices with wavelengths of ∼1.5 μm (∼0.8 eV) for use in optical fiber communication systems.

We have expected a direct transition semiconductor $Ge_{1-x}Sn_x$ nanodots with E_g of ∼0.8 eV. The quantum confinement effect in the nanodots enables us to control the value of E_g by changing the nanodot size [16, 17, 33, 34], in addition to the large optical oscillator strength of the nanodots.

We formed ultrasmall voids in the ultrathin SiO_2 films by predeposition of Ge in two monolayer (ML) (1 ML = 7.8×10^{14} atoms/cm^2) amounts at 650°C. For suppression of Sn surface segregation, codeposition of Ge and Sn was performed on these ultrathin SiO_2 films with ultrasmall voids at ∼200°C to form hemispherical epitaxial $Ge_{1-x}Sn_x$ nanodots with ultrahigh density (∼1×10^{12} cm^{-2}). The epitaxial growth of the $Ge_{1-x}Sn_x$ nanodots with a Si(111) crystallographic orientation was confirmed by RHEED observation. We annealed the $Ge_{1-x}Sn_x$ nanodots at 500°C for 3 min to improve the $Ge_{1-x}Sn_x$ nanodot crystallinity. The flux ratio of Ge to Sn during codeposition was kept at 0.85–0.15. The deposition amount of GeSn was changed in a range from 4 to 24 ML to control the nanodot diameters from 4 to 35 nm. We confirmed that x was about 0.15 by analyzing $Ge_{1-x}Sn_x$ lattice images [35] and also measuring photoemission spectra from $Ge_{1-x}Sn_x$ nanodots [36].

10.3.4 Electronic and Optical Properties of GeSn Nanodots

To remove the surface state contribution in the energy band gap, we performed atomic hydrogen termination of the nanodot surfaces by introducing hydrogen molecules up to 2×10^{-4} Pa for 70 min at room temperature after putting the samples in front of heated W filaments. Scanning tunneling spectroscopy (STS) experiments were conducted at room temperature using chemically polished PtIr tips cleaned by electron beam heating in UHV chamber. We considered that epitaxial $Ge_{1-x}Sn_x$ nanodots were in contact with Si substrates through the ultrasmall (<∼ 1 nm) voids in the SiO_2 films beneath the nanodots. We found that the electric potential difference between Si substrates and nanodots was negligible because of the contact between the epitaxial nanodots and Si substrates, similar to Ge nanodots [16].

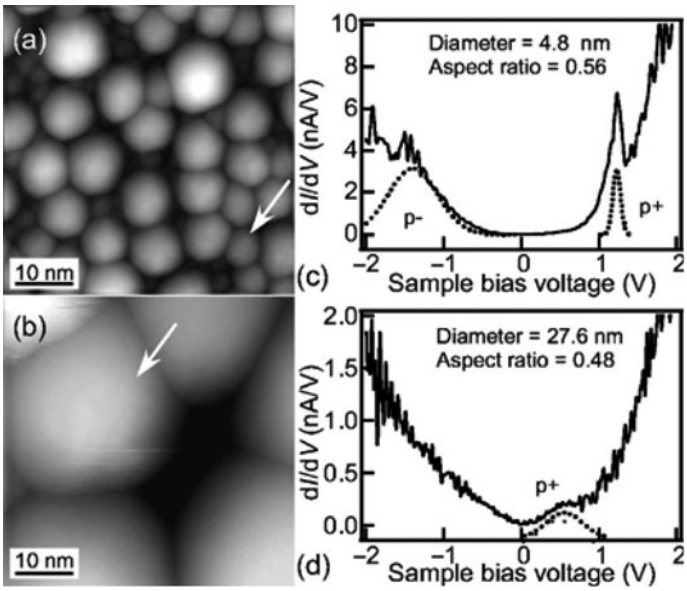

Fig. 10.8 STM images of hydrogen-terminated $Ge_{0.85}Sn_{0.15}$ nanodots with (**a**) 4 and (**b**) 24 ML amounts. The differential conductances dI/dV in (**c**) and (**d**) were measured by STS on $Ge_{0.85}Sn_{0.15}$ nanodots corresponding to those indicated by the *arrows* in (**a**) and (**b**), respectively

STM images in Fig. 10.8 show the hydrogen-terminated epitaxial $Ge_{0.85}Sn_{0.15}$ nanodots with amounts of 8 ML (a) and 24 ML (b) on the ultrathin SiO_2 films [37]. The differential conductances, dI/dV, in Fig. 10.8c, d were obtained by STS measurements on top of the $Ge_{0.85}Sn_{0.15}$ nanodots indicated by arrows in Fig. 10.8a, b, respectively. Peaks in the conduction (p^+) and valence (p^-) band regions were observed in these spectra, though the p^- peaks were sometimes not discernible. Figure 10.8 demonstrates that the p^+ peak up-shifted with the decrease in the nanodot size.

We measured the peak position and its width by deconvolution of the spectra using Gaussian functions with a standard deviation σ, as shown by dashed line in Fig. 10.8c, d. We defined the conduction band minimum (CBM) (valence band maximum, VBM) by subtracting (adding) 2σ from (to) the peak position of p^+ (p^-). Figure 10.9a shows the dependences of CBM and –VBM on the diameter of the nanodots. It is found that the absolute values of both VBM and CBM up-shifted by about 0.5 eV with the decrease in the nanodot diameter from 35 to 4 nm. The nanodot diameter dependence of the energy band gap, defined as CBM–VBM, is shown in Fig. 10.9b. The energy band gap increased with a decrease in nanodot size.

In the present situation, the nanodots are sandwiched between vacuum and SiO_2 films. The SiO_2 films work as the high barrier for the carriers in the nanodots. Therefore, the hard wall square potential model is thought to be reasonable. For the quantum confinement for size L, the absolute value of CBM (VBM) for confined structure, E_{confined}, is described as

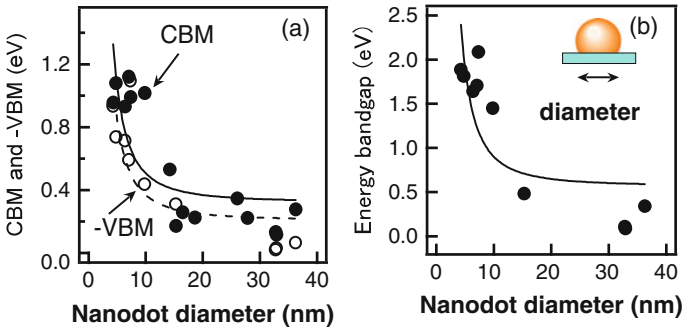

Fig. 10.9 (**a**) Nanodot diameter dependences of CBM and –VBM and (**b**) nanodot diameter dependence of the energy band gap

$$E_{\text{confined}}(L) = E_{\text{bulk}} + \frac{\hbar^2 \pi^2}{2mL^2} \tag{10.1}$$

where E_{bulk} is the absolute value of CBM (VBM) for the bulk structure and m is the effective mass of the electron (hole). For a quantum size effect in a nanodot, the size L is nanodot radius ($d/2$). The solid (dashed) lines in Fig. 10.9a are best-fitted curves, where E_{bulk} for the absolute values of CBM (VBM) with respect to the Fermi level and m for the electron (hole) were adjusted to 0.32 eV (0.21 eV) and 0.08 m_0 (0.09m_0) with free electron mass m_0, respectively. These values agree well with the theoretical ones [25].

This clearly shows the quantum confinement effect that can be explained by the confinement of carriers with bulk effective masses in simple spherical potential well [37]. We can estimate from these results that $Ge_{1-x}Sn_x$ nanodot with 10 nm size has the energy band gap of ~0.8 eV.

We formed a structure of 10 nm size $Ge_{0.85}Sn_{0.15}$ nanodots embedded in Si films of ~100 nm thickness. PL spectrum from the as-grown sample is shown in Fig. 10.10a. PL peak with high intensity is observed in the 0.8 eV region. This is different from the Ge nanodot case as shown in Fig. 10.4. We measured $Ge_{0.85}Sn_{0.15}$ nanodot size dependence (diameter: 7, 10, and 13 nm) of the PL peak positions by making the structures as shown in Fig. 10.10b. It is expected from the solid curve in Fig. 10.9b that the nanodots with 7, 10, and 13 nm sizes have the energy band gaps of 1.2, 0.8, and 0.7 eV, respectively. No size dependences, however, are observed suggesting that the PL peaks are not originated from $Ge_{0.85}Sn_{0.15}$ nanodots but from the radiative Ge–Si–O complexes influenced by Sn incorporation.

Figure 10.11 shows sample temperature dependence of integrated PL intensities in the 0.75–0.9 eV range shown in the inset. The integrated intensity profile can be fitted by a formula of $a/\{1 + b\exp(-E_a/kT)\}$, where a and b are some constants, E_a is the activation energy for thermal quenching of PL intensity. We obtained about 22 meV for E_a which is similar to that of the Ge nanodot case as shown in Fig. 10.5b. The detailed studies on the origin of the PL peak will be reported in the different article [38].

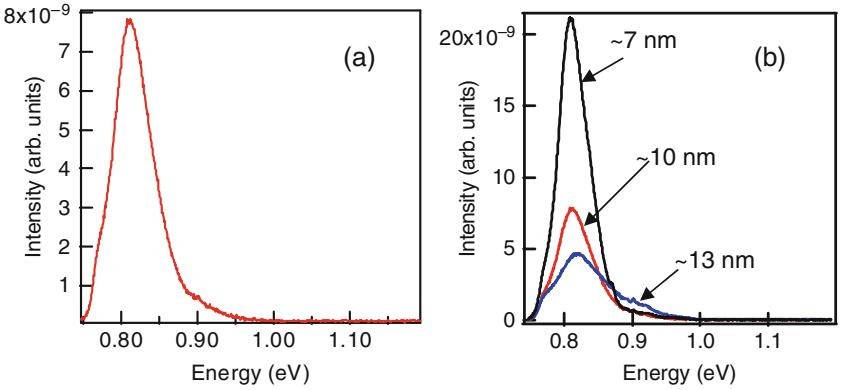

Fig. 10.10 (**a**) PL spectrum from the 10 nm size $Ge_{0.85}Sn_{0.15}$ nanodot structure in Si film (as grown) at 4 K and (**b**) nanodot size dependences of the PL spectra

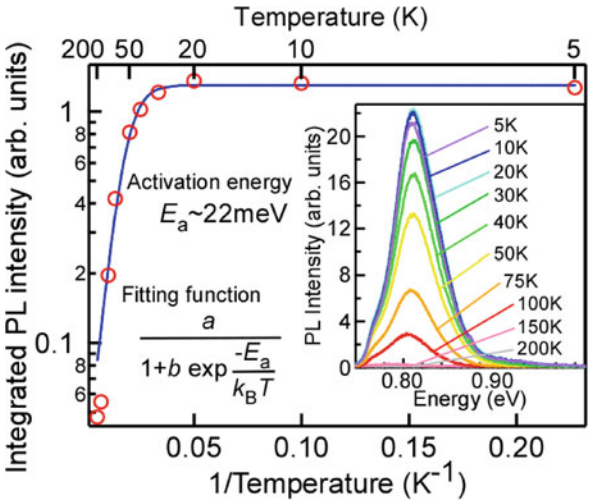

Fig. 10.11 Sample temperature dependence of integrated PL intensities in the 0.75–0.9 eV range shown in the *inset*

10.3.5 Formation of GaSb Nanodots

Epitaxial growth of GaSb films on Si substrates has been intensely studied [39–41] despite there being a large lattice mismatch between GaSb and Si (~12.2 %). Studies have been conducted since the direct transition semiconductor GaSb [42, 43] with an energy band gap of ~0.73 eV is a promising Si-based light-emitting material with a 1.5 μm wavelength (~0.8 eV) that may have applications in optical fiber communication systems. In comparison with films, nanodots possibly have a

larger light-emitting efficiency due to the concentrated density of states with certain energies and the reduction in their non-radiative recombination rate. The epitaxial growth of GaSb nanodots on Si(001) was studied under the Volmer-Weber (VW) growth mode, for which it is difficult to form small nanodots with a high nanodot density. In the case of the growth at 500°C [44], nanodots larger than ~200 nm were grown on Si(001) with a low density of $\sim 10^8$ cm^{-2}. By a small amount deposition, Jo et al. [45, 46] formed small GaSb nanodots directly on Si(001) substrates and successfully observed a strong luminescence of around 1 eV from the GaSb nanodots embedded in Si films. However, this luminescence was due to the recombination of electrons in nanodots and holes in Si near the interfaces because nanodots in this system were inherently of type II [47]. In general in the case of type I nanodots, the large spatial overlapping of the electron–hole wave function enhances their optical oscillator strength. Furthermore, the energy band gap of these nanodots can be tuned to be compatible with optical communication devices (~0.8 eV) by controlling the nanodot size owing to the quantum confinement effect [33, 34].

We grew GaSb nanodots on p-type float-zone Si(001) wafers that had a resistivity of 10–200 Ω cm using solid-source molecular beam epitaxy in an ultrahigh vacuum chamber (UHV) with a base pressure of $\sim 1 \times 10^{-10}$ torr [48]. The Si surfaces were then oxidized at 500°C in oxygen pressure of 2×10^{-6} torr for 10 min to form ultrathin SiO_2 films on the Si substrates. Two ML of Ge (1 ML = 6.78×10^{14} atoms/cm^2) was deposited on the ultrathin SiO_2 films at 650°C. A reaction between the deposited Ge atoms and the SiO_2 films formed ultrasmall Si bare areas, referred to as voids, in the ultrathin SiO_2 film, the size of which was approximately 1 nm [49]. This was followed by the epitaxial growth of ultrasmall Ge nuclei on these voids [35, 37]. Gallium and Sb were codeposited on these ultrathin SiO_2 films with the epitaxial Ge nuclei at various temperatures (200–550°C) to form epitaxial GaSb nanodots. The amount of deposited GaSb was estimated from the amount of deposited Ga which has a lower desorption rate. The V/III flux ratio was ~1–1.5 at temperatures lower than 300°C and ~4–9 for temperatures higher than 450°C.

We formed GaSb nanodots at various codeposition temperatures from 200 to 550°C. Figure 10.12a, b are typical RHEED patterns for GaSb nanodots formed by codeposition of 15 ML GaSb at 300°C and of 30 ML GaSb at 450°C, respectively. STM images in Fig. 10.12c, d correspond to the samples shown in Fig. 10.12a, b. These results demonstrate that the nanometer-sized nanodots were epitaxially grown with the same crystal orientation as that of the Si substrates. The weak spots in Fig. 10.12b indicated by arrows are observed at one-third the distance between the GaSb diffraction spots, indicating the existence of a twin crystal of GaSb. STM images also revealed that faceted nanodots with an average base length L of ~30 nm were formed at high temperature (Fig. 10.12d) and that small hemispherical nanodots ($L \leq \sim 10$ nm) were formed at temperatures lower than ~300°C (Fig. 10.12c). The densities of formed nanodots are shown in Fig. 10.12e, which demonstrates that the density of nanodots formed using this method was higher than that for VW-type GaSb nanodots on Si ($\sim 10^8$ cm^{-2}) [44]. The densities are thought to be determined by Ga atom diffusion lengths on the ultrathin SiO_2 films before being captured by the Ge nuclei [50].

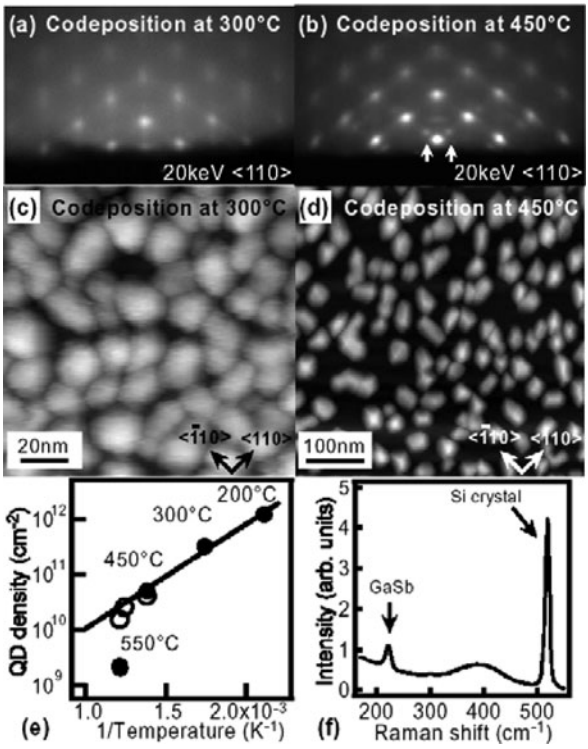

Fig. 10.12 RHEED patterns of GaSb nanodots formed by codeposition (**a**) of 15 ML GaSb at 300°C and (**b**) of 30 ML GaSb at 450°C. (**c**) and (**d**) STM images corresponding to (**a**) and (**b**), respectively. (**e**) Temperature dependence of densities of the formed nanodots (*solid circles*) and nanodot density estimated from Ga diffusion length on ultrathin SiO_2 surface (*open circles*). (**f**) Raman spectrum from the nanodots in (**d**)

With a decrease in the codeposition temperature, the spot patterns in RHEED became obscure as shown in Fig. 10.12a, b, indicating degradation in nanodot crystallinity. On the other hand, when the codeposition temperature was reduced, the nanodot density continuously increased to $3 \times 10^{11}\,\mathrm{cm}^{-2}$ at 300°C and the ultrahigh density ($\sim 1 \times 10^{12}\,\mathrm{cm}^{-2}$) at 200°C as shown in Fig. 10.12e. Figure 10.12f is Raman spectra for GaSb nanodots corresponding to Fig. 10.12b, d. The sharp peak related to Si crystal phonons near $520\,\mathrm{cm}^{-1}$ and the broad peak around $400\,\mathrm{cm}^{-1}$ also appeared for the Si substrates without GaSb nanodots, indicating that the sharp peak at $223\,\mathrm{cm}^{-1}$ is related to GaSb nanodots. This peak at $223\,\mathrm{cm}^{-1}$ was assigned to the transverse optical (TO) mode in GaSb nanodots from the TO mode in the GaSb bulk ($223.6\,\mathrm{cm}^{-1}$) [51]. The peak positions were independent of the amount of GaSb nanodots deposited in our experiment. The close peak positions of the nanodots and the bulk indicate that the lattice mismatch strains with Si almost relaxed in the nanodots. This was also confirmed by comparing RHEED spot spacings in Fig. 10.12b with those of homoepitaxial Si nanodots [14].

10.3.6 Optical Properties of GaSb Nanodots

We measured the PL of the 65 ML nanodots formed at various codeposition temperatures, as shown in Fig. 10.13. Only nanodots formed at 450°C were kept at 450°C for 30 min in Sb flux after nanodot formation to improve the nanodot crystallinity. All spectra showed the GaSb-related peak in the low-energy range of 0.75–0.85 eV in addition to several Si-related sharp peaks in the range of 1.0–1.1 eV. The PL spectra for the GaSb films were highly dependent on the formation method [52, 53]. Using our formation method, the low-energy peaks were positioned at ~0.76 eV for nanodots (or films) larger than 200 ML nanodots. Hence, the low-energy peak in the GaSb formed using our method was assigned to the optical transition between the GaSb conduction band and the acceptor, which fits the known optical properties of the GaSb bulk at 4.2 K [54]. It should also be noted that the nanodots formed at the higher temperature of 450°C showed higher PL intensity, which had higher crystallinity but lower density.

Figure 10.14 shows a the cross-sectional TEM image, (b) the high-resolution transmission electron microscope (HRTEM) image, (c) the RHEED pattern, and (d) the STM image of the 65 ML nanodots formed by codeposition and subsequently keeping the sample temperatures at 450°C for 30 min in Sb flux, which corresponds to the upper PL spectrum in Fig. 10.13. These results demonstrated that epitaxial nanodots were faceted as various shapes with L of ~80 nm and their aspect ratios (height/base length) were ~0.5. The HRTEM images revealed that the ultrathin SiO_2 films remained at the interfaces between the nanodots and Si substrates, as indicated by the arrow. Lines with bright contrast showing lattice defects were observed in HRTEM image as indicated by "SF" in Fig. 10.14b. These were twinning boundaries caused by stacking faults (SF) in the nanodots and do not influence the strain state in nanodots. The existence of the twin crystal in nanodots is consistent with the twin crystal spots in the RHEED patterns.

STM images showed the nanodot density to be 5×10^9 cm^{-2}, revealing that the process of keeping the sample temperatures at 450°C reduced the nanodot density

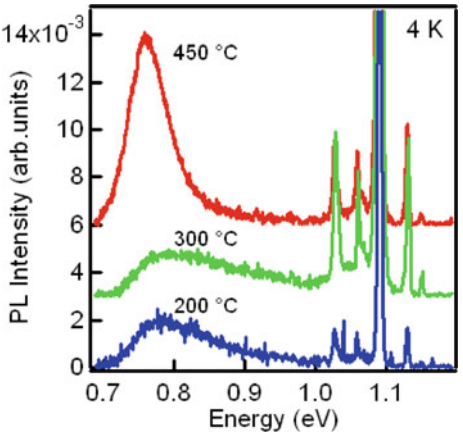

Fig. 10.13 PL spectra from 65 ML nanodots formed at various codeposition temperatures

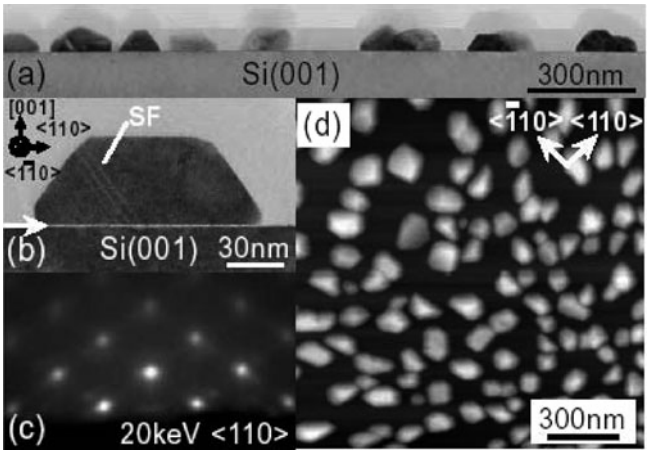

Fig. 10.14 (**a**) Cross-sectional TEM image, (**b**) high-resolution TEM image of GaSb nanodots, (**c**) RHEED pattern, and (**d**) STM image of 65 ML nanodots formed by codeposition at 450°C and subsequently keeping at 450°C for 30 min in Sb flux

when compared with the nanodots that had not undergone this process (Fig. 10.12d). We changed the GaSb deposition amount from 1 to 200 ML and some results are shown as STM images in Fig. 10.15a, b. As a result, L changed from 17 to ~100 nm and the nanodot density ($5 \times 10^9\,\mathrm{cm}^{-2}$) was unchanged. The PL spectra for these nanodots of various sizes were measured, as shown in Fig. 10.15c. The relation between the peak position and L in the inset of Fig. 10.15c shows the PL peak blue-shifted with the decrease of the nanodot size.

In our experiment, the nanodots were sandwiched by a vacuum and the SiO_2 films forming the type I structure. The void size in the SiO_2 films beneath the nanodots is so small that the SiO_2 films can work as a confinement barrier for the carriers in the nanodots [16, 37]. The hard wall square potential model is considered to be reasonable because these two barriers are high enough (a few electron volts). For an isotropic system, such as spherical nanodots with a radius r, therefore, PL energy E_{confined} is easily described as

$$E_{\mathrm{confined}}(L) = E_{\mathrm{bulk}} + \frac{h^2\pi^2}{2\mu r^2} \tag{10.2}$$

where E_{bulk} is PL energy for bulk material and μ is the reduced mass of electron and hole. Equation (10.2) can approximately be applied to domed nanodots with an aspect ratio between 1 and 0.3 by replacing r with $L/2$ [37]. In fact, the present nanodots have various anisotropic shapes, which make the formulation of the quantum confinement effect more complicated. The simple model in (10.2), however, represents the essential quantum confinement effect and serves as a good reference. We approximated the present nanodot shape to a dome with an aspect ratio of ~0.5, namely, a hemisphere and calculated the theoretical curve of E_{confined} in (10.2)

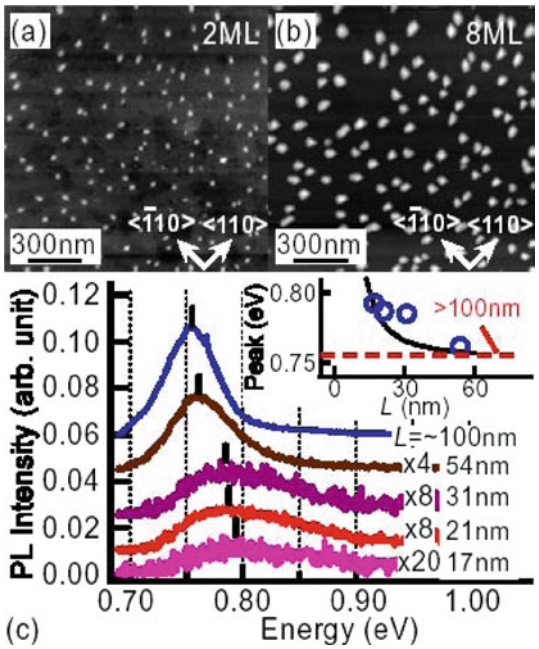

Fig. 10.15 STM images of (**a**) 2 ML and (**b**) 8 ML nanodots. (**c**) PL spectra of the nanodots with average base lengths L of 17, 21, 31, 54 nm. The *inset* shows the size dependence of the PL peak positions (*open circles*) and a theoretical curve plotted using (10.2) (*solid line*)

using $E_{\text{bulk}} = 0.76\,\text{eV}$ at 4.2 K (the energy of the optical transition between the GaSb conduction band and the acceptor), $\mu = 0.036m_0$ [54], and $r = L/2$ ($\approx$ the nanodot height), as shown by the solid line in the inset of Fig. 10.15c. We neglected the strain effect on the energy band gap because, from Raman spectroscopy results, all the present nanodots were found to have similarly small strains. The inset in Fig. 10.15c shows the results of the experiment were consistent with the theoretical curve, indicating that the nanodot size dependence of the PL peak position was due to the quantum confinement effect.

10.3.7 Application to Growth of GaSb Thin Films

The GaSb nanodots on ultrathin SiO_2 films have bulk lattice constant as described in Sect. 3.6, indicating that the lattice mismatch strains are almost relaxed in the nanodots due to the small contact areas on Si substrates. This implies that the GaSb nanodots can be used as seeding crystals for the growth of GaSb thin films on Si substrates. Figure 10.16a shows an STM image of the GaSb nanodots grown at the substrate temperature of 200°C with the size of $\sim$8 nm and density of $\sim 10^{12}\,\text{cm}^{-2}$. Gallium and Sb with $\sim$23 nm thickness were subsequently codeposited at 200°C on

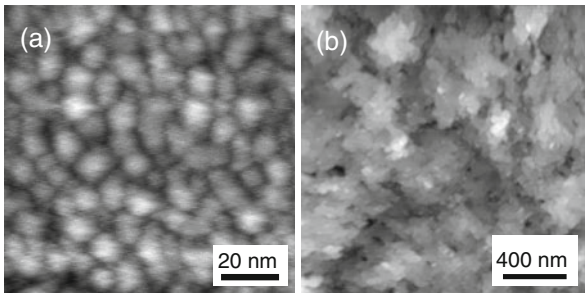

Fig. 10.16 (**a**) STM image of the GaSb nanodots grown at the substrate temperature of 200°C. (**b**) STM image of the sample after Ga and Sb with ~23 nm thickness were subsequently codeposited at 200°C and then, Ga and Sb with ~71 nm thickness were codeposited at 450°C

this surface. Then, Ga and Sb with ~71 nm thickness were further codeposited at 450°C. Figure 10.16b shows an STM image of the sample surface. The root mean square roughness (h_{rms}) of the surface is about 4 nm, that is, very small compared with that of the films grown by other methods [39–41]. RHEED patterns from this surface revealed that the GaSb film epitaxially grew with the same crystallographic orientations as those of the Si substrate.

Figure 10.17 shows a cross-sectional TEM images near the interface between the grown GaSb film and Si(001) substrate. The white horizontal line in the image indicates that the ultrathin SiO_2 film still remains at the interface. The inset is a high-magnification TEM image of the square area. The lattice image reveals that the strains caused by the lattice mismatch (~12.2 %) are almost relaxed just at the interface due to the ultrathin SiO_2 film. This result demonstrates a new technique to grow thin films on Si substrates even when the lattice mismatches are large.

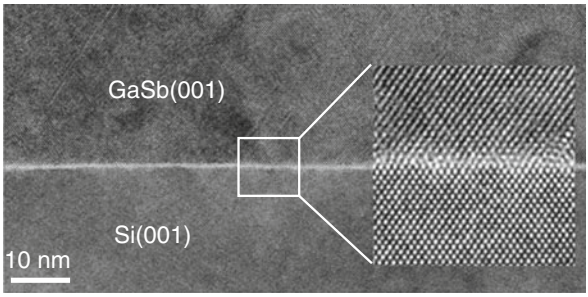

Fig. 10.17 Cross-sectional TEM images near the interface between the GaSb film and Si(001) substrate of the sample in Fig. 10.16b. The *inset* is a high-magnification TEM lattice image of the square area

10.4 Summary

We developed a method to form semiconductor nanodots on Si substrates by using ultrathin Si oxide technology and reported some results on their electronic and optical properties. We could form ultrasmall semiconductor nanodots with the size of $\sim$5 nm and ultrahigh density of $\sim 10^{12}\,\mathrm{cm}^{-2}$ on Si surfaces covered with ultrathin SiO_2 films of $\sim$0.3 nm thickness. We described electronic properties of the GeSn nanodots on Si substrates and optical properties of Ge and GeSn nanodots embedded in Si films, and those of GaSb nanodots on Si substrates. These structures exhibited clear quantum confinement effects at room temperature and intense PL and EL intensities in the energy region of about 0.8 eV that is of practical importance for optical fiber communication systems.

We also reported that the ultrathin SiO_2 technology could be applied to grow thin films on Si substrates even when the lattice mismatches between Si and thin films were large.

Acknowledgments We would like to thank Dr. Y. Nakamura of Osaka University and Dr. A. A. Shklyaev of The Institute of Semiconductor Physics, Novosibirsk, for their collaboration, and Prof. N. Tanaka and Dr. S.-P. Cho of Nagoya University for scanning transmission electron microscope observations. This work was partly supported by JSPS.KAKENHI (20360015).

References

1. M. Henini (ed.), *Handbook of Self Assembled Semiconductor Nanostructures for Novel Devices in Photonics and Electronics* (Elsevier, Amsterdam, 2008)
2. Y. Shiraki, A. Sakai, Fabrication technology of SiGe hetero-structures and their properties. Surf. Sci. Rep. **59**, 153 (2005)
3. K. Brunner, Si/Ge nanostructures. Rep. Prog. Phys. **65**, 27 (2002)
4. O.G. Schmidt (ed.), *Nanoscience and Technology: Lateral Alignment of Epitaxial Quantum Dots* (Springer, Heidelberg, 2007)
5. A.A. Shklyaev, M. Shibata, M. Ichikawa, High-density ultrasmall epitaxial Ge islands on Si(111) surfaces with a SiO_2 coverage. Phys. Rev. B **62**, 1540 (2000)
6. A.A. Shklyaev, M. Ichikawa, Extremely dense arrays of germanium and silicon nanostructures. Physics-Uspekhi **51**, 133 (2008)
7. A. Barski, M. Derivaz, J.L. Rouviere, D. Buttard, Epitaxial growth of germanium dots on Si(001) surface covered by a very thin silicon oxide layer. Appl. Phys. Lett. **77**, 3541 (2000)
8. I. Berbezier, A. Karmous, A. Ronda, A. Sgarlata, A. Balzarotti, P. Castrucci, M. Scarselli, M. De Crescenzi, Growth of ultrahigh-density quantum-confined germanium dots on SiO_2 thin films. Appl. Phys. Lett. **89**, 063122 (2006)
9. N. Miyata, H. Watanabe, M. Ichikawa, Thermal decomposition of an ultrathin Si oxide layer around a Si(001)-(2×1) window. Phys. Rev. Lett. **84**, 1044 (2000)
10. S. Maruno, S. Fujita, H. Watanabe, Y. Kusumi, M. Ichikawa, A combined apparatus of scanning reflection electron microscope and scanning tunneling microscope. Rev. Sci. Instrum. **68**, 116 (1997)
11. H. Watanabe, S. Fujita, S. Maruno, K. Fujita, M. Ichikawa, Electron-beam-induced selective thermal decomposition of ultrathin SiO_2 layers used in nanofabrication. Jpn. J. Appl. Phys. **36**, 7777 (1997)

12. A.A. Shklyaev, M. Ichikawa, Effect of interfaces on quantum confinement in Ge dots grown on Si surfaces with a SiO_2 coverage. Surf. Sci. **514**, 19 (2002)
13. M. Shibata, Y. Nitta, K. Fujita, M. Ichikawa, Pyramidal Si nanocrystals with a quasiequilibrium shape selectively grown on Si(001) windows in ultrathin SiO_2 films. Phys. Rev. B **61**, 7499 (2000)
14. A.A. Shklyaev, M. Ichikawa, Three-dimensional Si islands on Si(001) surfaces. Phys. Rev. B **65**, 045307 (2002)
15. Y. Nakamura, Y. Nagadomi, S.-P. Cho, N. Tanaka, M. Ichikawa, Formation of ultrahigh density and ultrasmall coherent β-$FeSi_2$ nanodots on Si (111) substrates using Si and Fe codeposition method. J. Appl. Phys. **100**, 044313 (2006)
16. Y. Nakamura, K. Watanabe, Y. Fukuzawa, M. Ichkawa, Observation of the quantum-confinement effect in individual Ge nanocrystals on oxidized Si substrates using scanning tunneling spectroscopy. Appl. Phys. Lett. **87**, 133119 (2005)
17. Y. Nakamura, R. Suzuki, M. Umeno, S.-P. Cho, N. Tanaka, M. Ichikawa, Observation of the quantum-confinement effect in individual β-$FeSi_2$ nanoislands epitaxially grown on Si (111) surfaces using scanning tunneling spectroscopy. Appl. Phys. Lett. **89**, 123104 (2006)
18. Y. Nakamura, M. Ichikawa, K. Watanabe, Y. Hatsugai, Quantum fluctuation of tunneling current in individual Ge quantum dots induced by a single-electron transfer. Appl. Phys. Lett. **90**, 153104 (2007)
19. N. Tanaka, S.-P. Cho, A.A. Shklyaev, J. Yamasaki, E. Okunishi, M. Ichikawa, Spherical aberration corrected STEM studies of Ge nanodots grown on Si(001) surfaces with an ultrathin SiO_2 coverage. Appl. Surf. Sci. **254**, 7569 (2008)
20. A.T. Blumenau, R. Jones, S. Oberg, P.R. Briddon, T. Frauenheim, Dislocation related photoluminescence in silicon. Phys. Rev. Lett. **87**, 187404 (2001)
21. A.A. Shklyaev, S. Nobuki, S. Uchida, Y. Nakamura, M. Ichikawa, Photoluminescence of Ge/Si structures grown on oxidized Si surfaces. Appl. Phys. Lett. **88**, 121919 (2006)
22. A.A. Shklyaev, S.-P. Cho, Y. Nakamura, N. Tanaka, M. Ichikawa, Influence of growth and annealing conditions on photoluminescence of Ge/Si layers grown on oxidized Si surfaces. J. Phys. Condens. Matter **19**, 136004 (2007)
23. M. Ichikawa, S. Uchida, A.A. Shklyaev, Y. Nakamura, S.-P. Cho, N. Tanaka, Characterization of semiconductor nanostructures formed by using ultrathin Si oxide technology. Appl. Surf. Sci. **255**, 669 (2008)
24. A.A. Shklyaev, Y. Nakamura, F.N. Dultsev, M. Ichikawa, Defect-related light emission in the $1.4-1.7\,\mu m$ range from Si layers at room temperature. J. Appl. Phys. **105**, 063513 (2009)
25. D.W. Jenkins, J.D. Dow, Electronic properties of metastable Ge_xSn_{1-x} alloys. Phys. Rev. B **36**, 7994 (1987)
26. K.A. Mader, A. Baldereschi, H. von Kanel, Band structure and instability of $Ge_{1-x}Sn_x$ alloys. Solid State Commun. **69**, 1123 (1989)
27. G. He, H.A. Atwater, Interband transitions in Sn_xGe_{1-x} alloys. Phys. Rev. Lett. **79**, 1937 (1997)
28. H.P.L. de Guevara, A.G. Rodríguez, H. Navarro-Contreras, M.A. Vidal, Determination of the optical energy gap of $Ge_{1-x}Sn_x$ alloys with $0 < x < 0.14$. Appl. Phys. Lett. **84**, 4532 (2004)
29. O. Gurdal, P. Desjardins, J.R.A. Carlsson, N. Taylor, H.H. Radmson, J.-E. Sundgren, J.E. Greene, Low-temperature growth and critical epitaxial thicknesses of fully strained metastable $Ge_{1-x}Sn_x$($x \lesssim 0.26$) alloys on Ge(001)2×1. J. Appl. Phys. **83**, 162 (1998)
30. R. Ragan, H.A. Atwater, Measurement of the direct energy gap of coherently strained Sn_xGe_{1-x}/Ge(001) heterostructures. Appl. Phys. Lett. **77**, 3418 (2000)
31. H.P.L. de Guevara, A.G. Rodríguez, H. Navarro-Contreras, M.A. Vidal, $Ge_{1-x}Sn_x$ alloys pseudomorphically grown on Ge(001). Appl. Phys. Lett. **83**, 4942 (2003)
32. V.R. D'Costa, C.S. Cook, A.G. Birdwell, C.L. Littler, M. Canonico, S. Zollner, J. Kouvetakis, J. Menéndez, Optical critical points of thin-film $Ge_{1-y}Sn_y$ alloys: A comparative $Ge_{1-y}Sn_y/Ge_{1-x}Si_x$ study. Phys. Rev. B **73**, 125207 (2006)
33. Y.M. Niquet, G. Allan, C. Delerue, M. Lannoo, Quantum confinement in germanium nanocrystals. Appl. Phys. Lett. **77**, 1182 (2000)

34. T. Bostedt, Van Buuren, T.M. Willey, N. Franco, L.J. Terminello, C. Heske, T. Möller, Strong quantum-confinement effects in the conduction band of germanium nanocrystals. Appl. Phys. Lett. **84**, 4056 (2004)
35. Y. Nakamura, A. Masada, S.-P. Cho, N. Tanaka, M. Ichikawa, Epitaxial growth of ultrahigh density $Ge_{1-x}Sn_x$ quantum dots on Si (111) substrates by codeposition of Ge and Sn on ultrathin SiO_2 films. J. Appl. Phys. **102**, 124302 (2007)
36. Y. Nakayama, K. Takase, T. Hirahara, S. Hasegawa, T. Okuda, A. Harasawa, I. Matsuda, Y. Nakamura, M. Ichikawa, Quantum-size effect in uniform Ge–Sn alloy nanodots observed by photoemission spectroscopy. Jpn. J. Appl. Phys. **46**, L1176 (2007)
37. Y. Nakamura, A. Masada, M. Ichikawa, Quantum-confinement effect in individual $Ge_{1-x}Sn_x$ quantum dots on Si(111) substrates covered with ultrathin SiO_2 films using scanning tunneling spectroscopy. Appl. Phys. Lett. **91**, 013109 (2007)
38. Y. Nakamura, N. Fujinoki, M. Ichikawa, Photoluminescence from Si-capped GeSn nanodots on Si substrates formed using an ultrathin SiO_2 film technique. J. Appl. Phys. **106**, 014309 (2009)
39. K. Akahane, N. Yamamoto, S. Gozu, N. Ohtani, Heteroepitaxial growth of GaSb on Si(001) substrates. J. Cryst. Growth **264**, 21 (2004)
40. K. Akahane, N. Yamamoto, S. Gozu, N. Ohtani, High-quality GaSb/AlGaSb quantum well grown on Si substrate. Jpn. J. Appl. Phys. **44**, L15 (2005)
41. G. Balakrishnan, A. Jallipalli, P. Rotella, S. Huang, A. Khoshakhlagh, A. Amtout, S. Krishna, L.R. Dawson, D.L. Huffaker, Room-temperature optically pumped (Al)GaSb vertical-cavity surface-emitting laser monolithically grown on an Si(100) substrate. IEEE J. Sel. Top. Quantum Electron. **12**, 1636 (2006)
42. F. Hatami, N.N. Ledentsov, M. Grundmann, J. Böhrer, F. Heinrichsdorff, M. Beer, D. Bimberg, S.S. Ruvimov, P. Werner, U. Gösele, J. Heydenreich, U. Richter, S.V. Ivanov, B.Ya. Meltser, P.S. Kop'ev, Zh. I. Alferov, Radiative recombination in type-II GaSb/GaAs quantum dots. Appl. Phys. Lett. **67**, 656 (1995)
43. E. Alphandéry, R.J. Nicholas, N.J. Mason, S.G. Lyapin, P.C. Klipstein, Photoluminescence of self-assembled InSb quantum dots grown on GaSb as a function of excitation power, temperature, and magnetic field. Phys. Rev. B **65**, 115322 (2002)
44. K. Akahane, N. Yamamoto, S. Gozu, A. Ueta, N. Ohtani, Initial growth stage of GaSb on Si(001) substrates with AlSb initiation layers. J. Cryst. Growth **283**, 297 (2005)
45. M. Jo, N. Yasuhara, K. Ishida, K. Kawamoto, S. Fukatsu, Highly efficient radiative recombination of electron–hole pairs localized at compound semiconductor quantum dots embedded in Si. Phys. E **21**, 354 (2004)
46. M. Jo, K. Ishida, N. Yasuhara, Y. Sugawara, K. Kawamoto, S. Fukatsu, A Si-based quantum-dot light-emitting diode. Appl. Phys. Lett. **86**, 103509 (2005)
47. C.G. Vande Walle, Band lineups and deformation potentials in the model-solid theory. Phys. Rev. B **39**, 1871 (1989)
48. Y. Nakamura, T. Sugimoto, M. Ichikawa, Formation and optical properties of GaSb quantum dots epitaxially grown on Si substrates using an ultrathin SiO_2 film technique. J. Appl. Phys. **105**, 014308 (2009)
49. S.-P. Cho, S. Kawano, N. Tanaka, In situ monitoring of nucleation and evolution of Ge nanodots on faintly oxidized Si(111) surfaces. Appl. Surf. Sci. **254**, 7868 (2008)
50. M. Shibata, S.S. Stoyanov, M. Ichikawa, Selective growth of nanometer-scale Ga dots on Si(111) surface windows formed in an ultrathin SiO_2 film. Phys. Rev. B **59**, 10289 (1999)
51. K. Aoki, E. Anastassakis, M. Cardona, Dependence of Raman frequencies and scattering intensities on pressure in GaSb, InAs, and InSb semiconductors. Phys. Rev. B **30**, 681 (1984)
52. M. Lee, D.J. Nicholas, K.E. Singer, B. Hamilton, A photoluminescence and Hall – effect study of GaSb grown by molecular – beam epitaxy. J. Appl. Phys. **59**, 2895 (1986)
53. D.J. Nicholas, M. Lee, B. Hamilton, K.E. Singer, Spectroscopic studies of shallow defects in MBE GaSb. J. Cryst. Growth **81**, 298 (1987)
54. P.S. Dutta, H.L. Bhat, V. Kumar, The physics and technology of gallium antimonide: An emerging optoelectronic material. J. Appl. Phys. **81**, 5821 (1997)

Chapter 11
Step Bunching on Silicon Surface Under Electromigration

S.S. Kosolobov and A.V. Latyshev

Abstract In situ ultra high vacuum reflection electron microscopy studies of structural and morphological transformations of silicon surface at condition of sample heating by direct electric current are reviewed. The kinetic instability of the diffusion-linked atomic steps affected by electromigration of adsorbed atoms on atomically clean and gold-deposited silicon (111) surface is studied in temperature range between 850 and 1350°C. Consequent changes of the silicon surface morphology during thermal annealing and gold adsorption were observed as reversible redistribution of regular atomic steps to step bunches and vice versa. Peculiarities of the atomic mechanism of the such morphological transitions observed on atomically clean and gold-deposited silicon surface at enhanced temperatures are discussed.

11.1 Introduction

The use of quantum effects in semiconductor nanostructures demands to solve problems associated with the fabrication of perfect crystals, thin films, heteroepitaxial multilayers, and low-dimensional structures. Knowledge of the fundamentals of the structural processes during synthesis of new materials is a key factor for controlled fabrication of highly perfect modulated structures, superlattices, and low-dimensional systems (quantum wires and quantum dots). The major problem is the analysis of the basic physical features of growth and defect formation in such systems with the purpose of goal-directed control of these processes.

Theory of crystal growth, developed in 1930 by I. Stranski and R. Kaishew, stimulated progress for fundamental condensed material physics and modern epitaxial technology [1, 2]. Atomic processes on a crystal surface are attracting the very close attention of researchers, not only because this clarifies the physical picture of structural processes on the surface but also because this offers the possibility of

S.S. Kosolobov (✉)
Institute of Semiconductor Physics, Siberian Branch, Russian Academy of Sciences, pr. Lavrent'eva 13, Novosibirsk, 630090 Russia
e-mail: kosolobov@thermo.isp.nsc.ru

M. Michailov (ed.), *Nanophenomena at Surfaces,* Springer Series in Surface Sciences 47,
DOI 10.1007/978-3-642-16510-8_11,

practical development of novel surface nanoobjects in which quantum effects can be observed.

In studies of the surface and bulk structure of crystalline objects, the most complete and adequate information is obtained by various methods of electron and scanning probe microscopies. These methods make it possible to study the structure of the surface, bulk, and interface at an atomic level by means of direct resolution of the atomic structure. The use of mutually complementary high-resolution diagnostic methods adapted to materials under study, in combination with unique objects of analysis, gives us new knowledge on their structure, morphology, defect formation and will extend the possibility of controlling the structural quality of epitaxial and low-dimensional systems [3].

An important aspect of contemporary and future technologies is the design of novel materials with tailored properties. Such new materials are produced using atomic assembly methods, which allow controlled association of atoms into isolated nanoclusters, layer-by-layer growth of various coatings, self-assembly, and self-ordering of nanoobjects. In this case, understanding of atomic-level structural reactions is of primary and crucial importance in the development of low-dimensional systems with quantum-size electronic properties. To solve such problems, high-resolution methods of nanomaterial characterization should be developed, preferably in situ diagnostic during nanostructure formation [4, 5].

Structural perfection and properties of stepped Si(111) surfaces depend crucially on the surface roughness that basically defined by spatial distribution of atomic steps. Generally the step allocation may be altered through surface morphology instability due to thermodynamic or kinetic reasons [6]. Thermodynamic instability deals with adsorption of impurity atoms on the surface, which may change the surface energy producing surface reconstruction, faceting, and/or step bunching. Atomic step distribution can be also changed during superstructural phase transitions. For example, during the $(1 \times 1) \Leftrightarrow (7 \times 7)$ phase transition that takes place on clean Si(111) surface at 830°C, atomic step shifts due to changing of the adatom density at the terraces [7]. During submonolayer deposition of foreigner atoms on Si(111) the formation of new surface phases occurs too. It was shown that nucleation and growth of the superstructural domains also can modify atomic step distribution forming step bunches. Detailed investigation of instability of the silicon (111) surface morphology induced by polycentric nucleation of reconstructed domains at adsorption of Ge [8], Au [9, 10], Ca [11], and Cu [12, 13] indicates that step bunching occurs during enlarging the reconstructed domains longer than the step–step width. Similar step bunching occurs during the $(1 \times 1) \Rightarrow (7 \times 7)$ transition on clean Si(111) surface on cooling when reconstructed domains cover non-uniformly the stepped surface [14].

The dramatic changes in step spatial distribution on Si(111) surface governed by direct electric current used for sample heating have been revealed first by Latyshev et al. [15] and latter confirmed by many others [16–20] and discussed theoretically in detail [21–26]. They have investigated in detail the kinetic instability of atomic steps on silicon surface during sublimation caused by direct electrical current heating. As a result of this instability the reversible transition from regular steps (RS) to step

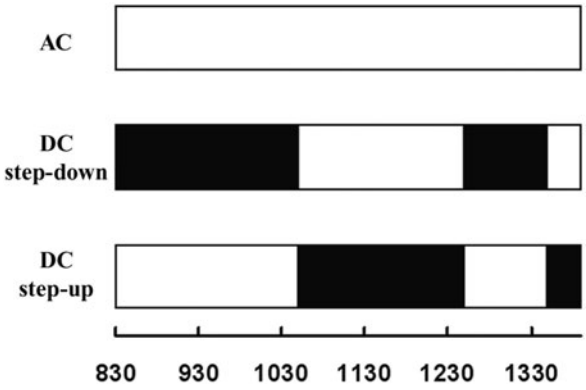

Fig. 11.1 Schematic representation of the step-bunching temperature ranges for different directions and types of the heating electrical current. *White areas* correspond to the regular steps and *dark areas* relate to the step bunches on the surface

bunches (SB) was observed on the silicon (111) surface. This RS⇔SB transition is dependent on the direction of the heating direct current (DC) and the sample temperature for the same direction of the heating current. This nontrivial dependence is shown schematically in Fig. 11.1. Dark areas correspond to the silicon surface morphology with step bunches and white areas appropriate to the regular distributed atomic steps on the surface. So DC heating of silicon crystal can drastically change atomic steps spatial distribution on the surface at elevated temperatures.

The size (the number of steps in the bunch) of step bunch is increased with the time of DC heating. For the sample heating by an alternative current with a frequency higher than 1 Hz, an uniformly stepped Si(111) surface was stable at any temperatures [27]. It should be pointed out that the origin of surface electromigration of silicon adatoms that seems to be responsible for step-bunching phenomena on silicon surface is still under discussion in spite of mutual experimental verifications.

Thus, there are at least two markable instabilities of the Si(111) surface: step bunching induced by electromigration at sublimation (at high temperature) and step bunching induced by surface reconstruction initiated by metal adsorption (at low temperature). While the importance of these instabilities is obvious and a lot of papers deal with detailed studies of step bunch instabilities, there is restricted number of investigations on the influence of the adsorbed atoms on step bunching at sublimation probably due to problems of carrying out in situ experiments at high temperatures.

It was reported that submonolayer gold adsorption has strong influence on the effect of step bunching during sublimation [28, 29]. Gold deposition of 0.003 ML on Si(111) at 950°C changed atomic step behavior. Step bunches, which usually observed at this temperature on clean silicon surface when the direct current flows in the step-down direction, dissolved in the system of regular steps after submonolayer gold deposition. On the contrary, when the direct electrical current flowed in the

step-up direction, the formation of step bunches was observed on the gold-deposited surface.

Recently the formation of new type of the step instability, called as a periodic step density wave, was reported after gold deposition on a high misoriented Si(111) surface [30–32]. After 0.3 ML of gold deposition on Si(111) and in the case of the step-up heating current direction, periodic array of extremely straight step bunches formed on the surface, whereas it had not been observed on clean Si(111).

In order to clarify the influence of gold on the surface morphology, we have investigated precisely atomic step distribution on Si(111) in wide temperature range (830–1260°C) at various gold coverage (0–0.7 ML) and different directions of the heating current (step-up and step-down). For surface instability experiments the gold was chosen because (i) adsorption of gold on silicon surface is well studied at least at temperatures below 800°C, (ii) gold has high melting temperatures, (iii) gold does not form gold silicide at enhance temperatures, and (iv) gold is a well-known surfactant for silicon substrate.

11.2 UHV Reflection Electron Microscopy

In situ observations of silicon surface morphology were performed using a reflection electron microscope (UHV REM) with an ultra high vacuum chamber. Detailed construction of the electron microscope was described previously [33]. REM is highly sensitive to surface structural elements and provides spatial resolution sufficient to visualize individual monatomic steps (0.31 nm high on Si(111) and 0.14 nm on Si(001)), two-dimensional islands, and superstructural domains even at high temperatures (e.g., 1300°C). The UHV REM system includes a differential cryogenic pumping device that provides an ultra high vacuum in the sample region and allows sample heating and cooling from liquid-nitrogen to melting temperatures; it is possible to deposit atoms of various elements from molecular beams onto the surface under study [34].

The samples, $8 \times 1 \times 0.3\ \mathrm{mm}^3$ in size, were cut from a nominally flat (111) silicon wafer with an average interstep distance of 100 nm. After cutting procedure, atomic steps were oriented perpendicular to the long side of the sample and the direction of the electron beam incidence was parallel to the step edge. Before installation into the microscope, the specimen was cleaned and chemically etched by ordinary treatments. After chemical treatments the sample was mounted to a holder and placed into the sample chamber. Then, the sample was outgassed in a UHV microscope chamber at the temperature about 900°C for several minutes. As the most convenient way the clean Si(111) surfaces were prepared by typical flashing to 1250°C in the UHV chamber of the microscope. The sample holder was designed for providing electrical current heating and rotating of the sample in azimuth and Bragg's planes. Before each experiment the sample was cleaned in the UHV chamber by several flash heating up to 1300°C for several minutes. After cleaning procedures, no any pinning centers for the motion of the atomic steps during sublimation were visualized. Moreover, the superstructural phase transition $(7 \times 7) \Leftrightarrow (1 \times 1)$ was observed

at 830°C at RHEED pattern that indirectly argues to atomic cleanness of the surface. To reduce a thermal drift, the specimen was kept at 900–1050°C about 30 min. After final cleaning treatments, the atomic steps without any pinning centers associated with the particles of contamination have been observed reproducibly in REM images [35].

For providing gold deposition, a small-sized gold evaporator, a wolfram crucible, was placed against the sample face. The amount of deposited gold measured in units of monolayer (1 ML$\approx 1.6\times 10^{15}$ atoms/cm^2) was monitored with time of applied current calibrated previously by the Au/Si(111) surface phase diagram known from other studies. The step transformations were analyzed with REM in imaging and diffraction modes at high temperatures and in real time due to video recorder system made by GATAN to picture quick surface reactions. It should be pointed out that recorded REM images are foreshortened by a factor of $\sim$1/50 in the direction of the electron beam incidence due to a small angle between surface and electron beam.

11.2.1 Monatomic Steps on Silicon Surface

Figure 11.2 represents REM image of atomically clean vicinal silicon (111) surface at 900°C after thermal annealing in a UHV chamber of a reflection electron microscope. White arrow indicates the direction of the electron beam incidence. Thin dark wavy lines at the image are atomic steps, 0.31 nm in height. The atomic step contrast in REM images is a superposition of two contrast types, i.e., diffraction and phase. The diffraction (Bragg) contrast is caused by deformed regions of the atomic lattice near monatomic steps, which locally change the diffraction conditions on steps. The phase (Fresnel) contrast is caused by the phase shift of electrons reflected from adjacent atomic planes separated by a monatomic step.

Atomic steps move over the crystal surface during sublimation, which is caused by atomic step generation into an adsorption layer from which atoms are detached into the vapor phase. Evaporation of a single monolayer displaces each step for a distance equal to the distance to the adjacent step [36]. The step motion is initiated by consequent detachment from the step, diffusion along the step, diffusion on the terraces, and subsequent evaporation of the silicon atoms during sublimation. The step rate depends on the terrace width with the sublimation energy of $\approx$4.2 eV [35, 37].

Atomic step distribution on the surface was not unchangeable during crystal evaporation. As it was described above, steps distribution was unstable upon fluctuations of the terrace width in the case of electrical current heating of the crystal [15]. In the case of the step-down DC direction, regular distribution of atomic steps was broken and formation of the step-bunched morphology was observed at 900°C (Fig. 11.2b). The redistribution of regular steps to step bunches and vice versa was observed after switching the electrical current direction. Increasing the sample temperature caused enhancing step mobility and redistribution of the atomic steps occurred faster. In the case of alternative electrical current (AC) heating the system of regular steps was stable on clean silicon (111) surface at any temperature.

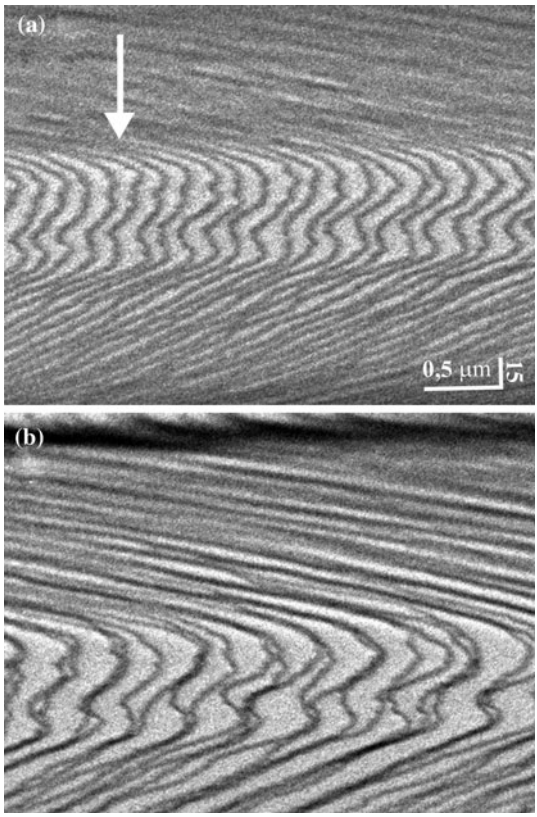

Fig. 11.2 Typical REM images of clean Si(111) surface at 900°C with regular atomic steps (**a**) and initial stage of step bunches (**b**)

Using UHV REM, the conditions under which atomically clean silicon surfaces form were optimized for ultra high vacuum technologies. Data were obtained on the surface structure and motion kinetics of monatomic steps that control diffusion processes on the surface and interfaces, on homogeneous and heterogeneous sources of monatomic steps, which are efficient sinks for adatoms on the surface of semiconductor substrate.

The interaction of monatomic steps with dislocations emerging at the crystal surface was detected, which slows down the step motion velocity in the dislocation strain field up to stopping of the step in the dislocation core [38, 39].

It has been found experimentally that there are different probabilities of adatom incorporation into the monatomic step from the side of upper and lower terraces, which is caused by different energy barriers for adatom incorporation into the step. It follows from the kinetics of monatomic step motion during sublimation that the energy barrier for adatom incorporation into the step from the side of the lower terrace is lower by 0.3 ± 0.1 eV than the barrier from the side of the upper terrace.

To control the substrate micromorphology, it seems important to detect self-assembly effects in the system of monatomic steps, which are accompanied by the formation of step bunches during sublimation and heteroepitaxial growth. The detected instability of the system of monatomic steps on the silicon (111) surface during sublimation, which is a necessary operation of thermal cleaning of the substrate, leads to redistribution of the regular system of monatomic steps into a system of step bunches, which consist of close monatomic steps and almost singular regions between bunches. A typical image of the initial stage of step bunch formation is shown in Fig. 11.2b. Step bunches are separated by surface areas with a low density of steps. The conditions of step bunch formation were studied, and the factors affecting the temperature ranges of step bunch formation were determined.

The effect of the direction of a direct electric current that heats the studied crystal on the temperature ranges of step bunching was detected. This effect deals with the transition from the regular system to step bunches and vice versa as the polarity changes. This suggests the existence of an effective charge of adatoms, caused by ionization of adatoms and the effects of adatom drag by carriers in semiconductors [40]. It seems important to use this phenomenon on vicinal silicon surfaces to form various self-assembled systems without lithography, including ordered systems of step bunches, and stripes of impurity-induced superstructures along step bunches and lateral surface superlattices.

It appears that a significant advantage of the UHV REM method is the possibility of obtaining quantitative data on atomic processes on the surface by analyzing the behavior of monatomic steps, including the characteristic time of quasi-equilibration, and the diffusion length and concentration of adsorbed atoms [41]. Conditions of implementation of both step-layer growth and growth by the formation of two-dimensional islands, i.e., the so-called two-dimensional quantum dots, during epitaxy were determined [42]. It was found that the silicon (111) surface with (1×1) structure above the phase transition temperature is not geometrically flat and contains disordered adatom clusters with a filling factor of 0.2 monolayers [7].

Direct evidence of the existence of an disordered layer of mobile adatoms on the silicon (111) face were obtained based on a quantitative study of the reflection high-energy electron diffraction (RHEED) patterns and an analysis of high-temperature scanning tunneling microscopy (STM) images [43, 44]. We note that the increased adatom concentration on the substrate changes the critical parameters for new-phase nucleation, which is of practical interest for the formation of nanoclusters with tailored volume and density.

Heteroepitaxial growth of a new epitaxial film is accompanied by superstructural transformations on the surface. Therefore, we comprehensively analyzed a reconstruction and showed that superstructural domain formation during reversible phase transitions is accompanied by reversible displacements of monatomic steps. In particular, we detected macrostep formation in superstructural phase transitions $(7\times7)\Leftrightarrow(1\times1)$ on the clean silicon (111) surface [45] and during the formation of impurity-induced superstructures Si(7×7)Ge, Si(5×5)Ge, Si(5×2)Au, Si(3×1)Ca at the initial stages of heteroepitaxial growth [9, 11]. The basic conditions of macrostep formation are polycentric nucleation of domains of a new surface

structure and diffusion of adatoms between domains. The density of macrosteps depends on the initial distance between monatomic steps, the substrate temperature, the superstructural transition rate, and it is controlled by kinetic limitations associated with the necessity of significant mass transfer over the surface [46].

Control of germanium monolayer formation on the step silicon (111) surface makes it possible to provide conditions for the growth of regular lateral superlattices, in which germanium strips along the monatomic steps of the surface alternate with silicon surface strips [35]. A major factor complicating lateral superlattice formation during germanium submonolayer deposition onto the silicon surface is the clustering of monatomic steps of the substrate during polycentric nucleation of the reconstructed domains induced by germanium [8].

To optimize the technological processes of the oxidation of a nanostructured object, the initial stages of the interaction of oxygen with the silicon (111) surface in the temperature range of 500–900°C were studied [47]. Intensity oscillations of the electron beam specularly reflected from the silicon surface were detected in the case of implementation of the two-dimensional-island mechanism of thermal etching of silicon in a molecular oxygen flow. The activation energy of surface diffusion of vacancies initiated by the interaction of oxygen with silicon was estimated as $1.35 + 0.15$ eV [48].

To improve the silicon substrate morphology, the structure and reconstruction of the silicon (001) surface, i.e., the most commonly used substrate in silicon micro- and nanoelectronics, were studied [49]. It was shown in [45] how the electric current heating of the crystal affects the surface reconstruction processes on the silicon (001) face. Based on quantitative data obtained by analyzing the step motion kinetics and diffusion of an array of adatoms and vacancies on the silicon (001) surface, step bunch formation was detected [16]. Possible models of the effect of electromigration on step-bunching processes are discussed in [50].

Another example of self-assembly is the formation of regular chains of gold clusters along monatomic step bunches [51]. It was shown that there were preferential displacements of three-dimensional gold islands adsorbed on the silicon (111) surface toward an overlying terrace [52]. This phenomenon led to the accumulation and coalescence of gold islands near the upper edge of step bunches. Thus, the mechanism of self-assembly of gold clusters is implemented due to preliminary self-assembly in the system of monatomic steps.

The above data on atomic processes on the silicon surface allowed not only optimization of the conditions for obtaining low-dimensional structures on the basis of conventional silicon technologies, but also created prerequisites for nanostructure formation based on the detected effects of self-assembly on the silicon surface. It seems that such complex multistage processes of bottom-up self-assembly on the size scale will become fundamental in the controlled formation of semiconductor nanostructures for the next-generation nanoelectronic elements and sensorics on a silicon surface. The presented data on atomic processes on the silicon surface lay the groundwork for nanotechnologies for controlled synthesis of silicon nanostructures with tailored configurations and the required electrical, mechanical, and other properties.

In analyzing the physical features of new-phase island nucleation under conditions of surfactant heteroepitaxy by in situ ultra high vacuum reflection electron microscopy, the effect of instability of the distribution of atomic steps over the silicon (111) surface was detected, which was caused by submonolayer adsorption of gold atoms at 900–1250°C [53]. The effect of kinetic instability of steps consists in a series of transformations of regularly arranged atomic steps (RS) to a system of step bunches (SB) and vice versa as the gold surface concentration increases. As the direction of the electric current heating the crystal was changed, the reversible transformations RS⇔SB and SB⇔RS occurred with an unchanged gold coverage. Critical concentrations of gold impurity atoms at which the distribution of atomic steps changes were estimated [54].

11.2.2 Surface Morphology During Gold Deposition

Let us reconsider typical impacts of the gold deposition on the silicon surface transformations: surface reconstruction nucleation, three-dimensional islands formation, and steps clustering. Figure 11.3a shows a REM image of the Si(111) surface at 500°C after deposition of 0.48 ML of gold. The inspection of RHEED pattern from this surface area clearly indicates the (5×2) surface reconstruction induced by gold adsorption. Three different contrasts on the image correspond to various orientation of the (5×2) domains. As the gold coverage increased, the domain spread and some parts of the atomic steps were found to merge with other forming macrostep, two- or several interplane distances in height, so-called step bunches. Similar step bunching was observed previously [8]. It is interesting that switching of the DC direction revealed no impact on the processes of the step bunching induced by gold adsorption at 500°C. During step bunching initiated by surface reconstruction, the width of adjacent terraces was increased in several times due to change of the atomic step distribution.

According to the phase diagrams [55, 56] and experimental data [57, 58] there are no surface phase transitions during gold deposition at crystal temperatures above 830°C. Moreover, at these temperatures there is no surface reconstruction on the clean silicon (111) surface too. While nucleation and growth of the superstructural domains can modify step distribution by forming step bunches it is complicate to compare the step bunching induced by gold and one by electromigration due to (i) surface reconstructions and (ii) different temperatures. That stimulates us to increase the temperature of the substrate up to 900°C to destroy any surface reconstructions and to make equal the temperature of gold deposition and step-bunching-induced electromigration.

Figure 11.3b shows the silicon surface area at 900°C after submonolayer gold deposition. No additional contrast related to the surface reconstruction was found at these experimental conditions that is consistent with the known phase diagrams [55, 56]. However, at increased gold coverage (above 1 ML) the formation of large three-dimensional islands was observed according to [8] (Fig. 11.3c). Thus, to avoid the influence of the phase transitions and three-dimensional island nucleation on

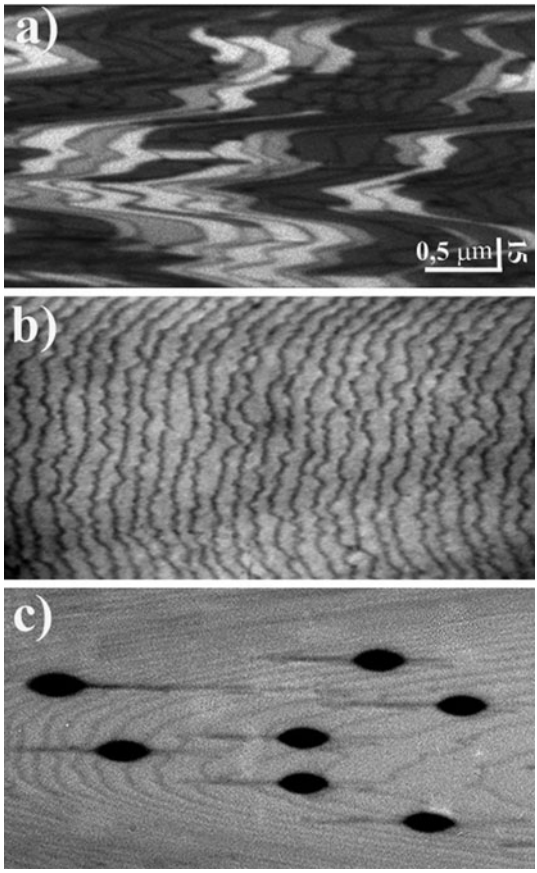

Fig. 11.3 REM images of Si(111) surface after deposition of 0.48 ML of gold at 500°C (**a**), the same amount of gold at 900°C (**b**), and three-dimensional islands on the surface after deposition of 1.2 ML of gold at 900°C (**c**)

the surface morphology, we have investigated the stability of the atomic steps at elevated temperatures and gold coverage below critical one, where the formation of three-dimensional gold islands occurs.

11.2.3 Gold Deposition

Figure 11.4 represents consequent stages of surface transformations at 900°C during gold deposition in case of the heating current passing in the step-down (a–d) and step-up (e–h) directions. For simplicity we describe first the left panel of the images only that corresponds to the case of the step-down direction. Some comments on the right panel of the image corresponding to the opposite DC direction will be made later. At the step-down DC direction and the sample temperature of 900°C the

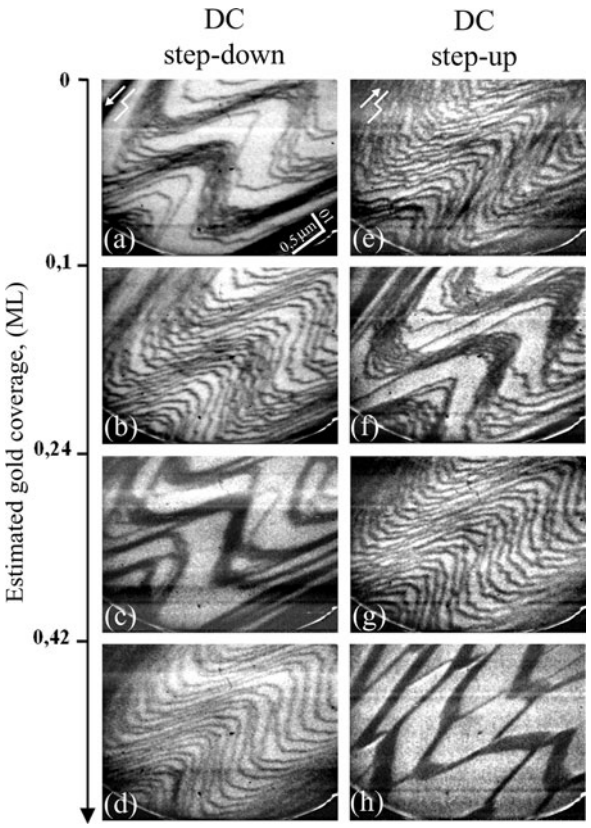

Fig. 11.4 Grabbed from REM video series of images showing the Si(111) morphology transformations at 900°C heated by DC in the step-down (**a**–**d**) and step-up (**e**–**h**) directions during gold deposition. Initial clean surfaces with step bunches (**a**) and regular steps (**e**). The same areas of the surfaces after gold deposition 0.1 (**b**,**g**), 0.24 (**c**,**h**), and 0.42 ML (**d**,**h**)

instability of diffusion-linked atomic steps on the atomically clean silicon surface leads to step bunching [15], which are clearly identified in Fig. 11.3a. Thin waived lines are monatomic steps whereas wide wavy bands of dark contrast, located in the middle and top parts of the image, are step bunches. During sublimation atomic step motion occurred from the bottom left to top right direction on the image. So the terraces, represented in the top right part of the image, are higher situated than ones in top-right part of the image. White arrow indicates the direction of the heating electrical current passing the crystal. It should be renounced again that due to foreshortening effect REM images are compressed in the direction of the electron beam incidence with factor of ∼50.

When small amount of gold (less than 0.1 ML) was deposited onto the silicon surface, the first transition of surface morphology was observed. Step bunches were dissolved into the regular distributed atomic steps (Fig. 11.4b). The system of regular steps was stable at this temperature if the gold coverage on the surface was

unchangeable. Actually at this temperature gold eliminates from the surface due to sublimation and/or dissolution into the bulk due to diffusion processes.

The phenomenon of the step instability under small amount (less 0.1 ML) of gold deposition was observed previously. Latyshev et al. [28, 29] attributed this effect to the reversing of an effective charge of adsorbed silicon atoms during gold deposition on the silicon (111) surface. Minimal critical surface concentration of gold atoms for this transition was estimated as 0.008–0.016 ML. Later it was proposed that this transition is caused by changing of atomic step properties, namely, due to the change of permeability of the atomic steps for silicon adatoms from the impermeable steps to the permeable ones [30, 59–62]. Minoda et al. [31] reported that step bunching at increased gold coverage and the step-down DC direction occurred due to changing a free energy of Si(111) and this step bunching caused by thermodynamics. While the observation of this transition was reported, the investigations of impact of the current direction and increased gold atom concentrations (higher 0.1 ML) on the silicon surface morphology have not been done.

By increasing the gold coverage above 0.24 ML, the surface morphology was changed by causing the second transformation of the silicon surface morphology by means of gold-induced step bunching (Fig. 11.4c). We found that bunches formed by gold adsorption were stable in the range of gold coverage between 0.24 and 0.42 ML. The process of gold-induced step bunching at these gold coverages occurred faster than one at clean silicon (111) surface.

Increasing gold coverage above 0.42 ML caused the third transition of the silicon surface morphology: from step bunches to regular steps (Fig. 11.4d). Further gold deposition (above 0.75 ML) on the silicon surface caused the formation of three-dimensional particles, probably gold-silicide islands on the surface similar to the one shown in Fig. 11.3c. Some of the moving particles were pinned at step bunches in agreement with [63].

We also have investigated the silicon surface transformations during gold deposition in the case when heating DC flowing in the step-up direction. Similar to the case of DC-induced step bunching on clean surface, the silicon surface transformations under gold deposition were found to be dependent on the DC directions. Figure 11.4e–h represents the surface relief at 900°C during gold deposition when heating direct current flows in the step-up direction. Figure 11.4e shows initially clean silicon surface at 900°C with regular atomic steps. The system of regular distributed atomic steps on the clean silicon surface was stable at these conditions. When gold was deposited, the several transitions of regular steps to step bunches and vice versa were occurred on the surface in agreements with one for the step-down DC direction assuming that regular step morphology was changed on step bunches and vice versa. Thus, the morphology of the silicon (111) surface depends crucially on the direction of the heating current and amount of deposited gold atoms.

Figure 11.5 schematically represents the surface morphology dependence on gold coverage for different directions (step-up and step-down) and types (DC and AC) of the heating electrical current at 900°C. Dark areas correspond to the step bunched morphology whereas white areas relate to the regular distributed atomic steps. There are four gold coverage ranges which can be characterized by alternative

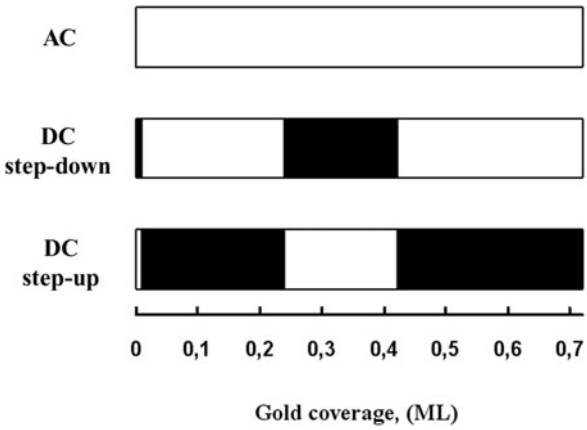

Fig. 11.5 Schematic representation of the silicon surface morphology at 900°C during gold deposition. *Dark areas* correspond to the step-bunched morphology; *white areas* deal with the regular distributed steps

surface morphologies (RS or SB). The first range (0-0.01 ML) (critical concentration measured in [28, 29]) corresponds to the clean silicon surface morphology, when step bunching occurs at the step-down DC direction and regular steps are stable for the step-up DC direction. The second range (0.01–0.24 ML) relates to reversal surface morphology - regular steps at the step-down direction and step bunches at the step-up one. The third range (0.24–0.42 ML) characterizes step bunching or regular steps at the step-down or step-up direction consecutively. The fourth range at gold coverage above 0.42 ML corresponds to reversal surface morphology comparing to the third range.

The detailed REM observations of the surface morphology in the case of AC heating of the sample was complicated due to influence of alternative electromagnetic fields on the electron beam. However, the final picture of step distribution after alternative heating of the crystal can be detected by two possible ways. The first is simply switching off heating of the sample and observation of the surface morphology at room temperature after cooling down the sample. In this case the surface morphology can be sufficiently changed due to several reasons. The nucleation and growth of the superstructural domains at lower temperatures during limited cooling rate can change the step distribution. Quenching the silicon sample also may be attended by generation of adatoms and vacancies that also have influence on the morphology of silicon surface [44, 64]. Another way for clarifying the impact of the alternative heating is rapid changing of the alternative power supply to the direct one without changing of sample temperature with simultaneously recording of REM images to a video recorder. Consequent analysis of the REM images, grabbed from the video tape, shows the initial distribution of atomic steps on the surface immediately after switching. We have used both ways, and the results were the same. Only regular atomic step distribution on the surface was observed after heating the sample by alternative electrical current of 50 Hz in all investigated gold coverage range.

Thus, atomic steps on silicon (111) surface at elevated temperature during gold deposition shows nontrivial behavior complicated by the impact of the DC heating. The physical reason for changing of the effective charge of the silicon adatoms still is not clear. It was reported that gold atoms on the silicon surface may act as an activator during the surfactant-mediated growth. During growth of silicon on the Si(111)–(5×2) Au surface gold atoms segregated to the topmost surface. The diffusion length of silicon atoms on gold-deposited silicon surface was reported to be larger than that on the (7×7) surface [65]. Aoki et al. [66] reported decreasing of adatom density on Si(111) surface, which was measured from atomic step shifting toward the step-down direction at 780°C after deposition of 0.3 ML of gold. The advance of the atomic steps means that silicon atom density on the gold-adsorbed (1×1) surface decreases with an increase of gold coverage. Taking into account these facts one can consider modification of the detachment/attachment rates of the atomic steps induced by gold atoms in a way similar to surfactant-mediated epitaxy. Our observations of the atomic step motion with increased rates in both directions (step-up and step-down) confirm this consideration. So we can conclude that gold atoms on the silicon surface produced drastic modifications of the diffusion properties on the surface at this temperature.

11.2.4 The Kinetics of the Gold-Induced Step Bunching

The kinetics of step bunching induced by gold adsorption was investigated in real time and compared with one of current-induced step bunching at the same temperature. Figure 11.6 demonstrates series of REM images illustrating the process of gold-induced step bunching at 900°C under the step-down DC direction. We found that step bunching at this condition occurs faster than one on clean silicon surface. The temporal measurement of average distance between neighboring bunches revealed that the bunching rate was at least two order times higher than one without gold deposition at the same temperature. It should be pointed out that the bunch formation in this case occurs mainly by means of atomic step moving in the direction of sublimation. However, some step bunches were observed to be moving in the growth direction producing coagulation of several step bunches in one.

While all presented results were obtained for the same sample temperature of 900°C, we also investigated the temperature dependence of the silicon morphology during gold deposition. In the first temperature range (830–1050°C) we have no observed significant differences in this effect and the same transitions were qualitatively registered. Only slow increasing of the critical gold concentration with temperature enlargement was found probably due to increased departing of gold atoms from the surface at higher temperatures. The most essential fact was observed in the second temperature range (1050–1250°C) where, in contradiction to the first temperature one, two critical gold concentrations were observed and the three gold coverage ranges were found only. At higher temperatures the investigations of gold-induced transformations are embarrassed due to high probability of gold atoms to depart from the surface and restricted power of gold evaporator. However,

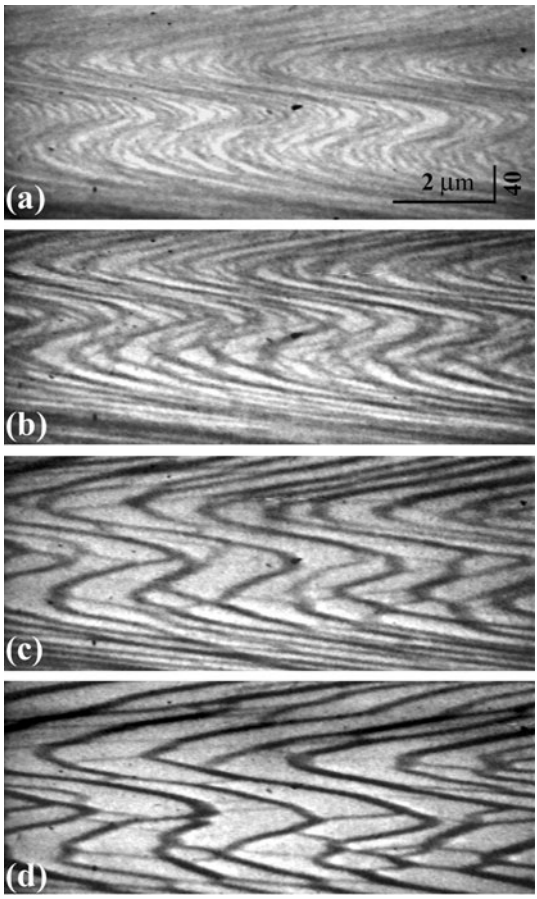

Fig. 11.6 REM images of consequent stages of step bunching induced by gold deposition of 0.28 ML on Si(111) surface at 870°C under DC heating in the step-down direction

we showed that step bunches transform into regular steps under gold deposition at extremely high rates at temperature of 1260°C in the case of heating electrical current passing in the step-down direction.

Figure 11.7 represents series of REM images which illustrated the Si(111) surface morphology transformations after deposition of 0.7 ML of gold and subsequent annealing at 900°C for the step-up current direction. After gold deposition on the silicon surface at 500°C, the evaporator was switched off and one can see appearance of additional RHEED patterns corresponded to the $(\sqrt{3} \times \sqrt{3})$ reconstruction. Then the sample temperature was increased to 900°C and the system of step bunches was observed similar to the initial surface before gold deposition (Fig. 11.7a). At once no additional reflections corresponding to surface reconstruction were observed at the RHEED pattern at this temperature. During high-temperature annealing a decreasing of gold concentration should be due to gold evaporation and gold dissolving

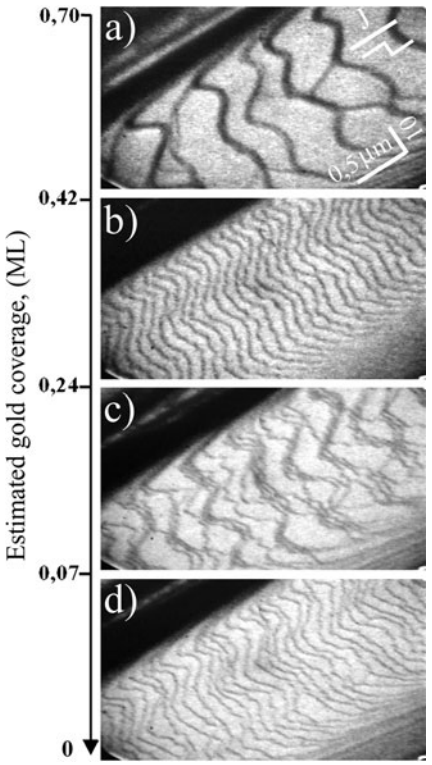

Fig. 11.7 REM images of Si(111) surface morphology during annealing at 900°C after deposition of 0.7 ML of gold (**a**–**d**)

into the bulk. After 16 min of annealing the step-bunched structure (Fig. 11.7a) was fluently transformed into an array of regular steps (Fig. 11.7b). This transformation was supplemented by atomic step motion in both (step-up and step-down) directions and increasing fluctuations of step shape. At the same time the observation of RHEED pattern revealed no any additional reflections at 900°C but the intensity of the basic (1×1) reflections increased in comparison with one measured immediately after gold deposition. After formation of regular array of atomic steps the sample temperature was reduced to 500°C and the RHEED picture was analyzed. Additional patterns corresponding to the Si(111)–(5×2)Au reconstruction were registered. According to the surface phase diagrams [55, 56] the formation of the (5×2) domains on gold-deposited silicon surface occurs in gold coverage range of 0.42–0.6 ML.

Subsequent isothermal annealing at 900°C in an ultra high vacuum chamber during 23 min caused step bunching (Fig. 11.7c). This transition was supplemented by increasing the (1×1) reflection intensity at RHEED pattern. Further annealing during 27 min caused the formation of regular steps on the surface (Fig. 11.7d). Decreasing to 500°C, RHEED picture clearly identified the (7×7) reflections that

correspond to atomically clean surface. Thus, periodical changing in step distribution was also observed during high temperature annealing of the gold-deposited silicon surface at 900°C.

11.2.5 Summary

In conclusion, the in situ observation of monatomic steps behaviour on the silicon surfaces by UHV REM allows to evaluate a lot of important parameters described the surface processes of sublimation, growth, thermal annealing, adsorption, gas reaction and phase transitions. UHV REM tolerates to carry out in situ experiments with a high spatial resolution on various physical phenomena on a crystal surface, to analyze the superstructural phase transitions on a surface, to examine atomic mechanisms of evaporation and epitaxial growth. In situ UHV REM investigations show impact of the adsorbed gold atoms on Si(111) surface morphological stability at elevated temperatures (830–1260°C) in the case of direct electrical current heating of the sample. Both DC heating and gold submonolayer adsorption produce the set of transitions from regular step-to-step bunches and vice versa. These transitions depend reversibly on the gold coverage and DC direction. There are four ranges of gold coverage and two types of silicon morphology (regular steps and step bunches) can be observed in the temperature ranges depending on the current direction. The critical gold concentrations required for changing of the surface relief were determined at different temperatures and directions of DC passing through the sample. The silicon (111) surface was characterized regular steps by distribution for sample heating by an alternative current in the investigated range of gold coverages (0–0.71 ML).

Acknowledgments We wish to acknowledge the valuable assistance in experiments and discussion to Prof. A.L. Aseev. This work has been partly supported by RFBR and by the programs of Ministry of Education and Science of Russian Federation.

References

1. I. Stranski, R. Kaishev, On crystal growth theory, Physics-Uspekhi (Russia), 1936, pp. 407–465.
2. R. Kaishev, I.N. Stranskii, Zur kinetischen Beschreibung der Keimbildungsgeschwindig-keit. Z. Phys. Chem. Abt. A **166**, 317 (1934)
3. O.P. Pchelyakov, A.I. Toropov, V.P. Popov, A.V. Latyshev, L.V. Litvin, Yu.V. Nastaushev, A.L. Aseev, Nanotechnologies in semiconductor electronics. Seventh international symposium on laser metrology applied to science, industry, and everyday life, in *Proceedings of SPIE, vol. 4900, 2002,* ed. by Yuri V. Chugui, Sergei N. Bagaev, A. Weckenmannn, P. Herbert Osanna, pp. 247–256
4. K. Yagi, Surface imaging using UHV-CTEM. Journal of Electron Microscopy **44**, 269 (1995)
5. A.V. Latyshev, A.B. Krasilnikov, A.L. Aseev, Direct UHV REM observation of the behaviour of monatomic steps on the silicon (111) surface. Phys. Stat. Solid. (a)**146**, 251 (1994)

6. H.-C. Jeong, E.D. Williams, Steps on surfaces experiment and theory. Surf. Sci. Rep. **34**, 171 (1999)
7. A.V. Latyshev, A.B. Krasilnikov, A.L. Aseev, L.V. Sokolov, S.I. Stenin, Reflection electron microscopy study of clean Si(111) surface reconstruction during the (7×7)-(1×1) phase transition. Surf. Sci. **254**, 90 (1991)
8. A.B. Krasilnikov, A.V. Latyshev, A.L. Aseev, S.I. Stenin, Monoatomic step clustering during superstructural transitions on Si(111) surface. J. Crystal Growth **116**, 178 (1992)
9. A.V. Latyshev, A.B. Krasilnikov, A.L. Aseev, In situ reflection electron microscope observation of two-dimensional nucleation on Si(111) during epitaxial growth. Ultramicroscopy, **48**, 377 (1993)
10. H. Minoda, Periodic step density wave on Si(111) vicinal surfaces studied by reflection electron microscopy. Phys. Rev. B **64**, 233305 (2001)
11. A.B. Krasilnikov, A.V. Latyshev, A.L. Aseev, Transformation of a Si(111) stepped surface during the formation of a Si(3×1) Ca superstructure. Surf. Sci. **290**, 232 (1993)
12. Y. Takahashi, H. Minoda, Y. Tanishiro, K. Yagi, Cu induced step bunching on a Si(111) vicinal surface studied by reflection electron microscopy. Surf. Sci. **433–435**, 512 (1999)
13. H. Minoda, Y. Takahashi, Y. Tanishiro, K. Yagi, In situ reflection electron microscopy study of Cu-induced step bunching on Si(111) vicinal surfaces. Surf. Sci. **438**, 68 (1999)
14. B.S. Swartzentruber, Y.-W. Mo, M.B. Webb, M.G. Lagally, Scanning tunneling microscopy studies of structural disorder and steps on Si surfaces. J. Vac. Sci. Technol. A **7**, 2901 (1989)
15. A.V. Latyshev, A.L. Aseev, A.B. Krasilnikov, S.I. Stenin, Transformations on clean Si(111) stepped surface during sublimation. Surf. Sci. **213**, 157 (1989)
16. L.V. Litvin, A.B. Krasilnikov, A.V. Latyshev, Transformations of the stepped Si(001) surface structure induced by heating the specimen by a current. Surf. Sci. Lett. **244**, L121 (1991)
17. E.D. Williams, E. Fu, Y.-N. Yang, D. Kandel, J.D. Weeks, Measurement of the anisotropy ratio during current-induced step bunching. Surf. Sci. **336**, L746 (1995)
18. Y.-N. Yang, E. Fu, E.D. Williams, An STM study of current-induced step bunching on Si (111). Surf. Sci. **356**, 101 (1996)
19. Y. Homma, M. Suzuki, Step bunching structure on vicinal Si(111) surfaces studied by scanning force microscopy. Appl. Surf. Sci. **60/61**, 479 (1992)
20. H. Tokumoto, K. Miki, H. Murakami, K. Kajimura, Heating current induced step motion on Si(111) surface by scanning tunneling microscopy. J. Vac. Sci. Technol. B **9**, 699 (1991)
21. B. Ranguelov, S. Stoyanov, Instabilities at vicinal crystal surfaces: competition between electromigration of adatoms and kinetic memory effect. Phys. Rev. B **77**, 205406 (2008)
22. B. Ranguelov, S. Stoyanov, Evaporation and growth of crystals: propagation of step-density compression waves at vicinal surfaces. Phys. Rev. B **76**, 035443 (2007)
23. J. Krug, V. Tonchev, S. Stoyanov, A. Pimpinelli, Scaling properties of step bunches induced by sublimation and related mechanisms. Phys. Rev. B **71**, 045412 (2005)
24. M. Sato, M. Uwaha, Growth of step bunches formed by the drift of adatoms. Surf. Sci. **442**, 318 (1999)
25. A. Natori, Step structure transformation induced by DC on vicinal Si(111). Jpn. J. Appl. Phys. **33**, 3538 (1994)
26. D. Kandel, J.D. Weeks, Step motion, patterns, and kinetic instabilities on crystal surfaces. Phys. Rev. Lett. **72**, 1678 (1994)
27. J.J. Metois, M. Audiffren, An experimental study of step dynamics under the influence of electromigration: Si(111). Int. J. Mod. Phys. B **11**, 3691 (1997)
28. A.V. Latyshev, H. Minoda, Y. Tanishiro, K. Yagi, Electromigration and gold-induced step bunching on the Si(111) surface. Surf. Sci. **401**, 22 (1998)
29. A.V. Latyshev, H. Minoda, Y. Tanishiro, K. Yagi, Adatom effective charge in morphology evolution on Si(111) surface. Appl. Surf. Sci. **130–132**, 60 (1998)
30. H. Minoda, Periodic step density wave on Si(111) vicinal surfaces studied by reflection electron microscopy. Phys. Rev. B **64**, 23305 (2001)
31. H. Minoda, Study of step instability on Si surfaces. Thin Solid Films **424**, 40 (2003)
32. H. Minoda, Direct current heating effects on Si(111) vicinal surfaces. J. Phys. Condens. Matter. **15**, 3255 (2003)

33. A.V. Latyshev, A.B. Krasilnikov, A.L. Aseev, Application of ultrahigh vacuum reflection electron microscopy for the study of clean silicon surfaces in sublimation, epitaxy, and phase transitions. Microsc. Res. Technique **20**, 341 (1992)
34. A.L. Aseev, A.V. Latyshev, A.B. Krasilnikov, Reflection electron microscopy observation of the behavior of monoatomic steps on the silicon surfaces. Surf. Rev. Lett. **4**, 551 (1997)
35. A.V. Latyshev, A.L. Aseev, A.B. Krasilnikov, S.I. Stenin, REM study of structural transformation on a clean silicon surface in sublimation, phase transition and homoepitaxy. Surf. Sci. **227**, 24 (1990)
36. A.L. Aseev, A.V. Latyshev, A.B. Krasilnikov, Direct observation of monoatomic step behaviour in MBE on Si by reflection electron microscopy. J. Crystal Growth **115**, 393 (1991)
37. C. Alfonso, J.C. Heyraud, J.J. Metois, About the sublimation of Si surfaces vicinal of {111}. Surf. Sci. Lett. **291**, L745 (1993)
38. A.V. Latyshev, H. Minoda, Y. Tanishiro, K. Yagi, Dynamical step edge stiffness on the Si(111) surface. Phys. Rev. Lett. **76**, 94 (1996)
39. A.V. Latyshev, H. Minoda, Y. Tanishiro, K. Yagi, Ultra high vacuum reflection electron microscopy study of step-dislocation interaction on Si(111) surface. Jpn. J. Appl. Phys. **34**, 5768 (1995)
40. A.V. Latyshev, A.L. Aseev, Monatomic steps on Si(111) surface. Usp. Fiz. Nauk. **168**, 1117 (1998)
41. A.V. Latyshev, A.B. Krasilnikov, A.L. Aseev, UHV REM study of the anti-band structure on the vicinal Si(111) surface under heating by a direct electric current. Surf. Sci. **311**, 395 (1994)
42. A.V. Latyshev, A.B. Krasilnikov, A.L. Aseev, Self-diffusion on Si(111) surfaces. Phys. Rev. B **54**, 2586 (1996)
43. M. Iwatsuki, S. Kitamura, T. Sato, T. Sueyoshi, Observation of surface reconstruction and nano-fabrication on silicon under high temperature using a UHV-STM. Appl. Surf. Sci. **60/61**, 580 (1992)
44. Y.-N. Yang, E.D. Willams, High atom density in the 1×1 phase and origin of the metastable reconstructions on Si(111). Phys. Rev. Lett. **72**, 1862 (1994)
45. A.V. Latyshev, A.B. Krasilnikov, A.L. Aseev, Anomalous behavior of the monatomic steps during (1×1)-(7×7) structural transition on atomically clean silicon surface. Pis'ma Zh. Eksp. Teor. Fiz. **49**, 448 (1988)
46. A.V. Latyshev, A.L. Aseev, A.B. Krasilnikov, A.V. Rzhanov, S.I. Stenin, Monatomic steps behavior on Si(111) surface during sublimation under electrical heating current conditions. Dokl. Akad. Nauk. USSR **300**, 84 (1988)
47. S.S. Kosolobov, A.L. Aseev, A.V. Latyshev, A.V. Rzhanov, In situ study of interaction of oxygen with the si(111) surface by ultrahigh-vacuum reflection electron microscopy. Fiz. Tekh. Poluprovodn. **35**, 1084 (2001)
48. A.L. Aseev, S.S. Kosolobov, A.V. Latyshev, S.A. Song, A.A. Saranin, A.V. Zotov, V.G. Lifshits, In situ REM and ex situ SPM studies of silicon (111) surface. Phys. Stat. Sol. (a), **202**, 2344 (2005)
49. E.E. Rodyakina, S.S. Kosolobov, D.V. Sheglov, D.A. Nasimov, S.A. Song, A.V. Latyshev, Atomic steps on sublimating Si(001) surface observed by atomic force microscopy. Phys. Low-Dim. Struct. **1–2**, 9 (2004)
50. A.V. Latyshev, L.V. Litvin, A.L. Aseev, Adatom effective charge in morphology evolution on Si(111) surface. Appl. Surf. Sci. **130–132**, 139 (1998)
51. A.V. Latyshev, D.A. Nasimov, V.N. Savenko, S.S. Kosolobov, A.L. Aseev, In situ REM studies of a Si(111) stepped surface during gold adsorption and oxygen treatments. Inst. Phys. Conf. Ser. **169**, 153 (2002)
52. A.V. Latyshev, A.B. Krasilnikov, A.L. Aseev, UHV reflection electron microscopy investigation of the monoatomic steps on the silicon (111) surface at homo- and heteroepitaxial growth. Thin Solid Films **306**, 205 (1997)
53. S.S. Kosolobov, A.V. Latyshev, S.A. Song, L.I. Fedina, A.K. Gutakovskij, Instability of the distribution of atomic steps on Si(111) upon submonolayer gold adsorption at high temperatures. Pis'ma Zh. Eksp. Teor. Fiz. **81**, 149 (2005)

54. S.S. Kosolobov, S.A. Song, E.E. Rodyakina, A.V. Latyshev, In situ study of interaction of oxygen with the Si(111) surface by ultrahigh-vacuum reflection electron microscopy. Fiz. Tekh. Poluprovodn. **41**, 462 (2007)
55. D. Grozea, E. Bengu, L.D. Marks, Surface phase diagrams for the Ag–Ge(111) and Au–Si(111) systems. Surf. Sci. **461**, 23 (2000)
56. S. Ino, Surface studies by RHEED (Reflection High Energy Electron Diffraction) MSA. Bulletin **23**, 109 (1993)
57. W. Swiech, E. Bauer, M. Mundschau, A low-energy electron microscopy study of the system Si(111)-Au. Surf. Sci. **253**, 283 (1991)
58. T. Kamino, T. Yaguchi, M. Tomita, H. Saka, In situ high resolution electron microscopy study on a surface reconstruction of Au-deposited Si at very high temperatures. Philos. Mag. A **75**, 105 (1997)
59. M. Sato, M. Uwaha, Y. Saito, Instabilities of steps induced by the drift of adatoms and effect of the step permeability. Phys. Rev. B **62**, 8452 (2000)
60. S. Stoyanov, New type of step bunching instability at vicinal surfaces in crystal evaporation affected by electromigration. Surf. Sci. **416**, 200 (1998)
61. S. Stoyanov, V. Tonchev, Properties and dynamic interaction of step density waves at a crystal surface during electromigration affected sublimation. Phys. Rev. B **58**, 1590 (1998)
62. N. Suga, J. Kimbara, N.-J. Wu, H. Yasunaga, A. Natori, Novel transition mechanism of surface electromigration induced step structure on vicinal Si(111) surfaces. Jpn. J. Appl. Phys. **39**, 4412 (2000)
63. A.V. Latyshev, D.A. Nasimov, V.N. Savenko, A.L. Aseev, UHV-REM study of gold adsorption on the Si(111) surface. Thin Solid Films **367**, 142 (2000)
64. D.A. Nasimov, D.V. Sheglov, E.E. Rodyakina, S.S. Kosolobov, L.I. Fedina, S.A. Teys, A.V. Latyshev, AFM and STM studies of quenched Si(111) surface. Phys. Low-Dim. Struct. **3–4**, 157 (2003)
65. H. Minoda, Y. Tanishiro, N. Yamamoto, K. Yagi, Growth of Si on Au deposited Si(111) surfaces studied by UHV-REM. Appl. Surf. Sci. **60/61**, 107 (1992)
66. K. Aoki, H. Minoda, Y. Tanishiro, K. Yagi, REM studies of adsorption-induced phase transition and faceting in the Si(111)-Au system. Surf. Rev. Lett. **5**, 653 (1998)

Chapter 12
Step-Bunching Instabilities of Vicinal Surfaces During Growth and Sublimation of Crystals – the Role of Electromigration of Adatoms

S. Stoyanov

Abstract This review is devoted to the mechanisms of a rather strange phenomenon – the step configuration at the vicinal surface of a Si crystal depends on the *direction* of the electric current through it. This phenomenon opens an easy way to manipulate the surface structure and to create a template for production of ordered arrays of nano-crystals on Si surface. The BCF model is generalized to account for the surface electromigration and the considerations are focused on the step-bunching instability induced by the drift of the adatoms. A simplified form of the equations of step dynamics at a vicinal crystal surface is presented and the results of the linear stability analysis are given. The non-linear effects in the step dynamics are studied in the frame of the continuum model equation and the treatment is restricted to the steady-state shape of the bunches of steps – the self-similarity of the bunch shape and the relation between the width and the height of the bunch. The scaling relations for the shape of the bunches opened a pathway for a number of interesting experiments, which are briefly described.

12.1 Introduction and Historical Overview

In 1989 A. Latyshev and his colleagues in Novosibirsk reported [1] rather strange observations on the distribution of steps at Si surfaces slightly deviated from the (111) face (such stepped surfaces are called vicinal). Carrying out experiments on step dynamics in high-temperature sublimation, they heated the Si crystal by passing direct electric current through it. The unexpected feature, discovered by Latyshev and co-workers, was that the step configuration at the vicinal surface depends on the *direction* of the electric current. For instance, in the temperature interval 1250–1350°C, an electric current with a step-down direction destabilized the initial regular distribution of the elementary steps at the vicinal crystal surface. In a relatively short time of heating with step-down current the steps formed bunches, separated by wide

S. Stoyanov (✉)
Department of Phase Transitions and Crystal Growth, Institute of Physical Chemistry, Bulgarian Academy of Sciences, 1113 Sofia, Bulgaria
e-mail: stoyanov@ipc.bas.bg

M. Michailov (ed.), *Nanophenomena at Surfaces,* Springer Series in Surface Sciences 47,
DOI 10.1007/978-3-642-16510-8_12,

terraces, which were almost free of steps. It is interesting to note that the rearrangement of the regularly distributed steps into step bands is a reversible process in the sense that one can transform the developed step bands into a regular system of steps by reversing the direction of the electric current. This phenomenon (electric current-induced bunching of steps) has a very complicated temperature dependence – there are three temperatures (in the interval between 1170 K and the melting temperature) where bunching–debunching transition takes place at a fixed direction of the electric current [1, 2]. It is instructive to mention again that the observations outlined above refer to the step dynamics at vicinal (111) face of Si crystal.

The electric current flowing through the Si crystal has also an impact on the step configuration of the (001) vicinal surface. The (001) surface of Si crystal is known to manifest surface reconstruction and to contain (2×1) and (1×2) domains formed by the dimerization of the surface atoms, which have two broken bonds each. Due to the surface reconstruction the terraces at the (001) vicinal surface are not identical – the direction of dimerization rotates by 90° when one moves from one terrace to the adjacent one. When the electric current through the Si crystal is perpendicular to the steps it has a dramatic effect on the ratio of the areas of the neighbouring terraces. One type of terraces (say (2×1)) increase in width on expense of the terraces of the other type (terraces with reconstruction (1×2)). If the electric current direction is reversed the narrow terraces increase their width whereas the wide terraces shrink [3, 4].

The REM observations of Latyshev et al. [1] and Kahata and Yagi [4] marked the beginning of rather active research on electric current-induced bunching of steps and conversion between 1×2 and 2×1 reconstruction domains at silicon surfaces. In 1990, Stoyanov [5] proposed a model explaining both phenomena step bunching and conversion of reconstruction domains. A fundamental feature of this model is the electromigration of the adatoms which are assumed to jump more frequently in the direction of the electric current (heating the crystal) than in the opposite direction. The proposed model, however, does not operate at the finest scale, where the crystal growth is described by hopping of adatoms between different lattice sites on the interface. Like the classic Burton–Cabrera–Frank (BCF) theory the model of crystal growth and sublimation in the presence of electromigration of the adatoms operates at the next scale where the basic elements are the terraces and the steps. Thus the crystal growth is reduced to diffusion of the adatoms on the terraces (this process is characterized by the coefficient D_s of surface diffusion) and their subsequent attachment to the steps. The processes at the steps are not simple. The adatoms find their "proper" sites in the crystal lattice after many "trials and errors." The atoms attach to the step edges, migrate along them, reach kinks, and attach into kink position. The last event does not mean that the atom attaches to the crystal phase "forever." In fact, this atom could later detach from the kink position and even leave the crystal surface by desorption. In the special case of crystal–vapour equilibrium an atom attaching to a kink position has zero probability to stay in the crystal phase "forever." If, however, the vapour pressure is higher than its equilibrium value, an atom attaching to a kink position has a chance to stay in the crystal phase "forever." As a result the crystal grows. In the scale where BCF operates the crystal growth

and sublimation are described by the motion of the elementary steps at the vicinal surface. The rate of step motion is assumed to be proportional to the local supersaturation, i.e., $v = K\Omega\left(n_s - n_s^e\right)$ where the step kinetic coefficient K reflects both the complicated structure of the steps and the more complicated processes of attachment and detachment of atoms to the step. The local supersaturation (or undersaturation) is given by the difference between the actual concentration n_s of adatoms in the vicinity of the step and the equilibrium concentration n_s^e at the temperature of the crystal. Finally, the area of one atom at the growing crystal surface is denoted by Ω. To find an expression for the actual concentration n_s of adatoms in the vicinity of the step one should solve the equation describing the diffusion of adatoms on a single terrace and accounting for both the deposition of atoms on the crystal surface and their thermal desorption.

The model proposed by Stoyanov [5, 6] involves an additional parameter which reflects the fact that the adatoms jump more frequently in the direction of the electric current, i.e. they have a drift velocity $v_{drift} = FD_s / kT$, where F is a force (related in some way to the electric current) acting on the adatoms. Thus the classic BCF theory is generalized to account for the drift velocity of the adatoms, i.e. for the asymmetry in the surface transport of the adatoms on the terraces between the steps. Actually, this is the second asymmetry introduced into the BCF model. The first one was proposed many years ago by Schwoebel [7] and it is based on the Ehrlich–Schwoebel effect – asymmetry in the attachment–detachment processes at the steps. Both asymmetries induce step-bunching instability of the vicinal surface. However, in contrast to the Ehrlich–Schwoebel effect, the electromigration can be controlled by manipulating the electric current flowing through the crystal. This fact provides a ground for a rich variety of experimental studies on the step dynamics and crystal growth kinetics.

The paper of Stoyanov [5] was focused on the impact of the electromigration on the stability of the vicinal surface. That is why the simplest case of annealing with negligible desorption was analyzed. Under this condition the only process that takes place at the crystal surface is transport of atoms between the steps. The atomic flux on the terraces was derived to be (in the physically interesting case $Fl / kT \ll 1$ with l being the terrace width)

$$j = \frac{FD_s}{kT} n_s^e \frac{1}{1 + \left(2d_s / l\right)} \tag{12.1}$$

where $d_s = D_s / K$ is a characteristic length. In the original paper somewhat different notation was used and the exact but heavy expression (equation (3) in [5]) is here simplified by series expansion of the exponential function $\exp(Fl / 2kT) \approx 1 + (Fl / 2kT)$.

This relatively simple expression for the electromigration-induced atomic flux during annealing with negligible desorption was able to explain a number of experimental observations. Let us first consider the formation of wide and narrow terraces during annealing of vicinal (001) Si surface. The key to understanding this effect is the electromigration in combination with the anisotropy of the surface diffusion.

On the reconstructed (1×2) and (2×1) surfaces the adatoms migrate preferentially along the dimmer rows, giving rise to an anisotropy in the surface diffusion. This anisotropy is essential for the step dynamics only when the surface diffusion is slow and the step kinetics is relatively fast, i.e. D_s is small and K is large. In this case the characteristic length $d_s = D_s / K$ is small ($d_s \ll l$) and the expression for the surface flux j can be further simplified to

$$j = \frac{FD_s}{kT} n_s^e = v_{drift} n_s^e \tag{12.2}$$

Since D_s is the coefficient of surface diffusion in a direction perpendicular to the steps the flux j has essentially different values on neighbouring terraces because they have 90° difference in the dimmer orientation. On terraces having dimmer rows perpendicular to the steps the diffusion is easy and the surface flux from one step to the neighbouring one is large. In contrast, on terraces having dimmer rows parallel to the steps diffusion of adatoms from one step to the neighbouring one is slow, the surface flux is small and has negligible contribution to the motion of the steps. So that one can account only for the surface flux on the terraces of the first type and write the expression

$$\frac{dl}{dt} = -2\Omega j = -2\Omega \frac{FD_s}{kT} n_s^e \tag{12.3}$$

for the rate of increase of the width of such a terrace. Here D_s is the coefficient of easy diffusion, i.e. diffusion along the dimmer rows. The sign minus appears in the right-hand side of the above expression because $F > 0$ is assumed for a step-up direction of the electromigration force (see Fig. 12.1). That is why the electromigration pushes the atoms detached from the descending step toward the ascending step where they attach to kink sites. As a result the terrace shrinks. The terraces of the other type increase their width. The process could be reversed by reversing the electric current direction. Then the wide terraces decrease in width whereas the narrow terraces expand.

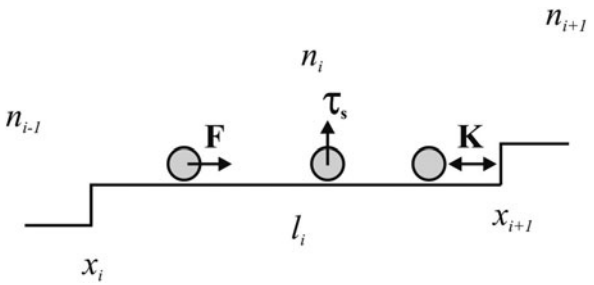

Fig. 12.1 Schematic view of a vicinal surface with straight steps. The adatoms have a drift velocity induced by an electric force F. The width of the ith terrace is $l_i = x_{i+1} - x_i$ and the concentration of adatoms on it is n_i

Equation (12.3) provided the first possibility to estimate the electromigration force F. This was done by Ichikawa and Doi [8, 34]. Essential feature of their experiments was the combined heating of the specimen – by radiation and by passing electric current through the Si wafer. In this way they were able to vary the temperature in the interval 600–900°C while keeping the electric current constant. The obtained data for the rate of increase of the terrace width were described by the expression

$$\frac{\mathrm{d}l}{\mathrm{d}t} = v_0 \exp\left(-\frac{E_l}{kT}\right) \tag{12.4}$$

with $v_0 = 1.7\,\mathrm{cm/s}$ and $E_l = 1.3\,\mathrm{eV}$. Comparing the pre-exponential terms in (12.3) and (12.4) and having in mind that $D_\mathrm{s} = \omega_0 \Omega \exp\left(-E_\mathrm{sd}/kT\right)$ and $n_\mathrm{s}^\mathrm{e} = \left(1/\Omega\right)\exp\left(-\Delta E_\mathrm{kink\text{-}ad}/kT\right)$ one obtains $v_0 = 2F\Omega\omega_0/kT$ with ω_0 being the frequency of vibrations of one adatom at the crystal surface. Let us note that here E_sd is the activation energy for surface diffusion and $E_\mathrm{kink\text{-}ad}$ is the difference between the energies of an atom in a kink position and an adatom. Assuming $\omega_0 = 10^{13}\,\mathrm{s}^{-1}$ one obtains $F = 0.8 \times 10^{-16}\,\mathrm{N}$ at $T = 1000\,\mathrm{K}$. It is worth noting that such a value of the force F can be produced by an electric field of 5 V/cm provided the adatom has an effective charge equal to the elementary electric charge (but having a positive sign).

As already mentioned, (12.1) can also explain the step-bunching instability of a vicinal surface. In fact, it could explain only bunching at step-down direction of the electromigration force F. Such a phenomenon was reported to exist in 900–1000 and 1250–1350°C temperature intervals [1, 2]. Step-bunching instability at step-up direction of F (reported to exist in the temperature intervals around 1150 and 1400°C) cannot be explained on the basis of (12.1). These observations, however, could be reproduced by a model accounting for the "transparency" of the steps (the adatoms prefer to jump to the next terrace instead to reach a kink and join the crystal phase). This more complicated model is outside the frame of this review.

To demonstrate the potential of (12.1) to explain step bunching at step-down direction of the force F we shall use an approach which is not rigorous, but it is instructive and easy to understand. We shall first consider the surface diffusion limited case ($d_\mathrm{s} \ll l$). In this limit the surface flux is approximately given by the expression

$$j = D_\mathrm{s}\frac{F}{kT}\, n_\mathrm{s}^\mathrm{e}\frac{1}{1+\left(d_\mathrm{s}/l\right)} \approx D_\mathrm{s}\frac{F}{kT}\, n_\mathrm{s}^\mathrm{e}\left(1-\frac{d_\mathrm{s}}{l}\right) \tag{12.5}$$

and the step rate is given by

$$v = \Omega\left(j_\mathrm{up} - j_\mathrm{d}\right) = -D_\mathrm{s}\Omega\,\frac{F}{kT} n_\mathrm{s}^\mathrm{e}\left(\frac{d_\mathrm{s}}{l_\mathrm{up}} - \frac{d_\mathrm{s}}{l_\mathrm{d}}\right) \tag{12.6}$$

where l_{up} and l_d are the widths of the upper and lower terraces, respectively. Introducing the density of steps at the crystal surface $\rho = 1/l$ we rewrite the expression for the step rate in the form

$$v = -D_s \Omega \frac{F d_s}{kT} n_s^e \frac{1}{\rho} \frac{\partial \rho}{\partial x} \tag{12.7}$$

Thus we move to a theory that operates in the next larger scale (relative to the scale of BCF theory). In this larger scale the step structure of the interface is described by a continuous function $\rho(x, t)$. Taking into account the conservation law for the number of steps

$$\frac{\partial \rho}{\partial t} = -\frac{\partial (\rho v)}{\partial x} \tag{12.8}$$

and substituting v with expression (12.7) one obtains

$$\frac{\partial \rho}{\partial t} = \Omega D_s \frac{F}{kT} n_s^e d_s \frac{\partial^2 \rho}{\partial x^2} \tag{12.9}$$

Thus, starting from (12.5) for the electromigration-induced surface flux we arrived to a diffusion equation for the density of steps (one can consider steps as quasi-particles) at the crystal surface. Obviously, when the expression in front of $\partial^2 \rho / \partial x^2$ is positive, any fluctuations in the step density will die out (the steps from the regions of high density will migrate to the regions of low step density to restore the uniform distribution of steps). In contrast, when this expression is negative (i.e. $F < 0$) the fluctuations will increase and the steps will form bunches, separated by large terraces. Therefore, electromigration force with step-down direction induces step bunching during sublimation of vicinal surfaces.

Historically, the model of electromigration-affected crystal sublimation was initially studied in the scale where BCF theory operates. In 1991, Stoyanov [6] used linear stability analysis to show that the regular distribution of steps at the crystal surface is unstable when the electromigration force has a direction from the high to the low terraces. The non-linear dynamics of steps was first studied by numerical integration of the equations of step motion in 1994 [9]. In the same year Natori [10] extended the model to include step repulsion (in fact, an earlier paper of Uwaha [11] accounted for the impact of the step repulsion on the step dynamics in a treatment of the relaxation of non-equilibrium crystal surface profile). The energy of repulsion between the steps is an essential element of the step dynamics. It is the repulsion between the elementary steps that prevents them from forming macrosteps. Instead, bunches of steps are formed on the crystal surface. The distances between the steps in the bunch are determined by a balance between the step repulsion and the electromigration-induced tendency to bunching.

Considerable progress in the quantitative theory of current-induced bunching of steps was reported in 1998 [12, 13]. The non-linear dynamics of steps during

sublimation was studied in the case of slow surface diffusion [12], and a scaling relation

$$L = 2.25N^{1/3}\left(\frac{\mathrm{a}g(T)}{|F|}\right)^{1/3} \tag{12.10}$$

between the width L of the bunch and the number N of steps in it was obtained. Here $g(T)$ is defined [14] through the expression

$$f(\rho) = f(0) + \kappa\rho + g\rho^3 \tag{12.11}$$

for the surface-free energy (per unit projected area) of a vicinal surface with a density of steps ρ. Equation (12.10) is a remarkable result – it predicts a simple relation between two measurable quantities (L and N) and contains the step repulsion coefficient $g(T)$ which is a fundamental quantity in the thermodynamics of stepped surfaces.

12.2 Generalized BCF Model – Electromigration of Adatoms

Step-bunching instability, induced by electric current, was a subject of intensive theoretical and experimental studies [9–28]. The understanding of the mechanisms of this phenomenon, achieved in these studies, will be briefly presented in this review. The considerations are focused on the step-bunching instability due to the drift of the adatoms. This task requires an analysis of the crystallization process in different scales. At the finest scale, where the crystal growth is described by hopping of atoms between different lattice sites the term electromigration simply means that an adatom jumps more frequently in the direction of the electric current (from + to −) than in the opposite direction. The drift of the Si adatoms in the direction of the electric current flowing through the Si crystal was proven in direct experiments on the evolution of the shape of artificially created groves at the crystal surface [29]. At the next scale, where the BCF theory operates, the surface diffusion on the terraces is described by the equation

$$D_\mathrm{s}\frac{\mathrm{d}^2 n_\mathrm{s}}{\mathrm{d}x^2} - \frac{D_\mathrm{s}F}{kT}\frac{\mathrm{d}n_\mathrm{s}}{\mathrm{d}x} - \frac{n_\mathrm{s}}{\tau_\mathrm{s}} + R = 0 \tag{12.12}$$

where n_s is the concentration of adatoms at the surface, D_s is the coefficient of surface diffusion, F is a phenomenological parameter that we call "electromigration force," τ_s is the average lifetime of an atom in a state of mobile adsorption, and R is the deposition flux. The boundary conditions for (12.12) are determined by the processes at the steps. Assuming the adatom exchange between neighbouring

terraces to be much smaller than the exchange between the adlayer and the crystal phase one can write

$$D_{\mathrm{s}}\left(-\frac{\mathrm{d}n_{\mathrm{s}}}{\mathrm{d}x}+\frac{Fn_{\mathrm{s}}}{kT}\right)=-K\left(n_{\mathrm{s}}-n_{\mathrm{s}}^{\mathrm{e}}(x_{j-1})\right),\qquad x=x_{j-1} \tag{12.13}$$
$$D_{\mathrm{s}}\left(-\frac{\mathrm{d}n_{\mathrm{s}}}{\mathrm{d}x}+\frac{Fn_{\mathrm{s}}}{kT}\right)=K\left(n_{\mathrm{s}}-n_{\mathrm{s}}^{\mathrm{e}}(x_{j})\right),\qquad x=x_{j}$$

where K is the step kinetic coefficient and $n_{\mathrm{s}}^{\mathrm{e}}\left(x_j\right)$ is the concentration of adatoms which is in equilibrium with the step positioned at x_j. The diffusion equation (12.12) and the boundary conditions (12.13) define a characteristic length $d_{\mathrm{s}}=D_{\mathrm{s}}\left/K\right.$.

12.3 Equations of Step Motion – Simplified Form and Linear Stability Analysis

Crystal growth or sublimation process can be formally described as a progression of unit steps across an appropriate reference face of a crystal. Substituting the exact solution of the steady-state diffusion problem ((12.12) and (12.13)) into

$$\frac{\mathrm{d}x_j}{\mathrm{d}t}=-K\Omega\left[\left(n_{j-1}(x_j)-n_{\mathrm{s}}^{\mathrm{e}}(x_j)\right)+\left(n_j(x_j)-n_{\mathrm{s}}^{\mathrm{e}}(x_j)\right)\right] \tag{12.14}$$

one obtains the explicit form of the equations of step dynamics. In this form the equations are rather complicated and not instructive. The procedure we follow here is to expand $\exp\left[\alpha\left(x_{j+1}-x_j\right)/\lambda_{\mathrm{s}}\right]$ (which appears in both nominator and denominator of the right-hand side of (12.14)) into series and neglect all terms after the linear one. In this way, the exact expression for the denominator of (12.14)

$$\left\{\left[1+2\alpha\frac{d_{\mathrm{s}}}{\lambda_{\mathrm{s}}}+\left(\frac{d_{\mathrm{s}}}{\lambda_{\mathrm{s}}}\right)^2\right]\exp\left[\alpha\left(x_{j+1}-x_j\right)/\lambda_{\mathrm{s}}\right]-\left[1-2\alpha\frac{d_{\mathrm{s}}}{\lambda_{\mathrm{s}}}+\left(\frac{d_{\mathrm{s}}}{\lambda_{\mathrm{s}}}\right)^2\right]\right.$$
$$\left.\exp\left[-\alpha\left(x_{j+1}-x_j\right)/\lambda_{\mathrm{s}}\right]\right\} \tag{12.15}$$

turns into

$$2\alpha\left\{2\frac{d_{\mathrm{s}}}{\lambda_{\mathrm{s}}}+\frac{\left(x_{j+1}-x_j\right)}{\lambda_{\mathrm{s}}}\right\} \tag{12.16}$$

Here $\lambda_{\mathrm{s}}=\sqrt{D_{\mathrm{s}}\tau_{\mathrm{s}}}$ is the mean diffusion distance and $\alpha=\sqrt{1+\left(F\lambda_{\mathrm{s}}\left/2kT\right.\right)^2}$. Now we easily see how to simplify the equations of step motion in the two limits $d_{\mathrm{s}}\gg x_{j+1}-x_j$ and $d_{\mathrm{s}}\ll x_{j+1}-x_j$. The first case is usually called atom attachment–detachment limited regime, whereas the second case is surface diffusion limited regime.

12.3.1 Step Dynamics with Slow Attachment and Detachment of Atoms

In the first limit ($d_s \gg l$ where l is the average terrace width) the simplified step dynamics equations are

$$v_j = \frac{\mathrm{d}x_j}{\mathrm{d}t} = \frac{K\Omega}{2}\left\{\begin{array}{l}\left[-\Delta n_s^e\left(x_j\right) + \Delta n_s^e\left(x_{j-1}\right)\right] + \frac{n_s^e(x_j)}{K\tau_s}\left[l_j + l_{j-1}\right] + \\ \frac{F}{2kT}\left[l_j \Sigma n_s^e\left(x_j\right) - l_{j-1}\Sigma n_s^e\left(x_{j-1}\right)\right]\end{array}\right\} \tag{12.17}$$

where the equilibrium concentrations of adatoms are

$$n_s^e\left(x_j\right) = n_s^e\left[1 + \tilde{A}\left(\frac{1}{l_{j-1}^3} - \frac{1}{l_j^3}\right)\right] \tag{12.18}$$

where $\tilde{A} = 2\Omega g \,/ kT$. Here g is the strength of the entropic and stress-mediated repulsion between the steps (see (12.11)), whereas $\Delta n_s^e\left(x_j\right) = n_s^e\left(x_{j+1}\right) - n_s^e\left(x_j\right)$, $l_j = x_{j+1} - x_j$, and $\Sigma n_s^e\left(x_j\right) = n_s^e\left(x_{j+1}\right) + n_s^e\left(x_j\right)$.

It is instructive to look at (12.17) in the special case of uniform distribution of steps at the vicinal surface (i.e. when all terraces are equal $l_j = l$). Then one obtains

$$v_j = \frac{\Omega n_s^e l}{\tau_s} \tag{12.19}$$

which is the rate of a train of equidistant steps during sublimation. The other two terms in the curly brackets describe the impact of the step–step repulsion (the first square brackets) and electromigration of adatoms (the product of F and the last square brackets). These terms (and the physical phenomena they reflect) are essential for the stability of the step train as well as for the shape of the step bunches in the case of instability of the vicinal crystal surface.

Expression (12.17) provides a ground to write down equations for the time evolution of the terrace widths $l_j = x_{j+1} - x_j$. These equations are non-linear because of the non-linear dependence of the equilibrium adatom concentration on the terrace widths l_j (see (12.18)). Leaving the non-linear dynamics for the next section, here we focus our attention on the linear stability analysis. It is convenient to introduce dimensionless variables $\eta_j = l_j \,/ l$ and consider small fluctuation of the uniform terrace distribution $\eta_j = 1 + \Delta\eta_j$ where $\Delta\eta_j \ll 1$. The time evolution of $\Delta\eta_j$ is approximately governed by linear equations having a solution in the form $\Delta\eta_j = \exp\left(i\mathrm{jq}\right)\exp\left(\mathrm{st}\right)$ where i is the imaginary unit and q is the wave number. As seen the vicinal surface will be unstable (the fluctuations will grow with the evaporation time) when the real part of the parameter s is positive. For small values of the wave number $q < 1$ the real part of s is approximately given by

$$s_{\text{real}} = B_2 q^2 - B_4 q^4 \tag{12.20}$$
$$B_2 = -\frac{n_s^e \Omega}{2d_s}\left[v_{\text{drift}} + V_{\text{cr}}\frac{d_s}{K\tau_s}\right]$$
$$B_4 = \frac{n_s^e \Omega}{24 d_s}\left[-v_{\text{drift}} + V_{\text{cr}}\left(\frac{6d_s}{l} - \frac{d_s}{K\tau_s}\right)\right]$$

Here $v_{\text{drift}} = FD_s \big/ kT$ is the drift velocity of the adatoms due to their electromigration, whereas the quantity

$$V_{\text{cr}} = 6K\left(\tilde{A}\big/ l^3\right) \tag{12.21}$$

has a dimension of velocity and characterizes the step–step repulsion.

It is instructive to see how the different terms in the right-hand side of (12.17) contribute to the constants B_2 and B_4. The term in the first square brackets in (12.17) describes the relaxation of the step distribution due to the step–step repulsion. This relaxation term has a non-zero contribution to B_4 and zero contribution to B_2. The term in the second square brackets in (12.17) has a contribution $-\left(V_{\text{cr}} d_s \big/ K\tau_s\right)$ to the constant B_2 and $-\left(V_{\text{cr}} d_s \big/ 12K\tau_s\right)$ to B_4. Finally, the drift velocity v_{drift} appears in B_2 and B_4 because of the last term in (12.17).

Equations (12.20) show that a vicinal surface is unstable ($B_2 > 0$) when the drift velocity v_{drift} is negative (i.e. drift velocity has a step-down direction) and its absolute value exceeds the value of the expression $V_{\text{cr}} d_s \big/ K\tau_s$. Near the critical point ($v_{\text{drift}} = V_{\text{cr}} d_s \big/ K\tau_s$) the instability occurs for small wave numbers

$$0 < q < \sqrt{\frac{B_2}{B_4}} \tag{12.22}$$

and the most unstable mode (defined by the requirement $s_{\text{real}}(q) = \max$) has a wave number

$$q_{\max} = \sqrt{\frac{B_2}{2B_4}} \tag{12.23}$$

When the inequality $l \ll K\tau_s$ is fulfilled, there exists an interval $(6V_{\text{cr}} d_s) \big/ l \gg v_{\text{drift}} \gg V_{\text{cr}} d_s \big/ K\tau_s$ of values of the drift velocity where the wave number of the most unstable mode is

$$q_{\max} = \sqrt{\frac{v_{\text{drift}} l}{V_{\text{cr}} d_s}} = \sqrt{\frac{Fl^4}{12g\Omega}} \tag{12.24}$$

Finally, let us note that linear stability analysis of the step dynamics controlled by the atom attachment–detachment kinetics at the steps was first performed by Sato and Uwaha [16].

12.3.2 Surface Diffusion Limited Regime

In this regime of sublimation the simplified equations of step motion are

$$\frac{\mathrm{d}x_j}{\mathrm{d}t} = \frac{D_\mathrm{s}\Omega}{\lambda_\mathrm{s}} \left\{ \begin{array}{l} \lambda_\mathrm{s}\left[-\frac{\Delta n_\mathrm{s}^\mathrm{e}(x_j)}{l_j} + \frac{\Delta n_\mathrm{s}^\mathrm{e}(x_{j-1})}{l_{j-1}}\right] + \alpha^2 \frac{n_\mathrm{s}^\mathrm{e}(x_j)}{2\lambda_\mathrm{s}}\left[l_j + l_{j-1}\right] + \frac{F\lambda_\mathrm{s}}{2kT}\left[\Delta n_\mathrm{s}^\mathrm{e}\left(x_j\right)\right. \\ \left. + \Delta n_\mathrm{s}^\mathrm{e}\left(x_{j-1}\right)\right] + \Delta n_\mathrm{s}^\mathrm{e}\left(x_{j-1}\right) + \frac{F\lambda_\mathrm{s}}{kT} d_\mathrm{s}\left[-\frac{\Sigma n_\mathrm{s}^\mathrm{e}(x_j)}{l_j} + \frac{\Sigma n_\mathrm{s}^\mathrm{e}(x_{j-1})}{l_{j-1}}\right] \end{array} \right\} \tag{12.25}$$

Here the term in the first square brackets stabilizes the regular step distribution, the second term accounts for the motion of the step train due to the sublimation, and the last term destabilizes the vicinal surface when $F < 0$.

The linear stability analysis of (12.25) gives expression (12.20) for s_real with

$$\begin{aligned} B_2 &= -\frac{d_\mathrm{s}}{l^2} n_\mathrm{s}^\mathrm{e}\Omega\left[v_\mathrm{drift} + V_\mathrm{cr}\alpha^2 \frac{l^2}{\lambda_\mathrm{s}^2}\right] \\ B_4 &= \frac{d_\mathrm{s}}{2l^2} n_\mathrm{s}^\mathrm{e}\Omega\left[-2v_\mathrm{drift} + V_\mathrm{cr}\left(1 - \frac{\alpha^2}{6}\frac{l^2}{\lambda_\mathrm{s}^2}\right)\right] \end{aligned} \tag{12.26}$$

Here again we can define an interval $V_\mathrm{cr}\alpha^2\left(l^2/\lambda_\mathrm{s}^2\right) \ll v_\mathrm{drift} \ll V_\mathrm{cr}$ where the wave number of the most unstable mode is

$$q_\mathrm{max} = \sqrt{\frac{v_\mathrm{drift}}{V_\mathrm{cr}}} = \sqrt{\frac{F d_\mathrm{s} l^3}{12\Omega g}} \tag{12.27}$$

12.4 Non-linear Dynamics and Self-Similarity of the Bunch Shape

The linear stability analysis provides information about the very early stages of the step-bunching instability evolution. At long sublimation time the role of the non-linear effects becomes essential and the theoretical treatment of the instability should be based on (12.17) or (12.25).

12.4.1 Sublimation Controlled by Slow Surface Diffusion

Following the history of the research activity [12, 30] we first analyze the sublimation in the surface diffusion limited regime, i.e. the case described by (12.25). A relatively simple way to study the non-linear dynamics at the crystal surface is provided by the continuum model equation, where the function $z(x, t)$ describes the shape of the vicinal surface in the moment t. Going back to the very first paper on the step bunching at crystal surfaces [31] we take the equation

$$\frac{\partial z}{\partial t} = -h_0 \frac{1}{x_i - x_{i-1}} \frac{\mathrm{d}x_i}{\mathrm{d}t} \tag{12.28}$$

which expresses the simple fact that the decrease of the crystal surface height during sublimation is equal to the product of the single step height h_0, the step density $1/(x_i - x_{i-1})$, and the velocity of the steps. Substituting expression (12.25) into (12.28) and making use of expression (12.18) one obtains an equation in partial derivatives ((12) in [12]). To simplify this equation we make use of the results from the linear stability analysis. We notice that the most important role in stabilizing the regular step distribution has the term which describes the relaxation due to the step–step repulsion. On the other hand, the drift velocity is the most essential destabilizing factor. Accounting only for these two terms into the equations for the motion of the steps one obtains for the surface diffusion limited regime [12, 30]

$$\frac{\partial z}{\partial t} = \frac{D_\mathrm{s} n_\mathrm{s}^\mathrm{e} \Omega}{kT} \left[-6g \frac{\Omega}{h_0} \frac{\partial^2}{\partial x^2} \left(\frac{\partial z}{\partial x} \frac{\partial^2 z}{\partial x^2} \right) + 2F d_\mathrm{s} \frac{\partial^2 z}{\partial x^2} \right] - \frac{\alpha^2 h_0 \Omega n_\mathrm{s}^\mathrm{e}(x)}{\tau_\mathrm{s}} \tag{12.29}$$

It is instructive to consider (12.29) as a continuity equation

$$\frac{\partial z}{\partial t} + \frac{\partial J}{\partial x} = -\frac{\alpha^2 h_0 \Omega n_\mathrm{s}^\mathrm{e}(x)}{\tau_\mathrm{s}} \tag{12.30}$$

where

$$J = \frac{D_\mathrm{s} n_\mathrm{s}^\mathrm{e} \Omega}{kT} \left[6g \frac{\Omega}{h_0} \frac{\partial}{\partial x} \left(\frac{\partial z}{\partial x} \frac{\partial^2 z}{\partial x^2} \right) - 2F d_\mathrm{s} \frac{\partial z}{\partial x} \right] \tag{12.31}$$

The requirement $J = J_\mathrm{st} = \text{const.}$ defines a steady-state shape of a bunch of steps at the crystal surface. As seen $z_\mathrm{st}(x)$ satisfies a non-linear differential equation which can easily be transformed into

$$m_\mathrm{p} \frac{\mathrm{d}^2 y}{\mathrm{d}x^2} = F_\mathrm{p} \sqrt{y} + J_\mathrm{st} = -\frac{\mathrm{d}U}{\mathrm{d}y} \tag{12.32}$$

which is an equation describing the motion of a classical "particle" with a "mass" $m_\mathrm{p} = \frac{D_\mathrm{s} n_\mathrm{s}^\mathrm{e} \Omega}{kT} \frac{3g\Omega}{h_0}$, "coordinate" $y = \left(\mathrm{d}z / \mathrm{d}x\right)^2$, and "time" x. This is the so-called mechanical analog, which is very useful in obtaining the bunch shape [32]. According to (12.32) the classical "particle" oscillates into a potential well

$$U(y) = -\frac{2}{3} F_\mathrm{p} y^{3/2} - J_\mathrm{st} y \tag{12.33}$$

where $F_\mathrm{p} = 2 \frac{D_\mathrm{s} n_\mathrm{s}^\mathrm{e} \Omega}{kT} F d_\mathrm{s}$. The "energy" conservation law reads

$$E = \frac{m_p}{2}\left(\frac{dy}{dx}\right)^2 + U(y) = U(y_{max}) \tag{12.34}$$

where y_{max} is the maximum value of the "coordinate" (the maximum slope in the bunch) that is attained when the total "energy" is E and the "kinetic energy" is zero.

To obtain information for the shape of the bunch we shall explore the solutions of the differential equation (12.34) in the limits where the "potential" energy (12.33) is dominated by the first or by the second term.

In the first case ($|J_{st}| << |F_p(h_0/l)|$) we have

$$\frac{m_p}{2}\left(\frac{dy}{dx}\right)^2 - \frac{2}{3}F_p y^{3/2} = -\frac{2}{3}F_p y_{max}^{3/2} \tag{12.35}$$

which can be rewritten as

$$\frac{dy}{dx} = \sqrt{-\frac{4F_p}{3m_p}}\left(y_{max}^{3/2} - y^{3/2}\right)^{1/2} = \sqrt{-\frac{4F_p y_{max}^{3/2}}{3m_p}}\left[1 - \left(\frac{y}{y_{max}}\right)^{3/2}\right]^{1/2} \tag{12.36}$$

Integrating from $y = 0$ to $y = y_{max}$ and taking into account that the corresponding values of x are $x = 0$ and $x = L/2$ (where L is the width of the bunch of steps) one obtains

$$y_{max}\int_0^1 \frac{d\xi}{\left(1-\xi^{3/2}\right)^{1/2}} = \frac{L}{2}\sqrt{-\frac{4F_p y_{max}^{3/2}}{3m_p}} = L\left(-\frac{2Fd_s h_0}{9g\Omega}\right)^{1/2} y_{max}^{3/4} \tag{12.37}$$

which requires negative values of the electromigration force, i.e. $F < 0$.

Taking approximately $y_{max} = z_x'^2 \approx (H/L)^2$ where H is the height of the bunch one finally gets

$$L = 2.37H^{1/3}\left(\frac{\Omega g}{h_0 d_s |F|}\right)^{1/3} \tag{12.38}$$

In the second limit $U(y) \approx -J_{st}y$ (with $|J_{st}| >> |F_p(h_0/l)|$) one can follow the same procedure to arrive to

$$L \sim H^{1/2} \tag{12.39}$$

As seen, expressions (12.38) and (12.39) predict rather different scaling of the bunch shape. It is interesting to note that the numerical integration of the ordinary differential equations (12.25) manifests [12] the scaling law (12.38).

12.4.2 Sublimation with Slow Atom Attachment–Detachment Kinetics

This regime was studied in detail by Krug et al. [32]. Substituting expression (12.17) into (12.28) one obtains again a continuity equation (similar to (12.30)) with

$$J = \frac{K n_s^e \Omega}{2kT}\left[6g\Omega\frac{1}{z_x'}\frac{\partial}{\partial x}\left(z_x'\, z_{xx}''\right) + Fh_0^2\frac{1}{z_x'}\right] \tag{12.40}$$

Here again the steady-state shape of the bunch is defined by $J = J_{st} = \left(K n_s^e \Omega \,/ 2kT\right) Flh_0$ [13]. The "mechanical analog" in this case requires a "potential energy"

$$U(y) = -\frac{2}{3}Flh_0 y^{3/2} + Fh_0^2 y \tag{12.41}$$

Krug et al. [32] found out that this "potential" admits two types of periodic trajectories depending on the "total energy" E (see (12.34)) being negative or positive. In other words, there are two bunch shapes with different scaling properties. When the maximum slope $z_x^{/} \le \frac{3}{2}\frac{h_0}{l}$ one has $L \sim H^{1/2}$ [32]. These shapes are not of physical interest since the slope of the vicinal surface is h_0/l and a bunch with a maximum slope, which is just 1.5 times larger, is difficult to distinguish in the real experiments, where $h_0/l \approx 0.01$. The observable bunch shapes correspond to the limit where the "potential energy" is dominated by the first term, i.e.

$$U(y) = -\frac{2}{3}Flh_0 y^{3/2} \tag{12.42}$$

and one should solve an equation similar to (12.35). Thus one obtains

$$L = 2.986H^{1/3}\left(\frac{g\Omega}{Flh_0}\right)^{1/3} \tag{12.43}$$

12.5 Important Experiments

The scaling relations for the shape of bunches (12.38), (12.39), and (12.43) are the basic quantitative results of the theoretical work on step bunching, induced by direct electric current heating of Si crystals. These results opened a pathway for a number of interesting experiments. Fujita et al. [15] used scanning tunnelling microscope to study the bunch shape and its scaling properties. The initial surface with uniform step train was created by passing a direct current in the step-up direction for 15 s at 1300°C. Step bunches were produced with currents in the step-down direction at 1250°C, and in the step-up direction at 1145°C. The cooling time from 1250 to 600°C and 1145 to 600°C was less than 3 and 4 s, respectively. The change of the

maximum slope of the bunch during the cooling time is assumed to be negligible. To produce bunches of different sizes (containing from 13 to 160 steps) the authors used different sublimation pulse durations (from 10 to 180 s at 1250°C and from 15 to 200 min at 1145°C). STM images and cross sectional profiles of step bunches provide a ground to check the predicted by (12.38) and (12.43) scaling relation $L \sim H^{1/3}$. The experimental data obtained at 1250°C fit the scaling relation $L \sim H^{\alpha}$ with a scaling exponent $\alpha = 0.68 \pm 0.03$ in good agreement with the theory. Comparing the expression for the pre-factor in (12.38) with the experimentally obtained value the authors arrived to the estimation $F/g = 2 \times 10^{-6}\,\mathrm{nm}^{-2}$. They even went further to estimate the electromigration force F and the effective electric charge of the adatoms. In fact, they used the value $g = 0.04\,\mathrm{eV\,nm}$ to obtain effective electric charge $z_{\mathrm{ef}} = 0.14\,|e|$. Having in mind the theoretical results of Akutsu [33] for a strong temperature dependence of the step repulsion coefficient $g(T)$ the authors assumed the value $g = 0.1\,\mathrm{eV\,nm}$ at 1250°C and obtained $z_{\mathrm{ef}} = 0.35\,|e|$. Similar experiments (but in wider temperature range) were carried out by Homma and Aizawa [2]. The obtained results were in good agreement with the theoretical expression (12.38).

A different kind of experiments were carried out by Stoyanov et al. [19]. These authors measured the width of a bunch, containing a fixed number of steps, at different temperatures and interpreted the results on the basis of (12.38) rewritten in a normalized form

$$\frac{g(T)}{g(T_0)} = \frac{L^3(T)}{L(T_0)}\,\frac{I(T)}{I(T_0)} \tag{12.44}$$

To obtain the last relation the authors made use of the findings of Ichikawa and Doi [34] that the electromigration force $F(T)$ is proportional to the electric current $I(T)$ through the Si crystal. The most reliable data were obtained in the case of crystal–vapour equilibrium since the REM image of the Si surface in this case is rather static – there is no steps crossing the large terraces and the requirement for a constant number of steps in the bunch is easy to meet. An Arrhenius plot of the temperature dependence of the right-hand side of (12.44) results in an activation energy of 4.2 eV [19].

12.6 Concluding Remarks

The evolution of non-equilibrium morphologies via kinetic step bunching at vicinal crystal surfaces is an interesting phenomenon which received recently a lot of attention. Contrary to the classical studies of surface shape evolution, driven by the reduction of the surface free energy, here one deals with the evolution, governed by an external driving force. The electromigration of the adatoms at the surface of the growing (or evaporating) crystal is a key feature of the mechanism of the step-bunching instability, induced by the electric current heating of Si crystals. The experiments on step bunching at step-down direction of the electric current [1, 2, 15]

are in perfect agreement with the predictions of the generalized BCF model ((12.12), (12.13), (12.14), (12.17), (12.25), (12.29) and (12.40)) for the self-similarity of the shape of step bunches ((12.38) and (12.43)).

As far as the step bunching at step-up direction of the electric current is concerned the mechanisms of the phenomenon are far from being clearly understood. An attempt to find a key to the problem was made by Stoyanov [17] who noted that the fast surface diffusion could make the surface flux of adatoms exceed the ability of the step to accommodate the arriving atoms in kink positions. In such a situation some of the migrating atoms cross the step without visiting a kink position. In other words the step becomes permeable for the adatoms. This property of the steps at the vicinal surface provides a ground for a completely different mechanism of step-bunching instability. It occurs at step-up direction of the adatom electromigration during sublimation, whereas during crystal growth step bunching appears at step-down drift velocity of the adatoms [17, 18, 35].

This model, however, has a weak point related to the unrealistically high values of the electromigration force necessary to obtain bunching by numerically integrating the equations of step motion. That is why the non-local electromigration can destabilize the vicinal surface with permeable steps, but some results of this model contradict the reported experimental observations [36, 37] in the temperature interval 1040–1190°C.

References

1. A.V. Latyshev, A.L. Aseev, A.B. Krasilnikov, S.I. Stenin, Transformations on clean Si (111) stepped surface during sublimation. Surf. Sci. **213**, 157 (1989)
2. Y. Homma, N. Aizawa, Electric-current-induced step bunching on Si(111). Phys. Rev. B **62**, 8323 (2000)
3. N. Inoue, Y. Tanishiro, K. Yagi, UHV-REM study of changes in the step structures on clean (100) silicon surfaces by annealing. Jpn. J. Appl. Phys. **26**, L293 (1987)
4. H. Kahata, K. Yagi, REM observation on conversion between single domain surfaces of Si(001) 2×1 and 1×2 induced by specimen heating current. Jpn. J. Appl. Phys. **28**, L858 (1989)
5. S. Stoyanov, Heating current induced conversion between 2×1 and 1×2 domains at vicinal (001) Si surfaces – can it be explained by electromigration of Si Adatoms? Jpn. J. Appl. Phys. **29**, L659 (1990)
6. S. Stoyanov, Electromigration induced step bunching on Si surfaces – how does it depend on the temperature and heating current direction? Jpn. J. Appl. Phys. **30**, 1 (1991)
7. R. Schwoebel, Step motion on crystal surfaces. II. J. Appl. Phys. **40**, 614 (1969)
8. M. Ichikawa, T. Doi, Observation of electromigration effect upon Si-MBE growth on Si(001) surface. Vacuum **41**, 933 (1990)
9. S. Stoyanov, H. Nakahara, M. Ichikawa, Dynamics of step bunching induced by DC resistive heating of Si wafer. Jpn. J. Appl. Phys. **33**, 254 (1991)
10. A. Natori, Step structure transformation induced by DC on vicinal Si(111). Jpn. J. Appl. Phys. **33**, 3538 (1994)
11. M. Uwaha, Relaxation of crystal shapes caused by step motion. J. Phys. Soc. Jpn. **57**, 1681 (1988)
12. S. Stoyanov, V. Tonchev, Properties and dynamic interaction of step density waves at a crystal surface during electromigration affected sublimation. Phys. Rev. B **58**, 1590 (1998)

13. D.-J. Liu, J. Weeks, Quantitative theory of current-induced step bunching on Si(111). Phys. Rev. B **57**, 14891 (1998)
14. H.-C. Jeong, E. Williams, Steps on surfaces: experiment and theory. Surf. Sci. Rep. **34**, 171 (1999)
15. K. Fujita, M. Ichikawa, S. Stoyanov, Size-scaling exponents of current-induced step bunching on silicon surfaces. Phys. Rev. B **60**, 16006 (1999)
16. M. Sato, M. Uwaha, Growth of step bunches formed by the drift of adatoms. Surf. Sci. **442**, 318 (1999)
17. S. Stoyanov, Current-induced step bunching at vicinal surfaces during crystal sublimation. Surf. Sci. **370**, 345 (1997); S. Stoyanov, New type of step bunching instability at vicinal surfaces in crystal evaporation affected by electromigration. Surf. Sci. **416**, 200 (1998)
18. J.J. Metois, S. Stoyanov, Impact of growth on the stability-instability transition at Si(111) during step bunching induced by electromigration. Surf. Sci. **440**, 407 (1999)
19. S. Stoyanov, J.J. Metois, V. Tonchev, Current induced bunches of steps on the Si(111) surface – a key to measuring the temperature dependence of the step interaction coefficient. Surf. Sci. **465**, 227 (2000)
20. M. Sato, M. Uwaha, Hierarchical bunching of steps in a conserved system. J. Phys. Soc. Jpn. **67**, 3675 (1998)
21. A. Pimpinelli, V. Tonchev, A. Videcoq, M. Vladimirova, Scaling and universality of self-organized patterns on unstable vicinal surfaces. Phys. Rev. Lett. **88**, 206103 (2002)
22. J. Krug, Introduction to step dynamics and step instabilities. Int Numer Math **149**, 69–95 (2005)
23. V. Popkov, J. Krug, Shape and scaling of moving step bunches. Europhys. Lett. **72**, 1025 (2005)
24. O. Pierre-Louis, Step bunching with general step kinetics: stability analysis and macroscopic models. Surf. Sci. **529**, 114 (2003)
25. Y. Yang, E. Fu, E. Williams, An STM study of current-induced step bunching on Si(111). Surf. Sci. **356**, 101 (1996)
26. O. Pierre-Louis, J.J. Metois, Kinetic step pairing. Phys. Rev. Lett. **93**, 165901 (2004)
27. V. Popkov, J. Krug, Dynamic phase transitions in electromigration-induced step bunching. Phys. Rev. B **73**, 235430 (2006)
28. O. Pierre-Louis, Dynamics of crystal steps. C.R. Physique **6**, 11 (2005)
29. M. Degawa, H. Minoda, Y. Tanishiro, K. Yagi, Direct-current-induced drift direction of silicon adatoms on Si(111)-(1×1) surfaces. Surf. Sci. **461**, L528 (2000)
30. S. Stoyanov, in *Surface Diffusion – Atomistic and Collective Processes*, ed. by M. Tringides (Plenum, New York, NY, 1997), p. 285
31. F.C. Frank, in: *Growth and Perfection of Crystals*, ed. by R. Doremus, B. Roberts, D. Turnbull (Wiley, New York, NY, 1962), p. 411
32. J. Krug, V. Tonchev, S. Stoyanov, A. Pimpinelli, Scaling properties of step bunches induced by sublimation and related mechanisms. Phys. Rev. B **71**, 045412 (2005)
33. N. Akutsu, Y. Akutsu, Statistical mechanical calculation of anisotropic step stiffness of a two-dimensional hexagonal lattice-gas model with next-nearest-neighbour interactions: application to Si(111) surface. J. Phys. Condens. Matt. **11**, 6635 (1999)
34. M. Ichikawa, T. Doi, Study of Si(001) 2×1 domain conversion during direct current and radiative heating. Appl. Phys. Lett. **60**, 1082 (1992)
35. M. Sato, M. Uwaha, Y. Saito, Growth of permeable step bunches formed by drift of adatoms. Surf. Sci. **493**, 480 (2001)
36. B. Gibbons, J. Noffsinger, J. Pelz, Influence of Si deposition on the electromigration induced step bunching instability on Si(111). Surf. Sci. **575**, L51 (2005)
37. F. Leroy, P. Muller, J.J. Metois, O. Pierre-Louis, Vicinal silicon surfaces: from step density wave to faceting. Phys. Rev. B **76**, 045402 (2007)

Index

M. Michailov (ed.), *Nanophenomena at Surfaces,* Springer Series in Surface Sciences 47,
DOI 10.1007/978-3-642-16510-8,